Experimental therapy and detection of glioblastoma: investigation of nanoparticles, ABCG2 modulators and optical imaging of intracerebral xenografts

Dissertation

zur Erlangung des Doktorgrades der Naturwissenschaften (Dr. rer. nat.)
der Naturwissenschaftlichen Fakultät IV - Chemie und Pharmazie -
der Universität Regensburg

vorgelegt von

Matthias Kühnle

aus Tübingen

2010

Die vorliegende Arbeit entstand in der Zeit von September 2006 bis Januar 2010 unter der Leitung von Herrn Prof. Dr. Armin Buschauer und Herrn Prof. Dr. Günther Bernhardt am Institut für Pharmazie der Naturwissenschaftlichen Fakultät IV - Chemie und Pharmazie - der Universität Regensburg.

Das Promotionsgesuch wurde eingereicht im Januar 2010.

Tag der mündlichen Prüfung: 16. Februar 2010

Prüfungsausschuss:

Prof. Dr. Frank-Michael Matysik	(Vorsitzender)
Prof. Dr. Armin Buschauer	(Erstgutachter)
Prof. Dr. Günther Bernhardt	(Zweitgutachter)
Prof. Dr. Jörg Heilmann	(Prüfer)

Für meine Familie

Danksagungen

An dieser Stelle möchte ich mich bedanken bei:

Herrn Prof. Dr. Armin Buschauer für die Gelegenheit, an diesem interessanten Projekt arbeiten zu dürfen, für die Vielfalt an Arbeitsmöglichkeiten sowie seine wissenschaftlichen Anregungen und die konstruktive Kritik bei der Durchsicht der Arbeit.

Herrn Prof. Dr. Günther Bernhardt für seine wissenschaftliche Anleitung und ausführliche Betreuung, seine allzeit umfassende Unterstützung bei der Lösung von Alltagsproblemen im Labor, sein stetes Interesse am Fortgang der Experimente sowie die kritische Durchsicht dieser Arbeit.

Herrn Dr. Thilo Spruß für die intensive Beratung und Betreuung bei den tierexperimentellen Versuchen sowie für die zahlreichen histologischen Untersuchungen.

Herrn Franz Wiesenmayer und Herrn Oskar Baumann für die umfangreiche Unterstützung bei der Durchführung der tierexperimentellen Versuche und die jahrelange äußerst gute Zusammenarbeit in den Tierlaboratorien.

Frau Petra Pistor für die Anfertigung der histologischen Schnittserien und den entsprechenden Färbungen.

Herrn Prof. Dr. Burkhard König, Herrn Dr. Michael Egger, Herrn Cristian Ochoa Puentes, Frau Xuqin Lin und Frau Carolin Fischer für die Synthese der Tariquidar Derivate und die hervorragende Zusammenarbeit.

Herrn Prof. Dr. Achim Göpferich für die Möglichkeit zur Nutzung des Fluoreszenzmikroskops.

Herrn Prof. Dr. Jörg Heilmann und Frau Dr. Birgit Kraus für die Möglichkeit zur Nutzung des Carl Zeiss Cell Observers.

Herrn Dr. U. Bogner für die Bereitstellung der PCO sensicam™ CCD Kamera sowie diverser Glasfiltersätze.

Herrn Peter Richthammer für die Planung und tatkräftige Unterstützung bei der Einrichtung des neuen „In vivo Imaging“-Labors.

Frau Susanne Bollwein, Frau Elvira Schreiber und Frau Brigitte Wenzl für die Unterstützung bei den Arbeiten mit der Zellkultur.

Herrn Prof. Dr. Jörg Kreuter (Universität Frankfurt) für die Bereitstellung der Doxorubicin-beladenen Nanopartikelformulierungen.

Herrn Prof. Dr. Rainer Schobert für die Synthese der Doxorubicin Derivate Sb-59 und Sb-63b.

Frau Anne Mahringer (Universität Heidelberg) für die Untersuchungen zur Modulation der Tariquidar Derivate am ABCC2 Transporter.

den Elektronik- und Feinmechanikwerkstätten der Universität Regensburg für die zahlreichen Modifikationen am „In vivo Imaging“-System und dem „In vivo Imaging“-Labor.

Herrn J. Kiermaier für die HPLC-MS Analyse der Tariquidar Derivate im Rahmen der Stabilitätsuntersuchungen.

Frau Dr. Christine Ertelt (geb. Müller) für die Unterstützung der Untersuchungen zur inhibitorischen Aktivität neuer Tariquidarderivate.

Frau Nathalie Pop für die Unterstützung bei den CLSM-Versuchen.

meinen Kollegen Dr. Christine Ertelt (geb. Müller), Dr. Dietmar Gross und Dr. Peter Jarzyna für die ausführliche Einweisung und Unterstützung beim Erlernen der verschiedenen Arbeitstechniken und Methoden, insbesondere zu Beginn meiner Promotion.

meinem Laborkollegen Peter Höcherl für die jahrelange gute Zusammenarbeit mit anregenden Diskussionen, seine stete Hilfsbereitschaft und seine Untersuchungen zur Modulation der Tariquidar Derivate am ABCB1 Transporter.

allen studentischen Hilfskräften, insbesondere I. Bartelt, J. Bock, S. Gunaratman, P. Kos, K. Schmid, A. Drinhaus, V. Thalhammer für Ihre engagierte Mitarbeit an einigen Projekten dieser Arbeit im Rahmen diverser Forschungspraktika.

meinen Kollegen und Freunden Dr. Christine Ertelt (geb. Müller), Dr. Patrick Igel, Dr. Max Keller, Uwe Nordemann sowie Peter Höcherl für viele anregende Diskussionen und eine wunderschöne Zeit in Regensburg.

allen Lehrstuhlmitgliedern für die Kollegialität und angenehme Arbeitsatmosphäre.

Mein weiterer Dank gilt:

meinen Schulkameraden und Freunden G. Sigel und S. Lutz für Ihren moralischen Beistand.

meiner wunderbaren Familie, auf deren großartige Unterstützung ich mich immer verlassen konnte, sowie insbesondere meiner Freundin Maria für Ihre Liebe, Geduld und Verständnis während unserer gemeinsamen Zeit in Regensburg.

Abstracts and publications

Prior to submission of this thesis, results were published in part or presented as posters or short lectures.

Publication:

Kühnle, Matthias; Egger, Michael; Müller, Christine; Mahringer, Anne; Bernhardt, Günther; Fricker, Gert; König, Burkhard and Buschauer, Armin (2009) *Potent and selective inhibitors of breast cancer resistance protein (ABCG2) derived from the p-glycoprotein (ABCB1) modulator tariquidar*. Journal of Medicinal Chemistry 52 (4), pages 1190-1197.

Poster Presentations:

Frontiers in Medicinal Chemistry (2008), Regensburg, March 2-5:
Kühnle, M.; Müller, C.; Egger, M.; König, B.; Bernhardt, G. and Buschauer, A.
Hoechst 33342 dye uptake: a rapid and sensitive method for the characterization of putative ABCG2 modulators in the 96-well formate.

4th Summer School Medicinal Chemistry (2008), Regensburg, September 29 – October 1:
Kühnle, M.; Müller, C.; Egger, M.; Fischer, C.; König, B.; Bernhardt, G. and Buschauer, A.
Two rapid fluorescence-based microtiter assays for the characterization of putative ABCG2 inhibitors.

Poster Award:

Frontiers in Medicinal Chemistry (2009), Heidelberg, March 15 - 18:
Kühnle, M.; Egger, M.; König, B.; Bernhardt, G. and Buschauer, A.
Optical imaging of orthotopic human brain tumors in nude mice to investigate the potential of ABCG2 modulators in the chemotherapy of glioblastoma.

Short Lectures:

BHS 2008, 10. Treffen der Blut-Hirn Schranke Experten und CaCo2-Anwender, Bad Herrenalb (Germany), May 19 – 21:
Charakterisierung neuer ABCG2-Modulatoren im Mikrotiterplattenformat.

DPhG Doktorandentagung 2009, Pichlarn (Austria), November 18 – 21:
Optical imaging of human orthotopic brain tumors in nude mice.

Contents

Chapter 1

Chapter 2

Chapter 3

Chapter 4

Chapter 5

Appendix

Abbreviations

ABCB1	member 1 of the ATP-Binding Cassette Transporter B subfamily
ABCC2	member 2 of the ATP-Binding Cassette Transporter C subfamily
ABCG2	member 2 of the ATP-Binding Cassette Transporter G subfamily
ABCP	ATP-binding cassette transporter expressed in the placenta (=ABCG2)
ATCC	American Type Culture Collection
ATP	adenosine triphosphate
BBB	blood-brain barrier
BCNU	carmustine
BCRP	Breast Cancer Resistance Protein (=ABCG2)
BCSFB	blood-cerebrospinal fluid barrier
BLI	bioluminescence in vivo imaging
CBTRUS	Central Brain Tumor Registry of the United States
CCD	charge coupled device
CCNU	lamustine
CLSM	Confocal-Laser Scanning Microscopy
CNS	central nervous system
CT	computer tomography
Da	dalton
DMEM	Dulbecco’s Modified Eagle’s Medium
DMSO	dimethylsulfoxide
DNA	desoxyribonucleic acid
Doxo	doxorubicin
DsRed2	enhanced version of the *Discosoma* species red fluorescent protein
EGFP	enhanced green fluorescent protein
EM	electron multiplying
EMEM	Eagle’s Minimum Essential Medium
FACS	Fluorescence Activated Cell Sorter
FCS	fetal calf serum
FSC	forward scatter
FLI	fluorescence in vivo imaging
FTC	fumitremorgin C
G418	geneticin

GeoMean	geometric mean value obtained by FACS measurements
GFP	green fluorescent protein
GF120918	elacridar
Hygro	hygromycin
IC_{50}	concentration of inhibitor required to give 50 % inhibition of activity
i.p.	intraperitoneal
Kat.	Katushka (far-red fluorescent protein)
LB	Luria Bertani (for *E. coli* culture)
Luc2	Luciferase2 (enhanced version of the firefly luciferase)
MDR	multi drug resistance
mRNA	messenger RNA
MRP2	Multidrug Resistance-associated Protein 2 (=ABCC2)
MXR	MitoXantrone Resistance (=ABCG2)
NP	nanoparticle
Orthotopic	occurring at the normal place
PBCA	Poly(ButylCyanoAcrylate)
PBS	phosphate buffered saline
PFA	paraformaldehyde
p-gp	p-glycoprotein 170 (=ABCB1)
pH	negative logarithm of the hydrogen ion concentration
PSC833	valspodar
Puro	puromycin
RNA	ribonucleic acid
RFU	relative fluorescence unit
RLU	relative light unit
s.c.	subcutaneous
SEM	standard error of the mean
SSC	sideward scatter
TFA	trifluoroacetic acid
Topo	topotecan
WHO	World Health Organization
XR9576	tariquidar

Chapter 1

Introduction

1.1 Malignant brain tumors

1.1.1 Classification

Malignant brain tumors comprise various groups of CNS neoplasms that can be divided into primary tumors, originating from cells physiologically present in the brain and secondary tumors, derived from extracranial neoplasms which have metastasized to the brain. Primary brain tumors are classified by the predominant cell type of the respective neoplasm according to clearly defined histopathological and clinical criteria. More than 30 years ago, the international classification of diseases for oncology (ICD-O) was established, which serves as an indispensable guideline for the grading of cancers by providing histopathology and mortality data for epidemiological as well as oncological studies [Louis et al., 2007]. In 1979, the first edition of histological typing of CNS tumors was published [Zülch, 1979] and since that time continuously updated, e.g. by the introduction of immunohistochemistry and genetic profiling as well as clinical signs, symptoms, imaging and many other aspects, aiming at a refined classification [Kleihues et al., 1993; Kleihues and Sobin, 2000]. Quite recently, the latest version of the WHO (World Health Organization) classification of tumors of the central nervous system was published [Louis et al., 2007]. It contains, amongst several new entities and histological variants the updated WHO grading scheme for malignant brain tumors.

Up to date, the so-called group of “glioma” represents a good portion of the primary malignant brain tumors, including astrocytomas, oligodendrogliomas, ependymomas and oligoastrocytomas. Gliomas constitute malignancies of the supporting tissue, which physiologically acts as a kind of protector and supporter for the nerve cells in the brain. Hence, the classification of different glioma types depends on the similarity of the tumor cells compared to healthy glial cells, namely astrocytes, oligodendrocytes and ependymal cells. Furthermore, several kinds of mixed gliomas contain great fractions of different cell types, for example astrocytes and oligodendrocytes or astrocytes and ependymal cells. According to the Central Brain Tumor Registry of the United States (CBTRUS), gliomas amount to 33 % of all brain tumors and even 80 % of the malignant brain neoplasms of addults. Moreover, 77 % of all primary malignant brain tumors belong to the astrocytoma class [CBTRUS, Online 2009].

1.1.2 Diagnosis procedure of brain tumors

At the beginning of brain tumor diagnosis, usually typical parameters such as vision, hearing, balance, coordination and reflexes are checked. Results of these preliminary enquiries rule the further procedure, which can contain the use of special imaging methods, such as CT, MRI or PET, to affirm the existence of a tumor. Furthermore, visualization of the brain by aforementioned techniques allows localizing the putative neoplasm as well as distinguishing the tumor from healthy tissue and, depending on the method, gives information on impaired brain activity and function caused by the tumor.

1.1.2.1 Imaging techniques

Computed X-ray Tomography (CT) describes the measurement of X-ray attenuation (≈ 40-80 keV) as the basis for a 2-dimensional imaging procedure. Despite of high spatial resolution (20 μm), simple applicability and relatively low costs, CT implies several drawbacks such as low sensitivity, high radiation doses, lack of functional information as well as poor soft tissue contrast (might be enhanced by contrast agents) [Laboratory for Preclinical Imaging Technologies, 2007].

Magnetic Resonance Imaging (MRI) represents an alternative method of noninvasive tumor imaging. MRI is characterized by high spatial resolution (50-500 μm) and the use of non-ionizing radiation. However, the low sensitivity (micromolar range) and mainly the high costs limit the application of Magnetic Resonance Imaging as a standard procedure in preclinical oncology [Laboratory for Preclinical Imaging Technologies, 2007].

An excellent technique for the visualization of metabolic and functional processes, e.g. in cardiology, immunology but also particularly in oncology, is Positron Emission Tomography (PET). For PET measurements, positron emitting short-lived radionuclides (half-life ideally several hours) are injected into the specimen. Thereby, the positron-electron annihilation leads to the generation of two 511 keV gamma rays which are emitted in an angle of 180° and are determined by a static detector. The path-length of the positrons depends on tissue density as well as positron energy.

Due to differences in metabolic processes in tumors and healthy tissues, PET techniques are very valuable methods in diagnostics, therapy planning and therapy control. Complex processing of radiotracers, limited resolution and little information on the correlation of morphology and PET signals restrict the application of PET imaging [Laboratory for Preclinical Imaging Technologies, 2007].

In view of the benefits and disadvantages of the aforementioned imaging techniques, the combination of different methods is a promising approach to improve noninvasive imaging. Such "Multi Modality Imaging" can be realized for example by combining Positron Emission Tomography with CT or MRI, respectively. Thereby, morphological information from CT / MRI can be connected with functional data obtained by the PET technique [Laboratory for Preclinical Imaging Technologies, 2007].

1.1.2.2 Histopathology

In order to confirm a putative brain tumor, suggested from preliminary imaging explorations, biopsy of the tissue for histopathology is essential. Moreover, biopsy is the prerequisite to distinguish between different subtypes of neoplasms and to grade malignancy. For example, the astrocytic origin of a tumor becomes obvious by the detection of star-shaped cells. Astrocytomas have been shown to extensively infiltrate into the healthy brain tissue, and especially glioblastoma multiforme proved to display a great variety in the extent, the geometry and the character of the infiltrating margin [Burger et al., 1988].

Brain tumors are classified according to histological grading which is considered as a "malignancy scale". The WHO classification contains 4 different grades representing ascending malignancy of the intracranial neoplasms. Whereas grade I tumors are characterized by a low proliferative potential and offer the chance of cure after resection, neoplasms ranked in grade II show infiltrative growth and tend to recur. Furthermore, some types of grade II tumors can progress to high grade malignancies, for instance, low-grade diffuse astrocytomas can develop to anaplastic astrocytoma or even glioblastoma. The classification of tumors as WHO grade III corresponds to histological evidence of malignancy such as vigorous mitotic activity or nuclear atypia.

Finally, the category WHO grade IV is applied to tumors characterized by microvascular proliferation and / or necrosis in addition to the aforementioned features [Louis et al., 2007].
An example of WHO grad IV classification includes glioblastoma as a subtype of astrocytomas, which account for more than 3 quarter of all astrocytic tumors. A synopsis of the current grading of the predominating group of brain neoplasms, namely the astrocytic tumors, is given in **Table 1.1**.

Table 1.1: WHO grading (I-IV) of astrocytic tumors according to "The 2007 WHO Classification of Tumours of the Central Nervous System". Modified from Louis et al. [Louis et al., 2007]

Astrocytic tumors	**I**	**II**	**III**	**IV**
Subependymal giant cell astrocytoma	●			
Pilocytic astrocytoma	●			
Pilomyxoid astrocytoma		●		
Diffuse astrocytoma		●		
Pleomorphic xanthoastrocytoma		●		
Anaplastic astrocytoma			●	
Glioblastoma				●
Giant cell glioblastoma				●
Gliosarcoma				●

However, the classification as well as the grading of the malignancy by means of histopathology is associated with several limitations. Since only small biopsy samples are taken, it is possible that the neoplasm is classified into the false subtype of CNS tumor. This can be explained by different histological grades of malignancy, which are found in various areas of the same tumor [Kepes, 1994]. Hence, inaccurate diagnosis might be responsible for underestimation of the degree of malignancy [Glantz et al., 1991] and cause suboptimal therapy of the malignant brain tumor [Jackson et al., 2001].

1.1.2.3 Molecular classification of tumor types

In recent years much effort has been spent on developing more accurate methods for the grading of CNS neoplasms. Predominantly, the highly specific molecular classification of tumor types by identifying genetic abnormalities in different subtypes of neoplasms has become a valuable tool for the detailed characterization of various malignancies. Such gene expression profiling studies were performed by several workgroups to distinguish between non-neoplastic brain tissue and gliomas of different pathology. Moreover, these methods might be helpful for identifying new therapeutic targets in the therapy of malignant brain tumors. For example, Shai et al. could characterize the key molecular differences between healthy brain tissue, grade II and III astrocytomas, oligodendrogliomas and glioblastomas by means of 170 selected genes [Shai et al., 2003]. Quite recent studies, using oligonucleotide microarrays and real-time quantitative PCR, indicated the presence of 18 over-expressed genes in human primary glioblastoma compared to non-neoplastic brain tissues. These investigations suggest a significant role of such over-expressed genes in the pathogenesis of brain tumors and might be promising starting points in the search for new targets in glioblastoma treatment [Scrideli et al., 2008].

Taken together, in addition to highly efficient noninvasive imaging techniques (e.g. CT, MRI and PET) for the early diagnosis of brain tumors, reliable histopathological examinations are indispensable for the confirmation as well as for the grading of the tumor. Beyond that, the genetic profiling of different tumor types demonstrating specific mutations and / or overexpression of genes in various neoplasms has become an alternative strategy to classify tumors and to identify putative new targets for cancer therapy.

1.1.3 Prognosis

The tumor grade is of critical prognostic value, but other criteria including age of the patient, tumor location, proliferation indices, genetic alterations and many more are to be considered in the prediction of survival time [Louis et al., 2007]. Despite extensive search for new approaches in the therapy of gliomas over the last 3 decades, the median survival time could not be appreciably enhanced.

Typically, patients bearing WHO grade II gliomas (diffuse astrocytoma, oligodendroglioma and mixed oligoastrocytoma) survive 5 to 7 years after diagnosis. For grade III gliomas (e.g. anaplastic astrocytoma), an averaged survival of 2-3 years is typical, whereas patients with high-grade glioblastoma multiforme (WHO grade IV) succumb to the disease in large part within 1 year after diagnosis [Rees, 2002; Louis et al., 2007]. A prolongation of the survival period from 12 to 15 months was recently achieved by concomitant and adjuvant application of temozolomide plus radiotherapy [Stupp et al., 2005]. Nevertheless, the increase by 3 months in the median survival reflects the deflating situation in the therapy of glioblastoma during the last 30 years. Only 3-5 percent of glioma patients are classified as long-term survivors who outlive the disease for more than 5 years. Definite reasons for such long-term survivals are still unclear, although several clinical factors seem to be beneficial, in particular a young age at the point of diagnosis [Krex et al., 2007].

1.1.4 Management of WHO grade III and grade IV gliomas

The current recommendations for the treatment of high grade (WHO grade III and IV) glioma, including anaplastic astrocytoma and glioblastoma, consider several different therapeutic strategies [Alberta Provincial CNS Tumor Team, 2009]:

(1) Aiming at both, debulking of the malignancy and obtaining of tissue for diagnosis, surgery represents the accepted starting point in the therapy of glioma. Moreover, neurosurgical literature advocates the maximally possible resection of tumor tissue [Quigley and Maroon, 1991; Alberta Provincial CNS Tumor Team, 2009], since, according to this approach, a survival benefit for glioma patients was proven in many studies [Ammirati et al., 1987; Nitta and Sato, 1995; Kiwit et al., 1996; Lacroix et al., 2001].

(2) Already in 1978, Walker et al. demonstrated the efficacy of postoperative radiotherapy (RT) in the treatment of anaplastic glioma [Walker et al., 1978]. Using a dose of 50-60 Gy, the median survival was increased to 8.4 months compared to the best supportive therapy [Alberta Provincial CNS Tumor Team, 2009]. Still today, a total dose of 60 Gy in 30 fractions is standard in external beam radiation therapy. Dose-effect studies on patients bearing anaplastic astrocytoma or glioblastoma multiforme revealed an increased median survival using a dose of 60 Gy compared to 45 Gy [Walker et al., 1979]. Despite several trials, using higher doses [Nelson et al., 1988; Chan et al., 2002], no significant improvement in survival time was reported so far [Alberta Provincial CNS Tumor Team, 2009]. Furthermore, trials with alternative fractionation regimens such as hyper-fractionation and super-fractionation, did not statistically significantly improve survival outcome [Alberta Provincial CNS Tumor Team, 2009].

(3) Due to poor brain penetration, the applicability of cytostatic agents in the therapy of malignant brain tumors is extremely limited. The most utilized chemo-therapeutics are the nitrosoureas carmustine (BCNU) and lomustine (CCNU) as well as the alkylating benzamide procarbazine.

Since 2005, the concomitant and adjuvant chemotherapy using the alkylating agent temozolomide (TMZ) combined with radiotherapy (RT) represents the standard regimen in the treatment of WHO grade IV glioma after surgery [Alberta Provincial CNS Tumor Team, 2009]. Temozolomide is an orally available prodrug which penetrates into the brain and spontaneously undergoes hydrolysis to its active metabolite MTIC [5-(3-dimethyl-1-triazenyl)imidazole-4-carbox-amide]. Subsequently, MTIC breaks down to methyldiazonium which causes methylation of guanine residues in the DNA [Koukourakis et al., 2009]. An overview of the metabolism of temozolomide is shown in **Figure 1.1**.

In contrast to other combined chemotherapy and radiation regimens, which showed no survival benefit, e.g. radiotherapy plus mitomycin [Halperin et al., 1996], the concomitant and adjuvant temozolomide application proved to result in survival advantage. Athanassiou et al. performed a multicenter randomized phase II study to compare the concomitant temozolomide RCT (radiochemotherapy) with RT alone, in newly diagnosed glioblastoma multiforme [Athanassiou et al., 2005]. For this purpose, 57 patients received TMZ (75 mg/m²/d; orally) concomitantly with RT (60 Gy in 30 fractions). Furthermore, the treatment consisted of 6 consecutive cycles of TMZ (150 mg/m² on days 1 through 5 and 15 to 19 every 28 days). In contrast, the second group (53 patients) was treated with RT alone (60 Gy in 30 fractions). These investigations revealed that the concomitant and adjuvant temozolomide radiochemotherapy (RCT) caused not only an increase of the median time to progression (10.8 months RCT vs. 5.2 months RT) but also yielded a higher 1-year progression-free survival rate (36.6% RCT vs. 7.7% RT). In addition, the median survival time (13.4 months RCT vs. 7.7 months RT) as well as the 1-year overall survival (56.3% RCT vs. 15.7% RT) proved to be significantly enhanced [Athanassiou et al., 2005].

A similar trial on 573 patients with newly diagnosed glioblastoma multiforme was conducted by Stupp et al. [Stupp et al., 2005]. The study showed a median survival of 14.6 months, when treated with radiotherapy plus temozolomide, whereas patients who received radiotherapy alone survived at an average of 12.1 months [Stupp et al., 2005].

Quite recently, investigations on the mechanism of action as well as on resistance effects of temozolomide were reviewed in detail by Koukourakis et al. [Koukourakis et al., 2009]. In addition, this review presents current clinical studies and applications of temozolomide.

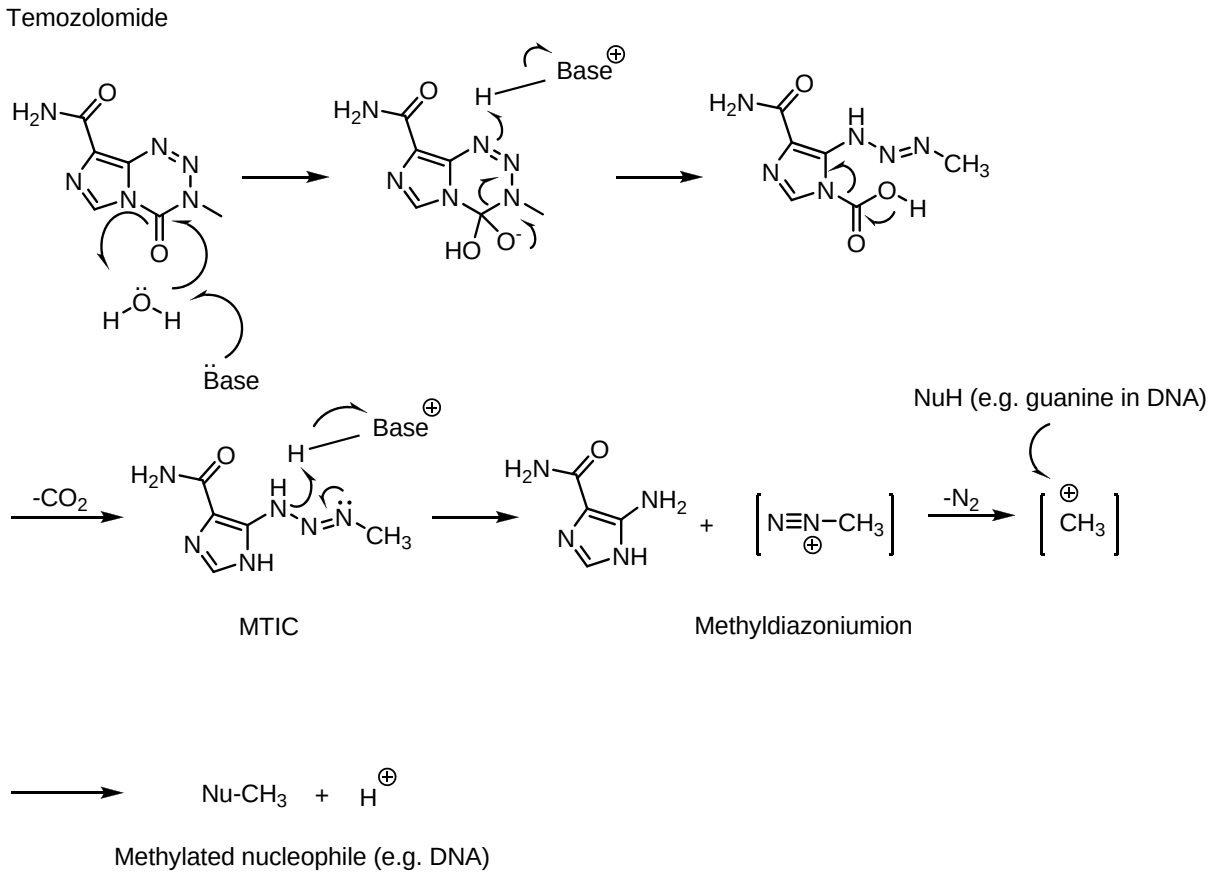

Figure 1.1: Metabolism of the alkylating chemotherapeutic temozolomide to its active metabolite MTIC and generation of the DNA alkylating methyldiazonium ion (modified from [Koukourakis et al., 2009]).

1.2 New approaches to the therapy of glioblastoma

Despite extensive oncological research aiming at improved therapy of malignant brain tumors, the prognosis, especially for glioblastoma multiforme (GBM) patients still remains unfavorable. Over the last 3 decades, the median survival of GBM patients could be only marginally prolonged. The concomitant and adjuvant temozolomide treatment combined with radiotherapy proved to be a survival benefit [Athanassiou et al., 2005; Stupp et al., 2005], but nevertheless yielded only a slight increase in average survival from 12 to 15 months. Hence, new approaches to the therapy of glioblastoma are still required. Some current aspects are discussed in more detail in the following. Prior to this, essential features of the blood-brain barrier (BBB) are summarized since many problems and limitations in the therapy of malignant brain tumors are caused by the morphology and functionality of the BBB.

1.2.1 Architecture and function of the blood-brain barrier (BBB)

Both, endogenous and exogenous toxins are prevented from entering the brain by 2 physiological barriers, namely the blood-brain barrier (BBB) and the blood-cerebrospinal fluid barrier (BCSFB). Whereas the BBB is formed by tight junctions connecting the cerebral endothelial cells, the blood-cerebrospinal fluid barrier represents a network of associated epithelial cells from the choroid plexus [Sugiyama et al., 1999]. However, the BCSFB is estimated to have a 5000-fold smaller area than the blood-brain barrier [Deeken and Löscher, 2007] and, consequently, plays a less important role in the homeostasis of the brain.

1.2.1.1 Characteristics of the cerebral endothelium

The cerebral endothelial cells at the blood-brain barrier are unique in their appearance since they show continuous tight junctions and lack of fenestration. Moreover, they possess low pinocytotic activity [Wolburg and Lippoldt, 2002]. Several transmembrane proteins, mainly occludine, claudins and the so-called JAM's (junctional adhesion molecules), interact with the brain endothelial cells and thereby contribute to the complexity of the tight junctions at the BBB [Cecchelli et al., 2007]. Hence, all these specifics arrange for an effective seal of the paracellular pathway into the brain.

In addition, the cerebral endothelial cells are not only surrounded by extracellular matrix and basal membrane but also by astrocytic and pericytic end-feets. More than 90 % of the cell surface of brain endothelial cells are covered by astrocytes, which have the ability to partially control the permeability of the BBB by releasing a great number of different chemical substances [Abbott et al., 2006; Deeken and Löscher, 2007]. Another characteristic of the brain capillaries is their 100-200 fold higher electrical resistance compared to the vasculature in the periphery (1000-2000 $\Omega \cdot cm^{-2}$ vs. 10 $\Omega \cdot cm^{-2}$) [Deeken and Löscher, 2007], which is thought to be reasoned by the great variability of transmembrane protein composition, mainly the high occludine expression [Hirase et al., 1997]. This electrical resistance mediates an additional prevention against the penetration of polar and ionic substances.

1.2.1.2 Physicochemical criteria of drugs to access to the brain

Due to the highly effective compartmentalization of the brain by the blood-brain barrier, drugs administered to target the brain, e.g. cytostatics in the therapy of malignant brain tumors, have to fulfill specific physicochemical criteria with respect to membrane permeation and access to the brain [Doan et al., 2002]. Whereas small (<400 Da) nonpolar compounds should be able to passively diffuse via the transcellular pathway [Pardridge, 2003], water-soluble or polar substances can only cross the BBB via transport systems [Deeken and Löscher, 2007].

1.2.1.3 Drug efflux transporters at the BBB

However, despite fulfilling the aforementioned criteria in terms of molecular weight and lipophilicity, many compounds including cytostatics show only limited brain penetration since they are actively extruded by a vast number of drug efflux transporters which are expressed at the blood-brain barrier. ATP-Binding Cassette (ABC) transporters represent a major family of such efflux pumps which compromise the efficacy of many anticancer drugs in the chemotherapy of malignant brain tumors. Predominantly, expression of the subtypes ABCB1 (MDR1, p-glycoprotein 170), ABCC2 (MRP2, multidrug related protein 2) and ABCG2 (MXR, breast cancer resistance protein) at the BBB were shown to play an important role in the resistance of CNS neoplasms. These transporters use the energy of ATP-hydrolysis to actively pump out a vast number of structurally unrelated compounds. Further details on ABC efflux pumps are given in chapter 4.

In recent years, a second class of drug efflux transporters, organic anion and cation transporters (OAT's and OCT's), has gained interest with respect to expression at the blood-brain barrier. Nevertheless, the research on OAT's and OCT's in the chemoresistance of malignant brain tumors is still at the beginning [Deeken and Löscher, 2007].

1.2.2 Strategies to overcome the blood-brain barrier

1.2.2.1 Osmotic opening of the BBB

An interesting approach to increase intracerebral levels of water-soluble and high molecular weight molecules represents the intermittent opening of the BBB by direct infusion of hypertonic solutions, e.g. arabinose or mannitol, into the carotid artery. More than 30 years of extensive pre-clinical studies have contributed to a more detailed understanding of the mechanism of action during osmotic opening [Bellavance et al., 2008]. Current opinions postulate that the tight junctions between the cerebral endothelial cells are widened by several processes, including endothelial cell shrinkage, vascular dilation as well as modulation of the endothelial cytoskeleton and junctional proteins [Rapoport, 2001]. These effects on the cytoskeleton and junctional proteins are caused by increased intracellular Ca^{2+} levels after administration of the hyperosmotic solution [Nagashima et al., 1997], and there is strong evidence that the duration of opening can be prolonged by pre-treatment with Na^{+}/Ca^{2+} exchange blockers [Nagashima et al., 1997; Bhattacharjee et al., 2001; Rapoport, 2001].

The procedure of osmotic opening has been utilized in the treatment of various malignant brain tumors [Bellavance et al., 2008]. For example, in a clinical study cyclophosphamide was intravenously administered to 41 patients bearing astrocytomas. Subsequently, osmotic opening of the BBB was performed on 28 patients, followed by intra-arterial application of carboplatin and etoposide (group A), whereas 13 patients obtained the chemotherapeutics without blood-brain barrier disruption (group B). The median survival of patients of group A turned out to be 90 weeks while the survival time of patients of group B was 50 weeks [Kraemer et al., 2002], suggesting a benefit from BBB disruption prior to chemotherapy.

Quite recently, osmotic opening of the BBB was applied to a small group of patients with diffuse pontine gliomas (DPG), a subtype of high grade astrocytoma, which typically occurs in children. The patients were treated monthly by osmotic BBB opening followed by intra-arterial application of carboplatin or methotrexate as well as intravenous injection of cyclophosphamide and etoposide. Efficiency of the therapy was monitored by MRI imaging, which demonstrated 2 partial responses, 5 cases of stable diseases and 1 patient with progressing disease. The median time to tumor progression was 15 months and the survival time averaged 27 months, indicating improved impact on both parameters compared to previous DPG studies [Hall et al., 2006].

The disruption of the BBB turned out to be a promising pre-treatment to improve the response to cytostatic agents in brain tumor patients. However, since this procedure represents a drastic and non-selective intervention, which facilitates the access of putative neurotoxic compounds to the brain, osmotic BBB opening must be carefully considered in each individual case.

1.2.2.2 Immunoliposomes

Certain endogenous large molecules such as insulin, the insulin-like growth factors IGF-1 and IGF-2, LDL (low density lipoprotein) and transferrin are transported into the brain by receptor-mediated trans- and / or endocytosis [Pardridge, 2007]. The underlying mechanisms pave the way to another interesting approach of drug delivery to the central nervous system. Drug-containing liposomes can be tagged with antibodies against suitable receptors (immunoliposomes) to induce endo- and / or transcytosis after recognition of the drug carrier as a receptor ligand [Deeken and Löscher, 2007].

1.2.2.2.1 Immunoliposomes targeting the transferrin receptor

Transferrin is a glycoprotein and represents the major iron binding carrier in the serum of vertebrates [Yang et al., 1984]. The transferrin receptor 1 (CD71, TfR) possesses a molecular mass of 85 kDa and affiliates to type II transmembrane proteins [Kasibhatla et al., 2005]. The expression of TfR on brain capillaries, which was already shown in 1984 [Jefferies et al., 1984], might be relevant due to extensive oxidative metabolism in neuronal cells.

After binding of transferrin to TfR, the iron ions can be channeled into the cell by either endo- and / or transcytosis. Both mechanisms were discussed by several workgroups on the basis of in vitro and in vivo results [Broadwell et al., 1996; Li and Qian, 2002].

This efficient uptake pathway of iron into the brain has already been exploited in the approach of site-specific drug delivery into the CNS by linking liposomes with incorporated drugs to specific antibodies against the transferrin receptor, which is expressed at the BBB [Qian et al., 2002]. OX26, a monoclonal antibody against TfR, was attached to the surface of daunomycin incorporated in liposomes [Huwyler et al., 1996]. The drug containing immunoliposomes, free daunomycin and non-functionalized daunomycin-loaded liposomes, respectively, were intravenously injected into rats, and the daunomycin concentrations in the brain of the animals were determined. Comparing daunomycin attached to OX26 immunoliposomes with administered free drug, the authors found increased brain delivery by using the drug carrier system resulting in about 10,000 fold higher brain concentrations of daunomycin [Huwyler et al., 1996; Deeken and Löscher, 2007]. Furthermore, OX26 immunoliposomes were also successfully applied in vitro to circumvent ABCB1 mediated digoxin resistance. In immortalized rat brain capillary endothelial cells, digoxin uptake was enhanced by a factor of 25 by incorporating the drug into OX26-immunoliposomes. The authors concluded that this immunoliposome-based drug delivery system might be generally useful to by-pass ABCB1, and thereby, to increase the levels of ABCB1 substrates in target cells [Huwyler et al., 2002].

These studies on immunoliposomes demonstrate the prospect of the drug-delivery system to increase drug concentrations in the brain and to circumvent efflux pump mediated drug resistance. Thus, with respect to chemotherapy of brain tumors, the application of cytostatics incorporated in immunoliposomes seems to be a promising approach to obtain sufficient drug levels in the brain.

1.2.2.3 Nanoparticles

The use of nanoparticles (NP) as carrier systems is another attractive strategy to deliver drugs across the blood-brain barrier. This approach can also be applied to compounds, which are physicochemically and / or biochemically unstable, e.g. due to enzymatic- or pH-dependent cleavage, as such drugs are efficiently protected by encapsulation into NP [Kawashima, 2001].

Nanoparticles consist of chemically different biodegradable macromolecules, which form nano-sized solid, colloidal drug carrier systems. The pharmacologically active compound is dissolved, entrapped or encapsulated in the NP or alternatively attached / adsorbed to the surface of the particles [Chopra et al., 2008]. Typically, their size ranges from 10 to 1000 nm with an average size of 50-300 nm [Olivier, 2005]. Polymers mostly used for the preparation of nanoparticulate systems are poly(D,L-lactide), poly(lactic acid), poly(D,L-glycolide), poly(lactide-co-glycolide), poly(lactic-co-glycolic acid) (PLGA) and poly(cyanoacrylate). However, nanoparticles have also been generated by using gelatin [Farrugia and Groves, 1999], chitosan [Fernández-Urrusuno et al., 1999] and sodium alginate [Aynie et al., 1998]. Additionally, in many cases the nanoparticles are coated with different kinds of surfactants such as poloxamers, polysorbates or cremophors [Kreuter et al., 1997]. This surface modification has been proven to significantly influence the effective targeting of particular tissues, predominantly the delivery to the brain [Kreuter et al., 1997]. Moreover, it was shown that surfactant coating reduced the adverse effects of toxic compounds to several organs [Gelperina et al., 2002].

Drug release and biodegradation of the nanoparticles are key issues. Desorption of the surface-bound / adsorbed drug, diffusion through the nanoparticle matrix, diffusion through the polymer wall (nanocapsules), erosion of the NP matrix and combined erosion / diffusion processes dictate the rate of drug release in vivo [Soppimath et al., 2001]. Many ideas, explaining the overcoming of the BBB, have been discussed over the recent decades. Current opinions suggest that the coated nanoparticles adsorb apolipoproteins on their surface enabling a receptor (e. g. LDL receptor) mediated uptake of the drug-loaded particles into the brain [Petri et al., 2007].

Nanoparticle drug carrier systems have been proven to transport a vast number of compounds including opioids [Alyautdin et al., 1997], growth factors [Kurakhmaeva et al., 2009] and cytostatics [Gulyaev et al., 1999; Huang et al., 2008] to the brain. Hence, the use of nanoparticles as delivery systems represents an attractive approach to improve the chemotherapy of malignant brain tumors. The suitability of drug-loaded and surfactant-coated poly(butylcyanoacrylate) nanoparticles is elaborately discussed in chapter 3.

1.2.2.4 Modulation of ABC-efflux transporters at the BBB

The activity of ATP-binding cassette transporters at the blood-brain barrier, predominantly ABCB1 and ABCG2 [Dauchy et al., 2008], limits the access of cytostatics to the central nervous system. Therefore, the chemotherapy of malignant brain tumors is strongly restricted. In order to improve the brain penetration of cytotoxic compounds, which are known to be ABC-transporter substrates, the inhibition of these efflux pumps by selective modulators represents an attractive strategy.

By means of this approach, an enhanced brain uptake of the ABCB1 substrate vinblastine was demonstrated by Cisternino et al. [Cisternino et al., 2001]. CF-1 mice were pre-treated with the ABCB1 modulators PSC 833 (valspodar) and GF 120918 (elacridar) respectively. Subsequently, radiolabeled vinblastine was administered via in situ brain perfusion techniques and the intracerebral drug transport was determined. Mice, pre-treated with the efflux pump inhibitors, showed a 3-fold increase in the brain transport of vinblastine compared the non-treated controls. Moreover, in a laborious proof-of-concept study with nude mice bearing intracerebral human glioblastoma, the co-administration of the 2nd generation ABCB1 inhibitor valspodar with the cytostatic paclitaxel yielded 6-8 fold higher brain levels of paclitaxel as obtained without valspodar application [Fellner et al., 2002]. The increased drug levels resulted in a decrease of tumor volume by approximately 90 %. Similarly, the brain penetration of the ABCG2 substrate imatinib mesylate in mice could be significantly enhanced by co-administration of an ABCG2 efflux pump inhibitor [Breedveld et al., 2005]. For this purpose, the animals obtained imatinib either alone or combined with the ABCG2 modulator pantoprazol, which is approved as a proton pump inhibitor. Mice, treated with both imatinib and pantoprazol showed 5.2-fold higher brain levels of imatinib, suggesting improved drug delivery to the CNS due to ABCG2 modulation.

Thus, compounds acting as modulators of ABC-efflux transporters are promising drug candidates in combination with cytostatics in order to improve the therapy of malignant brain tumors. In view of the clinically available chemotherapeutics, which are in principle applicable in the therapy of CNS neoplasms, but which are excluded from the brain by transporters, the development of potent inhibitors for different ABC-efflux pumps is of particular interest. Only a few potent inhibitors of the recently discovered ABCG2 transporter are known so far, including the dual ABCB1 / ABCG2 inhibitor elacridar [de Bruin et al., 1999] and the fumitremorgin C analog Ko143[Allen et al., 2002]. For this reason, the identification of highly potent ABCG2 modulators as appropriate candidates for combination treatment might contribute to the progress in the pharmacotherapy of malignant brain tumors. Further details on ABCB1 and ABCG2 modulators are given in chapter 4.

References

Abbott, N. J., Ronnback, L. and Hansson, E. (2006). Astrocyte-endothelial interactions at the blood-brain barrier. Nat. Rev. Neurosci. **7**(1): 41-53.

Alberta Provincial CNS Tumor Team (2009). Clinical Practice Guideline - Management of Glioblastoma Multiforme. Alberta Cancer Board.

Allen, J. D., van Loevezijn, A., Lakhai, J. M., van der Valk, M., van Tellingen, O., Reid, G., Schellens, J. H. M., Koomen, G.-J. and Schinkel, A. H. (2002). Potent and Specific Inhibition of the Breast Cancer Resistance Protein Multidrug Transporter in Vitro and in Mouse Intestine by a Novel Analogue of Fumitremorgin C. Mol. Cancer Ther. **1**(6): 417-425.

Alyautdin, R. N., Petrov, V. E., Langer, K., Berthold, A., Kharkevich, D. A. and Kreuter, J. (1997). Delivery of loperamide across the blood-brain barrier with polysorbate 80-coated polybutylcyanoacrylate nanoparticles. Pharm. Res. **14**(3): 325-8.

Ammirati, M., Vick, N., Liao, Y. L., Ciric, I. and Mikhael, M. (1987). Effect of the extent of surgical resection on survival and quality of life in patients with supratentorial glioblastomas and anaplastic astrocytomas. Neurosurgery **21**(2): 201-6.

Athanassiou, H., Synodinou, M., Maragoudakis, E., Paraskevaidis, M., Verigos, C., Misailidou, D., Antonadou, D., Saris, G., Beroukas, K. and Karageorgis, P. (2005). Randomized Phase II Study of Temozolomide and Radiotherapy Compared With Radiotherapy Alone in Newly Diagnosed Glioblastoma Multiforme. J. Clin. Oncol. **23**(10): 2372-2377.

Aynie, I. C., Vauthier, C., Fattal, E., Foulquier, M. and Couvreur, P. (1998). Alginate nanoparticles as a novel carrier for antisense oligonucleotide, in: J.E. Diederichs, R. Muler (Eds.), Future Strategies of Drug Delivery With Particulate Systems; Med-pharm Scientific Publisher, Stuttgart. 5-10.

Bellavance, M.-A., Blanchette, M. and Fortin, D. (2008). Recent Advances in Blood–Brain Barrier Disruption as a CNS Delivery Strategy. AAPS J. **10**(1): 166-177.

Bhattacharjee, A. K., Nagashima, T., Kondoh, T. and Tamaki, N. (2001). The effects of the Na+/Ca++ exchange blocker on osmotic blood-brain barrier disruption. Brain Res. **900**(2): 157-162.

Breedveld, P., Pluim, D., Cipriani, G., Wielinga, P., van Tellingen, O., Schinkel, A. H. and Schellens, J. H. M. (2005). The Effect of Bcrp1 (Abcg2) on the In vivo Pharmacokinetics and Brain Penetration of Imatinib Mesylate (Gleevec): Implications for the Use of Breast Cancer Resistance Protein and P-Glycoprotein Inhibitors to Enable the Brain Penetration of Imatinib in Patients. Cancer Res. **65**(7): 2577-2582.

Broadwell, R. D., Baker-Cairns, B. J., Friden, P. M., Oliver, C. and Villegas, J. C. (1996). Transcytosis of Protein through the Mammalian Cerebral Epithelium and Endothelium: III. Receptor-Mediated Transcytosis through the Blood-Brain Barrier of Blood-Borne Transferrin and Antibody against the Transferrin Receptor. Exp. Neurol. **142**(1): 47-65.

Burger, P. C., Heinz, E. R., Shibata, T. and Kleihues, P. (1988). Topographic anatomy and CT correlations in the untreated glioblastoma multiforme. J. Neurosurg. **68**(5): 698-704.

CBTRUS (Online 2009). CBTRUS Statistical Report: Primary and Central Nervous System Tumors Diagnosed in the United States in 2004-2005.

Cecchelli, R., Berezowski, V., Lundquist, S., Culot, M., Renftel, M., Dehouck, M.-P. and Fenart, L. (2007). Modelling of the blood-brain barrier in drug discovery and development. Nat. Rev. Drug Discov. **6**(8): 650-661.

Chan, J. L., Lee, S. W., Fraass, B. A., Normolle, D. P., Greenberg, H. S., Junck, L. R., Gebarski, S. S. and Sandler, H. M. (2002). Survival and Failure Patterns of High-Grade Gliomas After Three-Dimensional Conformal Radiotherapy. J. Clin. Oncol. **20**(6): 1635-1642.

Chopra, D., Gulati, M., Saluja, V., Pathak, P. and Bansal, P. (2008). Brain Permeable Nanoparticles. Recent Patents on CNS drug delivery **3**: 216-225.

Cisternino, S., Rousselle, C., Dagenais, C. and Scherrmann, J.-M. (2001). Screening of Multidrug-Resistance Sensitive Drugs by In Situ Brain Perfusion in P-Glycoprotein-Deficient Mice. Pharm. Res. **18**(2): 183-190.

Dauchy, S., Dutheil, F., Weaver, R. J., Chassoux, F., Daumas-Duport, C., Couraud, P.-O., Scherrmann, J.-M., Waziers, I. D. and Declèves, X. (2008). ABC transporters, cytochromes P450 and their main transcription factors: expression at the human blood-brain barrier. J. Neurochem. **107**(6): 1518-1528.

de Bruin, M., Miyake, K., Litman, T., Robey, R. and Bates, S. E. (1999). Reversal of resistance by GF120918 in cell lines expressing the ABC half-transporter, MXR. Cancer Lett. **146**(2): 117-126.

Deeken, J. F. and Löscher, W. (2007). The Blood-Brain Barrier and Cancer: Transporters, Treatment, and Trojan Horses. Clin. Cancer Res. **13**(6): 1663-1674.

Doan, K. M. M., Humphreys, J. E., Webster, L. O., Wring, S. A., Shampine, L. J., Serabjit-Singh, C. J., Adkison, K. K. and Polli, J. W. (2002). Passive Permeability and P-Glycoprotein-Mediated Efflux Differentiate Central Nervous System (CNS) and Non-CNS Marketed Drugs. J. Pharmacol. Exp. Ther. **303**(3): 1029-1037.

Farrugia, C. A. and Groves, M. J. (1999). Gelatin Behaviour in Dilute Aqueous Solution: Designing a Nanoparticulate Formulation. J. Pharm. Pharmacol. **51**: 643-649.

Fellner, S., Bauer, B., Miller, D. S., Schaffrik, M., Fankhänel, M., Spruss, T., Bernhardt, G., Gräff, C., Färber, L., Gschaidmeier, H., Buschauer, A. and Fricker, G. (2002). Transport of paclitaxel (Taxol) across the blood-brain barrier in vitro and in vivo. J. Clin. Invest. **110**(9): 1309-1318.

Fernández-Urrusuno, R., Calvo, P., Remuñán-López, C., Vila-Jato, J. L. and José Alonso, M. (1999). Enhancement of Nasal Absorption of Insulin Using Chitosan Nanoparticles. Pharm. Res. **16**(10): 1576-1581.

Gelperina, S. E., Khalansky, A. S., Skidan, I. N., Smirnova, Z. S., Bobruskin, A. I., Severin, S. E., Turowski, B., Zanella, F. E. and Kreuter, J. (2002). Toxicological studies of doxorubicin bound to polysorbate 80-coated poly(butyl cyanoacrylate) nanoparticles in healthy rats and rats with intracranial glioblastoma. Toxicol. Lett. **126**(2): 131-141.

Glantz, M. J., Burger, P. C., Herndon, J. E., 2nd, Friedman, A. H., Cairncross, J. G., Vick, N. A. and Schold, S. C., Jr. (1991). Influence of the type of surgery on the histologic diagnosis in patients with anaplastic gliomas. Neurology **41**(11): 1741-4.

Gulyaev, A. E., Gelperina, S. E., Skidan, I. N., Antropov, A. S., Kivman, G. Y. and Kreuter, J. (1999). Significant Transport of Doxorubicin into the Brain with Polysorbate 80-Coated Nanoparticles. Pharm. Res. **16**(10): 1564-1569.

Hall, W. A., Doolittle, N. D., Daman, M., Bruns, P. K., Muldoon, L., Fortin, D. and Neuwelt, E. A. (2006). Osmotic blood-brain barrier disruption chemotherapy for diffuse pontine gliomas. J. Neurooncol. **77**(3): 279-84.

Halperin, E. C., Herndon, J., Schold, S. C., Brown, M., Vick, N., Cairncross, J. G., Macdonald, D. R., Gaspar, L., Fischer, B., Dropcho, E., Rosenfeld, S., Morowitz, R., Piepmeier, J., Hait, W., Byrne, T., Salter, M., Imperato, J., Khandekar, J., Paleologos, N., Burger, P., Bentel, G. C. and Friedman, A. (1996). A phase III randomized prospective trial of external beam radiotherapy, mitomycin C, carmustine, and 6-mercaptopurine for the treatment of adults with anaplastic glioma of the brain. Int. J. Radiat. Oncol. Biol. Phys. **34**(4): 793-802.

Hirase, T., Staddon, J., Saitou, M., Ando-Akatsuka, Y., Itoh, M., Furuse, M., Fujimoto, K., Tsukita, S. and Rubin, L. (1997). Occludin as a possible determinant of tight junction permeability in endothelial cells. J. Cell Sci. **110**(14): 1603-1613.

Huang, L., Wang, C., Chen, Z., Xu, Y., Wang, Y., Zhong, Y. and Liu, Y. (2008). Targeting mice brain tissue by Tween 80-coated gemcitabine polybutylcyanoacrylate nanoparticles. Zhongguo Yiyuan Yaoxue Zazhi **28**(16): 1332-1336.

Huwyler, J., Cerletti, A., Fricker, G., Eberle, A. N. and Drewe, J. (2002). By-passing of P-glycoprotein using immunoliposomes. J. Drug Target. **10**(1): 73-9.

Huwyler, J. r., Wu, D. and Pardridge, W. M. (1996). Brain drug delivery of small molecules using immunoliposomes. Proc. Natl. Acad. Sci. U. S. A. **93**(24): 14164-14169.

Jackson, R. J., Fuller, G. N., Abi-Said, D., Lang, F. F., Gokaslan, Z. L., Shi, W. M., Wildrick, D. M. and Sawaya, R. (2001). Limitations of stereotactic biopsy in the initial management of gliomas. Neuro Oncol. **3**(3): 193-200.

Jefferies, W. A., Brandon, M. R., Hunt, S. V., Williams, A. F., Gatter, K. C. and Mason, D. Y. (1984). Transferrin receptor on endothelium of brain capillaries. Nature **312**(5990): 162-163.

Kasibhatla, S., Jessen, K. A., Maliartchouk, S., Wang, J. Y., English, N. M., Drewe, J., Qiu, L., Archer, S. P., Ponce, A. E., Sirisoma, N., Jiang, S., Zhang, H.-Z., Gehlsen, K. R., Cai, S. X., Green, D. R. and Tseng, B. (2005). A role for transferrin receptor in triggering apoptosis when targeted with gambogic acid. Proc. Natl. Acad. Sci. U. S. A. **102**(34): 12095-12100.

Kawashima, Y. (2001). Nanoparticulate systems for improved drug delivery. Adv. Drug Del. Rev. **47**(1): 1-2.

Kepes, J. J. (1994). Pitfalls and problems in the histopathologic evaluation of stereotactic needle biopsy specimens. Neurosurg. Clin. N. Am. **5**(1): 19-33.

Kiwit, J. C., Floeth, F. W. and Bock, W. J. (1996). Survival in malignant glioma: analysis of prognostic factors with special regard to cytoreductive surgery. Zentralbl. Neurochir. **57**(2): 76-88.

Kleihues, P., Burger, P. C. and Scheithauer, B. W. (1993). The new WHO classification of brain tumours. Brain Pathol. **3**(3): 255-68.

Kleihues, P. and Sobin, L. H. (2000). World Health Organization classification of tumors. Cancer **88**(12): 2887.

Koukourakis, G. V., Kouloulias, V., Zacharias, G., Papadimitriou, C., Pantelakos, P., Maravelis, G., Fotineas, A., Beli, I., Chaldeopoulos, D. and Kouvaris, J. (2009). Temozolomide with radiation therapy in high grade brain gliomas: pharmaceuticals considerations and efficacy; a review article. Molecules **14**(4): 1561-77.

Kraemer, D. F., Fortin, D. and Neuwelt, E. A. (2002). Chemotherapeutic dose intensification for treatment of malignant brain tumors: recent developments and future directions. Current Neurology and Neuroscience Reports **2**(3): 216-24.

Kreuter, J., Petrov, V. E., Kharkevich, D. A. and Alyautdin, R. N. (1997). Influence of the type of surfactant on the analgesic effects induced by the peptide dalargin after its delivery across the blood-brain barrier using surfactant-coated nanoparticles. J. Controlled Release **49**(1): 81-87.

Krex, D., Klink, B., Hartmann, C., von Deimling, A., Pietsch, T., Simon, M., Sabel, M., Steinbach, J. P., Heese, O., Reifenberger, G., Weller, M., Schackert, G. and for the German Glioma Network (2007). Long-term survival with glioblastoma multiforme. Brain **130**(10): 2596-2606.

Kurakhmaeva, K. B., Djindjikhashvili, I. A., Petrov, V. E., Balabanyan, V. U., Voronina, T. A., Trofimov, S. S., Kreuter, J., Gelperina, S., Begley, D. and Alyautdin, R. N. (2009). Brain targeting of nerve growth factor using poly(butyl cyanoacrylate) nanoparticles. J. Drug Target. **17**(8): 564-74.

Laboratory for Preclinical Imaging Technologies (2007). 2nd Small Animal Imaging Workshop, January 29 - February 1, 2007, Tuebingen. Practical Guide.

Lacroix, M., Abi-Said, D., Fourney, D. R., Gokaslan, Z. L., Shi, W., DeMonte, F., Lang, F. F., McCutcheon, I. E., Hassenbusch, S. J., Holland, E., Hess, K., Michael, C., Miller, D. and Sawaya, R. (2001). A multivariate analysis of 416 patients with glioblastoma multiforme: prognosis, extent of resection, and survival. J. Neurosurg. **95**(2): 190-198.

Li, H. and Qian, Z. M. (2002). Transferrin/transferrin receptor-mediated drug delivery. Med. Res. Rev. **22**(3): 225-250.

Louis, D. N., Ohgaki, H., Wiestler, O. D., Cavenee, W. K., Burger, P. C., Jouvet, A., Scheithauer, B. W. and Kleihues, P. (2007). The 2007 WHO classification of tumours of the central nervous system. Acta Neuropathol. (Berl). **114**(2): 97-109.

Nagashima, T., Ikeda, K., Wu, S., Kondo, T., Yamaguchi, M. and Tamaki, N. (1997). The mechanism of reversible osmotic opening of the blood-brain barrier: role of intracellular calcium ion in capillary endothelial cells. Acta Neurochir. Suppl. (Wien). **70**: 231-3.

Nelson, D. F., Diener-West, M., Horton, J., Chang, C. H., Schoenfeld, D. and Nelson, J. S. (1988). Combined modality approach to treatment of malignant gliomas--re-evaluation of RTOG 7401/ECOG 1374 with long-term follow-up: a joint study of the Radiation Therapy Oncology Group and the Eastern Cooperative Oncology Group. NCI Monogr.(6): 279-84.

Nitta, T. and Sato, K. (1995). Prognostic implications of the extent of surgical resection in patients with intracranial malignant gliomas. Cancer **75**(11): 2727-31.

Olivier, J.-C. (2005). Drug Transport to Brain with Targeted Nanoparticles. NeuroRX **2**(1): 108-119.

Pardridge, W. M. (2003). BLOOD-BRAIN BARRIER DRUG TARGETING: THE FUTURE OF BRAIN DRUG DEVELOPMENT. Mol. Interventions **3**(2): 90-105.

Pardridge, W. M. (2007). Blood-brain barrier delivery. Drug Discovery Today **12**(1-2): 54-61.

Petri, B., Bootz, A., Khalansky, A., Hekmatara, T., Mueller, R., Kreuter, J. and Gelperina, S. (2007). Mechanism of action and surfactant influence during chemotherapy of brain tumour using doxorubicin-loaded poly(butyl cyanoacrylate) nanoparticles. Nanotech 2007, Nanotechnology Conference and Trade Show, Santa Clara, CA, United States.

Qian, Z. M., Li, H., Sun, H. and Ho, K. (2002). Targeted drug delivery via the transferrin receptor-mediated endocytosis pathway. Pharmacol. Rev. **54**(4): 561-87.

Quigley, M. R. and Maroon, J. C. (1991). The relationship between survival and the extent of the resection in patients with supratentorial malignant gliomas. Neurosurgery **29**(3): 385-8; discussion 388-9.

Rapoport, S. I. (2001). Advances in osmotic opening of the blood-brain barrier to enhance CNS chemotherapy. Expert Opin Investig Drugs. **10**(10): 1809-18.

Rees, J. (2002). Glioma Therapy. ANCR **2**(2): 11.

Scrideli, C., Carlotti, C., Okamoto, O., Andrade, V., Cortez, M., Motta, F., Lucio-Eterovic, A., Neder, L., Rosemberg, S., Oba-Shinjo, S., Marie, S. and Tone, L. (2008). Gene expression profile analysis of primary glioblastomas and non-neoplastic brain tissue: identification of potential target genes by oligonucleotide microarray and real-time quantitative PCR. J. Neurooncol. **88**(3): 281-291.

Shai, R., Shi, T., Kremen, T. J., Horvath, S., Liau, L. M., Cloughesy, T. F., Mischel, P. S. and Nelson, S. F. (2003). Gene expression profiling identifies molecular subtypes of gliomas. Oncogene **22**(31): 4918-23.

Soppimath, K. S., Aminabhavi, T. M., Kulkarni, A. R. and Rudzinski, W. E. (2001). Biodegradable polymeric nanoparticles as drug delivery devices. J. Controlled Release **70**(1-2): 1-20.

Stupp, R., Mason, W. P., van den Bent, M. J., Weller, M., Fisher, B., Taphoorn, M. J. B., Belanger, K., Brandes, A. A., Marosi, C., Bogdahn, U., Curschmann, J., Janzer, R. C., Ludwin, S. K., Gorlia, T., Allgeier, A., Lacombe, D., Cairncross, J. G., Eisenhauer, E., Mirimanoff, R. O., Research, t. E. O. f., Tumor, T. o. C. B., Groups, R. and the National Cancer Institute of Canada Clinical Trials Group (2005). Radiotherapy plus Concomitant and Adjuvant Temozolomide for Glioblastoma. N. Engl. J. Med. **352**(10): 987-996.

Sugiyama, Y., Kusuhara, H. and Suzuki, H. (1999). Kinetic and biochemical analysis of carrier-mediated efflux of drugs through the blood-brain and blood-cerebrospinal fluid barriers: importance in the drug delivery to the brain. J. Controlled Release **62**(1-2): 179-186.

Walker, M. D., Alexander, E., Hunt, W. E., MacCarty, C. S., Mahaley, M. S., Mealey, J., Norrell, H. A., Owens, G., Ransohoff, J., Wilson, C. B., Gehan, E. A. and Strike, T. A. (1978). Evaluation of BCNU and/or radiotherapy in the treatment of anaplastic gliomas. J. Neurosurg. **49**(3): 333-343.

Walker, M. D., Strike, T. A. and Sheline, G. E. (1979). An analysis of dose-effect relationship in the radiotherapy of malignant gliomas. Int. J. Radiat. Oncol. Biol. Phys. **5**(10): 1725-31.

Wolburg, H. and Lippoldt, A. (2002). Tight junctions of the blood-brain barrier: development, composition and regulation. Vascul. Pharmacol. **38**(6): 323-337.

Yang, F., Lum, J. B., McGill, J. R., Moore, C. M., Naylor, S. L., van Bragt, P. H., Baldwin, W. D. and Bowman, B. H. (1984). Human transferrin: cDNA characterization and chromosomal localization. Proc. Natl. Acad. Sci. U. S. A. **81**(9): 2752-6.

Zülch, K. (1979). Histological typing of tumors of the central nervous system, Word Health Organization (WHO), Geneva.

Chapter 2

Scope and Objectives

Up to date, the treatment of malignant brain tumors, especially high grade gliomas, constitutes a major problem in cancer therapy. For more than 30 years, the prognosis of patients with glioblastoma multiforme (GBM), one of the most aggressive astrocytic gliomas, has not been substantially improved. Despite the recent combination of radiotherapy with temozolomide, the increase in median survival from 12 to 15 months represents only a minor step in search of effective therapy regimens for glioblastoma multiforme. Hence, there is still a great need for new strategies in the treatment of GBM. One of the most important reasons for the failure of the chemotherapy of malignant brain tumors is the restricted access of anticancer drugs to the CNS. In this context, the activity of ATP-binding cassette transporters at the blood-brain barrier (BBB), especially the efflux pumps ABCB1 and ABCG2, play a crucial role in the failure of the clinically available chemotherapeutics.

For example, doxorubicin is highly cytotoxic against human glioblastoma cells in vitro, but as an ABCB1 / ABCG2 substrate does not penetrate across the BBB to reach therapeutically active concentrations in the brain. Doxorubicin-loaded poly(butylcyanoacrylate) (PBCA) nanoparticles (NPs) are considered as a promising approach to overcome the BBB. It has been reported that by means of such PBCA NPs, coated with the surfactant polysorbate 80, doxorubicin concentrations were elevated in the brain [Gulyaev et al., 1999]. Thus, the objective of the first part of this thesis was to evaluate the in vitro toxicity profile for various doxorubicin formulations against 3 different human glioblastoma cell lines. For this purpose, the chemosensitivity of these ABCB1 and ABCG2 negative cells against doxorubicin in solution, doxorubicin loaded to PBCA NPs and polysorbate 80-coated doxorubicin-loaded PBCA NPs had to be investigated. To study interactions of such particles with drug efflux transporters, and to compare the antiproliferative activity of different nanoparticle formulations, ABCB1 overexpressing Kb-V1 cells and ABCG2 overexpressing MCF-7/Topo cells were selected as in vitro models. Aiming at the identification of new anticancer agents for the treatment of malignant brain tumors, new doxorubicin derivatives were considered as promising candidates for initial in vitro cytotoxicity assays against different human glioblastoma cell types.

Another interesting strategy to enhance the brain penetration of cytostatics, which are known to be substrates of ATP-binding cassette transporters, is the inhibition of these efflux pumps at the BBB. In continuation of previous work on the co-administration of ABC modulators with cytostatics [Fellner et al., 2002; Hubensack et al., 2008], the ABCB1 inhibitor tariquidar served as a starting point for the synthesis of a series of analogs, accomplished in the group of Prof. Dr. Burkhard König, Institute of Organic Chemistry, University of Regensburg. These new chemical entities had to be investigated for potency against ABCG2 and selectivity for ABCG2 versus ABCB1 (and in part versus ABCC2). To circumvent the time-consuming and costly flow cytometric (FACS) assays as well as to substantiate the results from FACS analysis, alternative methods were sought for routine studies. For this purpose, the ABCG2 substrates Hoechst 33342 and pheophorbide a were chosen for fluorescence readout in the 96-well plate format. Confocal-laser scanning microscopy, using fluorescence-labeled ABCG2 modulators, which had to be characterized with respect to their ability to modulate ABCG2, should provide information, if the tariquidar analogs are substrates or inhibitors of this transporter.

In view of intended in vivo studies, on the one hand, sufficient stability of the tariquidar analogs is a prerequisite. To assess stability, HPLC-MS was regarded as the appropriate methodology. On the other hand, a predictive orthotopic glioblastoma model is indispensible. Hence, the main part of this thesis focused on the refinement of an existing orthotopic glioblastoma model in nude mice by monitoring tumorigenicity and tumor growth using noninvasive optical imaging technology, namely bioluminescence and fluorescence. Therefore, human glioblastoma cell variants, had to be stably transfected with the genes encoding the enzyme luciferase2 (luc2) and the recently discovered far-red protein Katushka, respectively. The transfectants should ideally show identical growth kinetics, chemosensitivity and tumorigenicity compared with the respective wildtypes. The cardinal question was the feasibility of optical in vivo imaging to monitor take rates and the progression of intracerebral human glioblastomas in nude mice.

References

Fellner, S., Bauer, B., Miller, D. S., Schaffrik, M., Fankhänel, M., Spruss, T., Bernhardt, G., Gräff, C., Färber, L., Gschaidmeier, H., Buschauer, A. and Fricker, G. (2002). Transport of paclitaxel (Taxol) across the blood-brain barrier in vitro and in vivo. J. Clin. Invest. 110(9): 1309-1318.

Gulyaev, A. E., Gelperina, S. E., Skidan, I. N., Antropov, A. S., Kivman, G. Y. and Kreuter, J. (1999). Significant Transport of Doxorubicin into the Brain with Polysorbate 80-Coated Nanoparticles. Pharm. Res. 16(10): 1564-1569.

Hubensack, M., Müller, C., Höcherl, P., Fellner, S., Spruss, T., Bernhardt, G. and Buschauer, A. (2008). Effect of the ABCB1 modulators elacridar and tariquidar on the distribution of paclitaxel in nude mice. J. Cancer Res. Clin. Oncol. 134(5): 597-607.

Chapter 3

Antiproliferative activity of doxorubicin-loaded nanoparticles (NPs) and doxorubicin derivatives

3.1 Introduction

The transport of drugs into the brain, e.g. in the therapy of CNS diseases, is often limited by the architecture and function of the blood-brain barrier (BBB). Numerous physiological, morphological and functional properties of the BBB such as the continuous tight epithelium of the brain capillaries, the tight junctions between the cerebral endothelial cells and the activity of many different transporter proteins, for example ABC-efflux pumps (e.g. p-glycoprotein, breast cancer resistance protein) as well as organic anion and cation transporters (OAT's and OCT's), protect the brain from the uptake of numerous xenobiotics [Deeken and Löscher, 2007].

3.1.1 Drug delivery to the brain by nanoparticles (NPs)

Over the recent decades the use of nanoparticle formulations was described as a novel strategy for the delivery of drugs across the blood-brain barrier. Such nanoparticles (NPs) are colloidal structures with diameters up to 1000 nm [De Jong and Borm, 2008], consisting of biodegradable polymer matrices, e.g. poly(D,L-lactide) or poly(D,L-glycolide). These nanoparticles can be loaded with appropriate pharmacologically active compounds. Investigations by Gao and Jiang revealed a correlation between particle size and brain uptake. Methotrexate loaded polysorbate 80-coated nanoparticles were i.v. injected into mice. Thereby, coated particles smaller than 100 nm delivered more drug (according to C_{max} and AUC) to CSF and brain than observed for particles with an average diameter of 100-400 nm [Gao and Jiang, 2006].

In an early study, poly(butyl)cyanoacrylate (PBCA) nanoparticles were loaded with the Leu-enkephalin analog dalargin [Kreuter et al., 1995], which cannot penetrate into the brain, when injected as a solution. In addition, the drug-loaded particles were coated with surfactants such as polysorbate 20, 40, 60 and 80, various poloxamers, poloxamine 908, Cremophor EL, Cremophor RH 40 and Brij 35 [Kreuter et al., 1997]. Mice studies on the analgesic effect of different dalargin formulations showed that only polysorbate-coated, dalargin-loaded PBCA nanoparticles produced analgesia in the tail flick [Kreuter et al., 1995] and the hot plate test [Schroeder et al., 1998].

Similar results were reported for the intravenous administration of different formulations of the opioid loperamide [Alyautdin et al., 1997]: a long-lasting analgesic effect was only achieved by the application of polysorbate 80-coated loperamide loaded nanoparticles. Furthermore, the hydrophilic quaternary ammonium salt tubucurarine induced epileptiform spikes in EEG, when formulated as polysorbate 80-coated tubucurarine-loaded NPs [Alyautdin et al., 1998] in perfusion studies using rat brains. Very recently, poly(butyl)cyanoacrylate particles were used for brain targeting of nerve growth factor (NGF) [Kurakhmaeva et al., 2009]. In an acute-amnesia model in mice, scopolamine-induced amnesia was successfully reversed by the intravenous injection of polysorbate 80-coated NPs loaded with NGF. The outcome was measured via the passive avoidance reflex (PAR) test in which mice treated with the coated and drug-loaded particles showed a significant increase in the mean latent period. Moreover, in mice with provoked parkinsonian syndrome by intraperitoneal injection of 1-methyl-4-phenyl-1,2,3,6-tetrahydropyridine, NGF adsorbed to polysorbate 80-coated PBCA NPs produced a decrease in rigidity and a simultaneous increase in locomotor activity compared to non-treated control animals [Kurakhmaeva et al., 2008].

3.1.2 NPs as drug delivery systems for the treatment of malignant brain tumors

Another challenging application of drug-loaded nanoparticles is the therapy of malignant brain tumors. One of the first anticancer drugs, used for loading PBCA NPs, was the anthracycline doxorubicin. In investigations on the body distribution of the nanoparticle formulations, 4 preparations of doxorubicin were intravenously injected into rats [Gulyaev et al., 1999]. The polysorbate 80-coated and uncoated doxorubicin-loaded NPs as well as solutions of doxorubicin in saline with and without polysorbate 80 (1 %) were compared. The most important result of the studies by Gulyaev et al. [Gulyaev et al., 1999] was an over 60-fold higher concentration of doxorubicin in the brain of mice treated with polysorbate 80-coated nanoparticles (6 µg/g vs. < 0.1 µg/g in the other test groups). The therapeutic potential of the increased brain uptake of doxorubicin via the surface-modified drug carrier system was investigated by Steiniger et al. [Steiniger et al., 2004]. Rats bearing intracranial 101/8 glioblastomas were treated with different formulations of doxorubicin including the surfactant-coated loaded PBCA nanoparticles. In case of the latter formulation, the longest survival (100-180 days vs. 50 days) and the highest long-term remissions (over 20 %) were observed.

Lately, Hekmatara et al. [Hekmatara et al., 2009] investigated the therapeutic effects of coated doxorubicin-loaded nanoparticles in the orthotopic 101/8 glioblastoma model. Slower proliferating and less necrotic tumors were reported, when the animals were treated with the polysorbate 80-coated doxorubicin-loaded nanoparticles compared to the administration of doxorubicin in solution [Hekmatara et al., 2009]. Due to distinctive effects on vascularization, the authors suggest an antiangiogenic mechanism of action.

Recently, polysorbate 80-coated NPs were loaded with the antimetabolite gemcitabin (GCTB) and injected into a C6 glioblastoma model in Sprague Dawley rats [Wang et al., 2009]. The injection of these gemcitabin-loaded nanoparticles, coated with 1 % polysorbate 80, into the tail vein, yielded increased gemicitabin brain levels, determined by HPLC, compared to mice treated with GCTB solution, non-coated GCTB nanoparticles or a mixture of “empty” nanoparticles plus 1 % polysorbate 80 and gemcitabin [Huang et al., 2008]. These elevated GCTB concentrations in the brain resulted in an increase in survival time compared to vehicle treated control mice [Wang et al., 2009].

3.1.3 Tolerability of NP drug delivery systems

Toxicology studies by Gelperina et al. on healthy and glioblastoma bearing rats showed that non-loaded NPs were tolerated, when administered at a dose of 100-400 mg/kg. Doxorubicin associated toxicity was not increased by loading the drug to the surface of nanoparticles or by the presence of polysorbate 80 [Gelperina et al., 2002]. On the contrary, HPLC analysis of various tissue samples proved a drastic decrease in heart concentrations of doxorubicin, when the drug was adsorbed to the nanoparticles [Gulyaev et al., 1999]. This observation was of great value, since the cardiotoxicity of doxorubicin limits its therapeutic use. A very recent toxicology study, using male and female Wistar rats, confirmed the reduced doxorubicin-associated cardiotoxicity, when the cytostatic was administered intravenously as the coated nanoparticle formulation and, additionally, demonstrated a decreased testicular toxicity of surfactant-coated doxorubicin-loaded particles in male rats [Pereverzeva et al., 2008].

3.1.4 Mechanism of NP penetration across the BBB

In theory, there are only few mechanisms, namely transcellular passive diffusion, receptor-mediated transcytosis or the use of specific carrier systems, by which drugs can enter the brain, [Deeken and Löscher, 2007]. As described above, obviously only nanoparticles, coated with detergents, in particular with polysorbate 80, were able to overcome the blood-brain barrier. The mechanisms by which the polysorbate 80-coated PBCA nanoparticles enter the brain have been a matter of discussion. Kreuter [Kreuter, 2001] suggested various single and combined mechanisms including endocytosis, mimicry of LDL (low density lipoproteins) after adsorption of apolipoprotein E from blood plasma to the surface of the particles and subsequent interaction via LDL receptors as well as modulation of tight junctions or ABCB1 transporters. In recent studies, Petri et al. performed incubation experiments with rat plasma containing poloxamer 188 and polysorbate 80-coated doxorubicin-loaded nanoparticles [Petri et al., 2007]. Both types of nanoparticles showed high adsorption of apolipoprotein ApoA-I prompting the authors to assume a putative in vivo interaction of the particles with the scavenger receptor SR-BI expressed at the BBB.

3.1.4.1 Entry into cells

In spite of all these investigations, cellular uptake of polysorbate 80-coated doxorubicin-loaded nanoparticles remained unproven for a long period of time. Studies by Dr. Dietmar Gross using confocal laser scanning microscopy and flow cytometric techniques did not support an entry of the surfactant-coated particles into cancer cells [Gross, 2006]. Therefore, he speculated, that the drug-loaded nanoparticles might adsorb to the cell surface and maintain a high concentration gradient of released doxorubicin around the cell, resulting in enhanced diffusion of the drug into the cells [Gross, 2006].

In contrast to these assumptions, recent investigations by Reimold et al. [Reimold et al., 2008] proved the brain penetration of polysorbate 80-coated PBCA NP (10 %). The nanoparticles were loaded with fluorescein-isothiocyanate-dextran (FITC-dextran), rhodamine-123 or doxorubicin and injected intravenously into male Wistar rats. After several time periods, the rats were killed by cervical dislocation, and cryosections of the brain tissues were prepared for CLSM studies.

The investigations gave clear evidence that the particle-associated fluorescence was located within microvessels and beyond the brain capillaries, suggesting the internalization of polysorbate 80-coated PBCA nanoparticles by endothelial cells [Reimold et al., 2008].

3.2 Objective

In continuation of the aforementioned investigations by D. Gross [Gross, 2006] the toxicity of doxorubicin loaded nanoparticle formulations was evaluated against the human glioblastoma cell lines U-87 MG, U-118 MG and U-373 MG. Since these cell lines proved to be p-gp (ABCB1) and bcrp (ABCG2) negative [Gross, 2006], ABCB1 overexpressing Kb-V1 cells and ABCG2 overexpressing MCF-7/Topo cells [Hubensack, 2005] were used as in vitro models to investigate the effect of doxorubicin-loaded nanoparticles on these efflux pumps. Furthermore, the chemosensitivity of the corresponding Kb and MCF-7 wildtype cells against different doxorubicin formulations was examined.

In a subproject of the present work the toxicity of 2 newly synthesized doxorubicin derivatives was investigated on U-87 MG, U-118 MG and U-373 MG cells. In search of new compounds for the treatment of glioblastoma, these investigations were arranged as a prerequisite since, as mentioned before, the applicability of the parent compound doxorubicin in the therapy of malignant brain tumors, is limited due the active efflux by ATP-binding cassette transporters expressed at the blood-brain barrier.

3.3 Materials and methods

3.3.1 Chemicals and drugs

Doxorubicin was a kind gift from Prof. Kreuter (Institute of Pharmaceutical Technology, Johann Wolfgang Goethe Universität, Frankfurt, Germany). The compound was dissolved to a 10 mM stock solution in 70 % ethanol. The stocks were stored at -20 °C. Vinblastine sulfate (Sigma, Munich, Germany) was dissolved in 70 % ethanol to reach a concentration of 1 mM. The stock solutions were stored at 4 °C. Polysorbate 80 (Tween 80) was purchased from Merck, Darmstadt, Germany and stored at room temperature.

All polybutylcyanoacrylate (PBCA) nanoparticle (NP) formulations were produced and characterized in the workgroup of Prof. Kreuter. The preparation procedure has been described previously [Gross, 2006]. For storage, the lyophilized doxorubicin-loaded particles containing an equivalent amount of 1 mg doxorubicin hydrochloride were kept in light-protected glass vials at 4 °C. Investigations on the chemosensitivity of different human cancer cells against the nanoparticle formulations were performed by using 1 fresh vial for each experiment. Therefore, either a 0.9 % NaCl solution or phosphate buffered saline (PBS) with the following ingredients (Merck, Darmstadt, Germany) was prepared: 8.0 g/L NaCl, 1.0 g/L $Na_2HPO_4 \cdot 2\ H_2O$, 0.20 g/L KCl, 0.20 g/L KH_2PO_4, 0.15 g/L $NaH_2PO_4 \cdot H_2O$. The solution was sterile filtered and applied to produce a 1 mM stock suspension (referred to the amount of doxorubicin) of the drug-loaded particles. For coating of the NPs, the surfactant polysorbate 80 was warmed to 37 °C in order to reduce the viscosity. After sterile filtration, Tween 80 was diluted to a 10 % stock solution in PBS or 0.9 % NaCl, respectively. On the eve of experiments, 450 µL of sterile PBS or 0.9 % NaCl and 50 µL of the polysorbate 80 stock solution were added to the glass vial. Coating was achieved by stirring of the mixture under light-protection for 30 min at 300 rpm.

The doxorubicin derivatives Sb-59 and Sb-63b (**Chart 3.1**) were provided by Prof. Dr. Rainer Schobert, Institute of Organic Chemistry at the University of Bayreuth, Germany. 10 mM stock solutions in DMSO (Merck, Darmstadt, Germany) were stored at -20 °C.

Chart 3.1: Structures of doxorubicin and its hydrazone derivatives Sb-59 and Sb-63b.

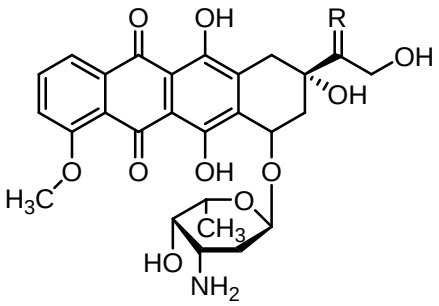

Compound	R
Doxorubicin	O
Sb-59	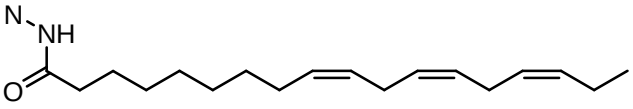
Sb-63b	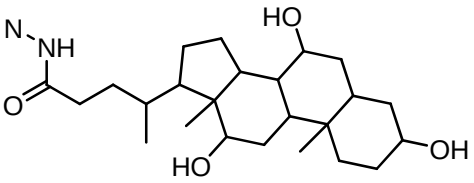

3.3.2 Cell culture

Human U-87 MG and U-373 MG glioblastoma cells were grown in Eagle's Minimum Essential Medium (Sigma, Munich, Germany) containing L-glutamine, 2.2 g/L $NaHCO_3$ (Merck, Darmstadt, Germany) and 0.11 g/L sodium pyruvate (Serva, Heidelberg, Germany) supplemented with 5 % fetal calf serum (FCS) (Biochrom AG, Berlin, Germany). U-118 MG cells, a further human glioblastoma cell line, were cultured in Dulbecco's Modified Essential Medium (DMEM) from Sigma, Munich, Germany. The medium contained L-glutamine, 3.7 g/L $NaHCO_3$, 0.11 g/L sodium pyruvate and was supplemented with 5 % FCS.

HeLa derived human Kb wildtype cells (Kbwt) were grown in the aforementioned DMEM supplemented with 10 % fetal calf serum. The ABCB1 overexpressing subclone Kb-V1 was obtained by the addition of increasing amounts of the ABCB1 substrate vinblastine to the culture medium. At a final concentration of 300 ng/mL vinblastine, cells showed sufficiently increased expression of the efflux transporter to perform ABCB1 inhibition studies [Hubensack, 2005].

Human MCF-7 breast adenocarcinoma cells were cultured in EMEM supplemented with 5 % FCS. Increasing amounts of the ABCG2 substrate topotecan in the culture medium of MCF-7 cells yielded the ABCG2 overexpressing subclone MCF-7/Topo. A final concentration of 0.55 µM topotecan, achieved after a period of approximately 40 days, guarantied sufficient expression of the ABCG2 transporter [Hubensack, 2005].

3.3.3 Crystal violet chemosensitivity assay

The assays were performed as described elsewhere [Bernhardt et al., 1992]. Briefly: Having reached the appropriate confluency, cells were detached from the surface of the culture flasks and seeded into 96-well plates at a density of 8-15 cells per microscopic field (320-fold magnification). Cells were allowed to grow for 48-72 h at 37 °C and 5 % CO_2. Subsequently, supernatant was removed from the cells by suction and replaced by fresh medium containing vehicle (growth control), a known toxic compound (positive control) or the test substances at increasing concentrations. In general, compounds were added to the medium as 1000-fold stock solutions. After various times of incubation at 37 °C / 5 % CO_2 the supernatants were drained and cells were immediately fixed with glutardialdehyde (Merck, Darmstadt, Germany) for at least 20 min. Subsequently, the cells were overlaid with phosphate buffered saline and stored at 4 °C until the end of experiment. All microplates were stained simultaneously, using an aqueous solution of crystal violet (0.02 %) (SERVA, Heidelberg, Germany). After 20 min the dye was removed by draining and excess of crystal violet was eliminated by rinsing the microplates with water for another 20 min. Finally, the dye bound by cell structures was re-dissolved in ethanol 70 % while shaking the plates for 2-4 h. As an indicator of cell mass, the absorbance at 578 nm was determined at a BIOTEK 309 Autoreader (TECNOMARA, Fernwald, Germany).

Effects mediated by the test compounds were expressed as corrected T/C values according to the following equation:

$$T/C_{corr.} = \frac{T - C_0}{C - C_0} \cdot 100\,[\%]$$

, where T is the mean absorbance of the treated cells, C the mean absorbance of the controls and C_0 the mean absorbance of the cells at the time (t=0) when drug was added. The extent of cell killing was calculated by the following equation, if the test compounds showed a cytocidal effect:

$$\text{Cytocidal effect [\%]} = \frac{C_0 - T}{C_0} \cdot 100$$

This was the case, when the absorbance of treated cells T was less than that of the culture at t=0 (C_0.).

3.3.4 Modified chemosensitivity assays for determination of the effects of short-term drug exposure

For investigations on the effect of short-term drug exposure, the aforementioned crystal violet assay was slightly modified. After incubation of the cells with various drug concentrations for 3 and 6 h, respectively, the media were removed by suction. Subsequently, 200 µL of drug-free culture medium were added to each well and cells were incubated for various times at 37 °C / 5 % CO_2. Except for this modification, the assay was performed as described above.

3.4 Results and discussion

3.4.1 Chemosensitivity of ABCB1 and ABCG2 negative U-87 MG, U-118 MG and U-373 MG glioblastoma cells against anthracyclines

3.4.1.1 Immunocytochemical detection of ABCB1 and ABCG2

There are controversial reports in the literature on the (over) expression of ABC cassette transporters by human glioblastoma cells, responsible for the multi-drug resistance phenotype [Kondo et al., 1996; Declèves et al., 2002; Bähr et al., 2003]. As doxorubicin is a substrate of ABCB1 / ABCG2 [Alqawi et al., 2004], the human U-87 MG, U-118 MG and U-373 MG human glioblastoma cells were investigated with respect to these efflux pumps by confocal laser-scanning microscopy experiments (CLSM) [Gross, 2006]. Images of fixed and anti-pgp immunostained human glioblastoma cells are presented in **Figure 3.1**. Kb-V1 cells, the ABCB1 overexpressing subclone of human Kbwt cells, served as positive control. In **Figure 3.2** corresponding CLSM investigations with anti-bcrp immunostaining are shown; topotecan induced ABCG2-overexpressing MCF-7/Topo were used as positive control.

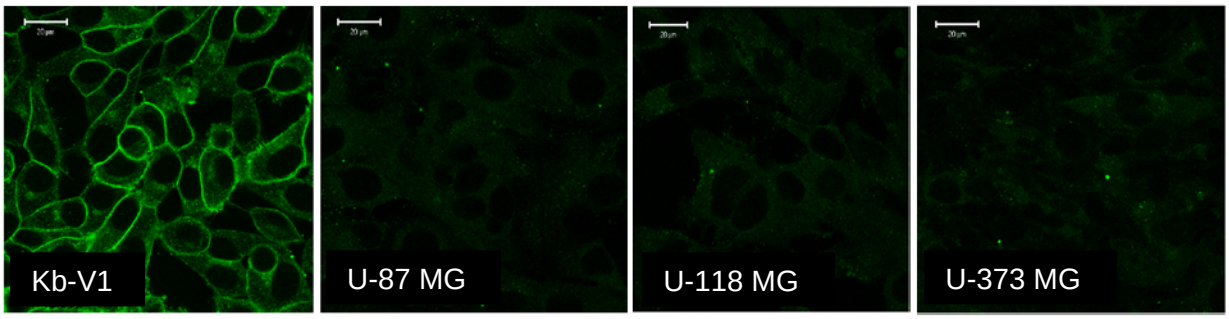

Figure 3.1: Expression of ABCB1 in vinblastine induced Kb-V1 cells and the 3 human glioblastoma cell lines U-87 MG, U-118 MG and U-373 MG. Cells were fixed with paraformaldehyde and incubated with the monoclonal mouse anti-human pgp Ab2 primary antibody Clone F4. After removing excess of the primary antibody and washing, the cells were incubated with the fluorescein-isothiocyanate (FITC)-conjugated polyclonal rabbit anti-mouse IgG secondary antibody. Whereas a high transporter expression was observed for the Kb-V1 cells, the human glioblastoma cell lines showed no antibody mediated FITC fluorescence demonstrating the absence of the transporter proteins.

CLSM experiments by Dr. Dietmar Gross.

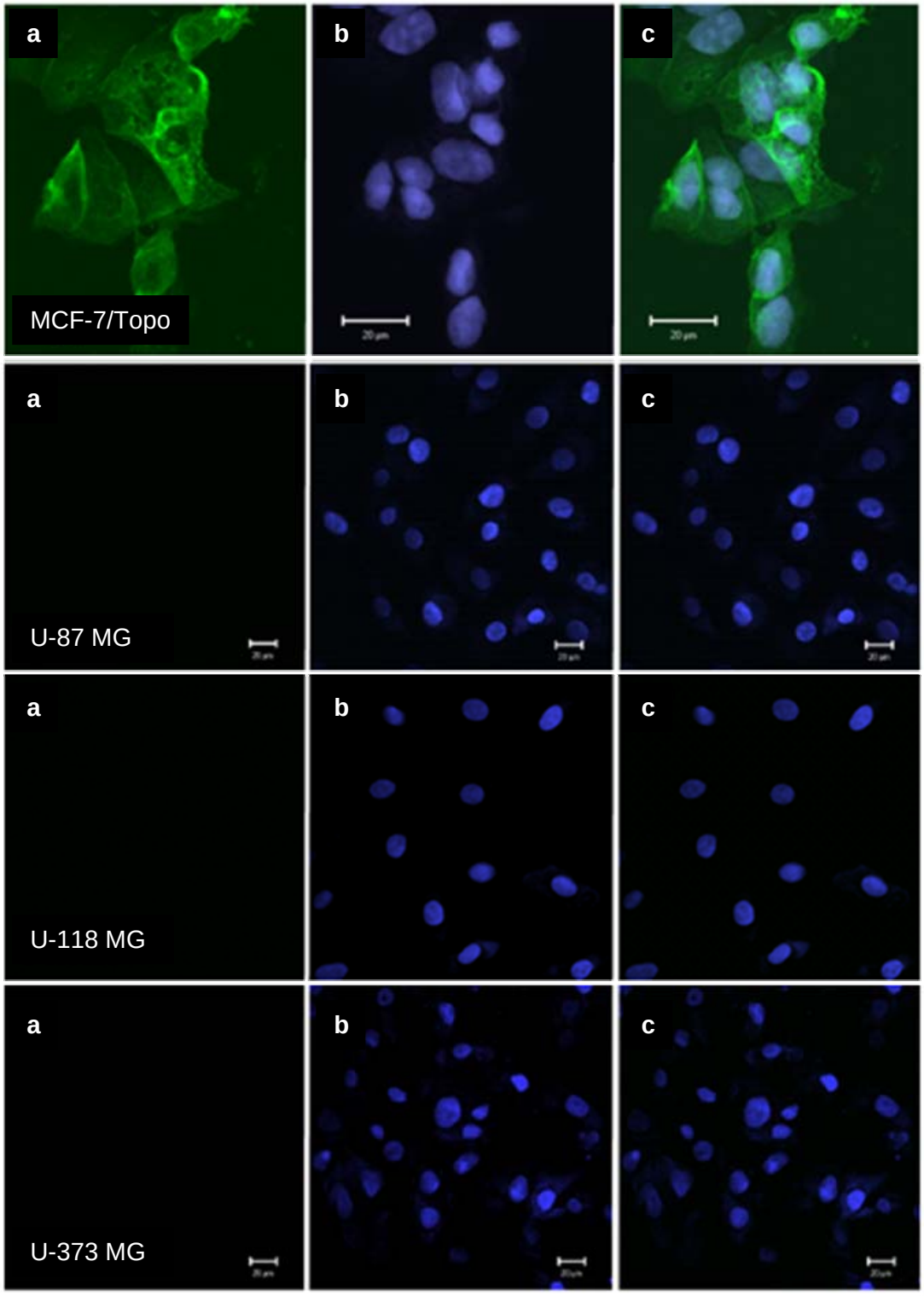

Figure 3.2: Expression of ABCG2 (bcrp). Immunostaining of human glioblastoma U-87 MG, U-118 MG and U-373 MG cells with anti-bcrp primary antibody and Cy5-conjugated secondary antibody revealed lack of ABCG2 expression. MCF-7/Topo cells served as positive control for bcrp-overexpression. Anti-bcrp (a), nuclei (b), merge (c).

CLSM experiments by Dr. Dietmar Gross.

3.4.1.2 Chemosensitivity of the glioblastoma cells against anthracyclines

3.4.1.2.1 Chemosensitivity against doxorubicin

With respect to the investigation of newly developed doxorubicin formulations, the chemosensitivity of human glioblastoma cell lines against non-modified doxorubicin in solution had to be investigated.

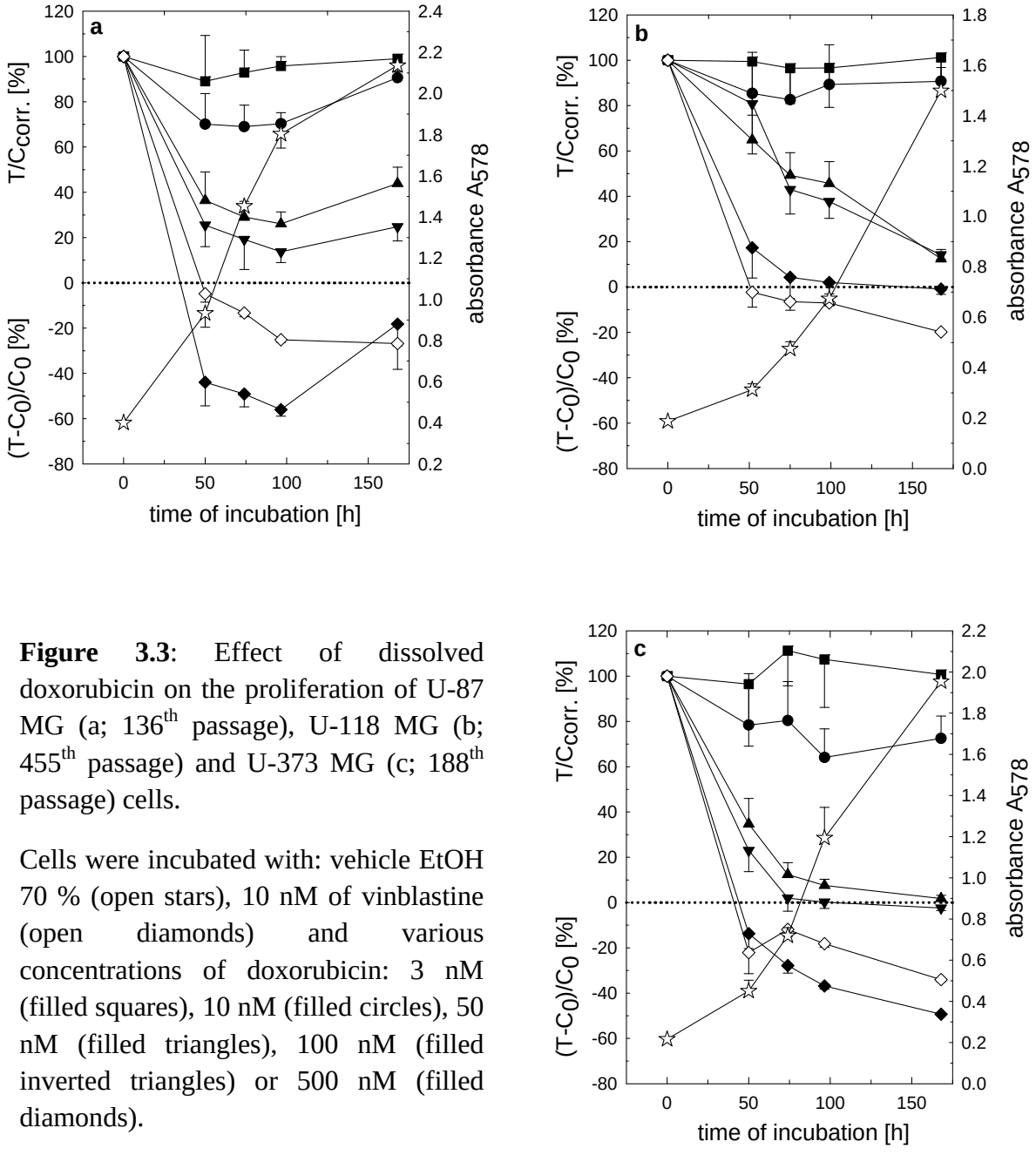

Figure 3.3: Effect of dissolved doxorubicin on the proliferation of U-87 MG (a; 136th passage), U-118 MG (b; 455th passage) and U-373 MG (c; 188th passage) cells.

Cells were incubated with: vehicle EtOH 70 % (open stars), 10 nM of vinblastine (open diamonds) and various concentrations of doxorubicin: 3 nM (filled squares), 10 nM (filled circles), 50 nM (filled triangles), 100 nM (filled inverted triangles) or 500 nM (filled diamonds).

Therefore, the cells were incubated with doxorubicin at increasing concentrations and afterwards processed according to the described procedure (see **3.3.3**). Results are shown in **Figure 3.3**.

As a positive control for assay correctness, 16 wells of the microtiter plate were incubated with 10 nM of vinblastine whereas effects of the solvent were checked by incubation of further 16 wells with the equivalent amount of ethanol 70 %.

Doxorubicin at a concentration of 10 nM caused only a slight cytotoxic effect on all investigated glioblastoma cells. However, incubation of the cells with 100 nM of doxorubicin yielded strong cytotoxic effects on U-87 MG and U-118 MG cells, whereas the same concentration resulted in a cytostatic effect on U-373 MG cells. These data are in good agreement with results of analogous chemosensitivity assays performed by Dr. Peter Altenschöpfer [Altenschöpfer, 1998]. At the highest tested concentration of 500 nM, doxorubicin caused a pronounced cytocidal effect on U-87 MG as well as on U-373 MG cells, whereas a strong cytostatic effect was observed for U-118 MG cells.

3.4.1.2.2 Chemosensitivity against doxorubicin derivatives

2 structural modified doxorubicin derivatives were investigated on their toxicity against U-87 MG, U-118 MG and U-373 MG cells. Basically, these compounds were synthesized with the idea of specifically targeting hormone-dependent breast cancers by addressing the estrogen receptor.

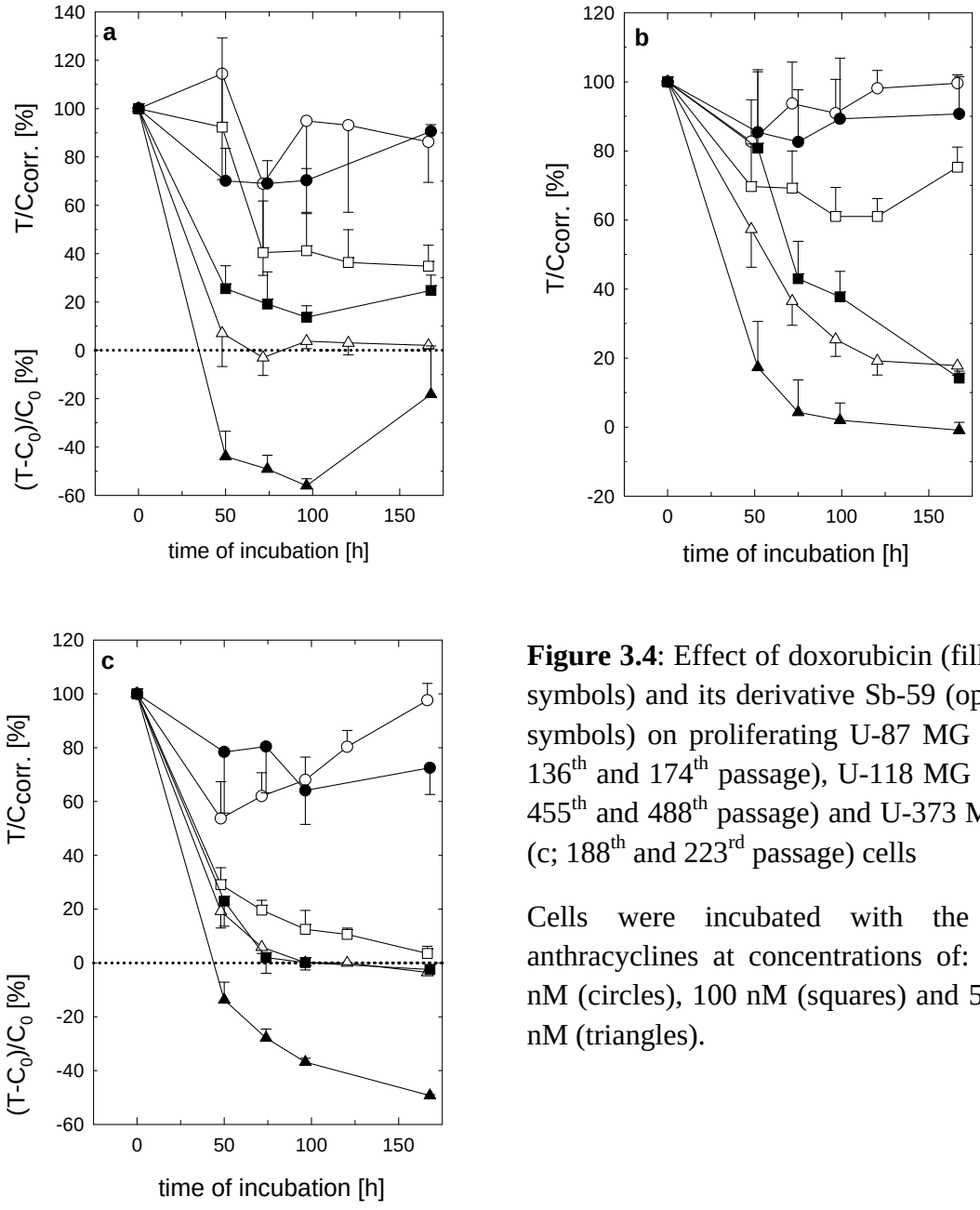

Figure 3.4: Effect of doxorubicin (filled symbols) and its derivative Sb-59 (open symbols) on proliferating U-87 MG (a; 136th and 174th passage), U-118 MG (b; 455th and 488th passage) and U-373 MG (c; 188th and 223rd passage) cells

Cells were incubated with the 2 anthracyclines at concentrations of: 10 nM (circles), 100 nM (squares) and 500 nM (triangles).

Since these compounds show increased lipophilicity compared to doxorubicin, and this might be beneficial to overcome the blood-brain barrier, the derivatives were regarded as promising candidates for preliminary toxicity studies on human glioblastoma cell lines. For this purpose, U-87 MG, U-118 MG and U-373 MG cells were incubated with 3 concentrations of the 2 derivatives, Sb-59 and Sb-63b, respectively using doxorubicin as a reference compound (**Figure 3.4** and **Figure 3.5**).

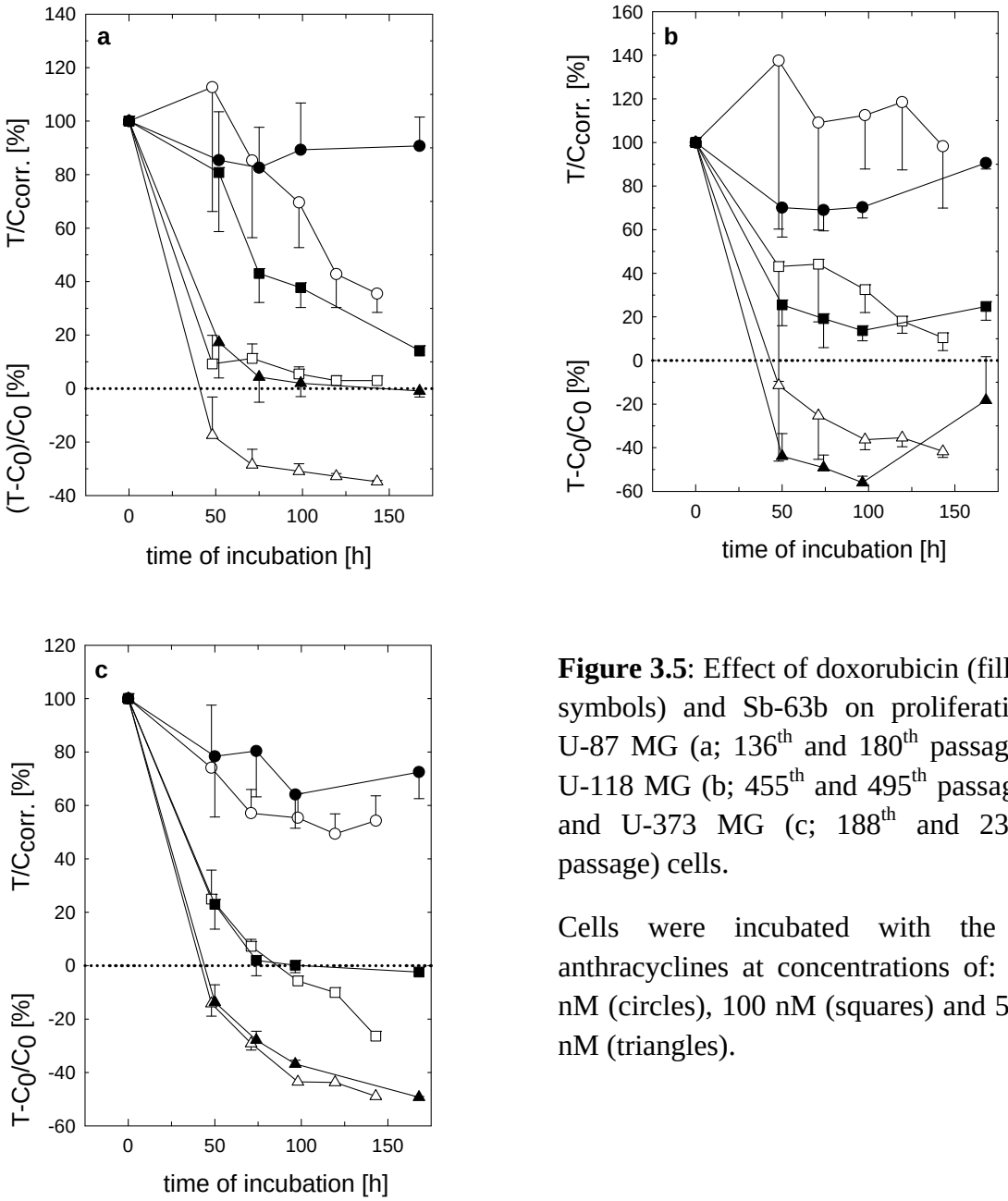

Figure 3.5: Effect of doxorubicin (filled symbols) and Sb-63b on proliferating U-87 MG (a; 136th and 180th passage), U-118 MG (b; 455th and 495th passage) and U-373 MG (c; 188th and 230th passage) cells.

Cells were incubated with the 2 anthracyclines at concentrations of: 10 nM (circles), 100 nM (squares) and 500 nM (triangles).

At a concentration of 10 nM, Sb-59 had a weak antiproliferative effect on human U-87 MG glioblastoma cells similar to that of 10 nM doxorubicin (**Figure 3.4a**). However, at concentrations as high as 100 and 500 nM, Sb-59 was less potent than doxorubicin. Whereas 500 nM Sb-59 caused a strong cytostatic effect, the same concentration of doxorubicin was cytocidal.

Similar results were obtained for U-118 MG cells in the presence of doxorubicin and Sb-59 (**Figure 3.4b**).

Among the 3 human glioblastoma cell types, U-373 MG turned out to be most sensitive against doxorubicin and Sb-59 (**Figure 3.4c**). Even at the lowest tested concentration of 10 nM, cytotoxic and cytostatic effects were observed. Moreover, incubation of U-373 MG cells with 100 and 500 nM of each compound resulted in distinctive cytostatic and cytocidal impact. Again, as noticed for U-87 MG and U-118 MG cells, doxorubicin was demonstrated to be more potent than its derivative Sb-59.

On U-87 MG cells Sb-63b caused increased antiproliferative activity compared to doxorubicin (**Figure 3.5a**). At a concentration of 10 nM, doxorubicin was ineffective, whereas Sb-63b mediated pronounced cytostatic effects. Moreover, at higher concentrations (100 and 500 nM), Sb-63b showed increased cytostatic effects compared to doxorubicin, or were even elevated to cytocidal impacts.

Contrarily, doxorubicin was more cytotoxic than Sb-63b against U-118 MG cells (**Figure 3.5b**), although incubation with 100 and 500 nM of Sb-63b resulted in strong cytostatic and cytocidal effects.

Proliferating U-373 MG cells showed comparable susceptibility against Sb-63b and doxorubicin (**Figure 3.5c**). Both compounds were cytotoxic at a concentration as low as 10 nM. Whereas at a concentration of 100 nM Sb-63b mediated cytocidal outcomes, doxorubicin caused strong cytostatic effects. In addition, incubation of U-373 MG cells with 500 nM of doxorubicin and Sb-63b, respectively, indicated equi-activity.

3.4.1.3 Cytotoxicity of different doxorubicin-loaded NP formulations

For investigations on the chemosensitivity of doxorubicin-loaded nanoparticle formulations, the human glioblastoma cells were incubated with the drug-loaded PBCA particles. Additionally, doxorubicin-loaded PBCA nanoparticles were coated with polysorbate 80 to examine the chemosensitivity of these surface-modified drug-carrier systems.

Figure 3.6 shows the results which were obtained after incubation of U-87 MG, U-118 MG and U-373 MG glioblastoma cells with non-coated doxorubicin-loaded nanoparticles. Similar to investigations performed with doxorubicin in solution, the incubation with 10 nM of doxorubicin-loaded nanoparticles caused only weak cytotoxic effects on both, U-87 MG and U-118 MG cells. Furthermore, the incubation of U-373 MG cells with 10 nM of the 2 different drug formulations (doxorubicin in solution vs. doxorubicin NP, respectively) revealed only a slightly enhanced cytotoxicity of the nanoparticle formulation. The highest tested concentration of doxorubicin-loaded NP (500 nM) resulted in a pronounced cytocidal effect against U-87 MG as well as U-373 MG cells, comparable to outcomes observed for doxorubicin in solution. At the latter concentration (500 nM), the doxorubicin-loaded NP mediated cytocidal effects to U-118 MG cells, whereas doxorubicin in solution caused only cytostatic outcome.

Nevertheless, a drastic increase in toxicity of doxorubicin by loading the drug to PBCA nanoparticles was not observed, whether for U-87 MG and U-118 MG nor for U-373 MG cells.

Overall, the doxorubicin-loaded PBCA nanoparticles proved to be equipotent with the drug in solution. Obviously, the nanoparticle formulation did not enhance the cellular uptake of doxorubicin.

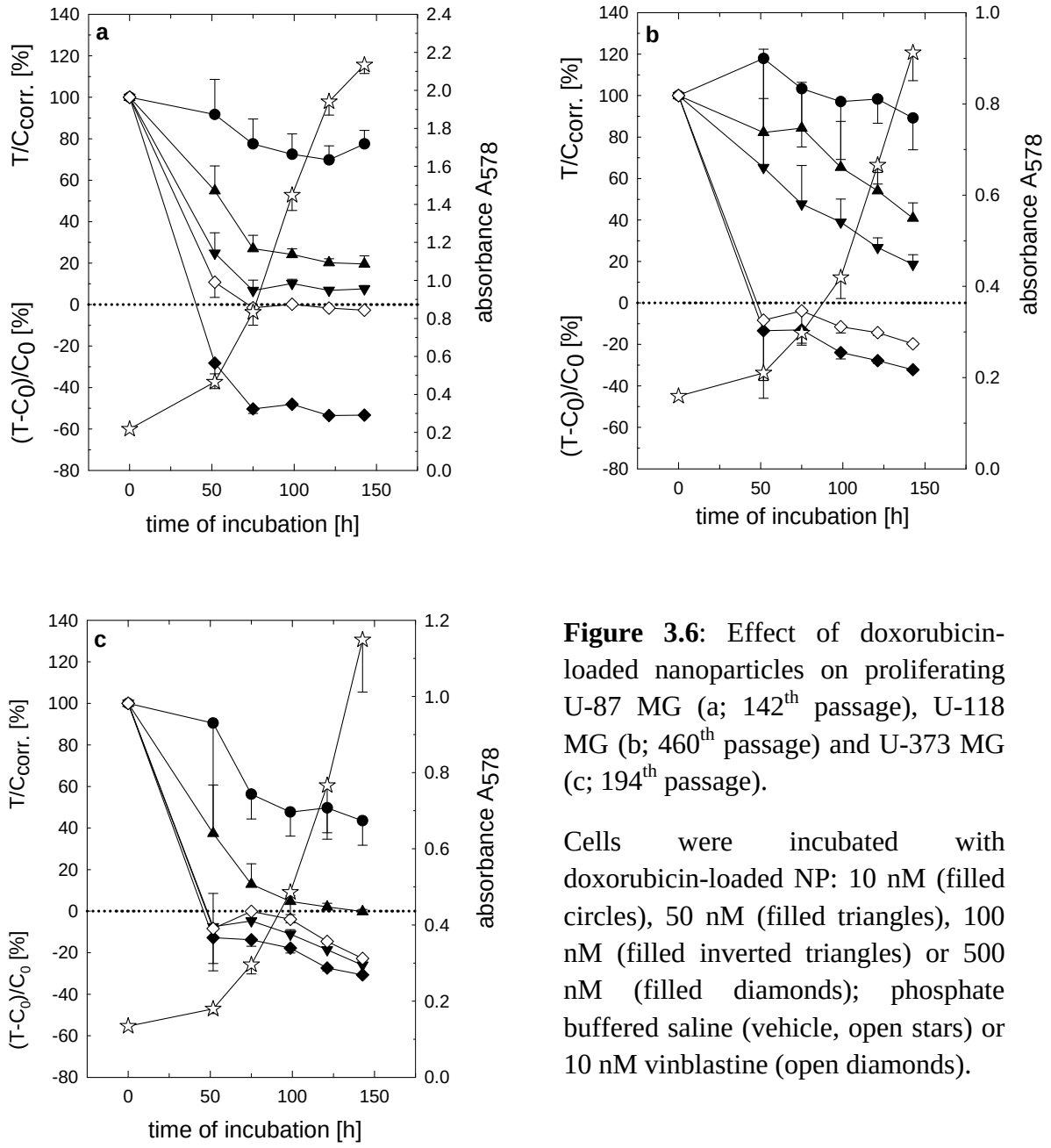

Figure 3.6: Effect of doxorubicin-loaded nanoparticles on proliferating U-87 MG (a; 142th passage), U-118 MG (b; 460th passage) and U-373 MG (c; 194th passage).

Cells were incubated with doxorubicin-loaded NP: 10 nM (filled circles), 50 nM (filled triangles), 100 nM (filled inverted triangles) or 500 nM (filled diamonds); phosphate buffered saline (vehicle, open stars) or 10 nM vinblastine (open diamonds).

Effects of polysorbate 80-coated, doxorubicin-loaded nanoparticles on proliferating human glioblastoma cells are shown in **Figure 3.7**. Coating procedure was performed in phosphate buffered saline and 0.9 % NaCl solution (data not shown), respectively.

At the lowest investigated concentration of 10 nM, the surfactant-coating did not increase the toxicity of doxorubicin-loaded nanoparticles. At higher concentrations of 100 and 500 nM, the coated doxorubicin-loaded nanoparticles had an enhanced antiproliferative effect on U-373 MG cells compared to the non-coated, drug-loaded NPs. Nevertheless, 500 nM of doxorubicin used as a solution turned out to be equipotent, indicating that coating of the drug-loaded nanoparticles with polysorbate 80 did not increase the cytotoxicity of doxorubicin.

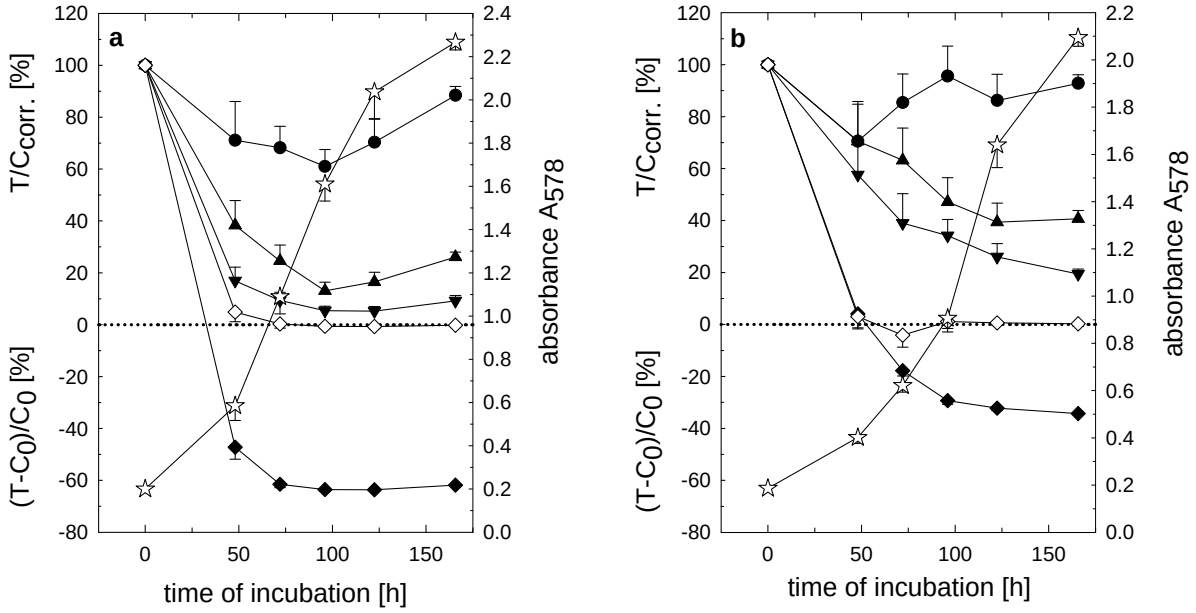

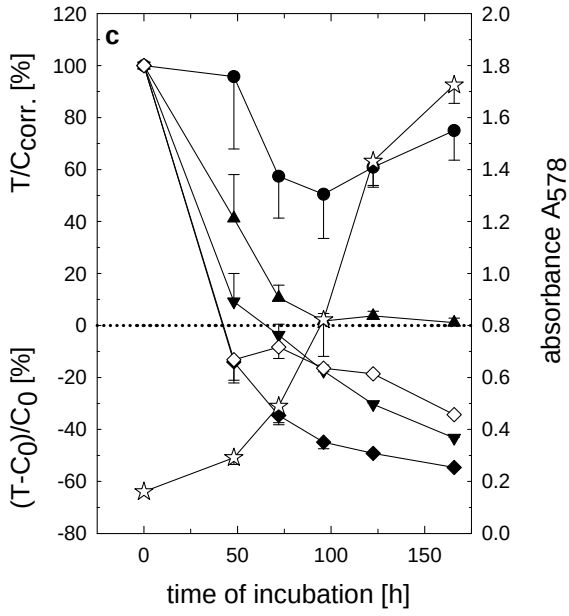

Figure 3.7: Effect of polysorbate 80-coated, doxorubicin-loaded NPs on proliferating U-87 MG (a; 145th passage), U-118 MG (b; 463th passage) and U-373 MG (c; 197th passage)

Cells were incubated with: sterile PBS (vehicle, open stars), 10 nM vinblastin (open diamonds) and different concentrations of polysorbate 80-coated, doxorubicin-loaded nanoparticles: 10 nM (filled circles), 50 nM (filled triangles), 100 nM (filled inverted triangles) and 500 nM (filled diamonds).

In **Figure 3.8** the cytotoxicities of doxorubicin-loaded nanoparticles and the polysorbate 80-coated doxorubicin-loaded nanoparticles against glioblastoma cells are compared at 2 different concentrations.

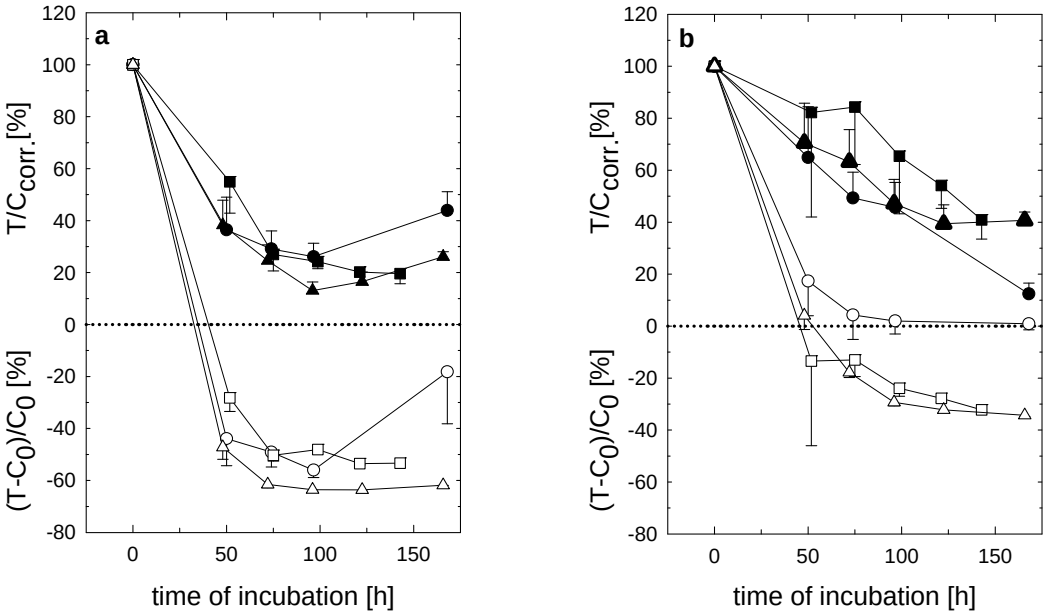

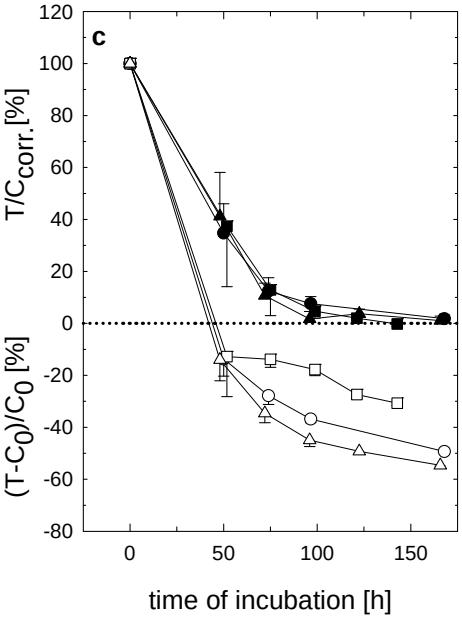

Figure 3.8: Comparison of the effects of different doxorubicin formulations on proliferating U-87 MG (a), U-118 MG (b) and U-373 MG (c) cells.

Cells were incubated with: doxorubicin in solution (circles), doxorubicin-loaded nanoparticles (squares) and polysorbate 80-coated, doxorubicin-loaded nanoparticles (triangles) at concentrations of 50 nM (black symbols) and 500 nM (white symbols).

There was no beneficial effect of doxorubicin-loaded nanoparticles at 50 nM against all investigated human glioblastoma cell lines. Even surface modification of the particles by coating with polysorbate 80 could not enhance the doxorubicin toxicity.

An increased antiproliferative effect was only observed on U-118 MG cells, when incubated with doxorubicin-loaded nanoparticles at a concentration of 500 nM.

Hence, the loading of doxorubicin to nanoparticles preserved the cytotoxicity of the anthracycline, but did not lead to an increased antiproliferative effect against human glioblastoma cells.

3.4.1.4 Effect of short-term drug exposure on the chemosensitivity of U-373 MG cells against different doxorubicin formulations

To investigate putative differences in the toxicity of various doxorubicin formulations during short-term drug exposure, the human U-373 MG glioblastoma cells were studied in a modified crystal violet assay. For this purpose, exposure of the cells to drug-containing media was restricted to 3 and 6 hours, respectively. Subsequently, doxorubicin-containing medium was exchanged by fresh drug-free medium. Finally, the cells were allowed to grow for different periods of time (**Figure 3.9**).

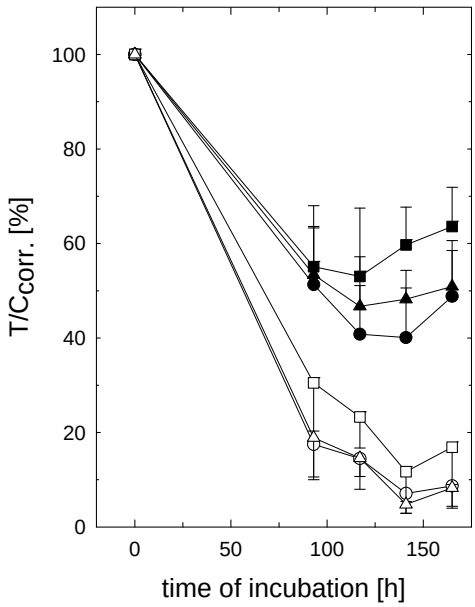

Figure 3.9: Effect of different doxorubicin formulations on proliferating U-373 MG cells. The different preparations affected the cells for 3 (filled symbols) and 6 hours (open symbols), respectively.

The cells were incubated with 50 nM of: doxorubicin in solution (circles), doxorubicin-loaded nanoparticles (squares) and polysorbate 80-coated, doxorubicin-loaded nanoparticles (triangles).

As expected, incubation of the cells for 6 hours yielded a stronger cytotoxic effect than noticed for a shortened incubation period of 3 hours.

This observation was true for all different types of doxorubicin formulation, including the ethanolic solution, the non-coated as well as the polysorbate 80-coated nanoparticle preparation. There was no enhanced antiproliferative effect of doxorubicin after loading of the drug to (surfactant)-coated PBCA nanoparticles and no difference in toxicity depending on the incubation period of the doxorubicin formulations.

3.4.1.5 Effect of different doxorubicin formulations on the ATP-binding cassette transporters ABCB1 and ABCG2

3.4.1.5.1 Immunocytochemical detection of ABCB1 and ABCG2

Dr. Dietmar Gross confirmed the overexpression of ABCB1 / ABCG2 on Kb-V1 / MCF-7/Topo cells by confocal laser-scanning micoscropy studies [Gross, 2006]. **Figure 3.10** shows the corresponding images of immunostained, induced and non-induced Kb- and MCF-7 cells.

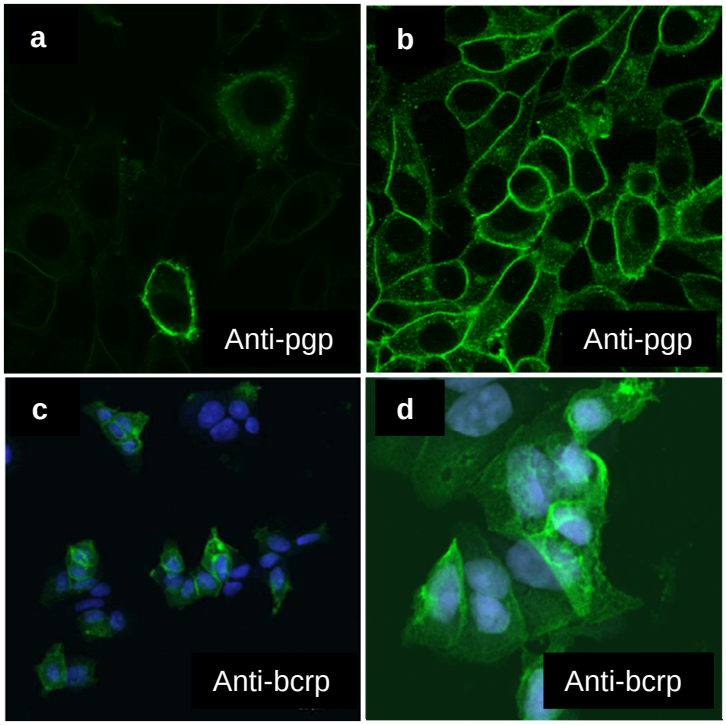

Figure 3.10: Immunostaining of different cell lines with anti-pgp/anti-bcrp by Dr. Dietmar Gross: non-induced Kb-cells (a) and vinblastine induced Kb-V1 cells (b) stained with anti-pgp; non-induced MCF-7 cells (c) and topotecan-induced MCF-7/Topo cells (d) immunostained with anti-bcrp. The expression of the ABC-transporters in wildtype cells (a,c) can be drastically enhanced via the addition of increasing amounts of known transporter substrates, e.g. vinblastine and topotecan to the cell culture medium.

Whereas a relatively weak expression of ABCB1 / ABCG2 in the non-induced cells was observed (**Figure 3.10a, c**), the addition of increasing concentrations of the ABCB1 substrate vinblastine, and the ABCG2 substrate topotecan respectively, yielded high expression levels of the efflux pumps (**Figure 3.10b, d**).

3.4.1.5.2 Cytotoxicity of different doxorubicin-loaded NP formulations

To investigate the effect of different doxorubicin formulations against ABCB1 and ABCG2, the ABCB1 overexpressing Kb-V1 and the ABCG2 overexpressing MCF-7/Topo cells were incubated with these preparations. For comparison, incubation of the non-induced Kb (Kbwt) and MCF-7 cells with the various doxorubicin formulations served as control.

There were no differences in cytotoxic potencies at 100 nM of the different doxorubicin formulations on Kbwt cells (**Figure 3.11).**

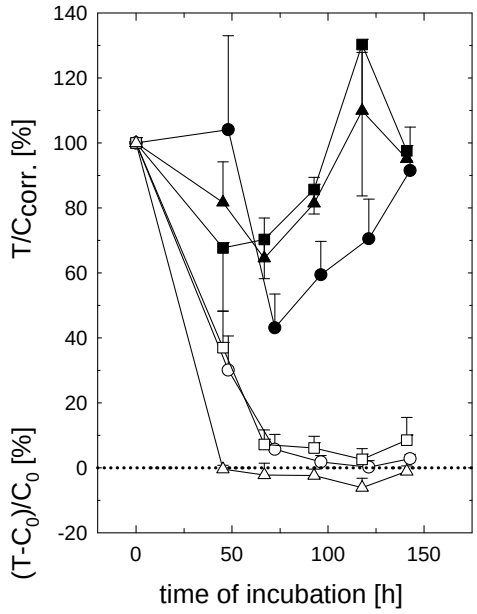

Figure 3.11: Effect of different doxorubicin formulations on proliferating Kbwt cells.

Cells were incubated with 100 nM (black symbols) and 1 µM (white symbols) of different doxorubicin formulations: doxorubicin in solution (circles), doxorubicin-loaded nanoparticles (squares) and polysorbate 80 coated, doxorubicin-loaded nanoparticles (triangles)

At a concentration of 1 µM, all doxorubicin formulations produced a strong cytostatic effect on the non-induced Kbwt cells. Cytotoxicity after incubation of the cells with Tween 80-coated doxorubicin-loaded nanoparticles was only slightly increased compared to the cytotoxicity mediated by doxorubicin in solution and the uncoated doxorubicin-loaded NP.

The experiments using dissolved doxorubicin were in good agreement with previously reported data [Gross, 2006] which showed that Kbwt cells recovered after incubation with 100 nM of the cytostatic. Even a concentration as high as 1 µM, was insufficient to induce a cytocidal effect. Due to overexpression of ABCB1, Kb-V1 cells acquire resistance against the transporter substrate doxorubicin.

This can be overcome by co-application of the ABCB1 inhibitor valspodar (**Figure 3.12**). Whereas incubation of the cells with 1 µM of dissolved doxorubicin alone resulted in a marginal cytotoxic effect, the combination of the cytostatic at non-toxic concentrations (250, 500 and 750 nM) with valspodar (1 µM) resulted in a strong cytostatic effect due to reversal of ABCB1 mediated resistance. Furthermore, incubation of Kb-V1 cells with 1 µM of valspodar alone showed no toxicity mediated by the modulator.

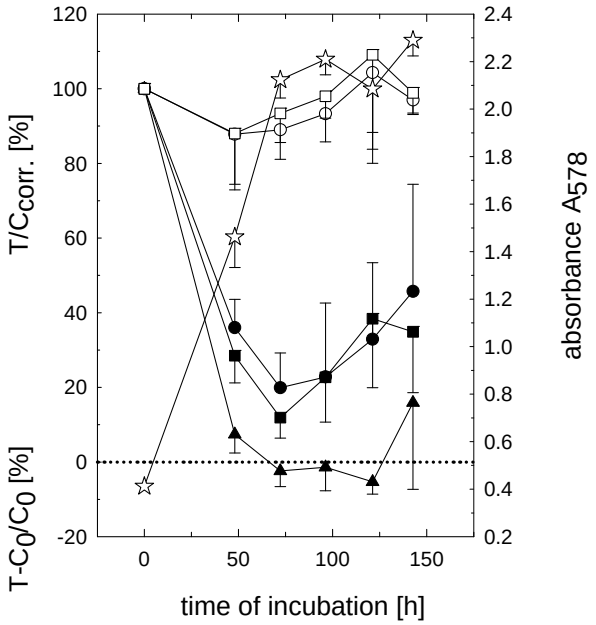

Figure 3.12: Effect of ethanol 70 % (open stars), 1 µM of doxorubicin in solution (open circles) and 1 µM of valspodar alone (open squares) or combined with different concentrations of doxorubicin: 250 nM (filled circles), 500 nM (filled squares) and 750 nM (filled triangles) on proliferating Kb-V1 cells.

For investigations on the effect of different doxorubicin formulations against ABCB1, the Kb-V1 cells were incubated with 1 µM of the ethanolic solution, the nanoparticle suspension and the Tween 80 coated nanoparticles (**Figure 3.13**), respectively. The coated doxorubicin-loaded nanoparticles caused the most distinctive antiproliferative effect on Kb-V1 cells.

At higher concentrations - equal to 3 µM doxorubicin - such differential toxic activities on Kb-V1 cells were also observed by Dietmar Gross [Gross, 2006], suggesting a more effective uptake of doxorubicin into resistant Kb-V1 cells when loaded to overcoated PBCA NP. Moreover, control experiments excluded that these effects were caused by the particles or the surfactants alone [Gross, 2006].

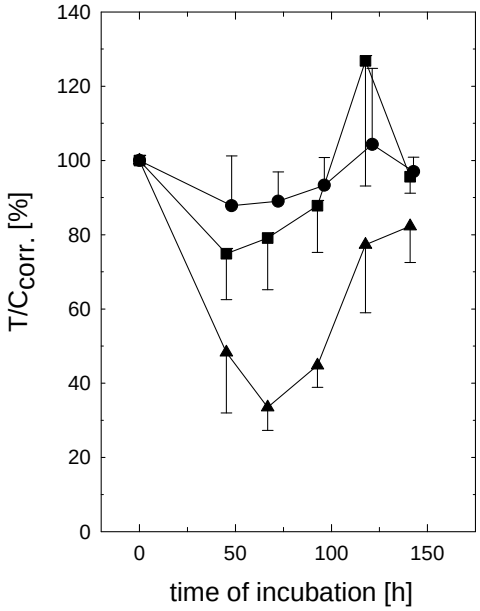

Figure 3.13: Effect of different doxorubicin formulations on proliferating Kb-V1 cells.

Cells were incubated with 1 µM of different doxorubicin formulations: doxorubicin in solution (filled circles), doxorubicin-loaded nanoparticles (filled squares) and polysorbate 80-coated doxorubicin-loaded nanoparticles (filled triangles).

To affirm putative increased cytotoxic effects on ABCB1 by Tween 80-coated PBCA nanoparticles, Kb-V1 cells were investigated in additional chemosensitivity assays using the aforementioned doxorubicin preparations. The cells were incubated with 250 nM of each formulation combined with 1 µM of valspodar to check for synergistic effects of the particles and the ABCB1 inhibitor (**Figure 3.14**).

However, an increased antiproliferative effect of coated doxorubicin-loaded NP combined with valspodar was not observed, compared to the other co-incubation experiments. Hence, the hypothesized ABCB1 modulating effect of polysorbate 80-coated nanoparticles could not be confirmed by these investigations.

Figure 3.14: Incubation of ABCB1-overexpressing Kb-V1 cells with 1 µM of valspodar and 250 nM of different doxorubicin formulations: doxorubicin in solution (filled circles), doxorubicin-loaded nanoparticles (filled squares) and polysorbate 80 coated doxorubicin-loaded nanoparticles (filled triangles).

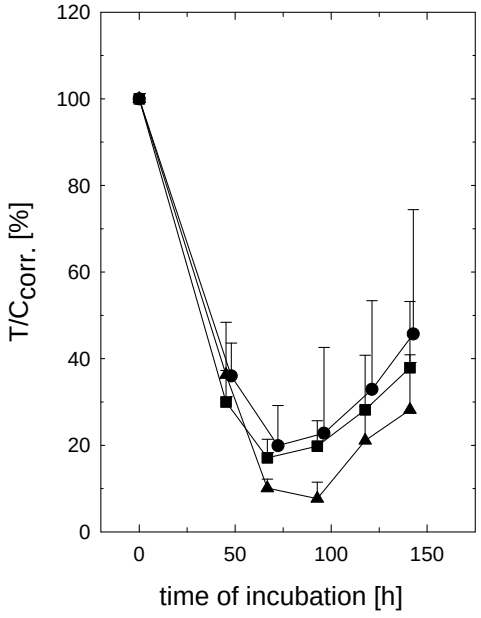

By analogy to investigations on the efflux pump ABCB1, the chemosensitivity of ABCG2-overexpressing MCF-7/Topo cells was studied by treatment with different doxorubicin preparations (**Figure 3.16**).

Additionally, the susceptibility of non-induced MCF-7 cells to these formulations was investigated (**Figure 3.15**) for comparison. This aspect is important not only to interpret the data obtained with the MCF-7/Topo cells, but also to identify anthracycline resistence resulting from point mutations (e.g. amino acid 482) of ABCG2 [Alqawi et al., 2004].

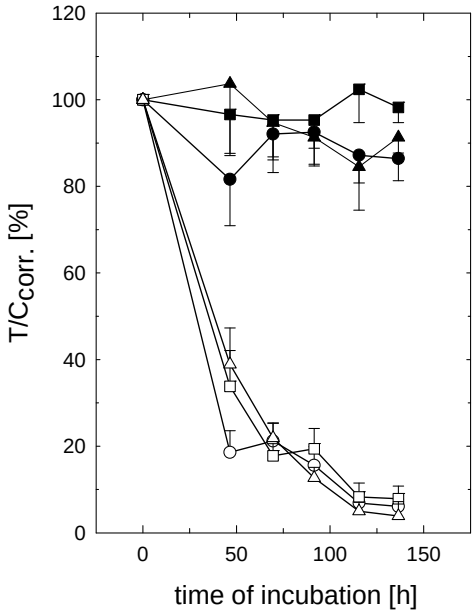

Figure 3.15: Effect of 10 nM (filled symbols) and 100 nM (open symbols) of different doxorubicin formulations on proliferating, non-induced MCF-7 cells.

Cells were incubated with: doxorubicin in solution (circles), doxorubicin-loaded nanoparticles (squares) and polysorbate 80-coated doxorubicin-loaded nanoparticles (triangles).

Differential antiproliferative activities of doxorubicin in solution or loaded to PBCA nanoparticles were not observed at a concentration of 10 nM (**Figure 3.15**). Furthermore, coating of the doxorubicin-loaded nanoparticles with the surfactant polysorbate 80 did not enhance the antiproliferative effect of the anthracycline. At a concentration of 100 nM, a pronounced cytostatic effect was mediated by all preparations of doxorubicin. However, as observed at lower concentrations, discrepancies in the cytotoxicity between various formulations were not detectable.

Overall, the chemosensitivity of non-induced MCF-7 cells against the different doxorubicin formulations was comparable to the susceptibility of the ABCB1 and ABCG2 negative human glioblastoma cell lines U-87 MG, U-118 MG and U-373 MG.

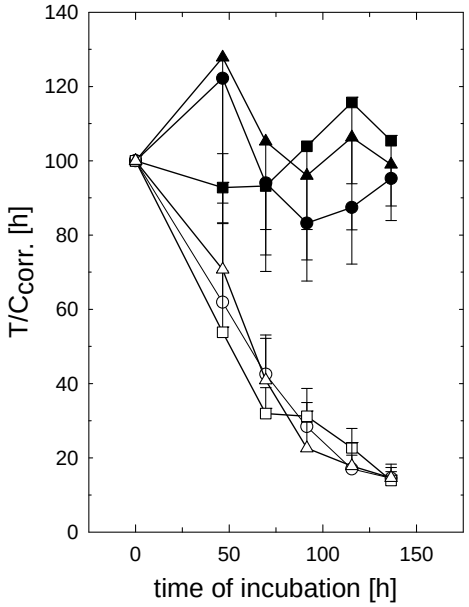

Figure 3.16: Effect of 10 nM (filled symbols) and 100 nM (open symbols) of different doxorubicin formulations on proliferating MCF-7/Topo cells.

Cells were incubated with: doxorubicin in solution (circles), doxorubicin-loaded nanoparticles (squares) and polysorbate 80 coated doxorubicin-loaded nanoparticles (triangles).

No differences between the cytotoxic effects of various drug applications were observed on MCF-7/Topo cells (**Figure 3.16**). Whereas 10 nM of each formulation did not affect the proliferation of ABCG2-overexpressing MCF-7/Topo cells, incubation with 100 nM resulted in strong cytostatic effects comparable to those observed on non-induced MCF-7 cells.

Thus, interactions of coated nanoparticles with the efflux pump ABCG2 are implausible, as suggested above for ABCB1 in Kb-V1 cells.

3.5 Summary and conclusions

Doxorubicin formulations (polysorbate 80-coated and uncoated doxorubicin-loaded nanoparticles (NP)) and new doxorubicin hydrazone derivatives (Sb-59 and Sb-63b) were investigated in chemosensitivity assays on human U-87 MG, U-118 MG and U-373 MG glioblastoma cells, using doxorubicin in solution as a reference:

Neither doxorubicin-loaded polybutylcyanoacrylate particles nor the polysorbate 80 coated drug-loaded NP did show enhanced antiproliferative activity compared to the solution of the cytostatic. In addition, short-term drug exposure studies on U-373 MG cells revealed no increased cytotoxicity of Tween 80-coated doxorubicin-loaded NP as well. Nevertheless, all tested formulations (doxorubicin in solution, doxorubicin-loaded nanoparticles and polysorbate 80-coated, doxorubicin-loaded nanoparticles) gave comparable results. Hence, it can be concluded the other way around that neither loading to PBCA-nanoparticles nor coating of the particles with Tween 80 caused a decrease in toxicity of doxorubicin.

On all investigated glioblastoma cell lines, the derivative Sb-59 proved to be less toxic than its parent compound doxorubicin, although the introduction of a highly lipophilic side chain into the molecule caused only a moderate decrease in cytotoxicity. This is demonstrated by strong cytotoxic / cytostatic effects on all investigated human glioblastoma cell lines at concentrations as low as 100 nM. By contrast, the introduction of a steroid moiety into doxorubicin yielded an equipotent (U-118 MG and U-373 MG cells) or even more potent (on U-87 MG cells) derivative (Sb-63b). Thus, it can be concluded that the structural modification of doxorubicin - by introducing a lipophilic side chain or a steroid moiety into the molecule - did not significantly decrease the toxicity of the anthracycline, making the derivatives interesting for ongoing predictive studies in the chemotherapy of malignant brain tumors.

To investigate the effect of doxorubicin-loaded nanoparticle formulations on the efflux pumps ABCB1 and ABCG2, the transporter overexpressing subclones Kb-V1 and MCF-7/Topo served as an in vitro model. Therefore, by analogy to the performed chemosensitivity studies on glioblastoma cell lines, the different doxorubicin formulations were investigated for their antiproliferative potential against Kb-V1 and MCF-7/Topo cells. For comparison, the corresponding non-induced wild type cells (Kbwt and MCF-7) were incubated with doxorubicin in solution, loaded to nanoparticles or loaded to polysorbate 80-coated nanoparticles:

Differential antiproliferating activities for the various modes of drug application were not observed, neither for Kbwt nor for MCF-7 cells. Furthermore, the incubation of ABCG2 overexpressing MCF-7/Topo cells with increasing concentrations of the different doxorubicin preparations revealed no increased toxicity of the cytostatic by application as (polysorbate 80-coated) nanoparticle formulation. In contrast, Kb-V1 cells showing resistance to doxorubicin due to overexpression of ABCB1 were most sensitive to the anthracycline when administered as surfactant coated nanoparticles (at a concentration of 1 µM). At concentrations corresponding to 3 µM of doxorubicin, similar observations were made by D. Gross [Gross, 2006]. Hence, high concentrations were necessary to discriminate toxic effects of different formulations. Moreover, co-incubation experiments with the ABCB1 inhibitor valspodar did not confirm a direct interaction of polysorbate 80-coated nanoparticles on the efflux pump ABCB1. Alternatively, it may be speculated that the Tween 80-coated particles act as a kind of Trojan horse, protecting a larger amount of doxorubicin from elimination via ABCB1. Thus, an increased intracellular concentration of the cytostatic might lead to enhanced cytotoxicity. However, in contrast to experiments by Reimold et al. [Reimold et al., 2008] penetration of the coated doxorubicin-loaded nanoparticles or uptake via endocytosis could not be proven by Gross [Gross, 2006]. Furthermore, it remains unclear whether doxorubicin is released after adsorption of the particles to the cell membrane, maintaining a concentration gradient counteracting the ABCB1 efflux to a certain extent by saturation of the transporter [Gross, 2006].

References

Alqawi, O., Bates, S. and Georges, E. (2004). Arginine482 to threonine mutation in the breast cancer resistance protein ABCG2 inhibits rhodamine 123 transport while increasing binding. Biochem. J. **382**(Pt 2): 711-6.

Altenschöpfer, P. (1998). Tumorpharmakologische und analytische Untersuchungen zur Optimierung neuer Zytostatika-beladener bioabbaubarer Implantate für die interstitielle Chemotherapie maligner Hirntumoren; Doctoral thesis.

Alyautdin, R. N., Petrov, V. E., Langer, K., Berthold, A., Kharkevich, D. A. and Kreuter, J. (1997). Delivery of loperamide across the blood-brain barrier with polysorbate 80-coated polybutylcyanoacrylate nanoparticles. Pharm. Res. **14**(3): 325-8.

Alyautdin, R. N., Tezikov, E. B., Ramge, P., Kharkevich, D. A., Begley, D. J. and Kreuter, J. (1998). Significant entry of tubocurarine into the brain of rats by adsorption to polysorbate 80-coated polybutylcyanoacrylate nanoparticles: An in situ brain perfusion study. J. Microencapsul. **15**(1): 67-74.

Bähr, O., Rieger, J., Duffner, F., Meyermann, R., Weller, M. and Wick, W. (2003). P-Glycoprotein and Multidrug Resistance-associated Protein Mediate Specific Patterns of Multidrug Resistance in Malignant Glioma Cell Lines, but not in Primary Glioma Cells. Brain Pathol. **13**(4): 482-494.

Bernhardt, G., Reile, H., Birnböck, H., Spruss, T. and Schönenberger, H. (1992). Standardized kinetic microassay to quantify differential chemosensitivity on the basis of proliferative activity. J. Cancer Res. Clin. Oncol. **118**(1): 35-41.

De Jong, W. H. and Borm, P. J. (2008). Drug delivery and nanoparticles:applications and hazards. Int J Nanomedicine **3**(2): 133-49.

Declèves, X., Fajac, A., Lehmann-Che, J., Tardy, M., Mercier, C., Hurbain, I., Laplanche, J.-L., Bernaudin, J.-F. and Scherrmann, J.-M. (2002). Molecular and functional MDR1-Pgp and MRPs expression in human glioblastoma multiforme cell lines. Int. J. Cancer **98**(2): 173-180.

Deeken, J. F. and Löscher, W. (2007). The Blood-Brain Barrier and Cancer: Transporters, Treatment, and Trojan Horses. Clin. Cancer Res. **13**(6): 1663-1674.

Gao, K. and Jiang, X. (2006). Influence of particle size on transport of methotrexate across blood brain barrier by polysorbate 80-coated polybutylcyanoacrylate nanoparticles. Int. J. Pharm. **310**(1-2): 213-219.

Gelperina, S. E., Khalansky, A. S., Skidan, I. N., Smirnova, Z. S., Bobruskin, A. I., Severin, S. E., Turowski, B., Zanella, F. E. and Kreuter, J. (2002). Toxicological studies of doxorubicin bound to polysorbate 80-coated poly(butyl cyanoacrylate) nanoparticles in healthy rats and rats with intracranial glioblastoma. Toxicol. Lett. **126**(2): 131-141.

Gross, D. (2006). New Approaches to the Chemotherapy of Glioblastoma:investigations on doxorubicin nanoparticles, inhibition of PDGF receptors and kinesin Eg5, with emphasis on confocal laser-scanning microscopy; Doctoral thesis. http://www.opus-bayern.de/uni-regensburg/volltexte/2006/707/pdf/Dissertation%20Dietmar%20Gross%20aus%20Schw%E4bisch%20Gm%FCnd%202006.pdf

Gulyaev, A. E., Gelperina, S. E., Skidan, I. N., Antropov, A. S., Kivman, G. Y. and Kreuter, J. (1999). Significant Transport of Doxorubicin into the Brain with Polysorbate 80-Coated Nanoparticles. Pharm. Res. **16**(10): 1564-1569.

Hekmatara, T., Bernreuther, C., Khalansky, A. S., Theisen, A., Weissenberger, J., Matschke, J., Gelperina, S., Kreuter, J. and Glatzel, M. (2009). Efficient systemic therapy of rat glioblastoma by nanoparticle-bound doxorubicin is due to antiangiogenic effects. Clin. Neuropathol. **28**(3): 153-164.

Huang, L., Wang, C., Chen, Z., Xu, Y., Wang, Y., Zhong, Y. and Liu, Y. (2008). Targeting mice brain tissue by Tween 80-coated gemcitabine polybutylcyanoacrylate nanoparticles. Zhongguo Yiyuan Yaoxue Zazhi **28**(16): 1332-1336.

Hubensack, M. (2005). Approaches to overcome the blood brain barrier in the chemotherapy of primary and secondary brain tumors: modulation of P-glycoprotein 170 and targeting of the transferrin receptor; Doctoral thesis. http://www.opus-bayern.de/uni-regensburg/volltexte/2005/471/pdf/Dissertation_MartinaHubensack.pdf

Kondo, S., Kondo, Y., Hara, H., Kaakaji, R., Peterson, J. W., Morimura, T., Takeuchi, J. and Barnett, G. H. (1996). mdm2 gene mediates the expression of mdr1 gene and P-glycoprotein in a human glioblastoma cell line. Br. J. Cancer **74**(8): 1263-8.

Kreuter, J. (2001). Nanoparticulate systems for brain delivery of drugs. Adv. Drug Del. Rev. **47**(1): 65-81.

Kreuter, J., Alyautdin, R. N., Kharkevich, D. A. and Ivanov, A. A. (1995). Passage of peptides through the blood-brain barrier with colloidal polymer particles (nanoparticles). Brain Res. **674**(1): 171-174.

Kreuter, J., Petrov, V. E., Kharkevich, D. A. and Alyautdin, R. N. (1997). Influence of the type of surfactant on the analgesic effects induced by the peptide dalargin after its delivery across the blood-brain barrier using surfactant-coated nanoparticles. J. Controlled Release **49**(1): 81-87.

Kurakhmaeva, K. B., Djindjikhashvili, I. A., Petrov, V. E., Balabanyan, V. U., Voronina, T. A., Trofimov, S. S., Kreuter, J., Gelperina, S., Begley, D. and Alyautdin, R. N. (2009). Brain targeting of nerve growth factor using poly(butyl cyanoacrylate) nanoparticles. J. Drug Target. **17**(8): 564-74.

Kurakhmaeva, K. B., Voronina, T. A., Kapica, I. G., Kreuter, J., Nerobkova, L. N., Seredenin, S. B., Balabanian, V. Y. and Alyautdin, R. N. (2008). Antiparkinsonian effect of nerve growth factor adsorbed on polybutylcyanoacrylate nanoparticles coated with polysorbate-80. Bull. Exp. Biol. Med. **145**(2): 259-62.

Pereverzeva, E., Treschalin, I., Bodyagin, D., Maksimenko, O., Kreuter, J. and Gelperina, S. (2008). Intravenous tolerance of a nanoparticle-based formulation of doxorubicin in healthy rats. Toxicol. Lett. **178**(1): 9-19.

Petri, B., Bootz, A., Khalansky, A., Hekmatara, T., Mueller, R., Kreuter, J. and Gelperina, S. (2007). Mechanism of action and surfactant influence during chemotherapy of brain tumour using doxorubicin-loaded poly(butyl cyanoacrylate) nanoparticles. Nanotech 2007, Nanotechnology Conference and Trade Show, Santa Clara, CA, United States.

Reimold, I., Domke, D., Bender, J., Seyfried, C. A., Radunz, H.-E. and Fricker, G. (2008). Delivery of nanoparticles to the brain detected by fluorescence microscopy. Eur. J. Pharm. Biopharm. **70**(2): 627-632.

Schroeder, U., Sommerfeld, P., Ulrich, S. and Sabel, B. A. (1998). Nanoparticle technology for delivery of drugs across the blood-brain barrier. J. Pharm. Sci. **87**(11): 1305-1307.

Steiniger, S. C. J., Kreuter, J., Khalansky, A. S., Skidan, I. N., Bobruskin, A. I., Smirnova, Z. S., Severin, S. E., Uhl, R., Kock, M., Geiger, K. D. and Gelperina, S. E. (2004). Chemotherapy of glioblastoma in rats using doxorubicin-loaded nanoparticles. Int. J. Cancer **109**(5): 759-767.

Wang, C.-X., Huang, L.-S., Hou, L.-B., Jiang, L., Yan, Z.-T., Wang, Y.-L. and Chen, Z.-L. (2009). Antitumor effects of polysorbate-80 coated gemcitabine polybutylcyanoacrylate nanoparticles in vitro and its pharmacodynamics in vivo on C6 glioma cells of a brain tumor model. Brain Res. **1261**: 91-99.

Chapter 4

Modulation of the efflux pump ABCG2

4.1 Introduction

ATP-binding cassette transporters use the energy of ATP-hydrolysis to transport a broad variety of substrates across the cell membrane. Under physiological conditions, these efflux pumps, including ABCB1 (p-glycoprotein 170, P-gp), ABCC2 (multidrug resistance related protein 2) [Borst et al., 1997; Kuwano et al., 1999] and ABCG2 (ABCP, BCRP, MXR) [Dean and Allikmets, 2001; Cervenak et al., 2006], appear to play a protective role in several tissues [Robey et al., 2007]. Highly expressed in the gastrointestinal tract, the placenta, the testis and the brain endothelium, ABCG2 presumably represents an important part in the protection from xenobiotics as well as in the regulation of oral bioavailability [Robey et al., 2009]. In the placenta ABCG2 appears to reduce the passage of substrates from the mother to the fetus and, as reasoned from mice studies [Staud et al., 2006], decreases the concentration of certain substrates in the fetal circulation. The expression of the aforementioned efflux pumps at the blood-brain barrier (BBB) is an important limiting factor in the therapy of central nervous diseases since numerous pharmacologically active compounds are actively extruded. This is also one of the primary causes for the failure of chemotherapy in the treatment of malignant brain tumors [Régina et al., 2001], since many anticancer agents are ABCB1 and ABCG2 substrates.

4.1.1 ABC transporter mediated multi-drug resistance (MDR)

Furthermore, ABC transporters play also an important role in conjunction with multi-drug resistance (MDR). According to estimations, multi-drug resistant tumors account for up to half of all cancer-related deaths [Leonard et al., 2003; Sheps and Ling, 2007]. Multi-drug resistance occurs by the overexpression of efflux pumps such as ABCB1 and ABCG2, located in the plasma membrane of cancer cells. The active transport of a vast number of structurally unrelated compounds, including many commonly used anticancer drugs, leads to low intracellular levels of these substances. Since its discovery in 1998 [Allikmets et al., 1998; Doyle et al., 1998], ABCG2 has been the subject of many investigations on its role in MDR. The overexpression of the efflux pump is associated with high-level of resistance to a large number of cytostatics.

4.1.2 ABCG2 as a potential marker of cancer stem cells

In addition, ABCG2 has recently attracted interest with respect to a new concept of tumor development and progression, the so-called cancer stem cell hypothesis. By contrast to the classical stochastic model (assuming that all cancer cells are involved in tumor initiation and progression), the stem cell concept is based on the idea that only a small side-population of cancer cells proliferates, analogously to hematopoietic stem cells in the bone marrow. Characteristically, members of the side-population cells divide slowly, are capable of long-term self-renewal and express ABCG2 [Bunting, 2002; Jonker et al., 2005; Sung et al., 2008]. In a large number of tumor cell lines and tumor biopsies [Hirschmann-Jax et al., 2004; Kondo et al., 2004; Haraguchi et al., 2006], such stem cells, which might be responsible for the long-term failure of many cancer chemotherapies, have been identified. Due to their slow proliferation and the expression of ABCG2 efflux pumps, they are inefficient targets for classical cytostatic agents. For this reason, alternative approaches for specifically targeting cancer-stem cells might be promising with respect to an eradication of this subpopulation. Recently, a drug called salinomycin was identified, which reduced the number of breast cancer stem cells in vitro more than 100 times more effectively than paclitaxel [Humphries, 2009]. Such effective targeting of cancer stem cells could help to avoid recurrence of tumors.

4.1.3 Effects of estrogens on ABCG2 expression

Another interesting aspect of ABCG2 transporters might be the putative involvement of estrogens in the regulation of efflux pump expression. Whereas Zhang et al. describe an up-regulation of ABCG2 mRNA and protein expression in MCF-7 cells under 17β – estradiol (E_2) treatment [Zhang et al., 2006], the exposure of the aforementioned cells to E_2 by Imai et. al resulted in a cytotoxic potentiation of the active metabolite of irinotecan SN-38, caused by lower levels of the transporter protein ABCG2 [Imai et al., 2005].

Hence, in many respects, the manipulation of the ABCG2 transporter might be a promising approach in cancer chemotherapy. Predominantly, inhibition of the efflux pump by potent and selective modulators might be a conceivable application to reverse ABCG2-mediated multi-drug resistance or to specifically target the cancer-stem cells.

Long-term survival of these cells, due to resistance against cytostatics, that are ABCG2 substrates, might be overcome by a specific ABCG2 inhibitor in combination with the pharmacologically active compound.

4.1.4 Modulation of ABC transporters expressed at the BBB

The modulation of the physiologically expressed ABCG2 transporters at the blood-brain barrier might be an interesting strategy to increase drug levels of ABCG2 substrates in the brain [Breedveld et al., 2006]. Such an approach was successful in a proof-of-concept study by the combination of the cytostatic paclitaxel, an ABCB1 substrate, and the 2nd generation ABCB1 modulator valspodar [Fellner et al., 2002]. The co-application of valspodar yielded 6-8 fold higher brain levels of paclitaxel as obtained in mice which were treated with paclitaxel alone. Furthermore, in an orthotopic human glioblastoma model in nude mice, these increased brain levels of paclitaxel yielded a decrease in tumor volume by 90 %. Similarly, the co-administration of the 3rd generation inhibitors elacridar and tariquidar resulted in higher intracerebral levels of paclitaxel [Hubensack et al., 2008].

4.1.5 Inhibitors of ABCG2

Due to its relatively recent discovery, only a few inhibitors of ABCG2 have been published so far [Ahmed-Belkacem et al., 2006; Boumendjel et al., 2007; Han et al., 2008; Jain et al., 2008; Liu et al., 2008]. The diketopiperazine fumitremorgin C (FTC, **Figure 4.1**), isolated from the fermentation broth of *Aspergillus fumigatus*, was reported first [Rabindran et al., 2000]. Neurotoxicity of the compound precluded its use in in vivo studies. Novobiocin, a coumermycin derivative and inhibitor of the prokaryotic enzyme gyrase was also identified as an inhibitor of the efflux transporter ABCG2. However, cytotoxicity and flow cytometric assays yielded an overcome of the ABCG2-mediated drug resistance to mitoxantrone, topotecan and SN-38, the active metabolite of irinotecan, only at micromolar concentrations of novobiocin [Shiozawa et al., 2004]. The original ABCB1 inhibitors elacridar (GF120918, **Figure 4.1**) and tariquidar (XR 9576, **Figure 4.1**) also act as modulators of ABCG2. It was demonstrated that this effect was more pronounced for elacridar [de Bruin et al., 1999] than observed for tariquidar [Robey et al., 2004] and their common analog WK-X-34 [Jekerle et al., 2006; Jekerle et al., 2007].

A very recent study identified the class of botryllamides, obtained by extractions of the marine ascidian *Botryllus tyreus*, as inhibitors of ABCG2 [Henrich et al., 2009]. Nevertheless, by means of a fluorescence-based microtiter assay containing the ABCG2 substrate pheophorbide a (PhA), these compounds were determined with IC_{50} values only in the micromolar range [Henrich et al., 2009]. The most potent inhibitor of ABCG2, known up to the time of our project, was a non-toxic analog of the previously mentioned fumitremorgin C [Allen et al., 2002]. The compound, called Ko143 (**Figure 4.1**), was applied in in vivo studies and resulted in an increased bioavailability of orally administered topotecan in mice [Allen et al., 2002].

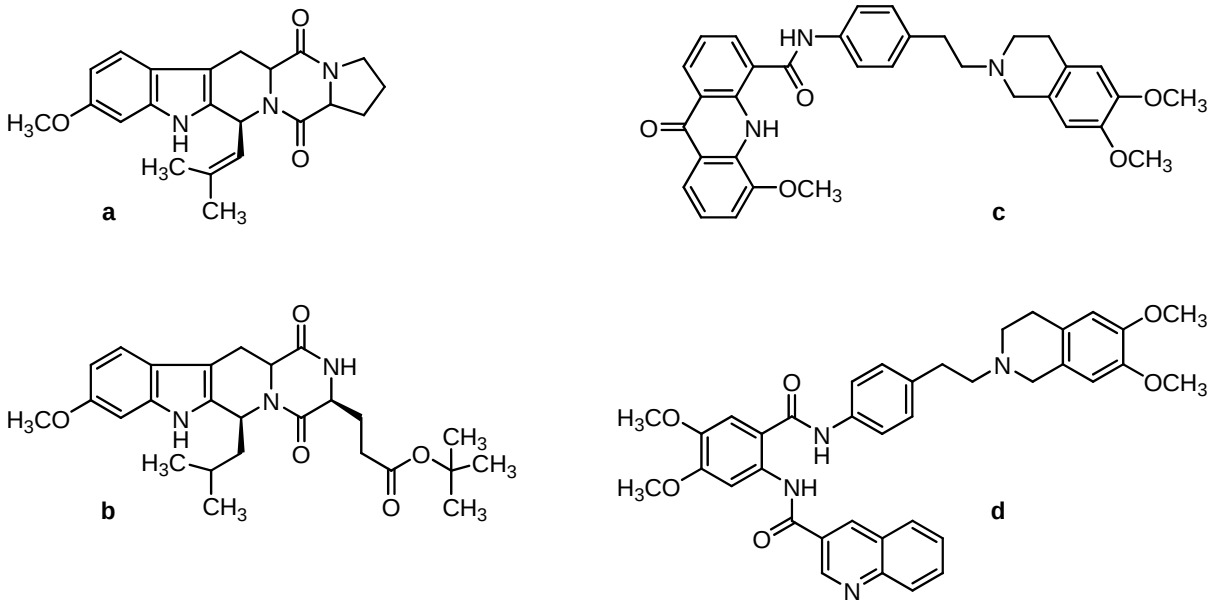

Figure 4.1: Structures of the ABCG2 modulators fumitremorgin C (**a**) and its analog, Ko143 (**b**), the dual ABCB1/ABCG2 inhibitor elacridar (**c**) and the ABCB1 inhibitor tariquidar (**d**).

4.2 Objective

As described above, in many respects, limitations in chemotherapy due to efflux pump-mediated resistance to cytostatics represent a major problem. Besides the (over) expression of these transporters in many tumor types as well as in cancer stem cells, the existence of such efflux pumps in healthy tissues, e.g. at the blood-brain barrier, can also cause problems in pharmacotherapy (e.g. in the treatment of malignant brain tumors). Increasing drug levels in the brain by co-application of an ABC transporter inhibitor with a cytostatic, known to be a substrate of the efflux pump, has already been proven with the ABCB1 modulator valspodar and the chemotherapeutic paclitaxel in the treatment of glioblastoma [Fellner et al., 2002]. Furthermore, such investigations have been performed with the ABCB1 inhibitor tariquidar yielding a higher brain / plasma ratio of paclitaxel, but did not result in higher brain levels of the cytostatic compared with valspodar [Hubensack et al., 2008]. It has been speculated that these relatively low paclitaxel brain level might be due to accumulation of the hydrophobic tariquidar in the lipid compartment of the brain. In the search for more hydrophilic tariquidar analogs as inhibitors of ABCB1 [Egger et al., 2007; Müller, 2007; Hubensack et al., 2008], we found that, interestingly, minimal structural changes at the benzamide core of the parent compound tariquidar resulted in potent ABCG2 inhibition.

The objective of this work was to investigate such ABCG2 selective tariquidar analogs in more detail. The inhibitory potency of the compounds against ABCG2 was examined in a flow cytometric mitoxantrone efflux assay, whereas the selectivity against ABCB1 and ABCC2 was investigated by Dr. Christine Müller, Peter Höcherl and Anne Mahringer. The results of these studies were published recently [Kühnle et al., 2009]. With regard to ABCG2 selectivity putative essential structural moieties of the substances were modified, further analogs as well as several partial structures and intermediates were synthesized, and the compounds were characterized by means of the aforementioned transporter assays. Moreover, to fortify the inhibition data of flow cytometric mitoxantrone efflux assays and to circumvent these costly as well as time-consuming test systems, 2 fluorescence-based 96-well plate assays were developed. For this purpose, the known ABCG2 substrates Hoechst 33342 and pheophorbide a were selected for the establishment of such rapid ABCG2 transporter assays.

As a prerequisite for planed in vivo studies, the most potent inhibitors were assessed with respect to their stability in mouse plasma by means of HPLC-MS analysis. With respect to investigations on the mode of ABCG2 inhibition by these tariquidar analogs, a small series of fluorescence-labeled tariquidar-like substances was synthesized by Carolin Fischer (Institute of Organic Chemistry, University of Regensburg), and IC_{50} values were determined in the newly established Hoechst 33342 assay. In addition, the labeled compounds were applied in confocal-laser scanning microscopy (CLSM).

Additionally, the contribution of estrogens to the regulation of ABCG2 protein expression should be investigated. Therefore, MCF-7/Topo cells were examined in the crystal violet chemosensitivity assays by checking their sensitivity to the cytostatic topotecan in the absence or presence of estradiol.

4.3 Materials and methods

4.3.1 Drugs and chemicals

A Milli-Q system (Millipore, Eschborn, Germany) was used for the purification of water in aqueous drug solutions. All chemicals used were of analytical grade, if not otherwise mentioned. Stock solutions of mitoxantrone were performed by diluting Novantron® (Wyeth Pharma, Muenster, Germany) in 70 % ethanol to a concentration of 2 mM. Hoechst 33342 (Invitrogen, Karlsruhe, Germany) was dissolved in sterile water to produce a 1.6 mM working solution. Pheophorbide a (PhA) (Frontier Scientific, Logan, UT) was dissolved in DMSO (Merck, Darmstadt, Germany) to a concentration of 10 mM. A working solution of 200 µM in DMSO was prepared for assay performance. Estradiol (Sigma, Munich, Germany) was dissolved in DMSO to a concentration of 10 mM. Estron sulfate was obtained from Sigma, Munich, Germany. All stocks were stored at -20 °C. Hycamtin® (GlaxoSmithKline, Munich, Germany) was diluted in 70 % ethanol to achieve a topotecan stock solution of 2 mM. Precipitates of topotecan were redissolved prior to use by ultrasound and slight heating. For cell culture supplementation, a 0.1 mM stock solution of topotecan in ethanol (70 %) was prepared. Vinblastine (vinblastine sulfate, Sigma, Munich, Germany) was dissolved in 70 % ethanol at a concentration of 1 mM. All topotecan and vinblastin stocks were stored at 4 °C. PBS (phosphate buffered saline) was made of 8.0 g/L NaCl, 1.0 g/L $Na_2HPO_4 \cdot 2\ H_2O$, 0.20 g/L KCl, 0.20 g/L KH_2PO_4 and 0.15 g/L $NaH_2PO_4 \cdot H_2O$. The pH-value was adjusted to 7.3 - 7.4 by using a 1 M NaOH or HCl solution. Phosphate buffered saline with calcium and magnesium was made by dissolving 0.2 g/L KCl, 0.2 g/L KH_2PO_4, 8.0 g/L NaCl, 1.15 g/L $Na_2HPO_4 \cdot 2\ H_2O$ in water followed by adding 0.132 g/L of $CaCl_2 \cdot 2\ H_2O$ and 0.10 g/L of $MgCl_2 \cdot 6\ H_2O$. Adjusting the pH-value to 7.3 was performed by the drop-wise addition of a 1 M NaOH solution. For buffer preparation all chemicals were obtained from Merck, Darmstadt, Germany. A solution of 3 % (m/m) of paraformaldeyde (Merck, Darmstadt, Germany) in $Ca^{2+/}Mg^{2+}$ containing PBS was made by stirring 1.5 g of paraformaldehyde per 50 g total solution while heating on a magnetic stirrer for approximately 30 min. Sodium phosphate buffer (0.1 M) was produced with 14.3 g/L of $Na_2HPO_4 \cdot 2\ H_2O$ (Merck, Darmstadt, Germany) and 11.1 g/L of $NaH_2PO_4 \cdot H_2O$ (Merck, Darmstadt, Germany) and adjusting the pH to 7.4. Ortho-nitrophenylbutyrate (Merck, Darmstadt, Germany) was dissolved in DMSO to a concentration of 100 mM and stored at 4 °C.

4.3.2 Test compounds

The free base of tariquidar was synthesized by Hubensack [Hubensack, 2005]. A 10 mM stock solution of tariquidar in DMSO was prepared. Elacridar was a kind gift of GlaxoSmithKline, Munich, Germany and dissolved in DMSO. Fumitremorgin C was either obtained from Merck, Darmstadt, Germany or a kind gift of Dr. Susan Bates from the NIH (Bethesda, MD, USA). The compound was dissolved in DMSO at a concentration of 10 mM and stored at -80 °C. The fumitremorgin C analog Ko143 was a kind gift of Dr. A. H. Schinkel from the Netherlands Cancer Institute (Amsterdam, NL). All new tariquidar analogs were synthesized, characterized and provided by the workgroup of Prof. Dr. Burkhard König, Institute of Organic Chemistry (University of Regensburg, Germany). If possible, 10 mM stock solutions of the test compounds in DMSO were prepared. Solid substances as well as stock solutions of all investigated tariquidar analogs were stored at – 20 °C. **Charts 4.1** – **4.5** give an overview of the different subseries of tariquidar-like compounds.

Chart 4.1: Structures of tariquidar analogs with variations of the heterocyclus.

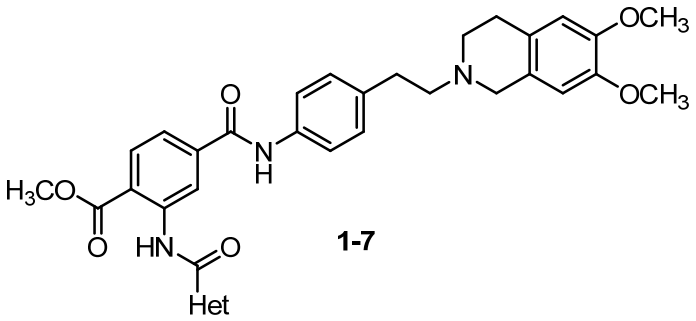

1-7

no. (lab code)	Het	no. (lab code)	Het
1 (ME 1-4)	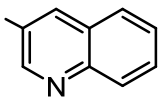	**5 (ME 21-1)**	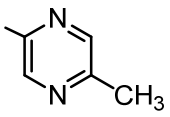
2 (ME 22-1)	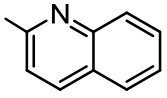	**6 (ME 14-1)**	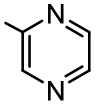
3 (ME 11-1)	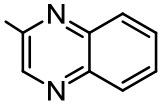	**7 (ME 12-1)**	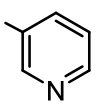
4 (ME 19-2)	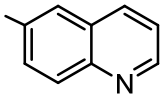		

Chart 4.2: Structures of tariquidar-like analogs with quinoline-3-carboxamido function and variations of R^1 and R^2.

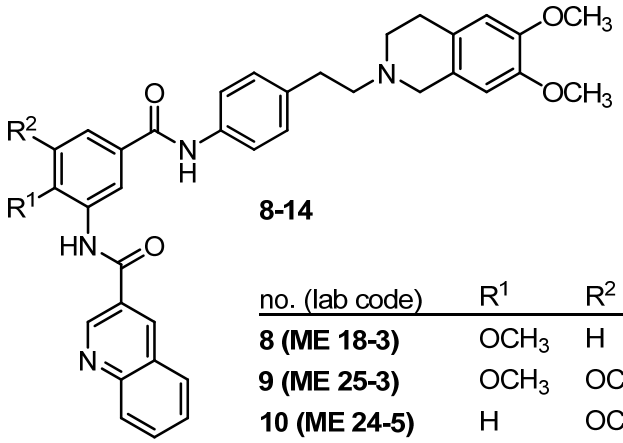

8-14

no. (lab code)	R^1	R^2
8 (ME 18-3)	OCH_3	H
9 (ME 25-3)	OCH_3	OCH_3
10 (ME 24-5)	H	OCH_3
11 (ME 17-3)	CH_3	H
12 (CP 09)	COOH	H
13 (CP 33)	$COCH_3$	H
14 (CP 60)	C_3H_5	H

Chart 4.3: Structures of tariquidar analogs with quinoline-2-carboxamido function and variations in R^1, R^2, R^3 and R^4.

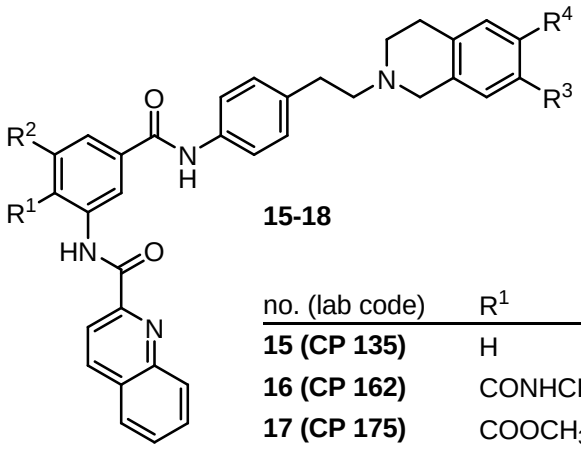

15-18

no. (lab code)	R^1	R^2	R^3	R^4
15 (CP 135)	H	H	OCH_3	OCH_3
16 (CP 162)	$CONHCH_3$	H	OCH_3	OCH_3
17 (CP 175)	$COOCH_3$	H	H	H
18 (CP 181)	$CONHCH_3$	H	H	H

Chart 4.4: Chemical structures of intermediates of tariquidar-like analogs bearing a tetrahydroisoquinolinylethyl-phenyl moiety.

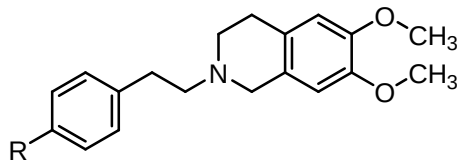

19-23

no. (lab code)	R
19 (CP 02a)	NH_2
20 (CP 199)	$NHCOCH_3$
21 (CP 130)	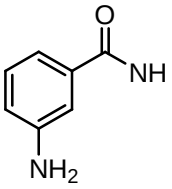
22 (CP 121)	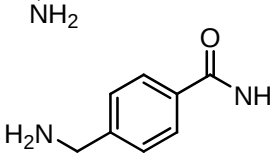
23 (CP 134)	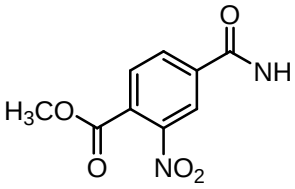

Chart 4.5: Chemical structures of building blocks with quinoline-2-carboxamido moiety and methyl ester.

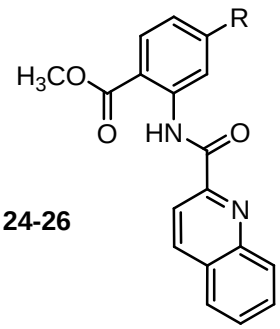

24-26

no. (lab code)	R
24 (CP 195)	COOH
25 (CP 204)	$CONHCH_3$
26 (CP 149)	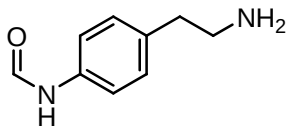

4.3.3 Cell culture

MCF-7 cells (ATCC HTB-22, a human breast adenocarcinoma cell line), were cultured in Eagle's Minimum Essential Medium containing L-glutamine (Sigma, Munich, Germany), 2.2 g/L $NaHCO_3$ (Merck, Darmstadt, Germany) and 110 mg/L sodium pyruvate (Serva, Heidelberg, Germany) supplemented with 5 % fetal calf serum (FCS) (Biochrom, Berlin, Germany). Cells were passaged every 3-7 days after trypsinization using 0.05 % trypsin / 0.02 % EDTA (PAA Laboratories, Pasching, Austria).

MCF-7/Estron sulfate cells were obtained by a stepwise increase of the ABCG2 substrate estron sulfate in the culture medium of MCF-7 cells, aiming at a final concentration of 1 µM. Cells were cultured for approximately 3 months before applying them for the flow cytometric assays.

MCF-7/Topo cells, an ABCG2 overexpressing subclone of MCF- cells, were obtained as described [Hubensack, 2005]. Briefly: Increasing concentrations of topotecan in Eagle's Minimum Essential Medium (final concentration: 0.55 µM) over approximately 40 days yielded sufficient quantities of the ABCG2 transporter.

The ABCB1 overexpressing Kb-V1 cells were cultured in Dulbecco's Modified Eagle's Medium (DMEM) (Sigma, Munich, Germany) supplemented with 10 % FCS and 300 ng/mL vinblastine. According to Hubensack [Hubensack, 2005] the cells expressed sufficient quantitities of the ABCB1 transporter after 3 passages.

Human epithelial colorectal adenocarcinoma CaCo2 cells were a gift of Prof. Dr. Jörg Heilmann, Institute of Pharmaceutical Biology, University of Regensburg. The cells were grown in DMEM supplemented with 10 % of fetal calf serum.

ABCC2 overexpressing MDCKII-MRP2 cells transfected with human ABCC2 were a kind gift from Prof. Dr. P. Borst (Netherland Cancer Institute, Amsterdam, NL). The cells were cultured in Dulbecco's Modified Eagle's Medium supplemented with 5 % FCS.

All cells were cultured in a water-saturated atmosphere (95 % air / 5 % CO_2) at 37 °C in 25, 75 and 175-cm^2 culture flasks (NUNC, Wiesbaden, Germany; Greiner, Frickenhausen, Germany; Sarstedt, Nümbrecht, Germany) respectively. Cell banking was performed according to the "seed stock concept" [Hay, 1988]. *Mycoplasma* contamination was routinely monitored by polymerase chain reaction (Venor GeM, Minerva Biolabs GmbH, Berlin, Germany), and only *mycoplasma* free cultures were used for assays.

4.3.4 Cell-based assays for the determination of ABCG2 inhibition

4.3.4.1 Flow cytometric mitoxantrone efflux assay

The assay was essentially performed as described elsewhere [Müller, 2007]. Briefly: having reached a confluency of approximately 80 % (3 - 7 days after passaging), MCF-7/Topo cells were trypsinized and resuspended in Eagle's Minimum Essential Medium plus 5 % FCS at room temperature. After adjusting the cell number to $1 \cdot 10^6$ per mL with culture medium, 10 µL of mitoxantrone (2 mM stock solution in 70 % ethanol) were added to the cell suspension in order to achieve a final concentration of 20 µM. Subsequently, various concentrations of the test compounds, solvent and the known ABCG2 inhibitor fumitremorgin C (final concentration 10 µM) were added, respectively. The samples were vortexed and incubated for 30 min at 37 °C / 5 % CO_2 to allow maximal mitoxantrone uptake into the cells. After 1 washing step with 0.8 mL of ice-cold PBS, the cells of the fumitremorgin C reference were resuspended in 0.5 mL phosphate buffered saline and placed on ice in the dark until measurement to avoid mitoxantrone efflux (determination of the 100 % mitoxantrone uptake). All other samples were incubated with 1 mL of drug-free culture medium for further 60 min at 37 °C / 5 % CO_2 to reach equilibrium of mitoxantrone between the cytoplasm and the surrounding medium. Subsequently, the medium was removed by centrifugation; the cell pellets were rinsed once with 0.8 mL of ice-cold PBS and finally resuspended in 0.5 mL of the aforementioned buffer for flow cytometry. A FACS calibur™ (Becton Dickinson, Heidelberg, Germany) was used to analyze the fluorescence intensity of the cells. Mitoxantrone accumulation in the cells was monitored by using an excitation wavelength of 635 nm, whereas emission was detected at a wavelength of 661 ± 8 nm. A minimum of 20,000 events was collected per sample. The events were gated according to forward and sideward scatter to exclude cell aggregates and debris. Analysis of the raw data was performed with the WinMDI 2.8 and WinMDI 2.9 software, respectively. The geometric means were calculated from the fluorescence intensity histogram and related to the controls. Afterwards, the mean values of different measurements were plotted against the concentration of the test compounds. Addition of increasing concentrations of the modulator led to sigmoidal concentration-response curves. IC_{50} values were calculated using SIGMA PLOT 9.0, Four parameter logistic curve fitting. Errors were expressed as standard error of the mean (SEM).

4.3.4.2 Hoechst 33342 and pheophorbide a microtiter plate assay

In order to minimize expenditure of time, material costs and required cell numbers for investigations of putative ABCG2 modulators as well as for the screening of large compound libraries, two alternative microtiter assays in the 96-well format were established. As fluorescent substrates of ABCG2, Hoechst 33342 and pheophorbide a were selected. The different spectral properties of these dyes should enable the determination of fluorescence-labelled compounds as putative ABCG2 modulators in order to investigate the mode of transporter inhibition. The assays were performed using a GENios Pro microplate reader (TECAN Deutschland GmbH, Crailsheim, Germany). For excitation and emission of the Hoechst 33342 dye, the following filter set was used: exc. BP 340/35, em. BP 485/20. Pheophorbide a was excited at a wavelength of 380/10 nm, whereas the emission was determined at 670/20 nm. In the start-up period of assay development, black microplates with clear bottom were used (μclear®, Greiner, Frickenhausen, Germany), which were later on replaced with clear, flat-bottomed plates to reduce material costs (sterile, F-Bottom, with lid, Cat.-No.655 180, Greiner, Frickenhausen, Germany).

4.3.5 Assays for the determination of ABCB1 and ABCC2 inhibition

4.3.5.1 Flow cytometric calcein-AM efflux assay for determination of ABCB1 inhibition

The assays were performed as described elsewhere [Müller, 2007].

4.3.5.2 Calcein-AM microtiter plate assay for determination of ABCB1 inhibition

The assay procedure will be described in detail in the doctoral thesis of Peter Höcherl. In brief: ABCB1-overexpressing Kb-V1 cells were seeded into clear 96-well plates at a density of 20,000 cells / well and allowed to attach to the surface for 18-24 h. Subsequently, cells were simultaneously incubated with 0.5 μM of calcein-AM and the test compounds at increasing concentrations. After 10 min of incubation at 37 °C / 5 % CO_2, the supernatant was removed, and cells were immediately fixed using paraformaldehyde (4 %) in PBS. Afterwards, cells were washed three times and finally overlaid with 100 μL of buffer per well. Relative fluorescence intensities were determined at the GENios Pro microplate reader. The excitation was performed at 485/20 nm, the emission was determined at 535/25 nm.

4.3.5.3 CMFDA microtiter plate assay for determination of putative ABCC2 modulation

The assay was performed by Anne Mahringer as described previously [Kühnle et al., 2009]. Briefly: ABCC2 overexpressing MDCK-cells were cultured in 24-well plates and incubated with 1 µM CMFDA in the absence or presence of the test compounds at increasing concentrations. After 90 min of incubation at 37 °C, cells were washed twice and finally lysed for 30 min by the use of 1 % Triton X-100. Subsequently, the relative fluorescence intensities were measured with a plate reader (Tecan Safire XFLUOR4, Tecan, Crailsheim, Germany) using an excitation wavelength of 485 nm, whereas the emission was detected at 516 nm.

4.3.6 Confocal laser-scanning microscopy (CLSM)

After trypsinization, ABCG2-overexpressing MCF-7/Topo cells were resuspended in culture medium supplemented with 5 % fetal calf serum and 0.55 µM topotecan. 250 µL of the cell suspension were seeded into each well of a sterile 1 µ-slide 8-well ibiTreat™ microscopy chamber (ibidi, Martinsried, Germany). Having reached the appropriate confluency of 70 % (approximately 48 h later), the medium was removed by suction, and the cells were washed with 280 µL of Leibovitz L15 medium containing L-glutamine (Invitrogen, Karlsruhe, Germany). Subsequently, the cells were overlaid with 240 µL of Leibovitz´s L15 medium. On the eve of the experiment, 40 µL of a 7-fold concentrated stock solution of the test compound were pipetted to the cells. Fluorescence imaging was performed with a Carl Zeiss Axiovert 200M LSM 510 confocal-laser scanning microscope (CLSM) encased by a tempered incubation chamber. Instrument settings (excitation wavelengths, beam paths, filter settings) for each experiment are given in the corresponding figure legends. For image processing the Carl Zeiss LSM Image Examiner and the LSM image Browser software were used.

2 subseries of fluorescence-labeled tariquidar-like compounds were synthesized by Carolin Fischer, Institute of Organic Chemistry, University of Regensburg. The structures of these substances are shown in **Charts 4.6** and **4.7**.

Chart 4.6: Structures of fluorescence-labeled compounds designed as ABCG2 modulators. The pyridinium fluorophore was incorporated in place of the tetrahydroisoquinoline moiety in the non-labeled tariquidar analogs.

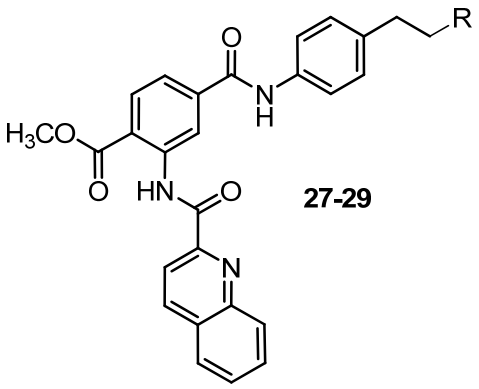

27-29

no. (lab code)	R	no. (lab code)	R	no. (lab code)	R
27 (CP 150)	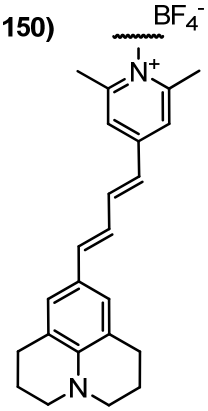	**28 (CP 151)**	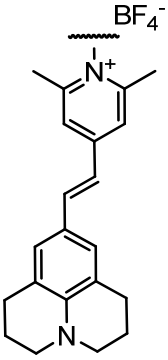	**29 (CP 152)**	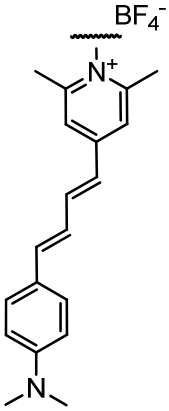

Chart 4.7: Structures of fluorescence-labeled compounds designed as ABCG2 modulators. The pyridinium fluorophore was incorporated by linkage of pyrylium dyes to the central benzamide moiety of ABCG2 modulators derived from tariquidar.

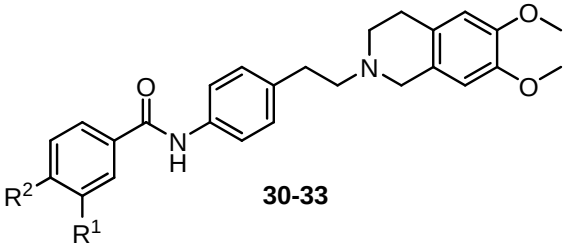

30-33

no. (lab code)	R^1	R^2	no. (lab code)	R^1	R^2
30 (CP 131)	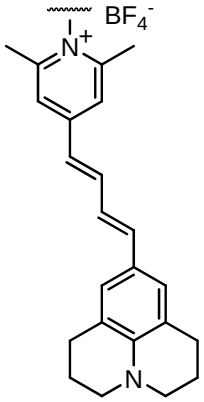	H	**32 (CP 141)**	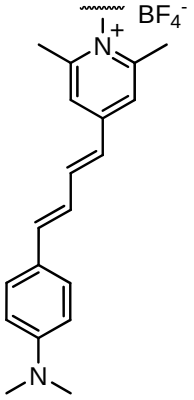	H
31 (CP 137)	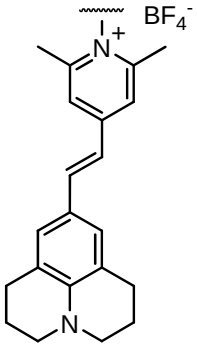	H	**33 (CP 122)**	H	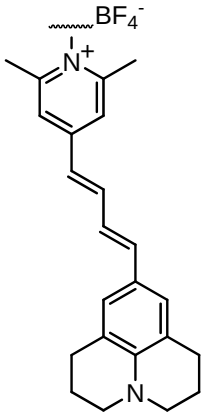

4.3.7 Chemosensitivity assays

The assays were performed as described previously [Bernhardt et al., 1992a]. In brief: 100 µL/well of a tumor cell suspension, yielding a density of 8-15 cells per microscopic field (magnification 320-fold), were seeded into 96-well plates (Greiner, Frickenhausen, Germany). Cells were allowed to grow for 2-3 days at 37 °C / 5 % CO_2 in a water-saturated atmosphere. Subsequently, supernatant was removed by suction and replaced by fresh medium (200 µL/well) containing varying drug concentrations or vehicle. In general, test compounds were added as 1000-fold concentrated feed solutions (16 wells per drug concentration). On every plate 16 wells served as growth control (vehicle) and 16 wells were supplied with a reference cytostatic as a positive control. Incubation of the cells was stopped after different periods of time by removal of medium and fixation with glutardialdehyde (Merck, Darmstadt, Germany). All plates were stored at 4 °C until the end of the experiment and afterwards simultaneously stained with 100 µL/well of a 0.02 % aqueous crystal violet solution (Serva, Heidelberg, Germany) for 20 min. Subsequently, the trays were rinsed with water for further 20 min in order to remove excess dye. Crystal violet stain bound by the fixed cells was redissolved in 70 % ethanol (180 µL/well) while shaking the microplates for 2-4 h. Absorbance (a parameter proportional to cell mass) was measured at 578 nm using a BIOTEK 309 autoreader (TECNOMARA, Fernwald, Germany). Drug effects were expressed as corrected T/C-values for each group according to:

$$T/C_{corr.} = \frac{T - C_0}{C - C_0} \cdot 100\,[\%]$$

, where T is the mean absorbance of the treated cells, C the mean absorbance of the controls and C_0 the mean absorbance of the cells at the time (t=0) when drug was added. When the absorbance of treated cells T was less than that of the culture at t=0 (C_0), the extent of cell killing was calculated as

$$\text{Cytocidal effect [\%]} = \frac{C_0 - T}{C_0} \cdot 100$$

SigmaPlot analysis software (Systat Software GmbH, Erkrath, Germany) was used for the creation of growth curves.

4.3.8. Stability of tariquidar-like ABCG2 inhibitors

4.3.8.1 Preparation of mouse plasma and determination of esterase activity

With respect to future in vivo studies, selected candidates out of a series of potent ABCG2 modulators developed in collaboration with the group of Prof. Dr. B. König, were investigated for stability in plasma. For this purpose, blood of BL6 mice was collected by heart puncture in deep anesthesia using heparin-coated syringes. Samples were immediately centrifuged for 7 min at 7,000 rpm (Eppendorf centrifuge 5415R, Eppendorf, Hamburg, Germany) and the supernatant was carefully removed. After pooling, the plasma was fractioned into small aliquots for long-term storage at -80 °C. The enzymatic activity of esterases in the plasma samples was measured spectrophotometrically. The colored product o-nitrophenol, formed by enzymatic cleavage of the chromogenic substrate nitrophenyl butyrate was determined as a function of time. Absorbance was plotted against time, the linear slope at the beginning of the reaction was determined and used for the calculation of volume activity:

$$V_A = \frac{\frac{\Delta A \cdot V}{t}}{\varepsilon \cdot d \cdot v}$$

The abbreviations of the present equation define the following parameters:

V_A = volume activity [U · mL^{-1}] multiplied with 1000 for [U· L^{-1}]
ΔA = absorbance of o-nitrophenol at 414 nm
t = time [min]
V = total volume [mL]
$\varepsilon_{o\text{-nitrophenol}}$ = 3190 [L · mol^{-1} · cm^{-1}]
d = path length [cm]
v = plasma volume [mL]

4.3.8.2 Assay procedure

The test compounds were dissolved in DMSO at a concentration of 1.5 mM. Subsequently, test compound stocks, mouse plasma, deproteinated plasma, culture medium and phosphate buffered saline were equilibrated on a Wealtec heat plate (Wealtec, Sparks, USA) to 37 °C for approximately 15 min. Thereafter, a 1:50 dilution of the substances with the corresponding medium was prepared in 1.5-mL polypropylene reaction vessels (Eppendorf, Hamburg, Germany). The samples were shortly vortexed and immediately incubated at 37 °C. After increasing periods of time, aliquots were taken, and the reaction was stopped by the addition of 2 parts of ice-cold acetonitrile. For quantitative precipitation of the denatured proteins, the samples were efficiently vortexed and stored at 4 °C for 30 min. Finally, samples were centrifuged for 5 min at 17,000 g, using an Eppendorf MiniSpin plus centrifuge, and the supernatants were transferred into new plastic cups. For HPLC analysis the samples were further diluted (1:2) with acetonitrile and stored at -80 °C until measurement.

4.3.8.3 HPLC and HPLC-MS analysis

4.3.8.3.1 HPLC analysis

HPLC analysis was performed according to the method established by P. Höcherl for the investigation of tariquidar-like ABCB1 modulators (part of Peter Höcherl's PhD project).

In brief: samples were unfrozen at room temperature and injected into the HPLC system (Waters, Eschborn, Germany). Analysis was accomplished by gradient elution with water containing TFA (0.05 %) and acetonitrile (0 min, 15 %; 19 min, 60 %; 20 min, 95 %; 24.5 min, 95 %; 25 min, 15 %; 38 min, 15 %), at a constant flow rate of 0.8 mL/min. The HPLC system was equipped with a Luna RP-18 (2), 3 µm, 150 mm x 4.6 mm column. Analysis was carried out via UV-detection at a wavelength of 210 nm.

4.3.8.3.2 HPLC-MS analysis

Structure determination of cleavage products was performed by HPLC-MS analysis. For this purpose, 2 alternative methods with the following characteristics were established:

HPLC (Agilent 1100, Palo Alto, CA):

Method 1: A Luna C18, 3 µm, 100 mm x 2 mm column (Phenomenex, Aschaffenburg, Germany) was used at 40 °C. Gradient elution with water containing formic acid (0.1 %) and acetonitrile (0 min, 20 %; 24 min, 60 %; 25 min, 98 %; 30 min, 98%; 31 min, 20 %; 40 min, 20 %) was performed at a flow rate of 0.3 mL/min with UV-detection at 220 nm.

Method 2: The gradient consisted of 0.1 % formic acid and acetonitrile (0 min, 0 %; 1 min, 0 %; 11 min, 98 %; 12 min, 98 %; 13 min, 0 %; 16 min, 0 %. A Gemini C18 column, 3 µm, 50 mm x 2 mm (Phenomenex, Aschaffenburg, Germany), was used at 40 °C. Compounds were detected at 220 nm.

Mass spectrometry:

The HPLC was coupled to a Finnigan ThermoQuest TSQ (Triple-Stage-Quadrupol) 7000 ESI (Electron-Spray-Ionization) mass spectrometer, capillary temperature: 250 °C, spray voltage: 4.0 kV, sheath and auxiliary gas: on.

4.3.9 In vivo experiments

4.3.9.1 Animals, husbandry and feeding

Tumorigenicity and in vivo growth kinetics of ABCG2-overexpressing MCF-7/Topo cells were investigated in NMRI nude mice (nu/nu).

NMRI (nu/nu) mice were randomly bred in the nude mouse laboratory at the University of Regensburg under specified pathogen-free (SPF) conditions at 26 °C, 70 % relative humidity and a 12 h light/ dark cycle [Spruss et al., 1996]. The animals were kept in type III cages from Tecniplast™ (Hohenpeißenberg, Germany), bedded with "3/4 Faser" from ssniff ™ (Soest, Germany) and fed ad libitum with combined breeding maintenance diet (Ssniff, Soest, Germany) and autoclaved tap water.

4.3.9.2 Tumor cell preparation and inoculation

For tumor cell implantation into nude mice, MCF-7/Topo cells were harvested by trypsinization using a trypsin/EDTA solution. They were washed 2 times with 5 mL serum-free medium and centrifuged at 1000 rpm for 7 min at room temperature, using a Minifuge T centrifuge from Heraeus Instruments GmbH (Hanau, Germany). The resulting cell pellet was resuspended in serum-free EMEM and the cell number was adjusted to a density of $1 \cdot 10^7$ and $2 \cdot 10^7$ cells per mL. The cell suspension was homogenized by repeated aspiration with a syringe and injected under the thoracic dermis of each mouse (100 µL / animal). Once a week, the bodyweight was controlled as a measure for detraction, and the tumor diameters were monitored. In order to allocate the measuring data of the mice, animals were labeled with tattoos on their pads.

Due to known growth retardation of human MCF-7 breast cancer cells in nude mice caused by to low estrogen levels compared with human females [Bernhardt et al., 1992b], for studies with ABCG2-overexpressing MCF-7/Topo cells, estradiol depots [Bernhardt et al., 1992b] were additionally implanted into a subgroup of female nude mice.

Mice were anesthetized with a mixture of 3 volumes of ketamine (Ketamin 10 %, WDT-Wirtschaftsgenossenschaft deutscher Tierärzte eG, Garbsen, Germany) and 1 volume of xylazine (Xylazin (2 %) Bernburg 50 mL, Serumwerk Bernburg AG, Bernburg, Germany). The intraperitoneal injection of 30-50 µL of this mixture yielded a 20-50 min lasting anesthesia for a 30-40 g weighty nude mouse.

4.4 Results and discussion

4.4.1 Inhibition of ABCB1, ABCC2 and ABCG2

The potency of new tariquidar-like analogs to modulate the ABCG2 transporter was determined in the flow cytometric mitoxantrone efflux assay. In ABCG2-overexpressing MCF-7/Topo cells red fluorescent mitoxantrone is not accumulated but extruded by the efflux pump. Therefore, ABCG2 inhibitors can easily be recognized by the determination of intracellular mitoxantrone levels. Different concentrations of efflux pump inhibitors cause changes in the mitoxantrone efflux that can be measured by the relative fluorescence intensity of the cells. Similarly, in ABCB1 overexpressing Kb-V1 cells, the accumulation of the fluorescent ABCB1 substrate calcein can be quantified by the use of flow cytometric techniques or the use of microplate readers. In the presence of ABCB1 inhibitors higher intracellular calcein levels lead to increased relative fluorescence intensities of the cells. The modulation of ABCC2 was investigated by the use of ABCC2-overexpressing MDCK-cells that were incubated with chloromethylfluorescein diacetate (CMFDA) in the presence or absence of increasing concentrations of test compounds. After intracellular formation of the ABCC2 substrate glutathione methylfluorescein, (GMSF), the extent of intracellular fluorescence was monitored with a plate reader in a concentration-dependent manner. Known modulators of the 3 efflux pumps were investigated as reference compounds.

Visible precipitations in the culture medium (EMEM / 5 % FCS), used for the mitoxantrone efflux assay, occurred at a number of tariquidar analogs at final concentrations above 10 µM. Therefore, unless otherwise stated, concentrations higher than 10 µM were not considered in the calculation of IC_{50} values. The data were used for the construction of concentration-response curves as depicted in **Figures 4.2, 4.3, 4.4** and **4.5**. For a summary of all data from the investigation of test compounds **1-26** and reference substances for inhibition of ABCG2, ABCB1 and ABCC2 cf. **Table 4.1**.

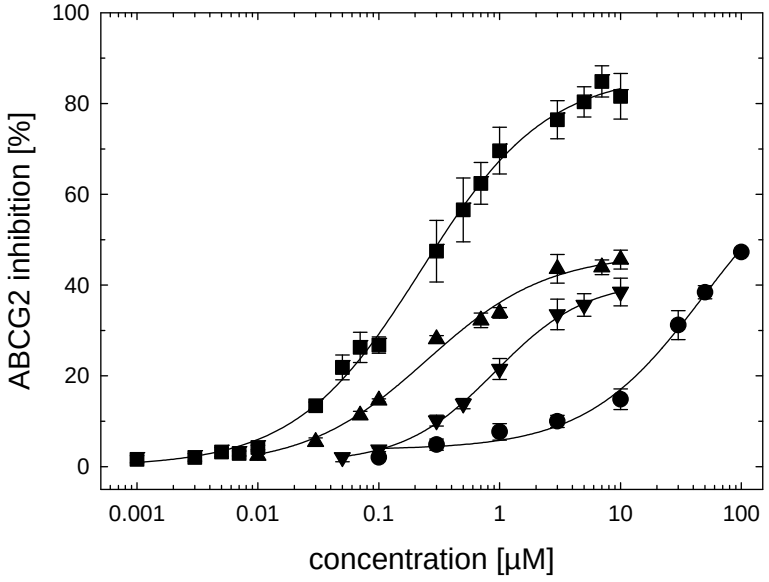

Figure 4.2: Concentration-response curves for ABCG2 modulation by the reference compounds fumitremorgin C (circles), Ko143 (squares), elacridar (triangles) and tariquidar (inverted triangles).

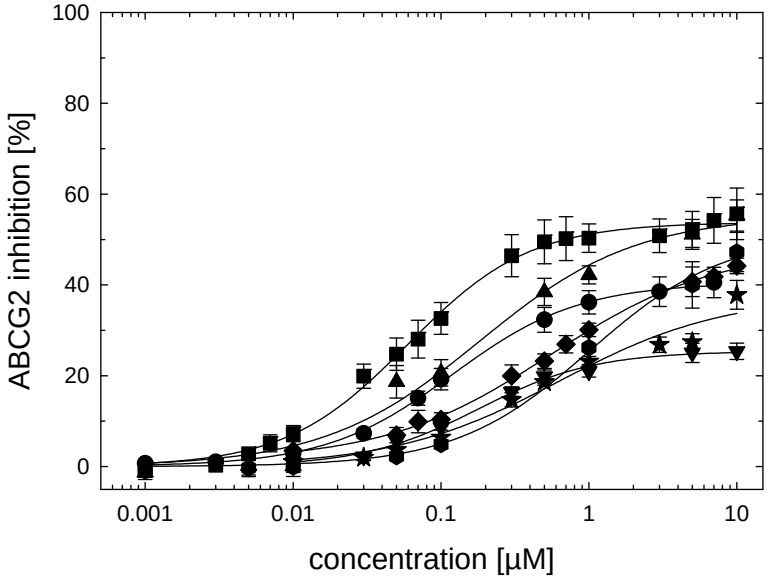

Figure 4.3: Concentration-response curves for ABCG2 modulation by the new tariquidar analogs **1**-**7**. Compound **1** (circles), **2** (squares), **3** (triangles), **4** (inverted triangles), **5** (diamonds), **6** (stars) and **7** (hexagons).

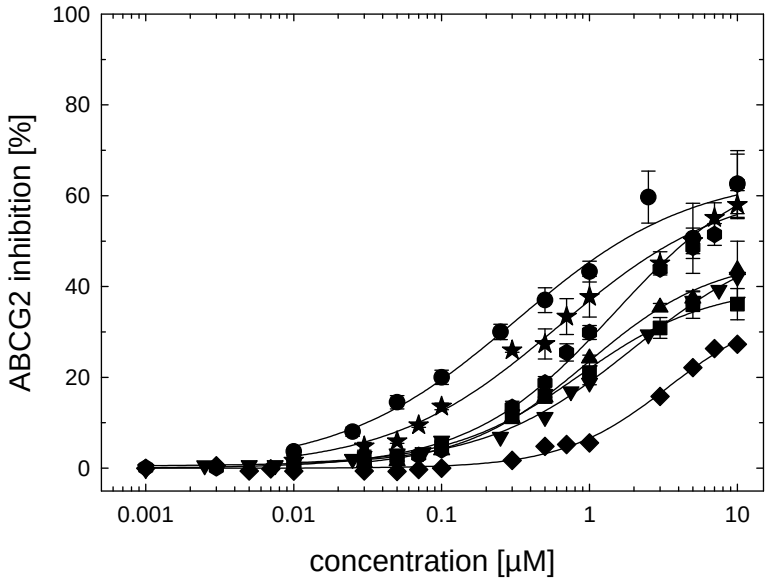

Figure 4.4: Concentration-response curves for ABCG2 modulation by the new tariquidar analogs **8-14**. Compound **8** (circles), **9** (squares), **10** (triangles), **11** (inverted triangles), **12** (diamonds), **13** (stars) and **14** (hexagons).

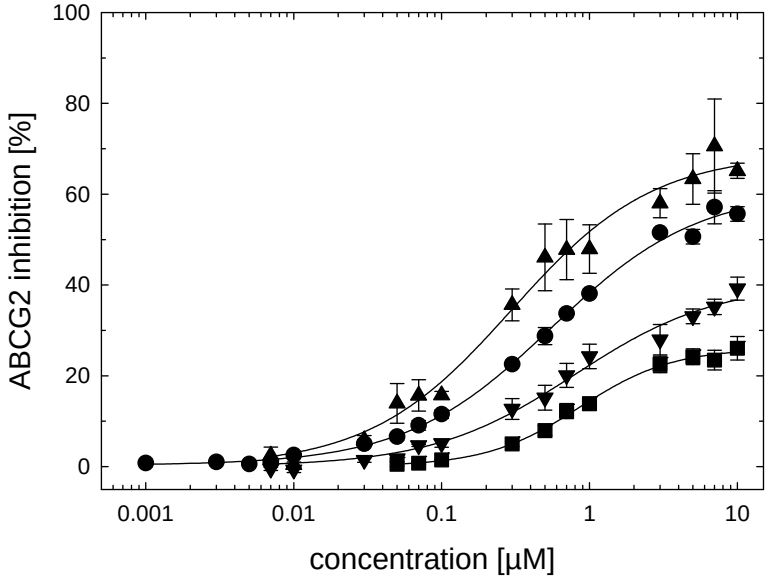

Figure 4.5: Concentration-response curves for ABCG2 modulation by the new tariquidar analogs **15-18**. Compound **15** (circles), **16** (squares), **17** (triangles), and **18** (inverted triangles).

Table 4.1: Inhibition of ABCG2, ABCB1 and ABCC2 by compounds **1-26** and reference substances.

Compound	**ABCG2 IC_{50} [nM][a]**	**ABCG2 Max. (%)[a,b]**	**ABCB1 IC_{50} [nM][c]**	**ABCC2 IC_{50} [nM]**
Fumitremorgin C	> 11 000	100	inactive [d]	inactive [e]
Ko143	225 ± 33	82 ± 5	inactive [d]	> 50 000
Elacridar	250 ± 45	46 ± 2	193 ± 18	inactive [e]
Tariquidar	916 ± 197	39 ± 3	223 ± 8	inactive [e]
MK571 [g]	n.d.	-	n.d.	> 1000
LTC_4 [g]	n.d.	-	n.d.	< 150
1	119 ± 22	41 ± 3 (7 µM)	9,450 ± 417	inactive [e]
2	60 ± 10	56 ± 6	> 29,000 [f]	> 20,000
3	183 ± 50	55 ± 3	> 34,000	n.d.
4	179 ± 35	25 ± 2	inactive [d]	n.d.
5	552 ± 125	44 ± 2	> 57,000 [f]	> 20,000
6	632 ± 222	38 ± 3	> 20,000 [f]	> 50,000
7	1,015 ± 403	47 ± 4	> 14,000 [f]	> 20,000
8	317 ± 131	63 ± 7	> 6,000 [f]	inactive [e]
9	858 ± 210	36 ± 3	> 17,000	inactive [e]
10	977 ± 244	43 ± 6	> 15,000	inactive [e]
11	1,990 ± 355	52 [f]	> 15,000 [f]	> 50,000
12	3,414 ± 724	27 [f]	inactive [h]	n.d.
13	622 ± 152	58 ± 3	95,308 ± 57,364 [h]	n.d.
14	1,470 ± 420	63 ± 7	103,417 ± 48,140 [h]	n.d.
15	555 ± 48	56 ± 2	> 50,000 [h]	n.d.
16	857 ± 122	26 ± 3	> 50,000 [h]	n.d.
17	297 ± 75	65 ± 2	> 50,000 [h]	n.d.
18	795 ± 194	39 ± 3	> 50,000 [h]	n.d.
19	inactive [e, f]	-	inactive [h]	n.d.
20	-	6 ± 3 (50 µM)	> 50,000 [h]	n.d.
21	-	61 ± 2 (50 µM) [f, i]	inactive [h]	n.d.
22	-	27 ± 1 (50 µM) [f, i]	inactive [h]	n.d.
23	7,664 ± 1,664	58 ± 6 (100 µM)	10,379 ± 1,018 [h]	n.d.
24	inactive [e]	-	> 50,000 [h]	n.d.
25	2,353 ± 251	105 ± 4 (100 µM)	> 50,000 [h]	n.d.
26	1,668 ± 590	64 ± 3 (15 µM) [i]	> 100,000 [h]	n.d.

[a] Mean values ± SEM, calculated from 2-3 independent experiments. [b] Maximal inhibitory effects (%) are expressed as inhibition caused by the highest concentration of the compound tested (10 µM, if not otherwise stated in parentheses) relative to the inhibitory effect caused by 10 µM fumitremorgin C (100% inhibition). [c] Mean values ± SEM, calculated from n=2-5. [d] No effect up to a concentration of 10 µM; Fumitremorgin C: 0.8 % inhibition at 10 µM, 22 % inhibition at 100 µM; Ko143: 1.6 % inhibition at 10 µM. [e] No effect up to a concentration of 50 µM; [f] N= 1. [g] MK571: 3-(((3-(2-(7-chloroquinoline-2-yl)ethenyl)phenyl)((3-dimethylamino-3-oxopropyl)thio) methyl) thio) propanoic acid; LTC_4: leukotriene C_4. [h] Values obtained by the Calcein-AM microtiter assay. [i] Values obtained by Hoechst 33342 assay (see **4.4.2**). IC_{50} values were calculated using SIGMA PLOT 9.0, four parameter logistic curve fitting and GraphPad Prism 5.0, respectively.

The fumitremorgin C analog Ko143 is a highly potent ABCG2 modulator with a maximal inhibitory effect of 82% at a concentration of 10 μM, referred to the control fumitremorgin C. The acridone carboxamide derivative elacridar strongly inhibits both transporters without a preference, whereas tariquidar was about equipotent with elacridar at ABCB1 but approximately 4 times less potent at ABCG2. Transporter inhibition data show that minimal structural changes at the benzamide core of tariquidar resulted in a drastic change from ABCB1 to ABCG2 modulation. The shift of the quinoline-3-carboxamido substituent from position 2 (tariquidar) to position 3 of the benzamide moiety (compound **9**) proved to be the key to increase the selectivity for ABCG2 over ABCB1: Whereas the moderate inhibition of ABCG2 was maintained (**9**: IC_{50} 858 nM, tariquidar 916 nM), the modulation of ABCB1 decreased by a factor of >75 (IC_{50} >17,000 vs. 223 nM for **9** and tariquidar, respectively). Furthermore, all compounds with bicyclic hetarylcarboxamides in position 3 and an ester group in position 4 (compounds **1-4** and **17**) were highly potent and selective ABCG2 modulators superior to compounds with monocyclic heteroaromatic moieties (**5-7**). The 2 most potent inhibitors were obtained with a quinoline-2-carboxamido (compound **2** with an IC_{50} of 60 ± 10 nM) and quinoline-3-carboxamido substituent (compound **1** with an IC_{50} of 119 ± 22 nM), respectively. Presumably, the ester group in these compounds contributes considerably to the interaction with ABCG2 since structural modifications in position 4 and 5 of the benzamide core (**8-18**) resulted in a decrease in potency. For instance, in the series of quinoline-2-carboxamides **15-18** the ester **17**, an analog of compound **2**, lacking the 2 methoxy groups at the tetrahydroisoquinoline moiety, is only slightly less potent (by a factor of 5) than **2** as an ABCG2 modulator, whereas all other structural variations (**15**, **16** and **18**) caused a more pronounced decrease in activity. This is specifically true for the amide analogs of **2** (**16** and **18**) in terms of both, potency and maximal response. Additional information on structure activity relationships is gained from the data for the substructures and intermediates (**19-26**). With the exception of compound **23**, bearing a nitro group in position 3 and the ester group in position 4, analogs containing an intact tetrahydroisoquinoline moiety but lacking the quinolinecarboxamide substituent (**19-23**) were almost inactive. In the building blocks **24-26,** both the ester group and the quinoline-2-carboxamide substituent are retained, but the characteristic benzamide N-substituent is lacking or truncated. The carboxylic acid **24** turned out to be inactive, whereas the benzamides **25, 26**, which are not negatively charged at physiological pH, showed a moderate inhibition of ABCG2. Thus, ABCG2 modulation appears to depend on an intact 3-(acylamino)benzoic amide moiety rather than on the substituent at the benzamide N-atom.

Only one compound (**23**) missed selectivity for ABCG2 vs. ABCB1 (ABCB1 transporter assays performed by Dr. Christine Müller and Peter Höcherl). The lack of selectivity of **23**, a moderate inhibitor of ABCG2 and ABCB1, seems to be due to the lack of a "selectivity-conferring" bulky residue in either position 2 or 3 of the benzamide. Furthermore, a set of representative ABCG2 inhibitors (**1-11**), turned out to be inactive (up to concentrations of 20 μM or 50 μM, respectively) when studied for modulation of ABCC2 (investigations performed by Anne Mahringer), underlining the high transporter selectivity of these compounds.

4.4.2 Fluorescence-based microtiter plate assays for the characterization of ABCG2 inhibitors

The routinely performed flow cytometric assays for studies on putative transporter inhibitors are time-consuming and costly. The throughput is limited to a rather small number of compounds. Furthermore, in order to investigate fluorescence-labeled substances as putative ABCG2 inhibitors via fluorescence-based assays, the spectral properties of the used transporter substrates must not interfere with those of the test compounds. For this reason, the 2 fluorescent ABCG2 substrates Hoechst 33342 and pheophorbide a were selected to establish rapid cell-based assays in the 96-well format. Validation of the elaborated assays was arranged on the basis of the published literature [Seigel and Campbell, 2004; Henrich et al., 2006] with different modifications. The structures of Hoechst 33342 (H33342) and pheophorbide a (PhA) are shown in **Figure 4.6**.

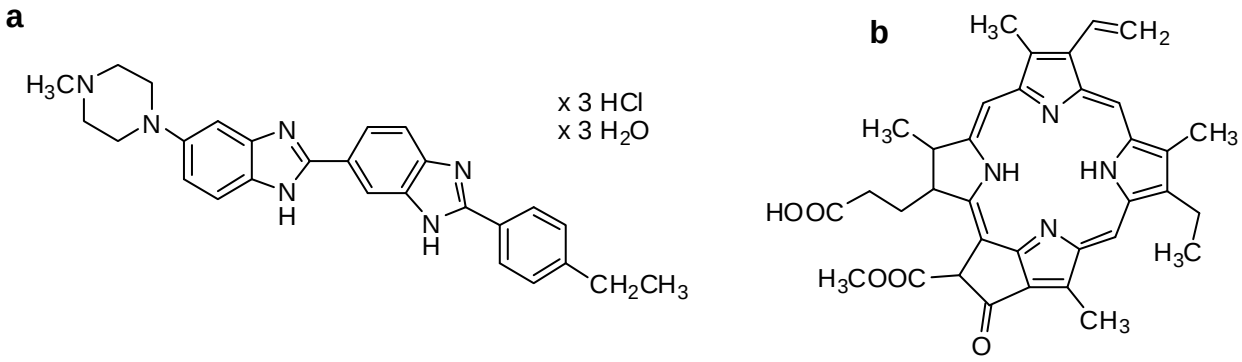

Figure 4.6: Chemical structures of the fluorescent ABCG2 substrates Hoechst 33342 (**a**) and pheophorbide a (**b**).

4.4.2.1 Validation of Hoechst 33342 and pheophorbide a assay

In order to check the linearity of the dye uptake and the sensitivity of the method, MCF-7/Topo cells were detached from the culture flask with trypsin/EDTA and resuspended in culture medium. Subsequently, cells were seeded into 96-well plates (black with clear, flat bottom in case of Hoechst 33342, total clear in case of pheophorbide a) at various densities and allowed to attach to the surface for approximately 4 h. Cells were incubated for 90 min (Hoechst 33342) or 120 min (pheophorbide a) in the presence of DMSO (vehicle control), 10 µM of fumitremorgin C (FTC), Hoechst 33342 or pheophorbide a alone and in combination with 10 µM of FTC. Afterwards, the supernatant of the Hoechst 33342 preparations was removed, cells were washed twice with Ca^{2+} / Mg^{2+} containing phosphate buffered saline, and the relative fluorescence intensities were measured at the microplate reader. In case of incubation with pheophorbide a, the supernatant was removed, cells were fixed with 3 % paraformaldehyde solution for 45 min and afterwards washed twice with Ca^{2+} / Mg^{2+} containing PBS. Subsequently, cells were overlaid with 100 µL of buffer and the fluorescence intensities were determined at the microplate reader.

Results of these preliminary experiments are shown in **Figure 4.7**.

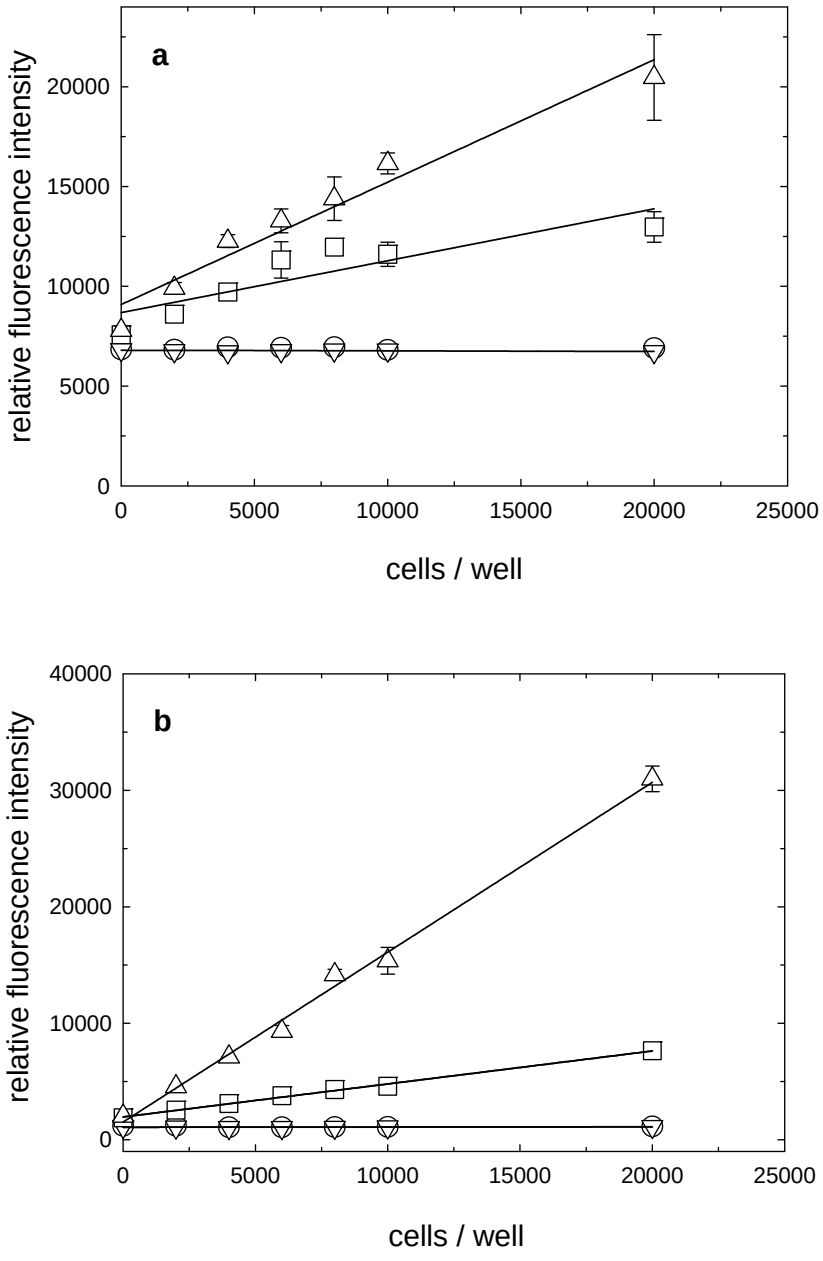

Figure 4.7: Correlation of cell number with fluorescence. Hoechst 33342 experiments (a), pheophorbide a studies (b).

Incubation of increasing cell numbers with DMSO (open circles) or fumitremorgin C alone (open inverted triangles) had no influence on fluorescence, whereas incubation with Hoechst 33342 or pheophorbide a (open squares) yielded a linear uptake of the dyes that could be strongly increased when combined with the ABCG2 inhibitor fumitremorgin C (open triangles). Furthermore, sensitive measurement of fluorescence intensities was feasible on living and fixed cells, and was applicable both, in black microtiter plates with clear bottoms and clear polystyrene plates.

As a part of the assay validation, incubation times and dye concentrations were systematically varied in order to ascertain the optimal conditions for a standard assay protocol. Hoechst 33342 was investigated at 1 final concentration of 8 µM according to Seigel and Campbell [Seigel and Campbell, 2004]. The results of preliminary experiments on pheophorbide a assays are shown in **Figure 4.8**. Whereas **4.8a-4.8c** show variations in the incubation time, **4.8d** represents a 2 hour incubation of MCF-7/Topo cells with different concentrations of pheophorbide a.

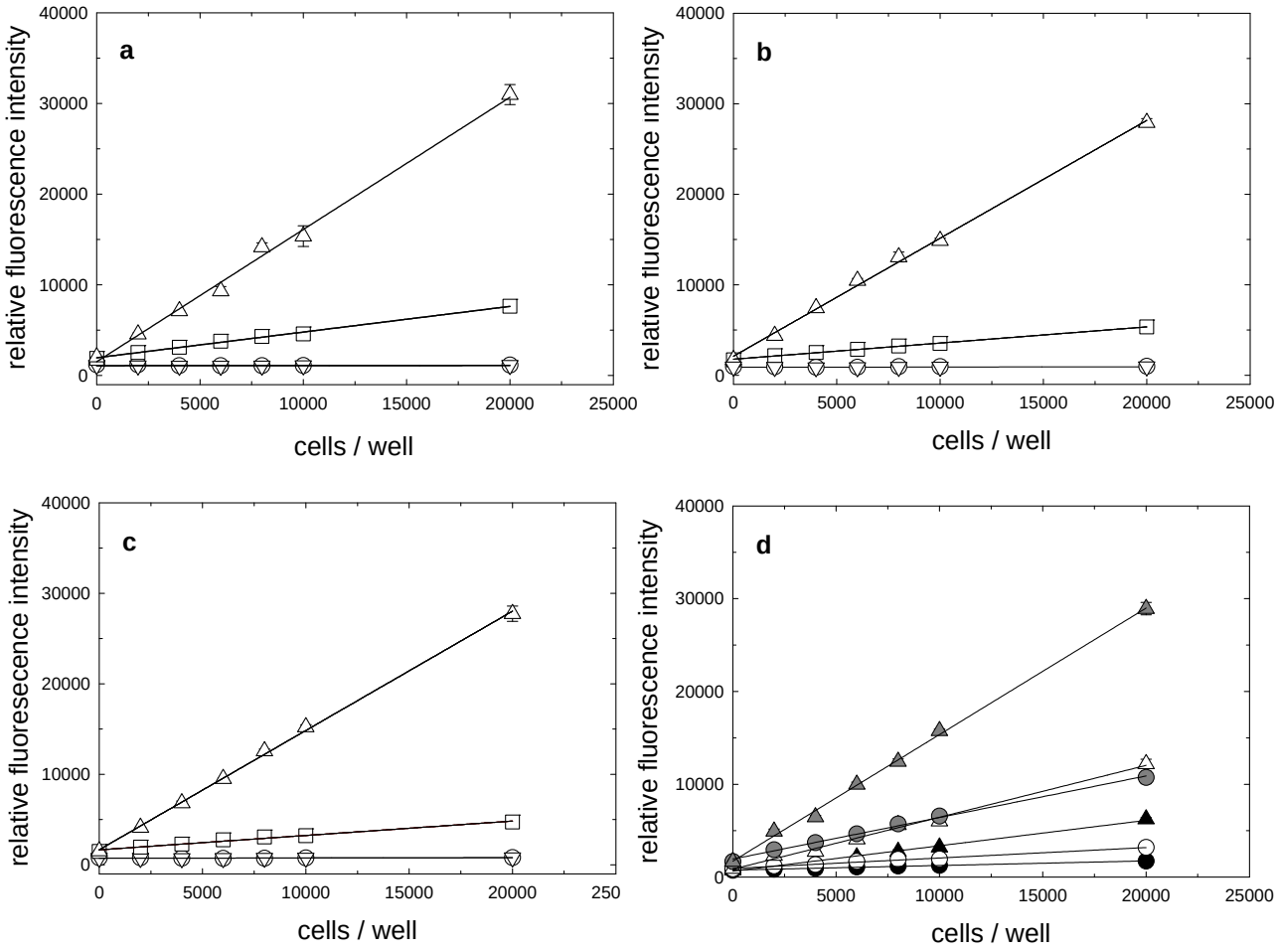

Figure 4.8a-4.8c: Incubation of MCF-7/Topo cells with DMSO (open circles), 10 µM of fumitremorgin C (open inverted triangles) and 1 µM of pheophorbide a alone (open squares) or combined with 10 µM of fumitremorgin C (open triangles) for 2 (a), 4 (b) and 6 h (c), respectively. Increasing incubation times yielded no improved ratio of unspecific vs. transporter-mediated dye uptake.

Figure 4.8d: Cells were incubated with different concentrations of pheophorbide a (black symbols 0.5 µM, white symbols 1 µM and gray symbols 5 µM) alone (circles) or in combination with 10 µM of fumitremorgin C (triangles). Increasing concentrations of pheophorbide a caused higher fluorescence intensities, but showed no improvement on the quotient of unspecific and transporter-mediated pheophorbide a uptake.

The final standard protocol for the performance of Hoechst 33342 and pheophorbide a assays was as follows: 3-5 days after passaging (70-90 % confluency), MCF-7/Topo cells were seeded into 96-well plates at a density of 20,000 cells / well (total volume 100 µL). Subsequently, the cells were allowed to attach to the surface of the microplates in a water saturated atmosphere (95 % air, 5 % carbondioxide) at 37 °C for at least 3 h. In 1.5 mL reaction vessels pre-mixtures of the test compounds were prepared by the following procedure: 1000 µL of pre-heated (37 °C) EMEM containing L-glutamine, 2.2 g/L of $NaHCO_3$ and 0.55 g/L of sodium pyruvate, supplemented with 5 % FCS, were transferred into the cups. Subsequently, 10 µL of a 1.6 mM Hoechst 33342 dye solution or 10 µL of a 200 µM pheophorbide a solution were added to the samples. Afterwards 10 µL of DMSO, FTC (10 mM) or the test compounds at increasing concentrations were added to the mixture, respectively. The samples were immediately vortexed and transferred into 50 mL polystyrene reagent reservoirs™ (BD, Heidelberg, Germany). By means of a multichannel pipette, 100 µL of the pre-mixtures were added to each well of the microplate achieving a final concentration of 50 µM fumitremorgin C (positive control) and 8 µM of Hoechst 33342 or 1 µM of pheophorbide a, respectively. In order to get homogenous solutions in each well, the microplates were slightly shaken horizontally for a couple of times and placed into an incubator (37 °C, 5 % carbondioxide) for 120 min. The supernatants were drained, and the cells were fixed for 30 min using 100 µL per well of a 3 % paraformaldehyde solution (plates were protected from light by covering with aluminium foil). Finally, MCF-7/Topo cells were washed twice with 250 µL of calcium and magnesium containing PBS for each well. Thereby, the supernatant of the first washing step was immediately removed, whereas the second portion of washing buffer allowed in contact with the cells for another 10 min in order to get rid of residual dye. Afterwards, cells were overlaid with 100 µL / well of Ca^{2+} / Mg^{2+}-containing PBS, and the relative fluorescence intensities were determined on the microplate reader.

Instrument settings were as follows: Measurement mode: fluorescence top; excitation filter (Hoechst 33342): 340/35, excitation filter (pheophorbide a): 380/10; emission filter (Hoechst 33342): 485/20, emission filter (pheophorbide a): 670/25; number of reads: 10; integration time: 40 µs; lag time: 0 µs; mirror selection: automatic; plate definition file GRE96ft.pdf or GRE96fb.pdf; multiple reads per well (Circle): 4x4; time between move and flash: 50 ms.

On each plate, the optimal gain was calculated by determination of the fluorescence intensity in the presence of the control substance, fumitremorgin C. After measurements, the microtiter plates were stored at 4 °C for the following cell quantification procedures. As a loss of cells and unspecific toxic effects of the test compounds during the incubation phase are to be considered, the obtained fluorescence values had to be normalized to the cell number of each well. Therefore, the microplates were processed with a 0.02 % aqueous crystal violet solution (100 µL / well) for 20 min. Excess dye was removed by rinsing the trays with water for 20 min. Crystal violet bound by the cells was re-dissolved in 70 % ethanol (180 µL / well) while shaking the microplates for 2-4 h. Subsequently, the absorbance as a parameter proportional to cell mass was measured at the TECAN plate reader. For normalization of the fluorescence intensities to the cell mass, detected fluorescence values were divided through the obtained absorbance data of each well. All values were corrected to the unspecific uptake of the dye (DMSO control value) and the data were referred to the maximal signal caused by 50 µM of the reference compound fumitremorgin C. Addition of increasing concentrations of the modulators led to sigmoidal concentration response curves. IC_{50} values were calculated using SIGMA PLOT 9.0, Four parameter logistic curve fitting. Errors were expressed as standard error of the mean (SEM). The required concentration of 50 µM fumitremorgin C in the final assay protocol, as a reference value for maximal transporter inhibition, was determined via the performance of the H33342 and pheophorbide a assay according to the standard protocol. Corresponding concentration-response curves are shown in **Figure 4.9**.

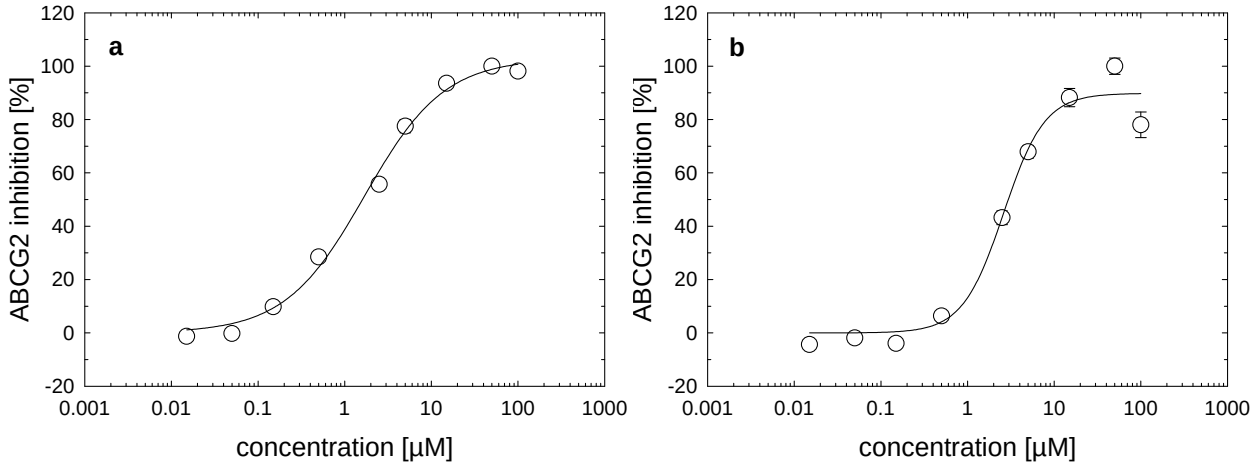

Figure 4.9: Hoechst 33342 (a) and pheophorbide a assay (b) performed with the ABCG2-modulator fumitremorgin C. Most effective transporter inhibition was observed at a concentration of 50 µM in both assays. Calculated IC_{50} values (H33342 assay: 1,701 nM ± 287 nM; pheophorbide a assay: 2,607 nM ± 495 nM) are in good agreement with data from literature [Henrich et al., 2006]

4.4.2.2 ABCG2 inhibition by tariquidar analogs determined in microtiter plate assays

With respect to comparability of data gained from different assays, the known ABCG2 modulators elacridar, tariquidar and the fumitremorgin C analog Ko143 were characterized in the newly developed microtiter assays. Furthermore, selected compounds of the synthesized tariquidar analogs were investigated in the Hoechst 33342 and pheophorbide a assay. Subsequently, the data were compared to the values obtained flow cytometry (**Table 4.2**)

Table 4.2: ABCG2 inhibition (IC_{50} values, maximal effects) by reference compounds and selected tariquidar analogs, determined by flow cytometry and the 2 microtiter assays.

Compd.	**IC_{50} [nM][a]** **Mitox. assay**	**Max. (%)[c]** **Mitox. assay**	**IC_{50} [nM][b]** **H33342 assay**	**Max. (%)[c]** **H33342 assay**	**IC_{50} [nM][b]** **Ph-a assay**	**Max. (%)[c]** **Ph-a assay**
Ko143	225 ± 33	82 ± 5 (10 µM)	117 ± 53	103 ± 7 (25 µM)	179 ± 12	83 ± 4 (5 µM)
Elacridar	250 ± 45	46 ± 2 (10 µM)	127 ± 41	63 ± 7 (5 µM)	1,136 ± 672	66 ± 8 (5 µM)
Tariquidar	916 ± 197	39 ± 3 (10 µM)	526 ± 85	69 ± 5 (15 µM)	1,756 ± 675	73 ± 13 (15 µM)
1	119 ± 22	41 ± 3 (10 µM)	104 ± 16	50 ± 1 (3.5 µM)	246 ± 58	26 ± 1 (5 µM)
2	60 ± 10	56 ± 6 (10 µM)	65 ± 8	63 ± 2 (12.5 µM)	126 ± 11	54 ± 2 (12.5 µM)
3	183 ± 50	55 ± 3 (10 µM)	125 ± 28	58 ± 5 (12.5 µM)	346 ± 41	49 ± 2 (5 µM)
4	179 ± 35	25 ± 2 (10 µM)	132 ± 38	50 ±2 (15 µM)	1,642 ± 2,380	16 ± 1 (15 µM)
5	552 ± 125	44 ± 2 (10 µM)	277 ± 57	43 ± 3 (12.5 µM)	1,015 ± 317	22 ± 1 (12.5 µM)
7	1,015 ± 403	47 ± 4 (10 µM)	390 ± 88	53 ± 5 (12.5 µM)	2,347 ± 466	37 ± 1 (12.5 µM)
8	317 ± 131	63 ± 7 (10 µM)	231 ± 103	75 ± 2 (5 µM)	722 ± 233	75 ± 4 (12.5 µM)
10	977 ± 244	43± 6 (10 µM)	359 ± 44	63 ± 3 (15 µM)	678 ± 79	53 ± 1 (15 µM)

[a] Mean values ± SEM, calculated from 3 independent experiments. [b] Mean values ± SEM from 2 independent experiments (n=10). [c] Max. (%) are expressed as inhibition caused by the highest concentration of the compound tested (see parentheses), relatively to the inhibition caused by FTC.

For the reference compound Ko143, results from the flow cytometric and the two microplate assays are in agreement with data from literature [Allen et al., 2002]. Furthermore, the new tariquidar analogs proved to be highly potent ABCG2 inhibitors in all 3 assays. Among these compounds analog **2** was the most potent modulator with a range of IC_{50} values from 60 – 126 nM.

All in all, comparing the results from the 3 different experimental protocols, Hoechst 33342 assays tended to give higher potencies, whereas pheophorbide a assays yielded lowest activities for most compounds. For some of the investigated compounds (e.g. compound **4**) discrepancies between the maximal responses might contribute to these assay-dependent differences. As one reason for varying maximal effects a different extent of precipitation of the compounds in the course of the experiments should be taken into account. Additionally, the tariquidar analogs might act as substrate-like inhibitors. Thus, competition of the modulators with the fluorescent compounds could occur and result in different effectiveness of dye transport depending on the substrate properties of the individual inhibitor compared to that of H33342 or PhA. The concentration-response curves for all compounds investigated in the mitoxantrone and the microtiter plate assays are shown in **Figures 4.10**, **4.11** and **4.12**.

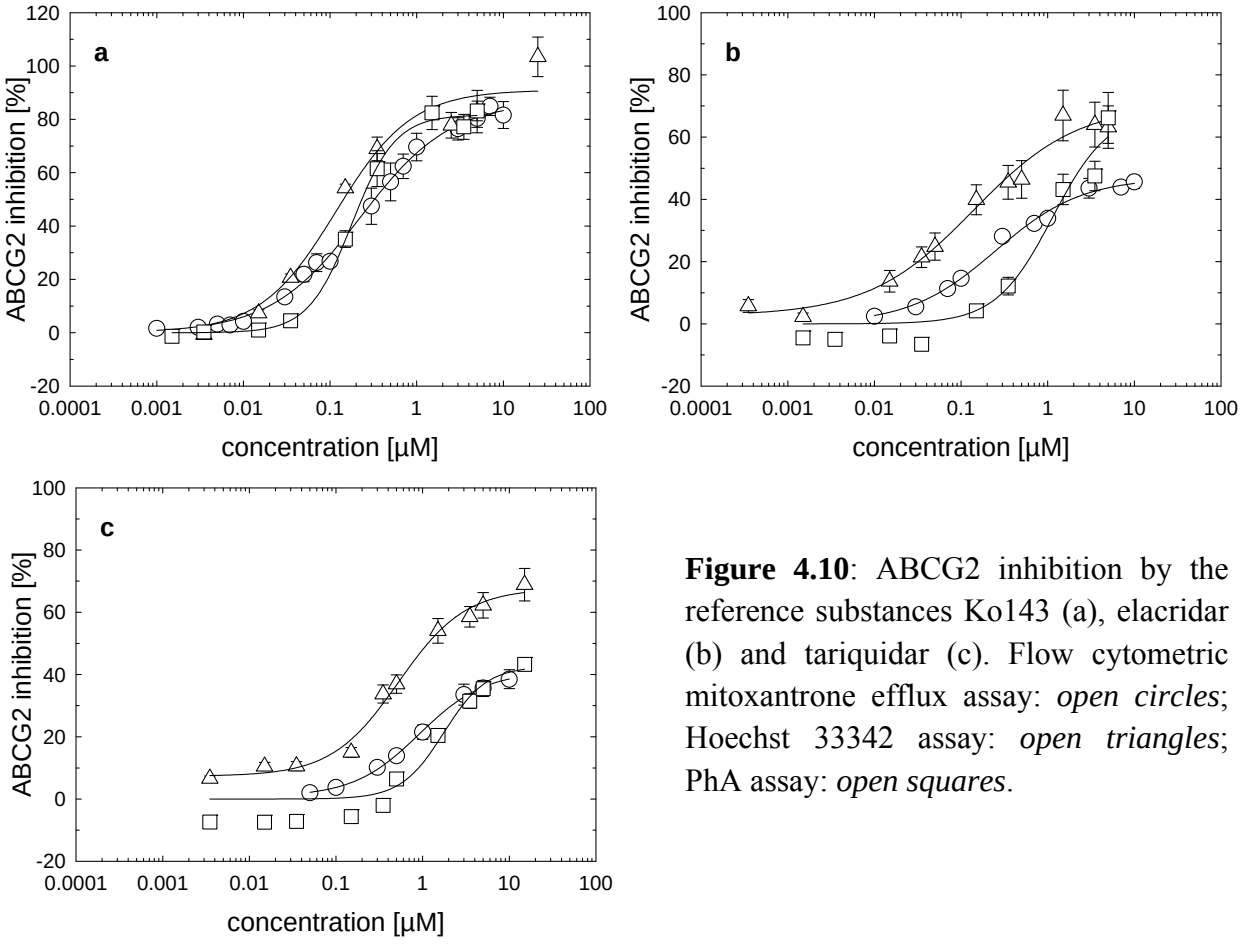

Figure 4.10: ABCG2 inhibition by the reference substances Ko143 (a), elacridar (b) and tariquidar (c). Flow cytometric mitoxantrone efflux assay: *open circles*; Hoechst 33342 assay: *open triangles*; PhA assay: *open squares*.

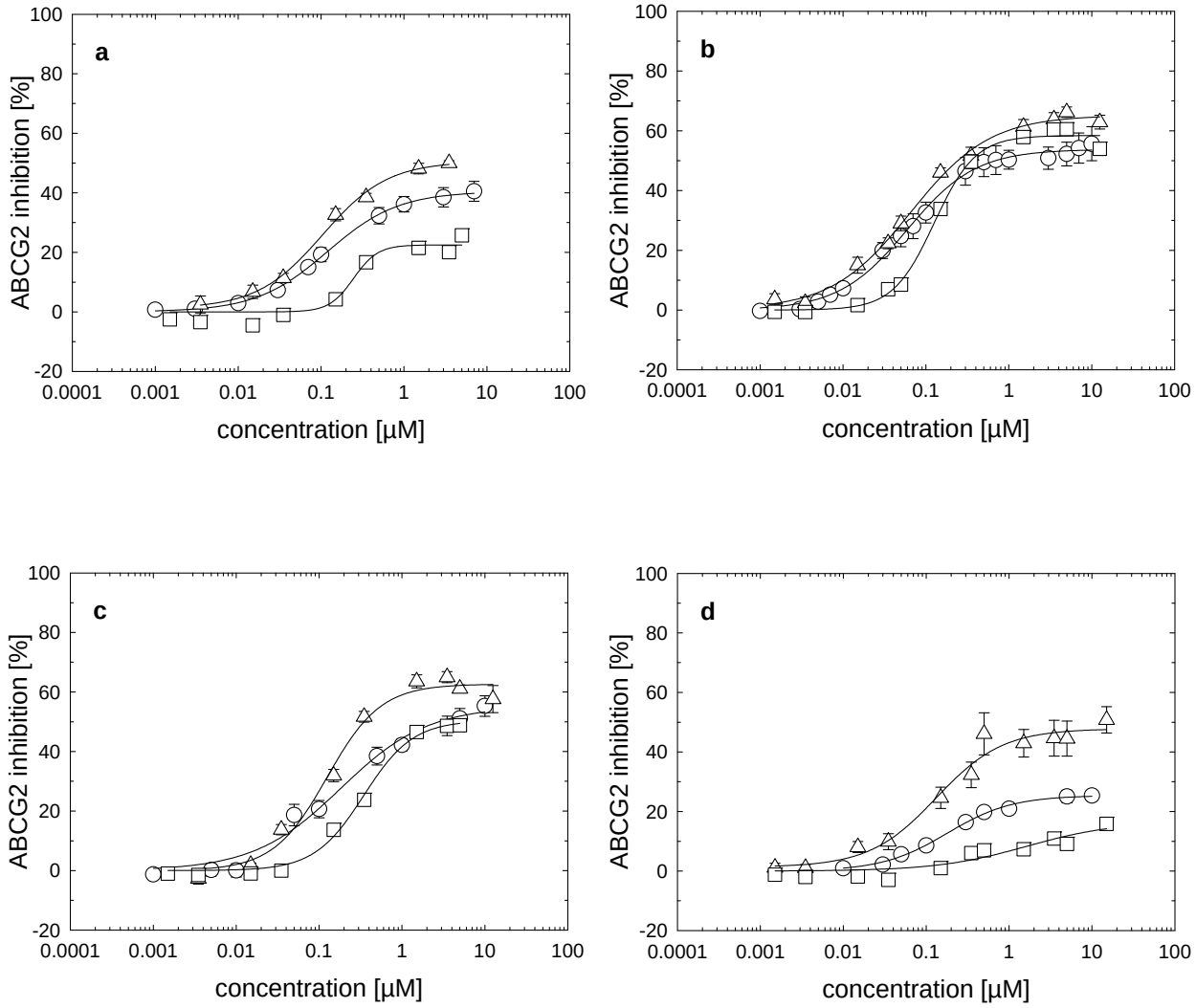

Figure 4.11: Concentration-response curves for ABCG2 inhibition by new tariquidar analogs. Compound **1** (a), compound **2** (b), compound **3** (c) and compound **4** (d). Flow cytometric mitoxantrone efflux assay: *open circles*; Hoechst 33342 assay: *open triangles*; PhA assay: *open squares*.

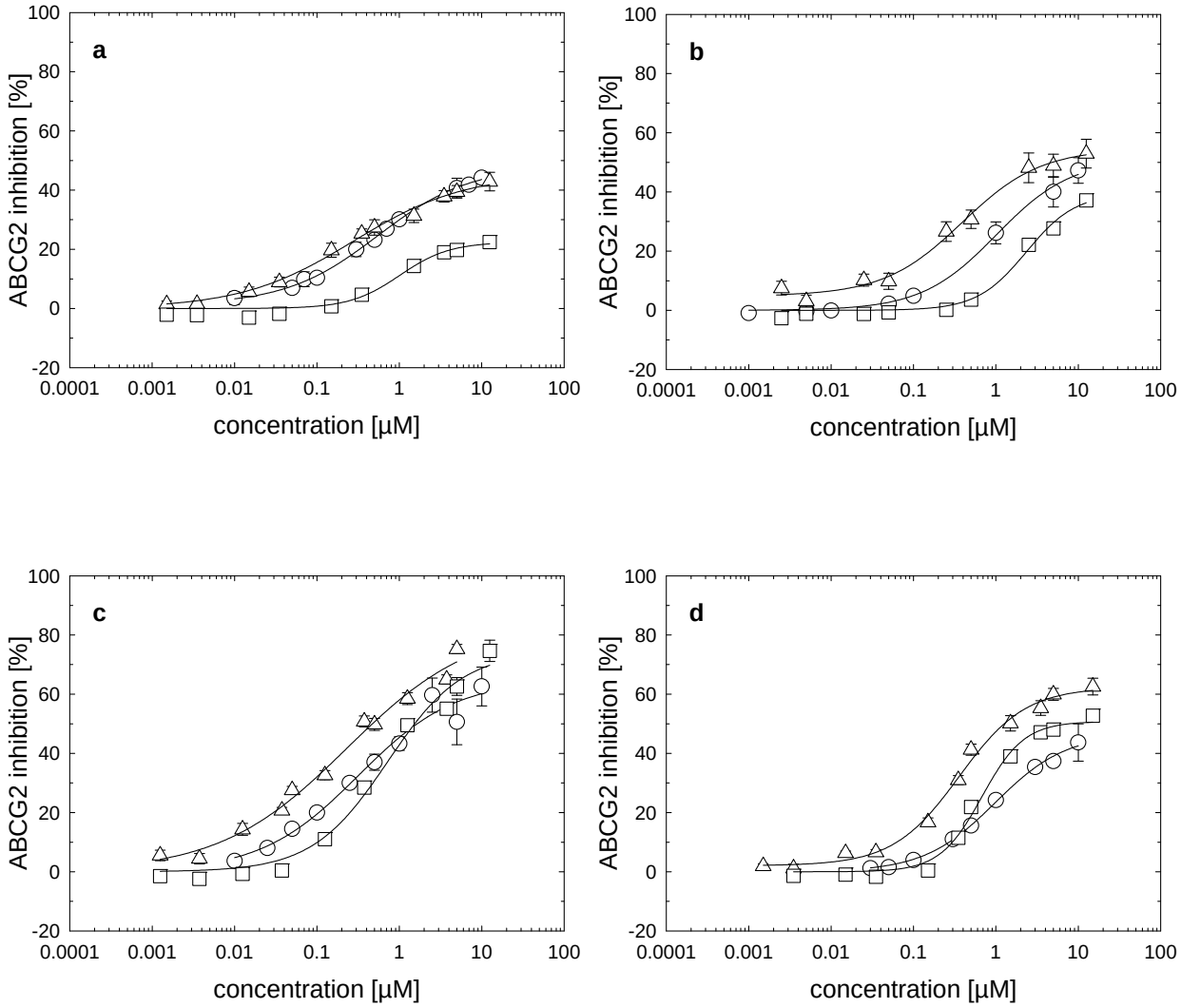

Figure 4.12: Concentration-response curves for ABCG2 inhibition caused by new tariquidar analogs. Compound **5** (a), compound **7** (b), compound **8** (c) and compound **10** (d). Flow cytometric mitoxantrone efflux assay: *open circles*; Hoechst 33342 assay: *open triangles*; PhA assay: *open squares*.

4.4.3 Fluorescent tariquidar analogs

By the performed functional assays, it is impossible to decide, if the tariquidar analogs are substrates or inhibitors of the transporter. Since, by analogy to previous projects, fluorescent pyridinium compounds turned out to be useful pharmacological tools [Keller, 2008], a small series of fluorescence-labeled compounds was produced (**27-29** and **30-33**) to gain inside into the mechanism of action. Therefore, partial structures of the modulator molecules were replaced with fluorescent pyridinium moieties by labeling with pyrylium dyes. These fluorophores were selected since their spectral properties are regarded suitable for imaging.

The fluorescent substances were investigated for inhibition of ABCG2 in the Hoechst 33342 assay and applied in confocal laser scanning microscopy.

4.4.3.1 ABCG2 modulation by fluorescence-labeled tariquidar analogs

Since the spectral properties of the labeled compounds led to interference with mitoxantrone fluorescence in the flow cytometric assay (data not shown), the substances were investigated for ABCG2 modulation in the Hoechst 33342 microtiter plate assay. Additionally, as a control, the MCF-7/Topo cells were incubated with high concentrations of the test compounds alone. The IC_{50} values of the fluorescence-labeled tariquidar analogs are summarized in **Table 4.3**.

Table 4.3: IC_{50} values and maximal inhibition effects (%) for ABCG2 modulation by fluorescence-labeled tariquidar analogs, determined in the H33342-assay.

Compd.	**IC_{50} [nM] [a] ABCG2**	**Max. (%) [b]**
27	-	61 ± 4 (50 µM)
28	4,483 ± 2,517	28 ± 1 (50 µM)
29	2,086 ± 1,589	37 ± 4 (50 µM)
30	21,296 ± 9,392	51 ± 2 (90 µM)
31	-	24 ± 7 (5 µM) [c]
32	16,381 ± 13,004	36 ± 1 (50 µM)
33	-	15 ± 1 (100 µM)

[a] Mean values ± SEM of 2 independent measurements (n=6). [b] Maximal response (%) are expressed as inhibition caused by the highest concentration of the compound tested (see parentheses), relative to the inhibition caused by 50 µM of FTC. [c] N=3 from 1 measurement.

The introduction of the fluorophores resulted in a drastic decrease in ABCG2 inhibitory potency, in particular when the 3-(acylamino)benzoic amide moiety was replaced with a pyridinium moiety (**30-33**), resulting in an additional net charge of the molecule. Introducing the fluorophore instead of the tetrahydroisoquinoline residue in the parent compound **2** was better tolerated and resulted in the most potent labeled tariquidar analog **29** (IC_{50}: 2,086 ± 1,589 nM).

This observation is in good agreement with investigations of partial structures of the non-labeled inhibitors (**19-26**). Potent ABCG2 inhibition seems to depend on an intact 3-(acylamino)benzoic amide moiety rather than on the substituent at the benzamide N-atom. With respect to transporter selectivity, the compounds were additionally investigated for ABCB1 modulation in the calcein-AM microtiter assay by Peter Höcherl. IC_{50} values could not be calculated (data not shown) due to low activities of these compounds. The most pronounced ABCB1 inhibition was achieved with compound **27** (14.7 % maximal response at a concentration of 100 µM). Obviously, for this class of compounds, ABCG2 modulation is more sensitive to structural modifications than ABCB1 inhibition.

4.4.3.2 Confocal-laser scanning microscopy (CLSM) studies

ABCG2-overexpressing MCF-7/Topo cells were incubated with different concentrations of the labeled compounds for various times. Subsequently, the living cells were imaged on the CLSM.

Instrument settings were as follows: Excitation wavelength: 543 nm (laser intensity 10%), emission filter: 650 LP, magnification 400-fold (Apochromat 40 x / NA 1.2W). CLSM images for the incubation of MCF-7/Topo cells with the most potent compounds **28** and **29** and the least active substance **33** are shown in **Figures 4.13**, **4.14** and **4.15**. Due to the weak potency of the compounds, concentrations as high as 10 µM were used for each substance.

All examined compounds entered the cells and accumulated in the cytoplasm. The compounds were not detected in the nuclei. Due to the positive charge of the molecules, these observations were unexpected and suggest an uptake by carrier mediated processes. A selective enrichment within the cell membranes, the localization of ABCG2 transporters, was not observed.

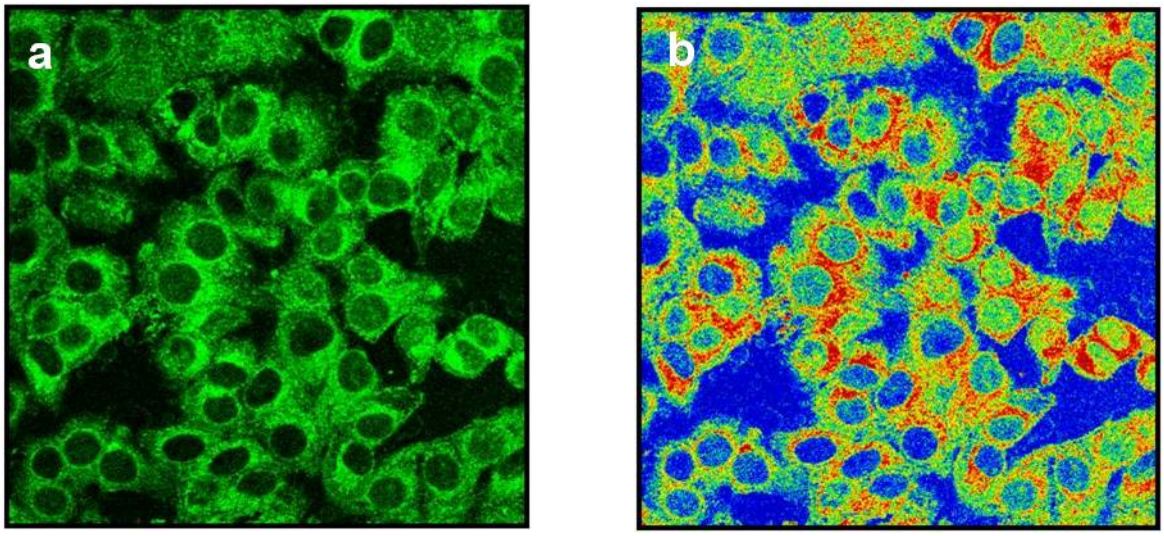

Figure 4.13: MCF-7/Topo cells, 177th passage, 5 min after incubation with compound **28** at a concentration of 10 µM. a) Green pseudo-color image, b) rainbow mode with relative fluorescence intensities.

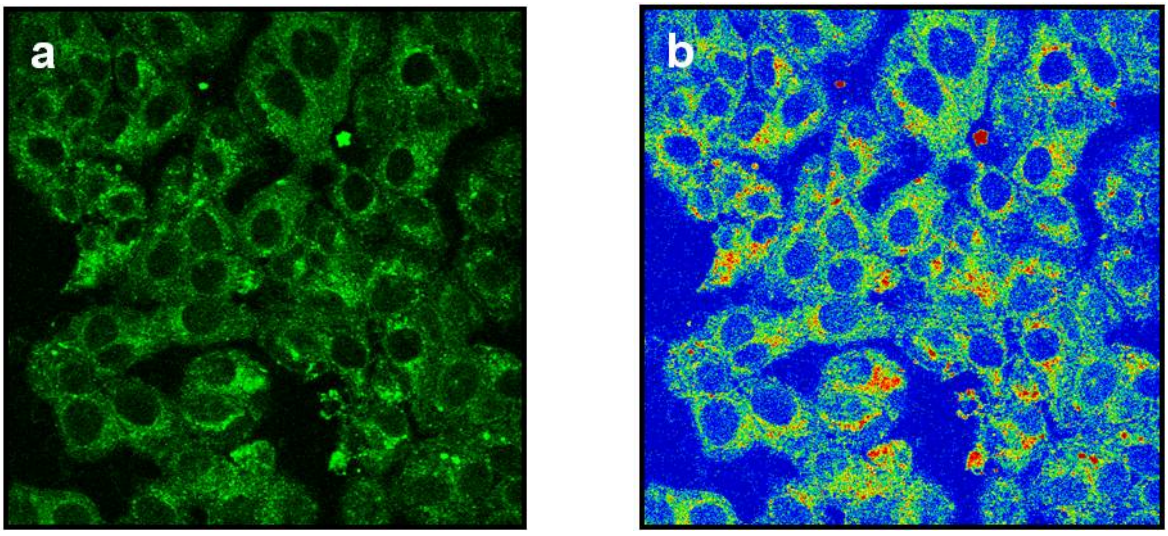

Figure 4.14: MCF-7/Topo cells, 177th passage, 11 min after incubation with compound **29** at a concentration of 10 µM. a) Green pseudo-color image, b) rainbow mode with relative fluorescence intensities.

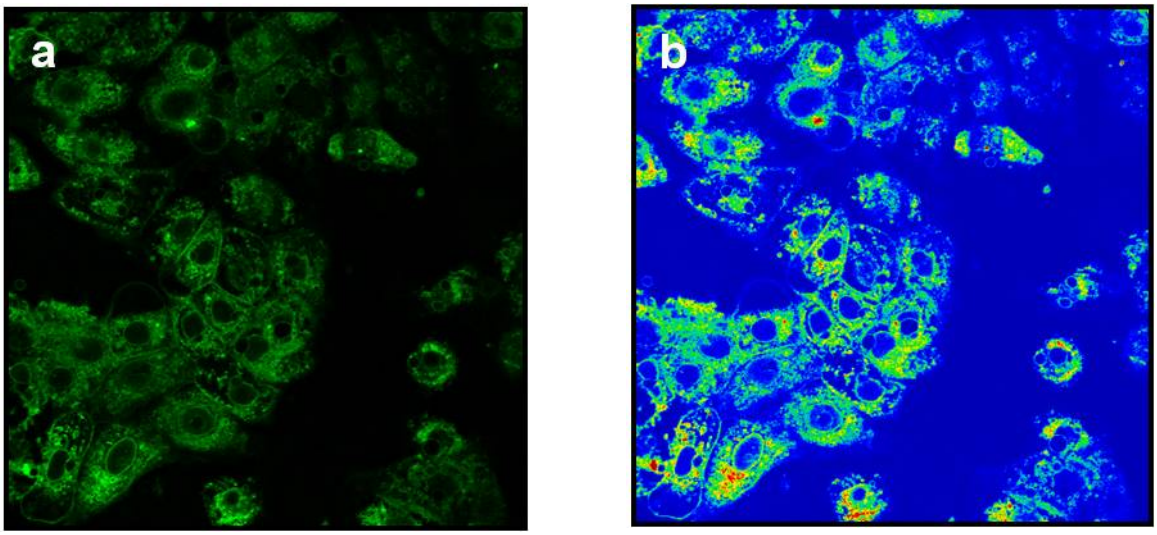

Figure 4.15: MCF-7/Topo cells, 153th passage, 30 min after incubation with compound **33** at a concentration of 10 µM. a) Green pseudo-color image, b) rainbow mode with relative fluorescence intensities.

As a control, MCF-7/Topo cells were incubated with a benzylated Py-dye (lab-code CP 157), which is considered neither a substrate nor an inhibitor of ABCG2, in order to investigate the contribution of the dye moiety. This experiment revealed that the dye component alone was also rapidly taken up into the cytoplasm (data not shown). Similar to the experiments with the labeled tariquidar analogs, neither a specific enrichment within the cell membrane nor an entry into the nuclei of the cells was observed. Presumably, the high concentrations of compounds used in the CLSM studies due to the weak potency of labeled tariquidar analogs against ABCG2 as well as the structural properties of the pyrylium dyes are responsible for the cellular uptake of the substances and the failure of detection of the transporter. Thus it remains unclear if the compounds are weak substrates or inhibitors of ABCG2

4.4.5 Effect of estradiol on the chemosensitivity of MCF-7/Topo cells against the ABCG2 substrate topotecan

Estrogens are reported to be involved in the regulation of ABCG2 expression [Imai et al., 2005; Zhang et al., 2006; Robey et al., 2009], although it is controversially discussed if the regulation occurs at the transcriptional or post-transcriptional level. According to Imai et al. [Imai et al., 2005], estradiol enhanced the cellular uptake of ABCG2 substrates resulting in a potentiation of cytotoxicity.

For this reason, non-induced MCF-7 wildtype and topotecan-resistant MCF-7/Topo cells were treated with estradiol and investigated with respect to their chemosensitivity against the cytostatic and ABCG2 substrate topotecan. The chemosensitivity assays were performed as described previously [Bernhardt et al., 1992a] with slight modifications. As a control, induced and non-induced MCF-7 cells were seeded into 96-well plates and allowed to grow for approximately 72 h. Subsequently, the supernatant was removed and exchanged by fresh medium containing topotecan at various concentrations. To investigate the effect of estradiol on ABCG2-mediated drug-resistance, the cells were either pre-incubated with 1 or 10 nM of estradiol during the 72 h period, or permanently co-incubated with the estrogen during the performance of the cytotoxicity assays. The results of these chemosensitivity assays are shown in **Figures 4.16**, **4.17** and **4.18**.

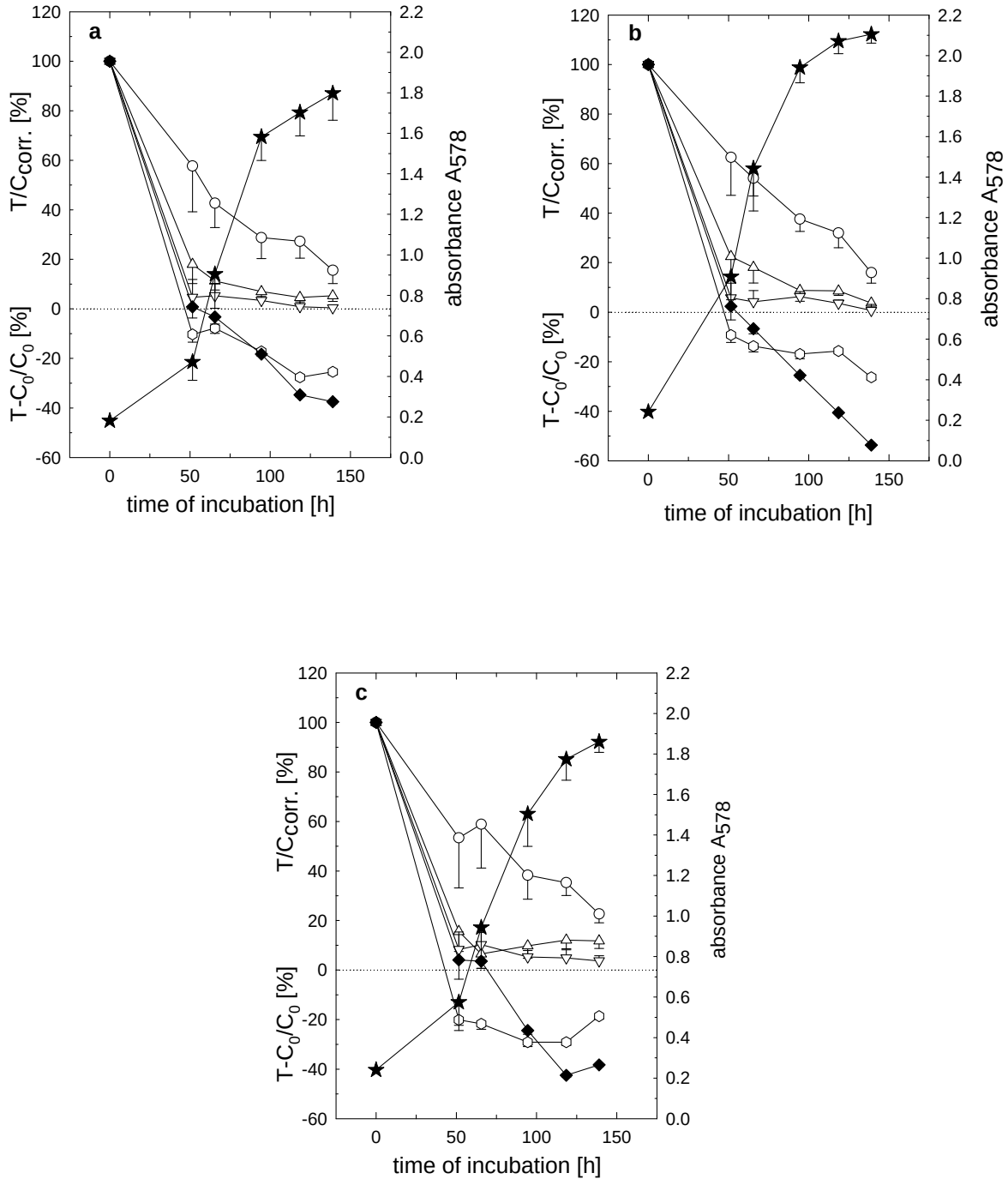

Figure 4.16: Effect of topotecan on proliferating, non-induced MCF-7 wildtype cells. a) Un-treated cells, b) pre-treated with 1 nM estradiol and c) pre-treated with 10 nM estradiol. Growth control (vehicle): filled stars, 10 nM topotecan (open circles), 50 nM topotecan (open triangles), 100 nM topotecan (open inverted triangles), 500 nM topotecan (open diamonds) and vinblastin 10 nM (filled diamonds, positive control).

Regardless of the concentration of the hormon, the chemosensitivity against topotecan remained unchanged comparing non-treated and estradiol supplemented MCF-7 wildtype cells (**Figure 4.16**). As expected, there was no resistance against topotecan due to the low expression of the ABCG2 efflux transporter in the MCF-7 cells. Already at the lowest investigated concentration of 10 nM, topotecan mediated pronounced cytostatic effects on both, the controls as well as on estradiol-treated cells.

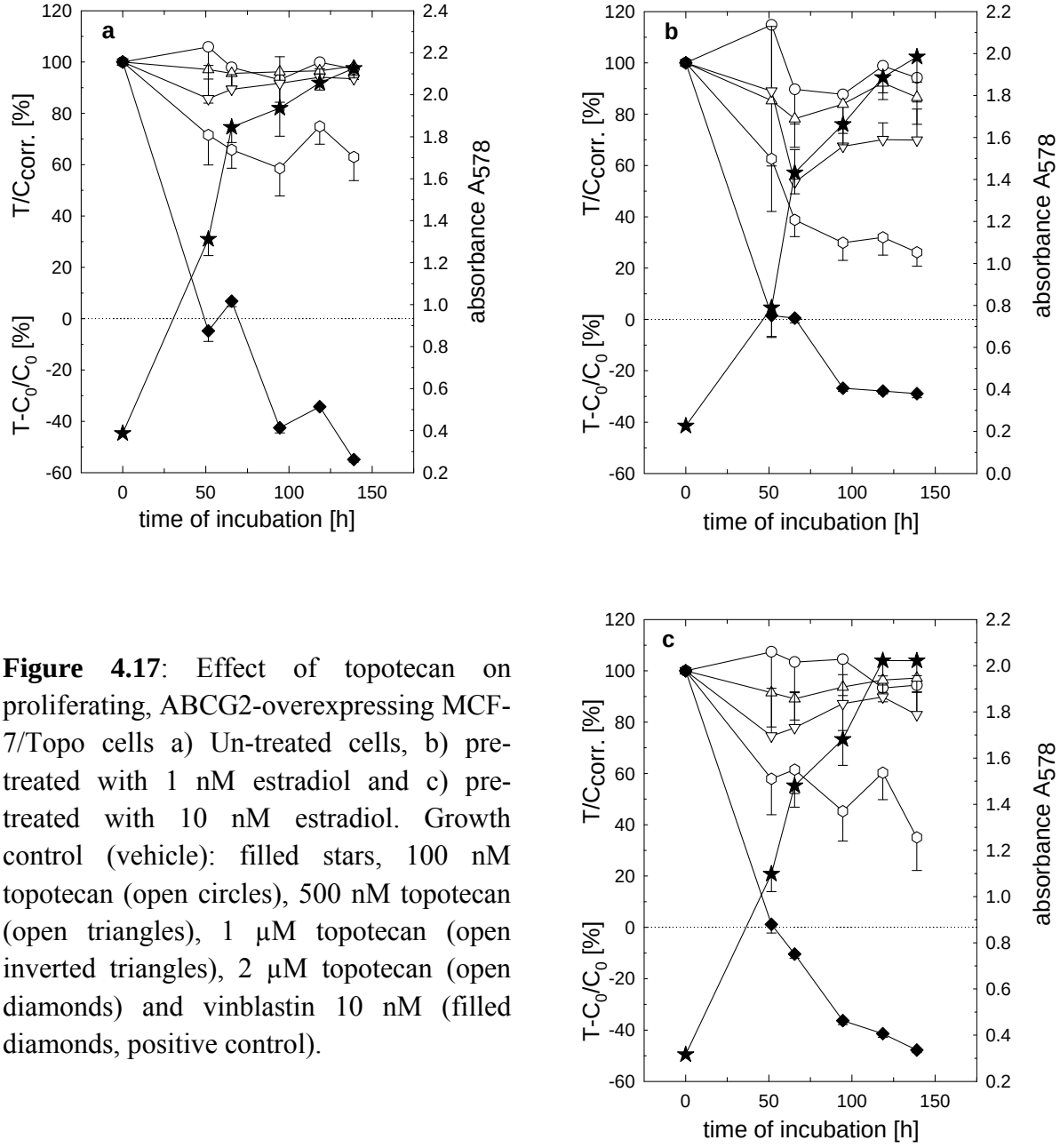

Figure 4.17: Effect of topotecan on proliferating, ABCG2-overexpressing MCF-7/Topo cells a) Un-treated cells, b) pre-treated with 1 nM estradiol and c) pre-treated with 10 nM estradiol. Growth control (vehicle): filled stars, 100 nM topotecan (open circles), 500 nM topotecan (open triangles), 1 µM topotecan (open inverted triangles), 2 µM topotecan (open diamonds) and vinblastin 10 nM (filled diamonds, positive control).

The overexpression of ABCG2 transporters in MCF-7/Topo cells caused resistance to topotecan up to concentrations as high as 500 nM in estradiol pre-treated cells as well as in the un-treated cells (**Figure 4.17**). Discrepancies in the chemosensitivity were only observed at the highest tested concentration of 2 µM topotecan. In this case, pre-treatment with 1 nM of estradiol caused a slightly increased sensitivity against topotecan, but this effect could not be enhanced by pre-incubation with 10 nM of estradiol.

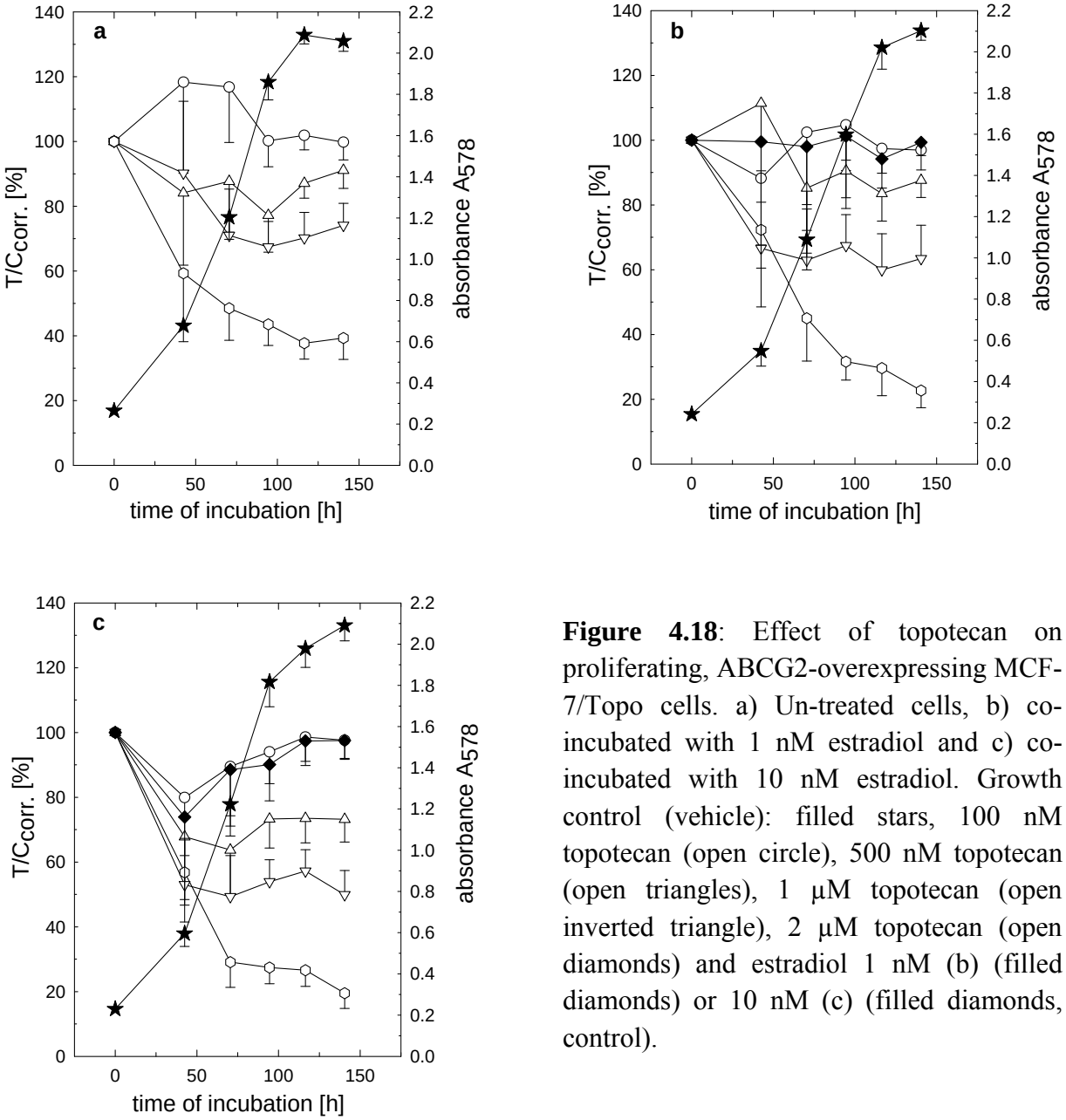

Figure 4.18: Effect of topotecan on proliferating, ABCG2-overexpressing MCF-7/Topo cells. a) Un-treated cells, b) co-incubated with 1 nM estradiol and c) co-incubated with 10 nM estradiol. Growth control (vehicle): filled stars, 100 nM topotecan (open circle), 500 nM topotecan (open triangles), 1 µM topotecan (open inverted triangle), 2 µM topotecan (open diamonds) and estradiol 1 nM (b) (filled diamonds) or 10 nM (c) (filled diamonds, control).

The toxicity of topotecan remained unaffected up to concentrations of 1 µM by co-incubation of MCF-7/Topo cells with estradiol (**Figure 4.18**). At a concentration of 2 µM topotecan, the co-incubation with estradiol resulted in slightly increased cytotoxicity. This effect was more pronounced in the presence of 10 nM of estradiol, however, at such high concentrations a cytotoxic effect of estradiol on MCF-7 breast cancer cell has to be taken into account.

4.4.6 Detection of ABCG2 expression in cancer cell lines by flow cytometry

In search for ABCG2-expressing cells other than MCF-7/Topo, 2 cancer cell lines were screened by means of a modified flow cytometric mitoxantrone efflux assay. As a control, the cells were incubated with mitoxantrone and the vehicle DMSO alone, whereas functional activity of ABCG2 was identified by incubation of the cells with mitoxantrone in combination with 10 µM of fumitremorgin C (FTC). The samples were treated as described for the reference compounds in the mitoxantrone efflux assay. The following cell lines were investigated:

A subclone of MCF-7 wildtype cells resulting from treatment with the ABCG2 substrate estron sulfate [Imai et al., 2003], the human epithelial colorectal adenocarcinoma CaCo2 and MCF-7 as well as MCF-7/Topo cells as a control. Estron sulfate treatment was performed with the idea of an up-regulation of ABCG2 by supplementation of the wildtype cells with a known transporter substrate.

Efflux pump activity was estimated using the following equation:

$$\mathrm{ABCG2-activity} = \frac{\mathrm{GeoMean[FTC]}}{\mathrm{GeoMean[DMSO]}}$$

, where GeoMean [FTC] represents the geometric mean values of cells co-incubated with fumitremorgin C, whereas the abbreviation GeoMean [DMSO] defines the geometric means of the vehicle controls.

The estron sulfate supplemented MCF-7 cells as well as the Caco2 cells showed no enhanced functional activity of the ABCG2 transporter compared to the non-induced MCF-7 wildtype cells. Co-incubation with 10 µM of fumitremorgin C revealed an increase of fluorescence intensity by a factor of approximately 1.5 in all 3 cell types. Contrarily, in the ABCG2-overexpressing control cell line MCF-7/Topo, the modulator yielded a nearly 14-fold elevated geometric mean value compared to the DMSO controls (**Figure 4.19**) indicating the effective blocking of overexpressed efflux pumps in these cells.

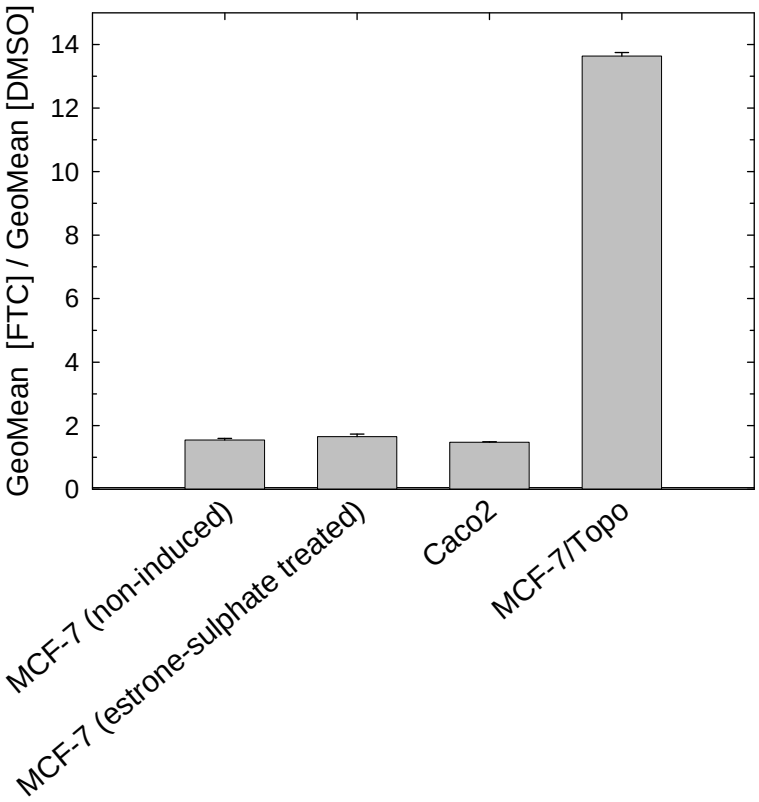

Figure 4.19: Results of the flow cytometric investigation for expression of functional ABCG2. The non-induced MCF-7 wildtype cells as well as the topotecan-treated induced MCF-7/Topo cells served as control for the estrone sulfate supplemented MCF-7 cells and the human epithelial colorectal adenocarcinoma CaCo2. Quotients are calculated by 8-25 measured values. Errors are expressed as standard error of the mean (SEM).

4.4.7 Attempts to establish a subcutaneous ABCG2 overexpressing tumor model

To proof the therapeutic benefit of a combination of an ABCG2 modulator with a cytostatic, which is a substrate of this transporter, in vivo, the reversal of ABCG2 mediated chemoresistance was investigated in vitro. Furthermore, it is essential that the ABCG2 transporter status is retained in vivo over a long period of time.

4.4.7.1 In vitro assays to determine stable ABCG2 transporter expression

For investigations on a stable transporter expression, MCF-7/Topo cells were subdivided into 2 groups. Whereas the first one was supplemented with topotecan as described (see materials and methods), the second group was cultured in the absence of the cytostatic. The cells were investigated for expression of functional ABCG2 in the flow cytometric mitoxantrone efflux assay over several passages after co-incubation with either DMSO (vehicle control) or 10 µM of fumitremorgin C, respectively. As a criterion for stable transporter expression and protein functionality, the obtained fluorescence intensities were analyzed according to the following equation:

$$\text{ABCG2 inhibition}[\%] = \frac{\text{GeoMean}_{\text{corr.}}\,(\text{MCF - 7/Topo})_{\text{non - suppl.}}}{\text{GeoMean}_{\text{corr.}}\,(\text{MCF} - 7/\text{Topo})_{\text{suppl.}}} \cdot 100$$

, with $\text{GeoMean}_{\text{corr.}}\ (\text{MCF-7/Topo})_{\text{non-suppl.}}$ representing the vehicle-corrected geometric means of fluorescence intensities for the non-topotecan supplemented MCF-7/Topo cells. The corrected GeoMean values obtained for the cells cultured in the presence of topotecan are abbreviated as $\text{GeoMean}_{\text{corr.}}\ (\text{MCF-7/Topo})_{\text{suppl.}}$. The results of the flow cytometric assays are shown in **Figure 4.20**.

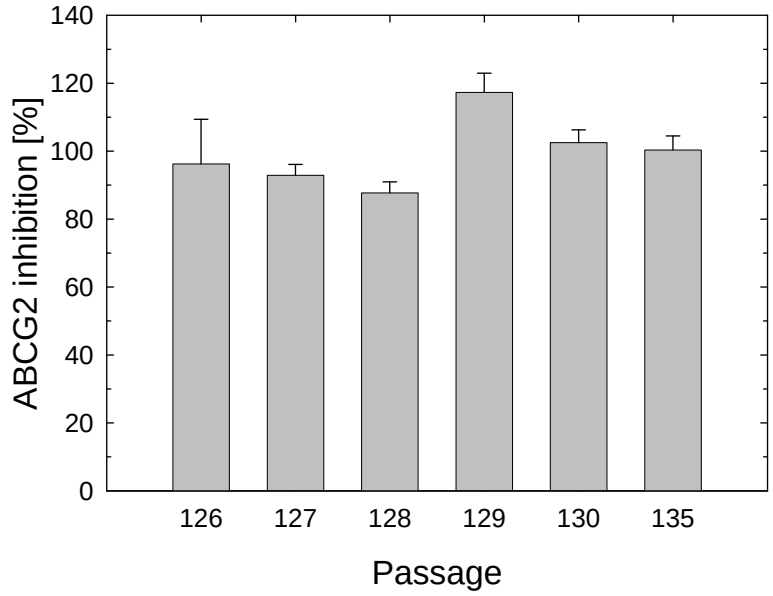

Figure 4.20: ABCG2 inhibition [%] by 10 µM of fumitremorgin C of MCF-7/Topo cells cultured in the presence of topotecan. Transporter modulation is expressed as the ratio of ABCG2 inhibition in non-topotecan supplemented and topotecan-treated MCF-7/Topo cells. The cells were analyzed over a period of 9 in vitro passages.

Flow cytometry confirmed a stable expression of the functionally active efflux pump ABCG2 even in the absence of topotecan. The investigations were arranged over 9 passages corresponding to a period of several weeks in which the overexpression of ABCG2 efflux pumps was preserved. This is an important result with respect to in vivo studies, as the lack of selection pressure due to leaving out topotecan treatment during tumor growth, should not affect the transporter levels.

4.4.7.2 Overcoming ABCG2-mediated drug-resistance in vitro by co-administration of efflux pump inhibitors

The crystal violet chemosensitivity assays were performed as previously described [Bernhardt et al., 1992a]. To examine the potential of ABCG2 modulators to reverse the efflux pump-mediated drug resistance, the assays were arranged as follows:

2-3 days after seeding, MCF-7/Topo cells were either treated with 100 nM of topotecan alone or combined with various concentrations of the known ABCG2 modulator Ko143 (**Figure 4.21**). In an additional experiment the cells were incubated with the ABCG2 substrate mitoxantrone alone or combined with the new tariquidar analog **2** (**Figure 4.22**). Moreover, as a control, the effect of the transporter modulators alone against the cells was determined in a concentration-dependent manner.

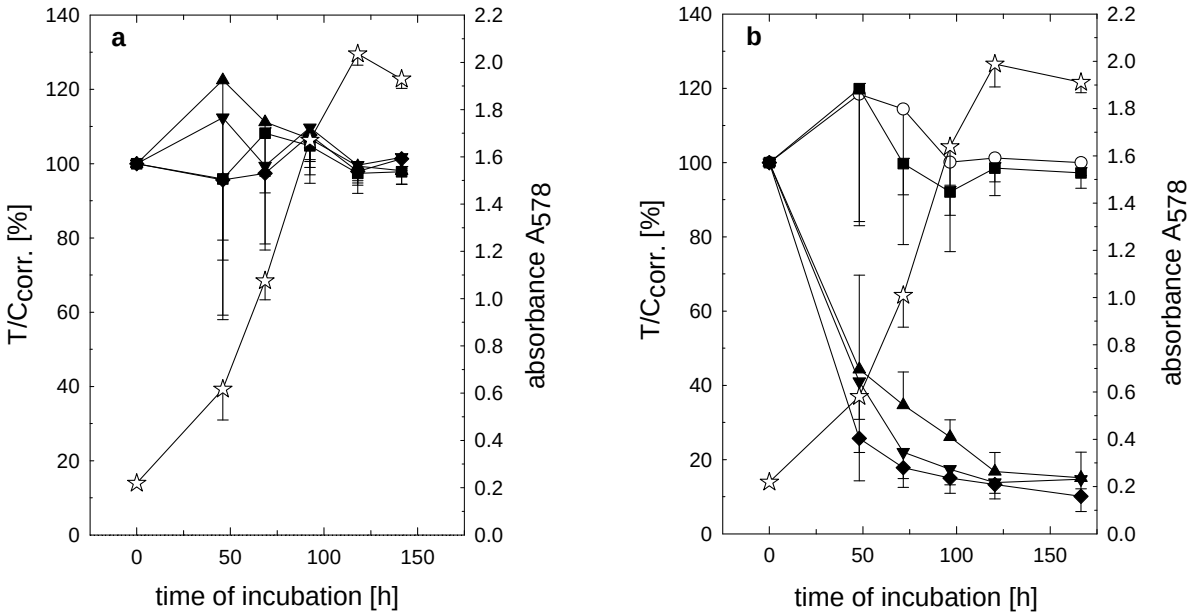

Figure 4.21: Effect of Ko143 alone (a) and in combination with 100 nM topotecan (b) on proliferating MCF-7/Topo cells (passage 138); vehicle (open stars), 100 nM topotecan (open circles) and Ko143 at different concentrations: 10 nM (filled squares), 50 nM (filled triangles), 100 nM (filled inverted triangles) and 500 nM (filled diamonds).

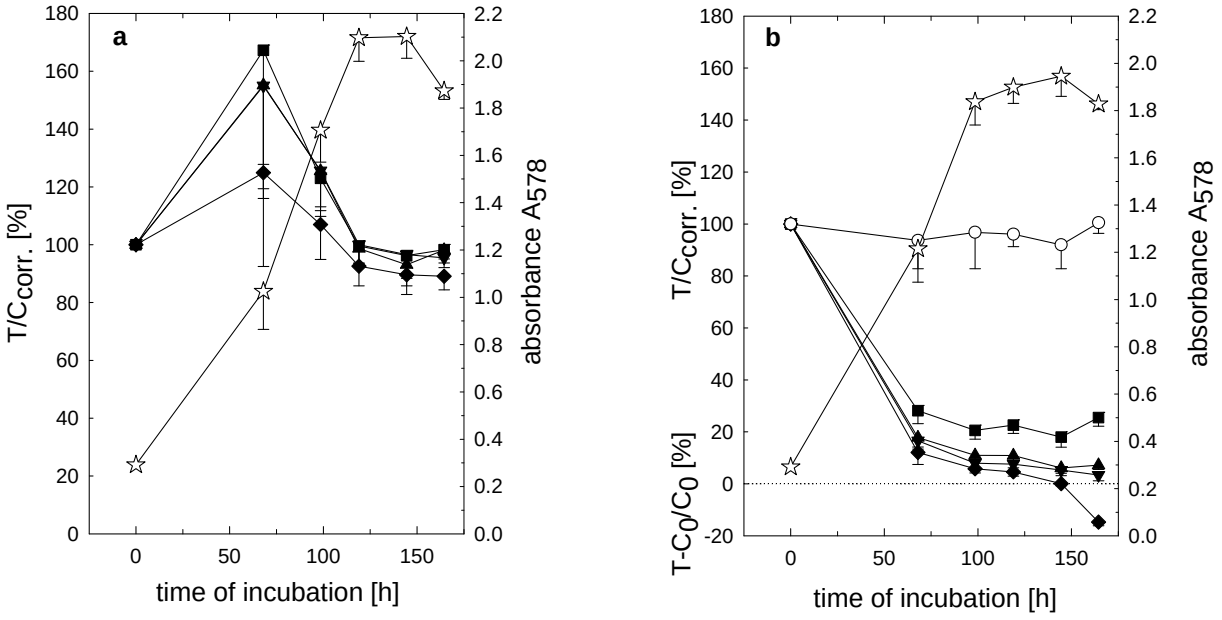

Figure 4.22: Effect of compound **2** alone (a) and in combination with 100 nM mitoxantrone (b) on proliferating MCF-7/Topo cells (passage 193); vehicle (open stars), 100 nM mitoxantrone (open circles) and compound **2** at different concentrations: 10 nM (filled squares), 50 nM (filled triangles), 100 nM (filled inverted triangles) and 500 nM (filled diamonds).

Incubation of MCF-7/Topo breast cancer cells with the ABCG2 inhibitor Ko143 alone caused no toxic effects up to concentrations of 500 nM (**Figure 4.21a**). The combination of 100 nM Ko143 with topotecan at a concentration of 100 nM, which was non-toxic in the absence of a ABCG2 modulator, resulted in total reversal of the ABCG2-mediated drug-resistance, i.e. a remarkable cytostatic effect (**Figure 4.21b**).

There was no cytotoxic effect detectable when MCF-7/Topo cells were incubated with the new tariquidar analog **2** alone up to a concentration of 500 nM (**Figure 4.22a**). However, compound **2** at a concentration of 10 nM combined with 100 nM mitoxantrone, a per se non-toxic concentration of the cytostatic in the ABCG2-overexpressing cells, yielded a strong antiproliferative effect (**Figure 4.22b**).

These in vitro investigations demonstrate that inhibition of the ABCG2 efflux pump is effective to reverse the transporter-mediated drug resistance against the cytostatics topotecan and mitoxantrone.

4.4.7.3 Subcutaneous injection of MCF-7/Topo cells into nude mice

Stimulated by the promising in vitro results, MCF-7/Topo cells were subcutaneously injected into nude mice to establish a subcutaneous tumor model. For this purpose, the human breast cancer cells were injected into both, male and female nude mice in order to check sex-dependent variations in tumor growth. Furthermore, female nude mice were subdivided into 2 groups:

One group of animals was left without additional hormone supplementation; in the other group estradiol depots were implanted to exclude growth retardations of MCF-7/Topo tumors due to estradiol deficiency.

Figure 4.23 shows the implantation procedure of estradiol depots according to Bernhardt et al. [Bernhardt et al., 1992b].

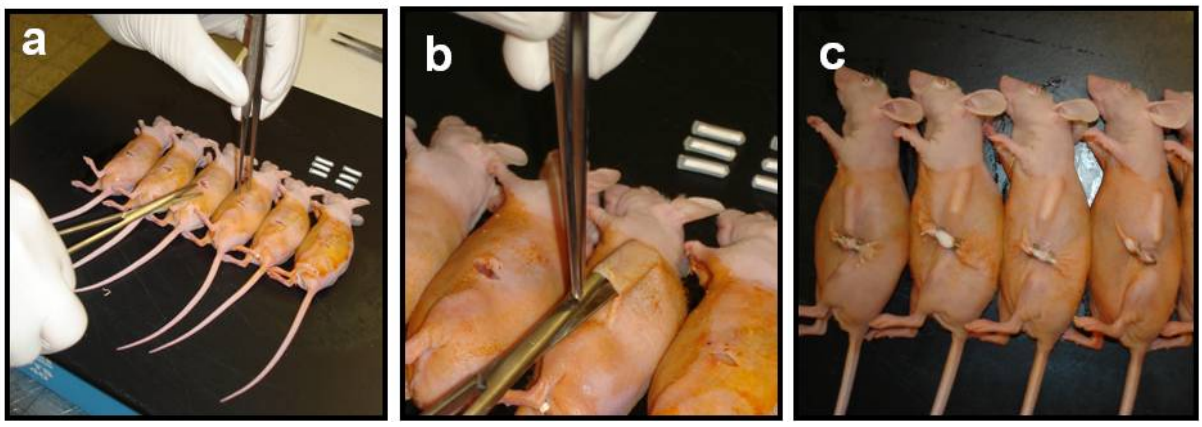

Figure 4.23: Implantation procedure of estradiol depots. a) Opening of skin on anesthetized female nude mice, b) subcutaneous placement of estradiol depots and c) mice with subcutaneous implanted estradiol depots after skin closure by brackets. Tumor cell suspensions were subcutaneously injected 7 days after estradiol depot implantation.

A total of 22 mice were included in this investigation on the in vivo growth of MCF-7/Topo cells. Over a period of more than 3 months, in none group, the subcutaneously injected breast cancer cells resulted in tumor growth. Therefore, these attempts to establish a subcutaneous model of ABCG2-overexpressing MCF-7/Topo tumors, failed.

4.4.8 Stability of selected tariquidar-like ABCG2 modulators

With regard to future in vivo studies, selected candidates of the new ABCG2 modulators were subjected to preliminary biopharmaceutical investigations with a focus on stability. For this purpose, the compounds were incubated with different media, including PBS, EMEM supplemented with 5 % FCS and murine plasma, and the samples were analyzed by HPLC. As a degradation of the compounds was detected in murine plasma, HPLC-MS methods were established in order to elucidate the structures of the cleavage products.

Basically, the investigations on plasma stability were performed to substantiate speculations about the lack of drug-like properties of ABCG2 inhibitors such as the most potent compounds **1** and **2,** which contain ester groups prone to enzymatic hydrolysis. The corresponding carboxylic acid of **1**, compound **12**, turned out about 80 times less potent that the parent compound in the mitoxantrone assay. However, HPLC-MS analysis revealed an enzymatic cleavage pathway as depicted in **Figure 4.24**. Surprisingly, the ester groups remained intact, whereas the benzoic amide was rapidly cleaved.

To discriminate between hydrolytic instability and enzymatic cleavage, control experiments were performed in phosphate buffered saline and deproteinated plasma. In both cases the compounds remained stable. Furthermore, there was no indication of degradation when the compounds were incubated in cell culture medium containing 5 % FCS (corresponding to the conditions of ABCG2 inhibition assays). The results indicate enzymatic cleavage in plasma.

In order to confirm the HPLC-MS data, all cleavage products (compounds **19**, **24** and **34**) were synthesized for comparison and analyzed by the chromatography method. The mass spectra and retention times of the reference compounds were in agreement with the data from the investigated plasma samples (**Figure 4.25**). Whereas compound **1** was almost totally degraded after 30 min, the structural isomer **2** turned out to be slightly more stable over the same period of incubation: approximately 50 % of the parent compound remained unchanged.

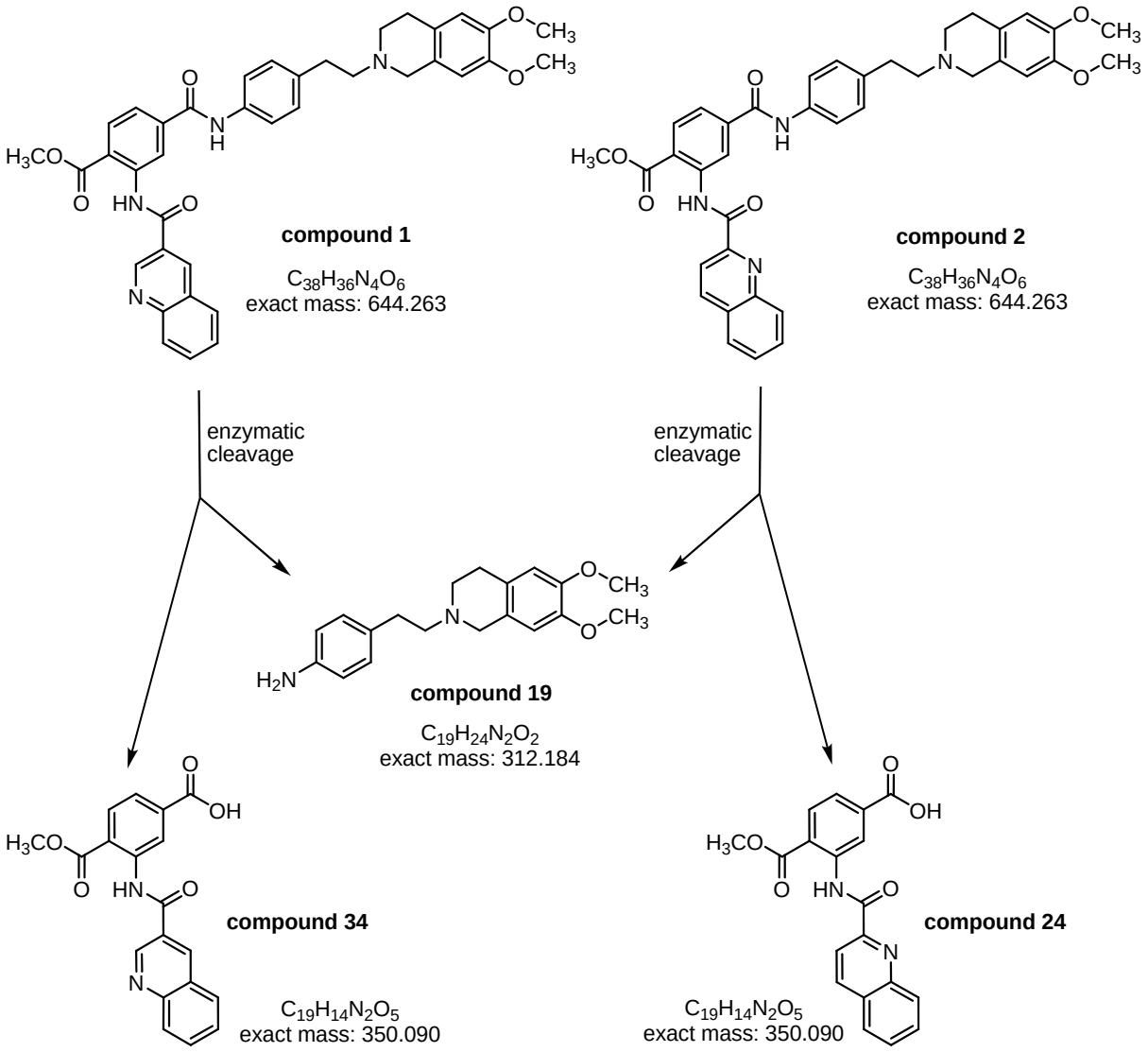

Figure 4.24: Enzymatic cleavage of the ABCG2 modulators **1** and **2** in murine plasma. Whereas the methyl ester in compounds **1** and **2** remained intact, the benzamide groups in both compounds were enzymatically cleaved to give the aniline substructure **19** and the carboxylic acids **24** and **34**.

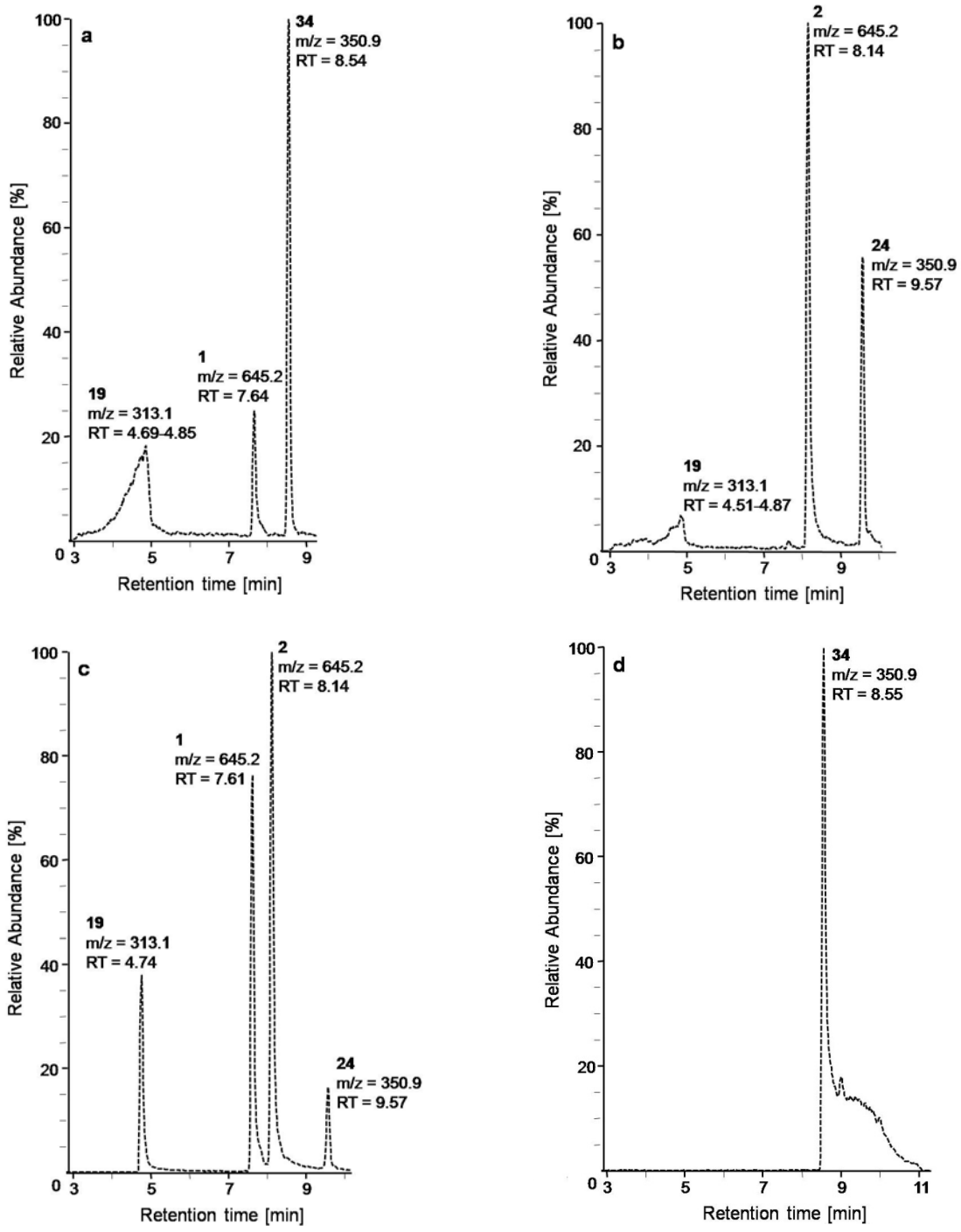

Figure 4.25: HPLC-MS analysis of compounds **1** and **2** after incubation in mouse plasma and reference mixtures. a) Detection of tariquidar analog **1** and the cleavage products compound **19** and **34** by HPLC-MS analysis in the plasma of BL6 mice, 15 min after incubation at 37 °C. b) HPCL-MS analysis of BL6 mouse plasma incubated for 25 min at 37 °C with compound **2**. The cleavage products **19** and **24** were detected in the samples. c) Simultaneous detection of reference compounds **1, 2** and the cleavage products compound **19** and **24** by HPLC-MS. d) Since up to the time of method development compound **34** had not been synthesized yet, the substance was determined later on separately by the same HPCL-MS method. Compound **34** elutes at a retention time (RT) of 8.55 min which is in agreement with the RT of the degradation product detected in plasma.

In order to investigate the inhibitory potency of the cleavage products against the efflux transporter ABCG2, the compounds were studied in the flow cytometric mitoxantrone efflux assay. Neither compound **19** nor the carboxylic acids **24** and **34** inhibited the ABCG2 transporter up to the highest tested concentration of 50 µM. These results confirm the assumption that the potent and selective inhibition of the efflux pump ABCG2 can only be attributed to the intact parent compounds **1** and **2**, and not to the cleavage products **19**, **24** or **34**.

4.5 Summary and conclusions

In the present study we investigated a series of tariquidar analogs that turned out to be among the most potent and selective ABCG2 inhibitors known so far [Kühnle et al., 2009]. Compared to tariquidar, in these compounds the hetarylcarboxamid substituent at the benzoic amide core was shifted from the ortho to the meta position. The ABCG2 modulators were studied in a routinely performed flow cytometric mitoxantrone assay and in 2 newly developed microtiter plate assays using the dyes Hoechst 33342 and pheophorbide a as fluorescent substrates. Thereby, derivative **2** showed the highest potency against ABCG2 with an IC_{50} value of 60, 65 and 126 nM respectively, determined by means of 3 different assays. Investigations on the highly potent ABCG2 inhibitor Ko143 [Allen et al., 2002] yielded IC_{50} values of 117, 179 and 225 nM, respectively. Thus, compound **2** was at least equipotent with the reference substance. The studies on tariquidar analogs, their corresponding partial structures and intermediates showed that the most potent inhibitors were obtained with bicyclic hetarylcarboxamides in position 3 and an ester group in position 4 at the benzamide core (substances **1-4** and **17**). Moreover, inhibition data obtained for the partial structures **19-23** and **24-26**, suggest that ABCG2 inhibition depends rather on an intact 3-(acylamino)benzoic amide moiety than on the substituent at the benzamide N-atom.

With respect to fluorescence-based cellular investigations including confocal-laser scanning microscopy (CLSM), a recently synthesized small series of fluorescence-labeled compounds (**27-33**) was investigated for ABCG2 and ABCB1 inhibition. In these substances, substructures of the tariquidar-like ABCG2 inhibitors were replaced with fluorophores chemically prepared from pyrylium dyes. Unfortunately, all these substances showed a very strong decrease in ABCG2 inhibitory potency: the most effective modulator, compound **29** achieved only an IC_{50} value of 2,086 nM corresponding to more than 30-fold lower potency compared to ABCG2 inhibitor **2** (IC_{50} = 65 nM). Surprisingly, CLSM studies revealed an accumulation of the labeled positively charged compounds in the cytoplasm of the cells as also observed for the dye component alone. If the compounds enter the cells by diffusion as ion pairs or by carrier-mediated processes remain a matter of speculation.

As estrogens are reported to be involved in the regulation of ABCG2 expression [Imai et al., 2005; Zhang et al., 2006], non-induced MCF-7 wildtype as well as the topotecan-induced MCF-7/Topo cells were investigated in cytotoxicity assays, comparing the influence of pre- or co-incubation with estradiol on the chemosensitivity of the cells against topotecan. An estradiol-induced reduction in ABCG2 activity was expected [Imai et al., 2005]. However, the topotecan-resistance of MCF-7/Topo cells was not reversed or significantly decreased by treatment with estradiol at relevant concentrations

In view of future in vivo studies, to evaluate the combination of cytostatics with ABCG2 modulators for reversing multidrug resistance, preliminary investigations in vitro and in vivo were performed in order to check the suitability of MCF-7/Topo cells to establish a tumor model in nude mice. In vitro, the ABCG2 expression remained stable over the duration of these experiments (9 passages) although topotecan as an ABCG2-inducing cytostatic was omitted. Furthermore, the ABCG2-mediated mitoxantrone resistance was reversed in vitro by co-administration of the efflux pump inhibitor **2**. Hence, the cells were subcutaneously injected into nude mice for the characterization of tumor growth in vivo. Unfortunately, in none of the nude mice solid tumor tissues were generated. Thus, due to the lack of tumorigenicity the ABCG2-overexpressing MCF-7/Topo cells are not suitable to establish a xenograft model.

Since the most potent ABCG2 inhibitors were considered to be not drug-like due to methyl ester groups prone to enzymatic cleavage, biopharmaceutical investigations on the stability of compounds **1** and **2** in mouse plasma compared to buffer and cell culture medium were performed. Surprisingly, incubation with plasma left the ester groups in **1** and **2** intact but resulted in the cleavage of the benzoic amide core to give the amine **19** and the corresponding carboxylic acids **24** and **34**. Thus, the key structural modification to obtain highly potent and selective ABCG2 modulators, i.e. the shift of the hetarylcarboxamido substituent from the ortho- to the meta-position of the benzamide core, was also decisive for instability against hydrolytic enzymes in plasma. These results suggest the major focus of subsequent projects on tariquidar-like ABCG2 modulators to be directed to the design and synthesis of more stable, drug-like compounds, for instance, by introduction of bulky groups preventing enzymatic attack at the benzamide moiety.

References

Ahmed-Belkacem, A., Pozza, A., Macalou, S., Perez-Victoria, J. M., Boumendjel, A. and Di Pietro, A. (2006). Inhibitors of cancer cell multidrug resistance mediated by breast cancer resistance protein (BCRP/ABCG2). Anticancer. Drugs **17**(3): 239-243.

Allen, J. D., van Loevezijn, A., Lakhai, J. M., van der Valk, M., van Tellingen, O., Reid, G., Schellens, J. H. M., Koomen, G.-J. and Schinkel, A. H. (2002). Potent and Specific Inhibition of the Breast Cancer Resistance Protein Multidrug Transporter in Vitro and in Mouse Intestine by a Novel Analogue of Fumitremorgin C. Mol. Cancer Ther. **1**(6): 417-425.

Allikmets, R., Schriml, L. M., Hutchinson, A., Romano-Spica, V. and Dean, M. (1998). A Human Placenta-specific ATP-Binding Cassette Gene (ABCP) on Chromosome 4q22 That Is Involved in Multidrug Resistance. Cancer Res. **58**(23): 5337-5339.

Bernhardt, G., Reile, H., Birnböck, H., Spruss, T. and Schönenberger, H. (1992a). Standardized kinetic microassay to quantify differential chemosensitivity on the basis of proliferative activity. J. Cancer Res. Clin. Oncol. **118**(1): 35-41.

Bernhardt, G., Spruss, T. and Rustler, M. (1992b). Comparison of MCF-7 and ZR-75-1 Cell Lines as Models for Studying Hormone-Dependent Breast Cancer in Nude Mice. Contrib Oncol. Basel, Karger 1992 **42**: 128-130.

Borst, P., Kool, M. and Evers, R. (1997). Do cMOAT (MRP2), other MRP homologues, and LRP play a role in MDR? Semin. Cancer Biol. **8**(3): 205-213.

Boumendjel, A., Macalou, S., Ahmed-Belkacem, A., Blanc, M. and Di Pietro, A. (2007). Acridone derivatives: design, synthesis, and inhibition of breast cancer resistance protein ABCG2. Bioorg. Med. Chem. **15**(8): 2892-2897.

Breedveld, P., Beijnen, J. H. and Schellens, J. H. M. (2006). Use of P-glycoprotein and BCRP inhibitors to improve oral bioavailability and CNS penetration of anticancer drugs. Trends Pharmacol. Sci. **27**(1): 17-24.

Bunting, K. D. (2002). ABC Transporters as Phenotypic Markers and Functional Regulators of Stem Cells. Stem Cells **20**(1): 11-20.

Cervenak, J., Andrikovics, H., Ozvegy-Laczka, C., Tordai, A., Nemet, K., Varadi, A. and Sarkadi, B. (2006). The role of the human ABCG2 multidrug transporter and its variants in cancer therapy and toxicology. Cancer Lett. **234**(1): 62-72.

de Bruin, M., Miyake, K., Litman, T., Robey, R. and Bates, S. E. (1999). Reversal of resistance by GF120918 in cell lines expressing the ABC half-transporter, MXR. Cancer Lett. **146**(2): 117-126.

Dean, M. and Allikmets, R. (2001). Complete Characterization of the Human ABC Gene Family. J. Bioenerg. Biomembr. **33**(6): 475-479.

Doyle, L. A., Yang, W., Abruzzo, L. V., Krogmann, T., Gao, Y., Rishi, A. K. and Ross, D. D. (1998). A multidrug resistance transporter from human MCF-7 breast cancer cells. Proc. Natl. Acad. Sci. U. S. A. **95**(26): 15665–15670.

Egger, M., Li, X., Müller, C., Bernhardt, G., Buschauer, A. and König, B. (2007). Tariquidar Analogues: Synthesis by Cu^{I}-Catalysed N/O-Aryl Coupling and Inhibitory Activity against the ABCB1 transporter. Eur. J. Org. Chem.(16): 2643-2649.

Fellner, S., Bauer, B., Miller, D. S., Schaffrik, M., Fankhänel, M., Spruss, T., Bernhardt, G., Gräff, C., Färber, L., Gschaidmeier, H., Buschauer, A. and Fricker, G. (2002). Transport of paclitaxel (Taxol) across the blood-brain barrier in vitro and in vivo. J. Clin. Invest. **110**(9): 1309-1318.

Han, Y., Riwanto, M., Go, M. L. and Rachel Ee, P. L. (2008). Modulation of breast cancer resistance protein (BCRP/ABCG2) by non-basic chalcone analogues. Eur. J. Pharm. Sci.

Haraguchi, N., Utsunomiya, T., Inoue, H., Tanaka, F., Mimori, K., Barnard, G. F. and Mori, M. (2006). Characterization of a Side Population of Cancer Cells from Human Gastrointestinal System. Stem Cells **24**(3): 506-513.

Hay, R. J. (1988). The seed stock concept and quality control for cell lines. Anal. Biochem. **171**(2): 225-237.

Henrich, C. J., Bokesch, H. R., Dean, M., Bates, S. E., Robey, R. W., Goncharova, E. I., Wilson, J. A. and McMahon, J. B. (2006). A high-throughput cell-based assay for inhibitors of ABCG2 activity. J. Biomol. Screen. **11**(2): 176-183.

Henrich, C. J., Robey, R. W., Takada, K., Bokesch, H. R., Bates, S. E., Shukla, S., Ambudkar, S. V., McMahon, J. B. and Gustafson, K. R. (2009). Botryllamides: Natural Product Inhibitors of ABCG2. ACS Chemical Biology **4**(8): 637-647.

Hirschmann-Jax, C., Foster, A. E., Wulf, G. G., Nuchtern, J. G., Jax, T. W., Gobel, U., Goodell, M. A. and Brenner, M. K. (2004). A distinct "side population" of cells with high drug efflux capacity in human tumor cells. Proc. Natl. Acad. Sci. U. S. A. **101**(39): 14228-14233.

Hubensack, M. (2005). Approaches to overcome the blood brain barrier in the chemotherapy of primary and secondary brain tumors: modulation of P-glycoprotein 170 and targeting of the transferrin receptor; Doctoral thesis. http://www.opus-bayern.de/uni-regensburg/volltexte/2005/471/pdf/Dissertation_MartinaHubensack.pdf

Hubensack, M., Müller, C., Höcherl, P., Fellner, S., Spruss, T., Bernhardt, G. and Buschauer, A. (2008). Effect of the ABCB1 modulators elacridar and tariquidar on the distribution of paclitaxel in nude mice. J. Cancer Res. Clin. Oncol. **134**(5): 597-607.

Humphries, C. (2009). Killing Cancer Stem Cells. http://www.technologyreview.com/biomedicine/23222/

Imai, Y., Asada, S., Tsukahara, S., Ishikawa, E., Tsuruo, T. and Sugimoto, Y. (2003). Breast Cancer Resistance Protein Exports Sulfated Estrogens but Not Free Estrogens. Mol. Pharmacol. **64**(3): 610-618.

Imai, Y., Ishikawa, E., Asada, S. and Sugimoto, Y. (2005). Estrogen-Mediated Post transcriptional Down-regulation of Breast Cancer Resistance Protein/ABCG2. Cancer Res. **65**(2): 596-604.

Jain, H. D., Zhang, C., Zhou, S., Zhou, H., Ma, J., Liu, X., Liao, X., Deveau, A. M., Dieckhaus, C. M., Johnson, M. A., Smith, K. S., Macdonald, T. L., Kakeya, H., Osada, H. and Cook, J. M. (2008). Synthesis and structure-activity relationship studies on tryprostatin A, an inhibitor of breast cancer resistance protein. Bioorg. Med. Chem. **16**(8): 4626-4651.

Jekerle, V., Klinkhammer, W., Reilly, R., Piquette-Miller, M. and Wiese, M. (2007). Novel tetrahydroisoquinolin-ethyl-phenylamine based multidrug resistance inhibitors with broad-spectrum modulating properties. Cancer Chemother. Pharmacol. **59**(1): 61-69.

Jekerle, V., Klinkhammer, W., Scollard, D. A., Breitbach, K., Reilly, R. M., Piquette-Miller, M. and Wiese, M. (2006). In vitro and in vivo evaluation of WK-X-34, a novel inhibitor of P-glycoprotein and BCRP, using radio imaging techniques. Int. J. Cancer **119**(2): 414-422.

Jonker, J. W., Freeman, J., Bolscher, E., Musters, S., Alvi, A. J., Titley, I., Schinkel, A. H. and Dale, T. C. (2005). Contribution of the ABC Transporters Bcrp1 and Mdr1a/1b to the Side Population Phenotype in Mammary Gland and Bone Marrow of Mice. Stem Cells **23**(8): 1059-1065.

Keller, M. (2008). Guanidine-Acylguanidine Bioisosteric Approach to Adress Peptidergic Receptors: Pharmacological and Diagnostic Tools for the NPY Y1 Receptor and Versatile Building Blocks Based on Arginine Substitutes; Doctoral thesis. http://www.opus-bayern.de/uni-regensburg/volltexte/2009/1111/pdf/Dissertation_Max_Keller.pdf

Kondo, T., Setoguchi, T. and Taga, T. (2004). Persistence of a small subpopulation of cancer stem-like cells in the C6 glioma cell line. Proc. Natl. Acad. Sci. U. S. A. **101**(3): 781-786.

Kühnle, M., Egger, M., Müller, C., Mahringer, A., Bernhardt, G., Fricker, G., König, B. and Buschauer, A. (2009). Potent and Selective Inhibitors of Breast Cancer Resistance Protein (ABCG2) Derived from the p-Glycoprotein (ABCB1) Modulator Tariquidar. J. Med. Chem. **52**(4): 1190-1197.

Kuwano, M., Toh, S., Uchiumi, T., Takano, H., Kohno, K. and Wada, M. (1999). Multidrug resistance-associated protein subfamily transporters and drug resistance. Anticancer. Drug Des. **14**(2): 123-131.

Leonard, G. D., Fojo, T. and Bates, S. E. (2003). The Role of ABC Transporters in Clinical Practice. Oncologist **8**(5): 411-424.

Liu, X. L., Tee, H. W. and Go, M. L. (2008). Functionalized chalcones as selective inhibitors of P-glycoprotein and breast cancer resistance protein. Bioorg. Med. Chem. **16**(1): 171-180.

Müller, C. (2007). New approaches to the therapy of glioblastoma: investigations on RNA interference, kinesin Eg5 and ABCB1/ABCG2 inhibition. http://www.opus-bayern.de/uni-regensburg/frontdoor.php?source_opus=816&la=de

Rabindran, S. K., Ross, D. D., Doyle, L. A., Yang, W. and Greenberger, L. M. (2000). Fumitremorgin C Reverses Multidrug Resistance in Cells Transfected with the Breast Cancer Resistance Protein. Cancer Res. **60**(1): 47-50.

Régina, A., Demeule, M., Laplante, A., Jodoin, J., Dagenais, C., Berthelet, F., Moghrabi, A. and Béliveau, R. (2001). Multidrug Resistance in Brain Tumors: Roles of the Blood–brain Barrier. Cancer Metastasis Rev. **20**(1): 13-25.

Robey, R., Polgar, O., Deeken, J., To, K. and Bates, S. (2007). ABCG2: determining its relevance in clinical drug resistance. Cancer Metastasis Rev. **26**: 39-57.

Robey, R. W., Steadman, K., Polgar, O., Morisaki, K., Blayney, M., Mistry, P. and Bates, S. E. (2004). Pheophorbide a Is a Specific Probe for ABCG2 Function and Inhibition. Cancer Res. **64**(4): 1242-1246.

Robey, R. W., To, K. K. K., Polgar, O., Dohse, M., Fetsch, P., Dean, M. and Bates, S. E. (2009). ABCG2: A perspective. Adv. Drug Del. Rev. **61**(1): 3-13.

Seigel, G. M. and Campbell, L. M. (2004). High-throughput microtiter assay for Hoechst 33342 dye uptake. Cytotechnology **45**(3): 155-160.

Sheps, J. and Ling, V. (2007). Preface: the concept and consequences of multidrug resistance. Pfluegers Arch./Eur. J. Physiol. **453**(5): 545-553.

Shiozawa, K., Oka, M., Soda, H., Yoshikawa, M., Ikegami, Y., Tsurutani, J., Nakatomi, K., Nakamura, Y., Doi, S., Kitazaki, T., Mizuta, Y., Murase, K., Yoshida, H., Ross, D. D. and Kohno, S. (2004). Reversal of breast cancer resistance protein (BCRP/ABCG2)-mediated drug resistance by novobiocin, a coumermycin antibiotic. Int. J. Cancer **108**(1): 146-151.

Spruss, T., Schlemmer, R., Bernhardt, G., Wiesenmayer, F. and Baumann, O. (1996). Five-year breeding data, immunology and tumor take rates of an NMRI nude mouse colony. Contrib. Oncol. **51**(In: Arnold, W. (Editor) Immunodeficient Laboratory Animals): 12-18.

Staud, F., Vackova, Z., Pospechova, K., Pavek, P., Ceckova, M., Libra, A., Cygalova, L., Nachtigal, P. and Fendrich, Z. (2006). Expression and Transport Activity of Breast Cancer Resistance Protein (Bcrp/Abcg2) in Dually Perfused Rat Placenta and HRP-1 Cell Line. J. Pharmacol. Exp. Ther. **319**(1): 53-62.

Sung, J. M., Cho, H. J., Yi, H., Lee, C. H., Kim, H. S., Kim, D. K., Abd El-Aty, A. M., Kim, J. S., Landowski, C. P., Hediger, M. A. and Shin, H. C. (2008). Characterization of a stem cell population in lung cancer A549 cells. Biochem. Biophys. Res. Commun. **371**(1): 163-167.

Zhang, Y., Zhou, G., Wang, H., Zhang, X., Wei, F., Cai, Y. and Yin, D. (2006). Transcriptional Upregulation of Breast Cancer Resistance Protein by 17β-Estradiol in ERα-Positive MCF-7 Breast Cancer Cells. Oncology **71**(5-6): 446-455.

Chapter 5

Optical imaging of orthotopic human glioblastoma in nude mice

5.1 Introduction

5.1.1 Bioluminescence Imaging

5.1.1.1 Bioluminescence

Bioluminescence is a special form of chemoluminescence, i. e. the enzymatic conversion of chemical energy into light [Day et al., 2004]. Such reactions frequently occur in the marine world from bacteria over dinoflagellates, coelenterates, crustacean to teleosts [Hastings, 1983]. However, luminous organisms also inhabit the land and are predominantly found within the order of coleopta in the family of the *Lamprydiae* or closely related beetle families [Day et al., 2004]. The most prominent members of these families represent fireflies and glow-worms. During the last decades, many different roles of bioluminescence in the various organisms have been discussed such as prey attraction [Sivinski, 1998], communication on sexual level [Carlson and Copeland, 1985], evasion of predators (aposematism) [Underwood et al., 1997; Cock and Matthysen, 1999; De Cock and Matthysen, 2003] or even stimulation of DNA-repair processes and detoxification of oxygen radicals [Wegrzyn et al., 2004].

The emission of bioluminescence requires enzymes (luciferases), which act as oxygenases. Such luciferases oxidize substrates, namely luciferins or coelenterazines, by utilizing molecular oxygen [Hastings, 1996]. Hereby, product molecules are produced in electronically excited states, resulting in the emission of light upon relaxation. The terms luciferases and luciferins are generic names for different enzymes and substrates. Since there are several isozymes and substrates, the emitted light shows different spectral properties [Hastings, 1996]. For example, fireflies, which are endowed with the wildtype luciferase emit yellow and green light of wavelengths between 540-580 nm [Tagami et al., 2009], whereas click beetles or railroad worms are known to send out green to red light [Wood, 1995; Hastings, 1996]. One of the best studied bioluminescent reactions is the enzymatic conversion of luciferin by luciferase in the North American firefly *Photinus pyralis*. In the presence of ATP, Mg^{2+} and oxygen, D-luciferin is decarboxylized over multiple steps under formation of the final product oxyluciferin. This reaction is associated with the emission of light, which is characterized by a broad spectrum (530-640 nm) and a maximum at 562 nm. An overview of the reaction mechanism is shown in **Figure 5.1**.

In the first steps of the reaction, the luciferase-bound luciferin-adenylate is generated, and oxygen is added to the complex. Finally, the elimination of carbon dioxide yields oxyluciferin, which spontaneously decays to the singlet electronically excited singulet state [Day et al., 2004].

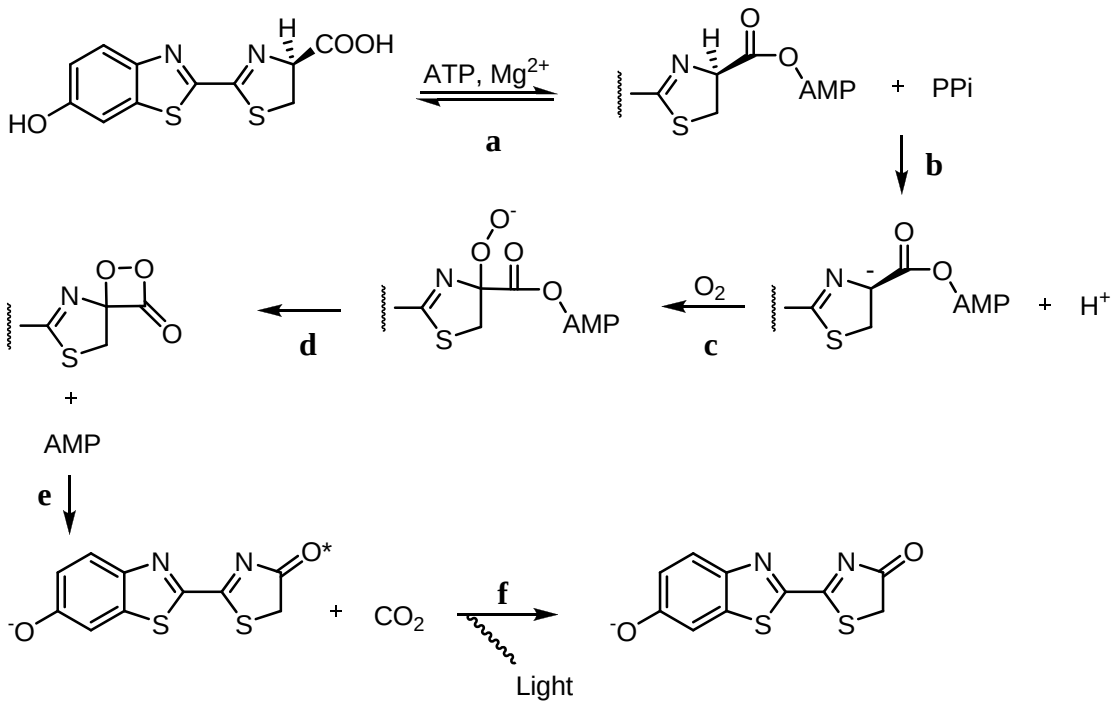

Figure 5.1: Reaction of the firefly luciferase with D-luciferin: (a) generation of luciferase-bound luciferin adenlylate, (b) abstraction of a proton, (c) addition of oxygen, (d) formation of a cyclic peroxide and (e) decarboxylation to the final product oxyluciferin, which emits light upon relaxation from the electronically excited singlet level to the ground state (f); modified from [Day et al., 2004].

5.1.1.2 Bioluminescence imaging in preclinical oncological research

Whereas such bioluminescent reactions were originally used for the quantification of adenosintriphosphate (ATP) in bioanalytical assay systems, their application in preclinical oncological research has become more and more important over the recent years. Thereby, the genetic engineering of tumors cells by introduction of luciferase reporter genes proved to be a powerful technique for the highly sensitive and non-invasive detection of malignancies in vivo.

Several orthotopic tumor models detectable by BLI have been described in literature, including breast cancer bone metastasis [Murray et al., 2003], intraperitoneal neoplasms [Buchhorn et al., 2007] and bladder carcinoma [Pfost et al., 2009].

A very attractive target for bioluminescence in vivo imaging in oncology is the investigation of orthotopic tumors in the brain. The successful application of BLI in monitoring such brain tumors was demonstrated in some reports, indicating the access of D-luciferin to the brain across the blood-brain barrier. For example, in 2002, Vooijs et al. [Vooijs et al., 2002] described a model, which allowed the non-invasive monitoring of tumor progression in pituitary glands of mice by bioluminescence in vivo imaging (BLI). Furthermore, the efficiency of doxorubicin in the chemotherapy of the aforementioned tumors was also monitored by means of BLI. Moriyama et al. performed BLI studies on orthotopic glioblastoma in rats [Moriyama et al., 2004]. For this purpose, 9L rat gliosarcoma cells were transfected with the gene encoding luciferase, before implantation into the brain of female Fischer rats. After intraperitoneal injection of D-luciferin, the tumor development was monitored by BLI, and the efficacy of photodynamic therapy using protoporphyrin IX was visualized.

Thus, there is a broad and permanently growing field of applications of bioluminescence for in vivo imaging. Due to the high sensitivity and specificity of signals, BLI is a very useful technique in preclinical oncological research.

5.1.2 Fluorescence Imaging

5.1.2.1 Fluorescent proteins

Over the recent decades, a great number of various fluorescent proteins has been identified, which turned out to be powerful tools for the visualization of dynamic processes in living animals. Predominantly in preclinical oncologic research, the use of such fluorescent proteins has become indispensable for monitoring cancer dynamics, including inter alia, tumor growth, angiogenesis and metastasis [Hoffman, 2009].

The green fluorescent protein (GFP) of the jellyfish *Aequorea victoria*, a 238 amino acid containing polypeptide, which serves as an energy-transfer acceptor, was the first identified fluorescent protein [Prasher et al., 1992]. In the course of research in this field several gain-of-function mutants of wildtype GFP with enhanced brightness and optimized mammalian expression were generated [Hoffman, 2009]. Cormack et al. [Cormack et al., 1996] constructed a library of GFP mutants in *E. coli* strains, showing a 100-fold increase in the fluorescence intensity detected by flow cytometry. The altered fluorescence properties resulted from strongly shifted excitation maxima and improved protein folding of the mutants in prokaryotes compared to wt GFP. Intensified GFP fluorescence was also obtained by DNA-shuffling methods, which yielded, for instance, mutants with 45-fold higher total cell-associated fluorescence intensities than that of the natural protein [Crameri et al., 1996], even without changes in the excitation and emission spectrum. Improved GFP expression in mammalian cells, mainly in cell types from human origin, was accomplished by multiple base substitutions in the coding-sequence leading to efficient codon usage [Zolotukhin et al., 1996].

In 1999 and 2000, the discoveries of red fluorescent proteins in several reef corals were reported [Matz et al., 1999; Fradkov et al., 2000; Gross et al., 2000]. DsRed, a red-fluorescent protein from *Discosoma sp.*, is characterized by massive brightness, pH-stability as well as resistance against denaturants and photobleaching [Campbell et al., 2002]. Furthermore, by mutations an enhanced version of the red fluorescent protein, referred as DsRed2, was generated, which is more soluble and faster in fluorophor maturation than the parent protein. In search for better red emitting labels, Shaner et al. described a series of new proteins, which were also obtained by mutations of DsRed [Shaner et al., 2004].

Although emission maxima at wavelengths as long as 649 nm are favorable with respect to bioanalytical applications, these proteins are compromised by low quantum yields, resulting in reduced brightness of the fluorescence [Hoffman, 2009].

Quite recently, the isolation of a red fluorescent protein from the sea anemone *Entacmaea quadricolor* allowed the generation of a new bright protein, named Katushka, emitting far-red light [Shcherbo et al., 2007]. For this purpose, the natural protein was modified with respect to increased velocity of fluorophore maturation, pH-stability and brightness. These modifications yielded the red fluorescent protein TurboRFP [Merzlyak et al., 2007], which served as a starting point for the generation of Katushka by performing multiple cycles of random mutagenesis. Katushka was proven to possess excellent properties for whole body imaging with an excitation peak at 588 nm and an emission maximum at 635 nm. Furthermore, rapid fluorophor maturation (20 min), an extinction coefficient of 65,000 M^{-1} cm^{-1} and a quantum yield of 0.34 render Katushka the most promising red fluorescent protein for fluorescence imaging applications up to now. However, the labeling of cellular proteins by Katushka is compromised due to its dimeric structure. For this reason, a monomeric version of TurboRFP (called TagRFP) was generated [Merzlyak et al., 2007]. In addition, modifications of TagRFP yielded the monomeric version of Katushka, termed mKate [Shcherbo et al., 2007].

5.1.2.2 Fluorescent proteins in preclinical oncology

In preclinical oncology, the great number of available fluorescent proteins with different properties enables the monitoring of multiple processes during cancer development. Already in 1997, Chishima et al. [Chishima et al., 1997] described the visualization of cancer invasion and micrometastases in live tissue by using CHO-cells, genetically engineered to stably express the green fluorescent protein [Chishima et al., 1997]. The transfectants were subcutaneously injected into nude mice, and small pieces of s.c. growing tumors were used for the orthotopic implantation into the ovary of nude mice. After 4 weeks, the animals were killed, and micrometastases were microscopically detected in different organs due to GFP fluorescence. As an advancement, noninvasive imaging of GFP-expressing B16F0 mouse melanoma tumors and AC3488 human colon cancer as well as metastases in live mice was performed by Yang et al. [Yang et al., 2000].

With respect to noninvasive whole-body imaging, the spectral properties of fluorescent proteins are the key. Due to the fact that longer excitation wavelengths cause fewer damages in cellular proteins as well as in DNA, and that the absorbance of emitted light by tissues, containing biomolecules such as hemoglobin, is also less pronounced at longer wavelengths, whole-body imaging can be improved by using red fluorescent proteins [Hoffman, 2009]. The successful application of DsRed2 for in vivo imaging has been demonstrated in several cases [Katz et al., 2004; Bouvet et al., 2005; Jarzyna, 2007]. In contrast, so far, only few reports exist on the application of the promising far-red protein Katushka for visualization of cancer processes in vivo.

A rather new application of fluorescent proteins in cancer research is the so-called color-coded fluorescence imaging, which offers the potential of monitoring tumor-host interactions. Tumor cells, which express a complementary fluorescent protein are implanted into transgenic nude mice , which expresses either a green or red fluorescent protein in all cells or specific cell types [Hoffman and Yang, 2006]. Moreover, many other applications, for example investigations on tumor angiogenesis [Amoh et al., 2008] or studies on the tumor's microenvironment [Yang et al., 2009], become feasible by color-coded fluorescence imaging.

Taken together, fluorescent proteins proved to be valuable tools for the visualization of cancer dynamics in vivo, including tumor growth, metastasis or angiogenesis. The recent discovery of bright red-shifted proteins, in particular Katushka, appears promising for whole-body imaging, since limitations of proteins emitting at shorter wavelength, such as the depth of tissue penetration and light absorbance by physiologically present molecules, can be overcome.

5.2 Objective

The objective of this central part of the thesis was to refine an already existing orthotopic human glioblastoma model in nude mice with regard to noninvasive monitoring by optical imaging. For this purpose, the human glioblastoma cell lines U-87 MG and U-373 MG were (co-) transfected with the genes encoding an enhanced version of the firefly luciferase (luc2) and the recently discovered far-red emitting protein Katushka, respectively. A prerequisite for studies in animals was the in vitro characterization of the transfectants with respect to luc2 / Katushka protein expression, growth kinetics and chemosensitivity. The most promising transfectants had to be examined in a subcutaneous tumor model in nude mice concerning tumorigenicity and the stability of luc2 / Katushka expression. To establish a new orthotopic brain tumor model, the transfected malignant human glioblastoma cells U-87 Luc2 / U-87 Katushka were implanted intracerebrally into nude mice to monitor tumor progression. In addition, the advantages and limitations of both techniques, namely BLI and FLI, should be comparatively evaluated by orthotopically implanting U-87 Luc2 / Katushka co-transfectants into the brain of nude mice.

5.3 Materials and methods

5.3.1 Drugs and chemicals

Water, used for the preparation of drug solutions and culture media, was purified by a Milli-Q system (Millipore, Eschborn, Germany). The selection antibiotics ampicillin sodium (Sigma, Deisenhofen, Germany), puromycin·2HCl (Sigma, Deisenhofen, Germany) and geniticin disulfate (G418, Biochrom AG, Berlin, Germany) were dissolved in water to achieve concentrations of 100 mg/mL (ampicillin sodium), 1 mg/mL (puromycin·2HCl) and 150 mg/mL or 300 mg/mL (G418). The stocks were stored at -20 °C. D-luciferin potassium salt was purchased from Molecular Imaging Products Company, Ann Arbor, MI, USA and SYNCHEM OHG, Felsberg/Altenburg, Germany. For in vivo imaging experiments, 40 mg of D-luciferin potassium salt were dissolved in 1 mL of PBS (8.0 g/L NaCl, 1.0 g/L $Na_2HPO_4 \cdot 2 H_2O$, 0.20 g/L KCl, 0.20 g/L KH_2PO_4, 0.15 g/L $NaH_2PO_4 \cdot H_2O$; all chemicals for buffer preparation were purchased from Merck, Darmstadt, Germany). The solution was sterile filtered and aliquoted into autoclaved Eppendorf reaction vessels (Eppendorf, Hamburg, Germany). All preparations of D-luciferin were stored light-protected at -80 °C.

5.3.2 Luria Bertani (LB) media, selective agar plates and SOC media

For the preparation of LB media, 10 g of bacto tryptone (Difco, Detroit, USA), 5 g of yeast extract (Roth, Karlsruhe, Germany) and 5 g of sodium chloride (Merck, Darmstadt, Germany) were dissolved in 1000 mL of millipore water. The pH value was adjusted to 7.5 by drop-wise addition of 1 M NaOH. Subsequently, the medium was autoclaved at 121 °C / 2 bar for 20 min. 100 µL of ampicillin stock solution (100 mg/mL) were added to 100 mL of sterile Luria Bertani medium. All media were stored at 4 °C and used at most for 2 weeks. Selective agar plates were prepared by dissolving 7.5 g of agar (Roth, Karlsruhe, Germany) in 500 mL of heated, sterile LB medium under continuous stirring. Subsequently, the solution was autoclaved and transferred into a tempered water bath (55 °C) for 30 min. Finally, 100 µL of ampicillin stock solution (100 mg/mL) were added to the medium, and agar plates were casted under sterile conditions. The plates were stored at 4 °C and used for a maximum of 4 weeks.

SOC medium for transformation procedures, derived from Super Optimal Broth (SOB), was prepared by dissolving 0.25 g of yeast extract and 1.00 g of bacto tryptone in approximately 35 mL of millipore water. Subsequently, 1 mL of a 0.5 M NaCl stock solution, 1 mL of a 0.125 M KCl stock, 1 mL of 0.5 M $MgCl_2 \cdot 6\ H_2O$ solution and 1 mL of a 0.5 M $MgSO_4 \cdot 7\ H_2O$ stock were appended to the dissolved yeast extract / bacto tryptone, and the resulting solution was autoclaved. After cooling down, 1 mL of a sterile-filtered 1 M glucose monohydrate stock was added to the medium, and the volume was adjusted to 50 mL by using sterile-filtered millipore water.

5.3.3 Cell culture

The human glioblastoma cell lines U-87 MG and U-373 MG were purchased from the American Type Culture Collection (ATTC, Rockville, MD, USA). Wildtype cells were grown in Eagle's Minimum Essential Medium (EMEM, Sigma, Munich, Germany) containing 2.2 g/L $NaHCO_3$, 110 mg/L sodium pyruvate, L-glutamine and 5 % fetal calf serum (FCS, Biochrom AG, Berlin, Germany).

Mono-transfectants, expressing luciferase2, were maintained in the aforementioned medium supplemented with puromycin· 2 HCl at a final concentration of 1 µg/mL.

U-87 MG and U-373 MG cells, which were transfected with the genes encoding the red fluorescent proteins DsRed2 and Katushka, respectively, were cultured in Eagle's Minimum Essential Medium supplemented with 5 % fetal calf serum and 750 µg/mL of G418.

Luciferase2 and DsRed2 / Katushka co-transfected human glioblastoma cells were grown in EMEM supplemented with 5 % FCS. With respect to exertion of selection pressure, puromycin·2 HCl (final concentration 1 µg/mL) and G418 (final concentration 750 µg/mL) were added to the culture medium.

All cells were cultured in a water-saturated atmosphere of 37 °C / 5 % CO_2 and routinely screened by PCR for *Mycoplasma* contamination using the VenorGEM™ detection kit from Minerva Biolab, Berlin, Germany. For all in vitro and in vivo investigations, only *Mycoplasma*-free cell cultures were used.

5.3.4 Amplification and purification of plasmid DNA

5.3.4.1 The pGL4.20 (luc2/puro), pDsRed2-C1 and pTurboFP635-N vectors (Figure 5.2)

As a shuttle vector, the pGL4.20 plasmid (Promega, Mannheim, Germany) bears the gene encoding the codon optimized firefly luciferase2 (from *Photinus pyralis*) for expression in mammalian cells and a gene for a prokaryotic (ampicillin) as well as for a mammalian (puromycin) selection marker. According to the providers manual, the pGL4 vectors also show a reduced background and risk of expression artifacts by the removal of several cryptic DNA regulatory elements as well as transcription factor binding sites [Promega, 2004-2007].

The purified plasmid DNA of pDsred2-C1 (BD Bioscience Clontech, Heidelberg, Germany) was a kind gift from ACGT ProGenomics (Halle a. d. Saale, Germany). The vector contains the gene which encodes the enhanced version of the red fluorescent protein DsRed, namely DsRed2. Plasmid amplification in prokaryotic cells is enabled by kanamycin selection, whereas stable mammalian tranfectants are identified by G418 resistance.

The pTurboFP635-N vector (BioCat, Heidelberg, Germany) is a mammalian expression vector bearing the gene encoding for the far-red fluorescent protein Katushka and the DNA sequences for G418 and kanamycin resistance [Evrogen].

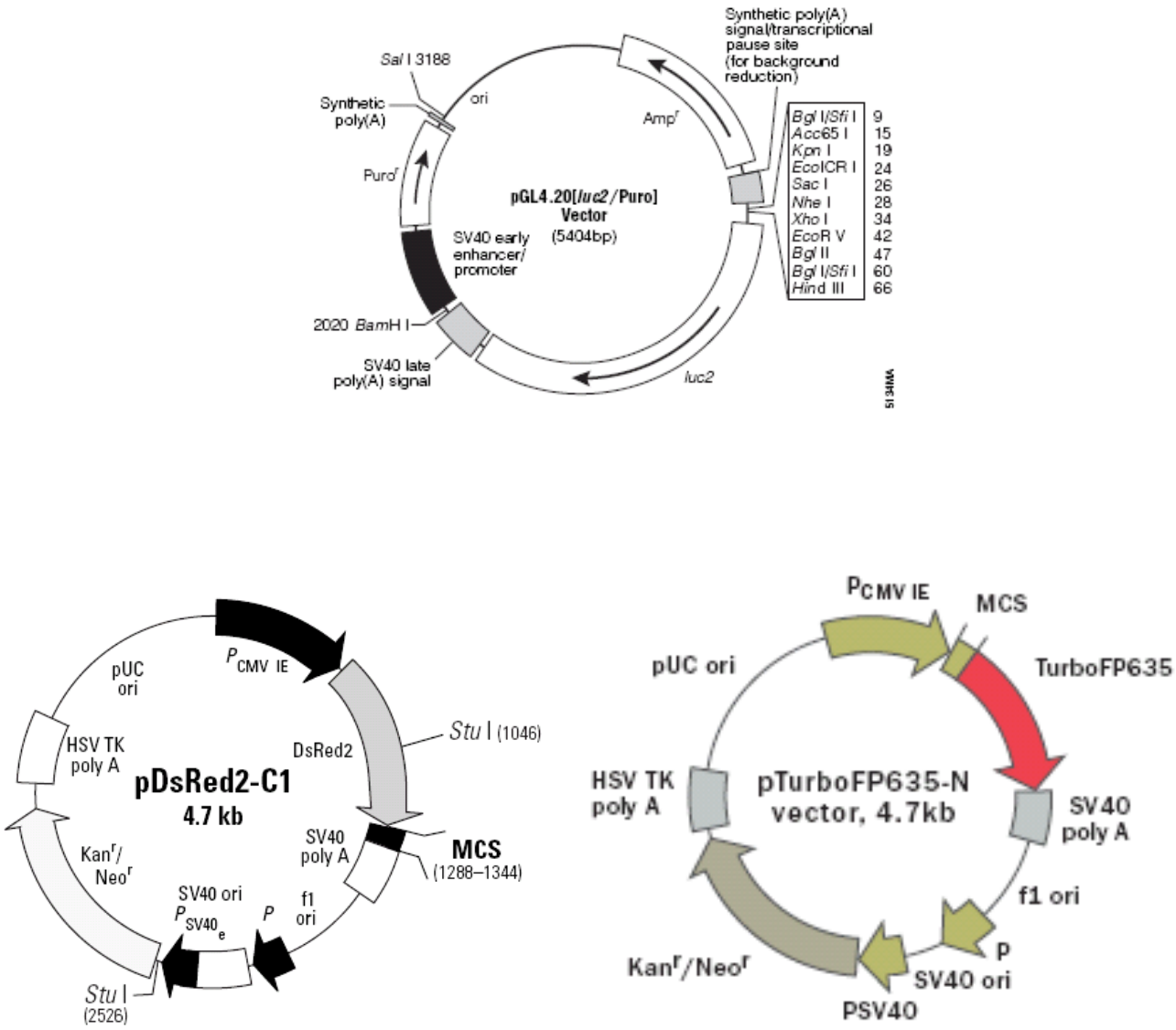

Figure 5.2: Maps of pGL4.20 (luc2/puro), pDsRed2-C1 and pTurboFP635-N vectors

5.3.4.2 Transformation of competent *E. coli* cells

pGL4.20, pDsRed2-C1 and pTurboFP635-N plasmids were amplified via transformation in competent *E. Coli TOP10* cells. Therefore, frozen competent *E. coli* cells were thawed and immediately transferred on ice. After a period of 10 min, 5 µL of plasmid DNA (2 ng/µL) were added to 100 µL of the bacterial cell suspension. Subsequently, the mixture was incubated on ice for 30 min and heat shocked to 42 °C for a period of exactly 60 s. The suspension was incubated on ice for another 3 min. After the addition of 900 µL of sterile SOC medium, the mixture was shaken (200 rpm) at 37 °C for 1 h.

Finally, 100 µL of the suspension were streaked on ampicillin (100 µg/mL) or kanamycin selective (30 µg/mL) agar-plates and incubated at 37 °C overnight. The remaining cell suspension was used to concentrate the bacteria for a second preparation. Therefore, the bacteria were centrifuged at 3,000 rpm for 5 min and 800 µL of the supernatant were carefully removed by suction. Subsequently, the cell pellet was resuspended in the residual medium, transferred on the selective agar plates and also incubated at 37 °C overnight. The next day, resistant colonies had formed, which were used for large scale preparations of the DNA.

5.3.4.3 Maxi-preparation (Maxi-Prep) of plasmid DNA

With respect to large scale alkaline lysis for isolation of plasmid DNA, 250 mL of sterile and selective LB medium (ampicillin or kanamycin) were transferred into an autoclaved 1000 mL Erlenmeyer flask. Subsequently, the medium was inoculated with resistant colonies from the selective agar plates and incubated at 37 °C overnight, while shaking the flask at 200 rpm. The next day, maxi-preparation was performed using a Qiagen Plasmid Purification Kit (Quiagen, Hilden, Germany) according to the manufacturer's instructions.

In brief: 200 mL of the overnight culture were centrifuged at 4 °C and 6,000 rpm for 15 min. The supernatant was carefully removed, and the pellet was efficiently resuspended in 10 mL of resuspension buffer P1 (50 mM Tris · Cl, pH 8.0; 10 mM EDTA; 100 µg/mL RNase A, LyseBlue reagent (provides visual identification of exhaustive mixture)). 10 mL of lysis buffer P2 (200 mM NaOH, 1 % SDS (w/v)) were added to the mixture and the suspension was vigorously shaken up to the appearance of a homogenous blue-colored batch.

5 min after incubation at room temperature, 10 mL of pre-chilled neutralization buffer P3 (3.0 M potassium acetate, pH 5.5) were added to the mixture, and the homogenized suspension was incubated on ice for 20 min. Thereby, a fluffy white material containing genomic DNA, proteins and cell debris, became visible. Afterwards, the lysate was centrifuged at 4 °C and 11,500 rpm for 30 min. The supernatant, containing the plasmid DNA, was removed and centrifuged at 4 °C and 11,500 rpm for another 15 min to eliminate residual lysate. After equilibration of the Qiagen-tip by addition of 10 mL of equilibration buffer QBT (750 mM NaCl; 50 mM MOPS, pH 7.0; 15 % isopropyl alcohol (v/v); 0.15 % Triton® X-100 (v/v)), the plasmid containing supernatant was applied to the tip. Subsequently, the plasmid DNA was rinsed twice with washing buffer QC (1.0 M NaCl; 50 mM MOPS, pH 7.0; 15 % isopropyl alcohol (v/v)) and finally eluted from the tip by using 15 mL of elution buffer QF (1.25 M NaCl; 50 mM Tris · Cl, pH 8.5; 15 % isopropyl alcohol (v/v)). After precipitation of DNA by the addition of isopropyl alcohol, the pellet was immediately washed with 70 % ethanol. The air-dried DNA pellet was re-dissolved in Millipore water, and the DNA concentrations as well as the purity were determined photometrically: a 1:70 dilution of Maxi-Prep DNA was prepared, and the absorbance was determined at 260 and 280 nm, respectively. Finally, the DNA concentration was calculated using the following equation:

$$C\,[\mu g / mL] = (70 \cdot A_{260} - 40 \cdot A_{280}) \cdot df$$

, where df is the dilution factor of investigated DNA solution, A_{260} the absorbance measured at 260 nm and A_{280} the absorbance detected at 280 nm at a path length of 1 cm. Preparations with an A_{260}/A_{280} quotient > 1.3 were considered to have a sufficient purity. The identification of plasmid DNA was carried out by sequencing by Entelechon, Regensburg, Germany.

5.3.5 Stable transfection of U-87 MG and U-373 MG glioblastoma cells

The transfection of U-87 MG and U-373 MG wildtype cells with pGL4.20 (luc2/puro) as well as co-transfection experiments of the aforementioned glioblastoma cells with pGL4.20 and pDsRed2-C1 were performed in passage 138 and 193, respectively.

For experiments using the far-red protein Katushka, U-87 MG and U-373 MG cells were transfected with pTurboFP635-N in passage 169 and 223, respectively.

The co-transfection of U-87 MG and U-373 MG with the genes encoding luc2 and Katushka was performed by transfecting the stably expressing transfectants U-87 Luc2_Clone 3 (passage 10) and U-373 Luc2_Clone 5 (passage 10) with pTurboFP635-N. All experiments were carried out with the transfection reagent FUGENE® HD (Roche Diagnostics GmbH, Mannheim, Germany) according to the manufacturer's instruction.

In brief: cells (confluency: approximately 80 %) were seeded into 24-well plates in a total volume of 500 µL of culture medium (EMEM plus 5 % FCS) for transfection. On the eve of experiments, serum-free EMEM was transferred into pyrogen-, DNAase- and RNAase-free reaction vessels in order to prepare DNA dilutions with a concentration of 2 µg of DNA / 100 µL. In case of co-transfection, using pGL4.20 (luc2/puro) and pDsRed2-C1, the total amount of plasmid DNA was the same as used in single transfection experiments.

Subsequently, 3, 6 and 9 µL of FUGENE® HD were added per 100 µL of the DNA solution, respectively. The mixtures were homogenized and incubated for 15 min at room temperature. Afterwards, 25 µL of the transfection complex were added drop-wise to each well, and the plates were carefully shaken to ensure a homogenous distribution. 3 wells for each FUGENE® HD / DNA ratio were incubated with the transfection mixture. After 48 h of incubation at 37 °C / 5 % CO_2, the supernatant was removed by suction, and cells were detached from the surface by short trypsinization. The triplicates of equivalent FUGENE® HD transfection reagent/DNA ratios were pooled and transferred into 12.5-cm² culture flasks (BD, Heidelberg, Germany) containing EMEM, supplemented with 5 % FCS and the respective selection antibiotic (puromycin·2HCl, G418 or a combination of both compounds). As a control, U-87 MG and U-373 MG wildtype cells were cultured in the presence of equal concentrations of the antibiotics to verify the selection of transfected cells by resistance against puromycin and G418, respectively. The selective culture media were removed every 3-7 days by suction and replaced by fresh one. Over a period of 2-4 weeks, several resistant colonies of transfected cells had grown, whereas wildtype cells were killed by the antibiotics. After short trypsinization, parts of several colonies were picked and transferred into 1 well of a 24-well plate, which contained EMEM plus 5 % FCS, supplemented with the appropriate selection antibiotic. Having reached adequate confluency, the cells were expanded by up-scaling in 75-cm² flasks. Thereafter, the cells were aliquotted, cryopreserved and stored in liquid nitrogen for further characterization.

5.3.6 Crystal violet assays

5.3.6.1 Chemosensitivity assays

Crystal violet chemosensitivity assays [Bernhardt et al., 1992] were performed as described elsewhere (chapters 3 and 4).

5.3.6.2 Growth kinetic assays

For the characterization of in vitro growth kinetics of different cell lines, including several transfectants, the aforementioned crystal violet chemosensitivity assay was slightly modified. For this purpose, the tumor cell suspensions were seeded into 96-well plates at a total volume of 200 µL/well and stored in the incubator (37 °C / 5 % CO_2) for various times. Afterwards the cells were treated according to the protocol [Bernhardt et al., 1992] and the absorbance was determined at 580 nm on a Tecan GENios Pro microplate reader. Finally, the obtained absorbance values were plotted against the period of cell growth.

5.3.7 Characterization of luciferase2 expression in vitro

5.3.7.1 Assay procedure using cell lysates

Tumor cells were detached from the culture flasks, resuspended in the appropriate culture medium and finally seeded into 24-well plates in a total volume of 500 µL for each well. Afterwards, the cells were allowed to grow at 37 °C / 5 % CO_2 for approximately 48 h to reach a confluency of 80-100 %. Subsequently, the supernatant was removed by suction, and cells were washed with phosphate buffered saline in order to get rid of phenol red from the culture medium. Depending on the cell density, 60-200 µL of lysis buffer (25 mM Tricine™ (N-[2-hydroxy-1,1-bis(hydroxymethyl)ethyl]glycine; pH 7.8; Sigma); 10 % (v/v) glycerol (Merck, Darmstadt, Germany); 2 mM ethyleneglycoltetraacetic acid (EGTA) (Merck, Darmstadt, Germany); 1 % (v/v) Triton™ X-100 (Serva, Heidelberg, Germany); 5 mM $MgSO_4 \cdot 7\ H_2O$ (Merck, Darmstadt, Germany), 1 mM dithiotreitol (DTT; Sigma, Munich, Germany)) were added to each well and incubated for 20 min, while slightly shaking the microtiter plates. 30 µL of the lysate were transferred into polystyrene tubes (Sarstedt, Nümbrecht, Germany).

The tube was placed into a Lumat LB 9501 luminometer (Berthold, Bad Wildbad, Germany) and 100 µL of a 0.2 mg/mL D-luciferin solution in assay buffer (25 mM Tricine™ (pH 7.8); 5 mM $MgSO_4 \cdot 7H_2O$; 2 mM EGTA; 2 mM ATP (Boehringer, Mannheim, Germany); 50 µM or 100 µM coenzyme A were added (CoA; Sigma, Munich, Germany), when indicated) were automatically injected into the solution. D-luciferin was stored as stocks at -80 °C with a concentration of 10 mg/mL in 25 mM tricine buffer (pH 7.8), supplemented with 10 mM DTT. Over a period of 10 s the photon counts of the bioluminescent reaction were integrated and values were expressed as RLU (relative light units).

5.3.7.2 Normalization of luminescence to protein concentration (Bradford)

The RLUs of each sample were normalized to the total protein content, which was determined according to the method of Bradford [Bradford, 1976]. Therefore, 5 µL of the cell lysate were added to 95 µL of lysis buffer and incubated with 1000 µL of Bradford´s dye reagent (Bio Rad Laboratories, Munich, Germany) for 10 min. Afterwards, the absorption at 595 nm was determined with an Uvikon 930 spectrophotometer (Kontron, Düsseldorf, Germany). The corresponding protein contents were calculated from a standard calibration curve using human serum albumin (HSA; Behringwerke, Marburg, Germany), which was dissolved in lysis buffer to compensate for matrix effects. The corrected RLU values were expressed as relative light units per µg of protein ($RLU/\mu g_{Protein}$).

5.3.7.3 Determination of luciferase2 activity in living cells in microtiter plates

For the evaluation of luciferase2 activity in living cells, a microtiter plate-based assay, was established according to the following procedure: cells were detached from the culture flask by short trypsinization and resuspended in culture medium. The tumor cell suspensions were transferred into 10-mL Falcon™ tubes (BD, Heidelberg, Germany) and centrifuged at 1200 rpm for 3 min using a Minifuge T centrifuge from Heraeus Instruments GmbH (Hanau, Germany). Subsequently, the supernatant was discarded, and cells were washed with phenolred- and serum-free EMEM (Biochrom AG, Berlin, Germany) to minimize interference with the luminescence measurements. To investigate the correlation between the cell number and the photon count, a dilution series of the tumor cells was prepared in phenolred- and FCS-free medium. Afterwards, 150 µL of the cell suspensions were pipetted into each well of a totally black Nunclon™ 96-well plate (Nunc, Langenselbold, Germany), and the cells were allowed to attach to the surface of the plates at 37 °C / 5 % CO_2 for at least 1 h.

On the eve of experiments, 50 µL of a D-luciferin solution in PBS (prepared by the dilution of 100 µL D-luciferin stock solution (40 mg/mL in PBS) with 5900 µL of phosphate buffered saline) were added to each well of the microtiter plates. After 5 min of incubation, the microtiter plates were imaged with the Andor EMCCD camera DV887 ECS-BV (cooled down to -89 °C). The instrument and camera settings (stage height, exposure time, electron multiplying gain etc.) are described in the legends of the corresponding figures.

5.3.8 Determination of DsRed2 and Katushka fluorescence in vitro

5.3.8.1 Fluorescence microscopy

Fluorescence detection in living human glioblastoma cells, genetically modified to express the DsRed2 or the Katushka protein, was performed on a Leica DM-IRB microscope (Texas Red filter cube; exc. 560/40 nm, em. 645/75 nm) and a Carl Zeiss Cell Observer (Zeiss, Munich, Germany; Zeiss filter set *No. 43* (excitation wavelength 545/25 nm; FT 570; emission wavelength 605/70 nm)), respectively.

5.3.8.2 Fluorescence detection by the means of a microtiter plate reader and the Maestro™ imaging system

For quantification of fluoresecence emitted by Katushka-expressing cells, a microtiter assay was established according to the following protocol: after trypsinization, the cells were resuspended in culture medium and immediately centrifuged at 20 °C and 1500 rpm for 5 min, using a Minifuge T centrifuge from Heraeus Instruments GmbH (Hanau, Germany). The supernatant was removed, and cells were washed twice with phenolred- and serum-free culture medium.

Subsequently, the cell number was adjusted by resuspension of the cell pellet in an appropriate volume of EMEM, without phenolred and FCS. 150 µL of the tumor cell suspension were transferred into each well of a flat-bottomed polystyrene 96-well plate (sterile, F-Bottom, with lid, Cat.-No.655 180, Greiner, Frickenhausen, Germany). Afterwards, the plates were stored at 37 °C and 5 % CO_2 for approximately 2 h allowing the cells to adhere to the surface.

The relative fluorescence intensities were recorded with a Tecan GENios Pro microtiter plate reader (settings: measurement mode: fluorescence top; excitation wavelength: 580/10 nm; emission wavelength: 670/20 nm; number of reads: 5; integration time: 40 µs; lag-time: 0 µs; mirror selection: automatic; plate definition file: GRE96ft.pdf; multiple-reads per well (circle): 4 x 4; time between move and flash: 50 ms).

To explore the sensitivity of the Maestro™ in vivo imaging system, the same procedure as described for the plate reader was pursued. However, instead of clear 96-well plates, the cells were seeded into black microtiter plates with clear and flat bottoms (µclear®; Greiner, Frickenhausen, Germany). The filter settings for the fluorescence of DsRed2 and Katushka-expressing cells were as follows: excitation 503-555 nm; emission 580 nm cut off; for further instrument settings (stage height, exposure time etc.) see legends to the respective figures.

5.3.9 Installation of a laboratory for in vivo imaging and in vivo experiments

5.3.9.1 Laboratory for in vivo imaging

Fluorescence in vivo imaging (FLI) studies were performed with a Maestro™ (500 FL system, wavelength range from 500-950 nm) according to the instructions of the user manual (Cambridge Research and Instrumentation, Inc., Maestro™, Revision 1.2.6). Bioluminescence in vivo imaging (BLI) studies were carried out by adaptation of the commercial Maestro™ system, i.e. exchanging the liquid crystal tunable filter camera from CRI™ with an Andor™ DV887 ECS-BV EMCCD camera. All devices are explained in detail in the doctoral thesis of Peter Jarzyna [Jarzyna, 2007].

This highly sensitive back-illuminated camera uses electron multiplying technology and is cooled down to -89 °C. The extremely high sensitivity of EMCCD cameras makes the detection of specific photon emission prone to any kind of stray light from external sources (e. g. daylight, illuminants such as LED's etc.). For this reason, the Maestro™ system was further modified, to exclude extraneous light (**Figure 5.4**) and placed in a specially devised dark room (**Figure 5.3**)

Figure 5.3: In vivo imaging laboratory. a) Dark room equipped with the tailor-made Maestro™ system (black arrow) suited for macroscopic fluorescence / bioluminescence imaging, the fluorescence camera system for microscopy studies (red arrow), the EMCCD camera Andor™ DV887 ECS-BV (green arrow) and a circulation thermostat to cool the Peltier element of the EMCCD (blue arrow); b) Blinds for laboratory door to prevent incident light.

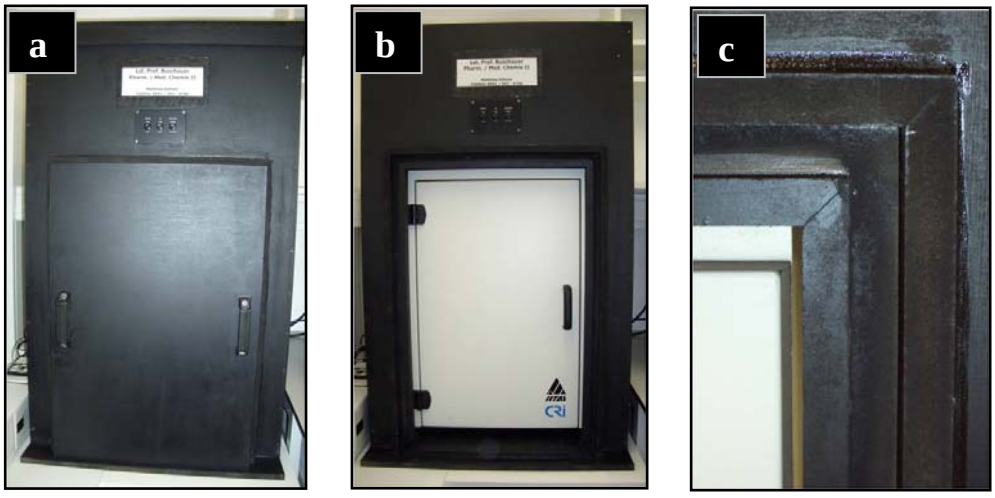

Figure 5.4: Dark box to shield the imaging device from extraneous light. Front view of the closed (a) and opened (b) dark box, detail showing overlapping edges (c) and top view of the integrated Maestro™ system, equipped with the Andor™ EMCCD camera (d).

5.3.9.2 Implantation of human glioblastoma cells into nude mice

5.3.9.2.1 Subcutaneous tumors

The procedure was performed according to the method described in chapter 4 ("Animals, husbandry and feeding").

5.3.9.2.2 Intracerebral tumors

To investigate the growth characteristics of human glioblastoma transfectants in the brain of nude mice, genetically modified U-87 cells cells were prepared in vitro as described above. After washing twice with FCS-free EMEM, the cell pellet was resuspended in serum-free culture medium, and the cell number was adjusted to $5 \cdot 10^4$ per 10 µL. For the orthotopic implantation, the animals were anesthetized as described in Chapter 4. The parietal bone was drilled through with a 1-mm diameter bit, 3 mm on the right-hand side of the sagittal suture and 3 mm rostral of the coronal suture. Tumor cell suspensions were carefully homogenized and 10 µL containing 50,000 cells were injected 3 mm deep into the brain tissue by using a Hamilton syringe with a blunt tip. Finally, a surgical clamp was used to close the skin wound and the pads of the mice were labeled by tattooing.

Figure 5.5 shows the various steps of the orthotopic transplantation procedure.

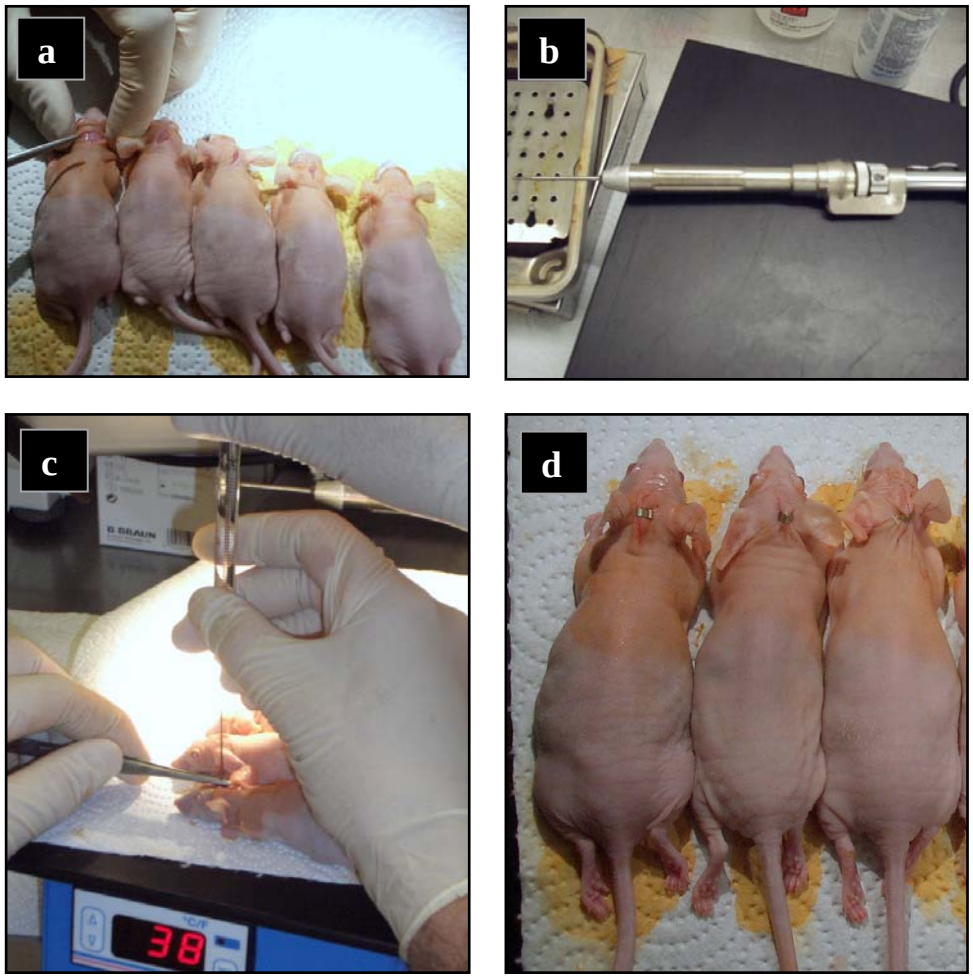

Figure 5.5: Orthotopic implantation of human glioblastoma cells into the brain of nude mice. Mice were placed on a heated stage to prevent a decline of body temperature during anesthesia. Skin incision and position of the drill (a); diamante drill for parietal bone perforation (b); injection of tumor cell suspension via a Hamilton syringe (c); wound closure with surgical clamps (d).

5.3.9.2.3 Bioluminescence imaging (BLI) of subcutaneous and orthotopic glioblastoma in nude mice

Prior to each bioluminescence imaging (BLI) experiment, the specimen stage was heated to 39.5 °C in order to achieve a desired temperature of 37 °C on the surface of the table. The mice were anesthetized by intraperitoneal injection of 30-50 µL of the aforementioned mixture containing ketamine and xylazine. According to the body weight (25-40 g) of the nude mice anesthesia persisted for 20-50 min.

For imaging of subcutaneous tumors, 100 µL of freshly thawed D-luciferin solution (40 mg/mL in sterile PBS) were injected intraperitoneally. For BLI measurements of orthotopic human glioblastoma, surgical clamps were removed from the animals, and 200 µL of the D-luciferin solution, containing 8 mg of D-luciferin, were injected i.p.. After a period of 5 min, the mice were positioned on the heated stage and emitted photon counts were integrated (instrument settings are given in the figure legends). Analysis of the data was performed with the "Andor Solis imaging software 4.3".

5.3.9.2.4 Fluorescence imaging (FLI) of subcutaneous and orthotopic glioblastoma

The specimen stage was heated to 39.5 C, and mice were anesthetized (see **5.3.9.2.3**). Subsequently, the animals were placed on the table and fluorescence imaging was performed with the Maestro™ device (500 FL system with a wavelength range of 500-950 nm). Used filters as well as further instrument settings (stage height, exposure time etc.) are given the respective paragraphs. Data analysis was carried out with the "Maestro Software 2.6.0B".

5.3.10 Histology

Histological paraffin sections of tumor tissues and organs were prepared according to the procedure by Walter et al. [Walter et al., 2000] with various modifications. Animals were killed by cervical dislocation, and tissue were excised and dissected. For a period of at least 3 days, the tumors and / or organ samples were fixed at room temperature in Bouin's solution containing picric acid, formaldehyde and acetic acid. After washing with phosphate buffered saline, tissues were dehydrated by using a Histokinette Shandon Processor 2LE (Frankfurt am Main, Germany). Dehydration was performed by an ascending isopropyl alcohol series at room temperature. Thereafter, the specimen were placed in paraffin Paraplast X-tra® (Sherwood Medical, Roth GmbH, Karlsruhe, Germany) and left at 50-54 °C for 4 h (4 times). Finally, the tissues were embedded in Paraplast®, cut into 6 µm-thick sections by using a Leica Microtome RM2255 (Leica, Bensheim, Germany) and transferred on poly-L-lysine (Sigma)-coated glass slides. For staining, the sections were deparaffinized with xylene and rehydrated by means of descending alcohol series. Haematoxylin-Eosin (HE) staining was performed according to the procedure by Romeis [Romeis, 1989]. Alternatively, the samples were stained by the method of Masson-Goldner

5.4. Results

5.4.1 Determination of the required concentrations of selection antibiotics G418, hygromycin and puromycin

As a prerequisite for the identification of human U-87 MG and U-373 MG glioblastoma cells, transfected with the pGL4.20, pDsRed2-C1 and pTurboFP635-N vectors, the chemosensitivity against eukaryotic selection markers G418, puromycin and hygromycin was investigated in the crystal violet chemosensitivity assay.

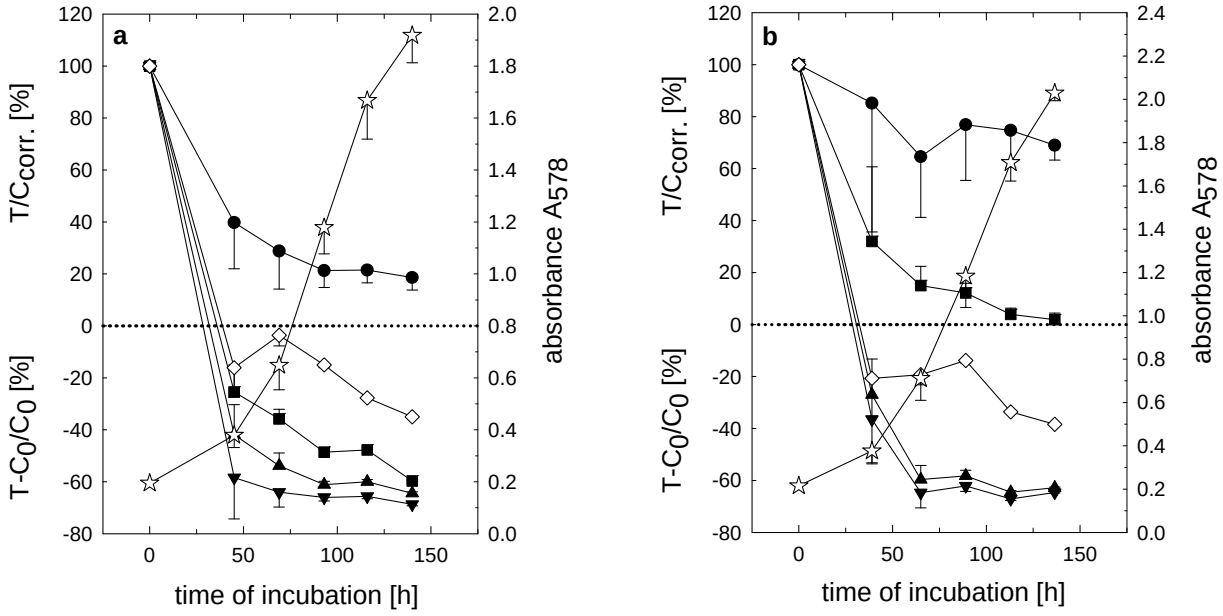

Figure 5.6: Effect of G418 on proliferating U-87 MG wildtype cells (a), 137th passage, and U-373 MG wiltype cells (b), 250th passage.

Cells were incubated with G418 at concentrations of: 50 µg/mL (filled circles), 250 µg/mL (filled squares), 750 µg/mL (filled triangles) and 1500 µg/mL (filled inverted triangles). As a control, both cell lines were incubated with the vehicle water (open stars) and 10 nM of vinblastin (open diamonds).

As becomes obvious from **Figure 5.6**, G418 showed comparable cytotoxicity at the highest concentrations tested (750 and 1500 µg/mL) against both glioblastoma variants.

The same holds for puromycin ·2HCl at concentrations of 0.75 µg/mL and 1.5 µg/mL (**Figure 5.7**).

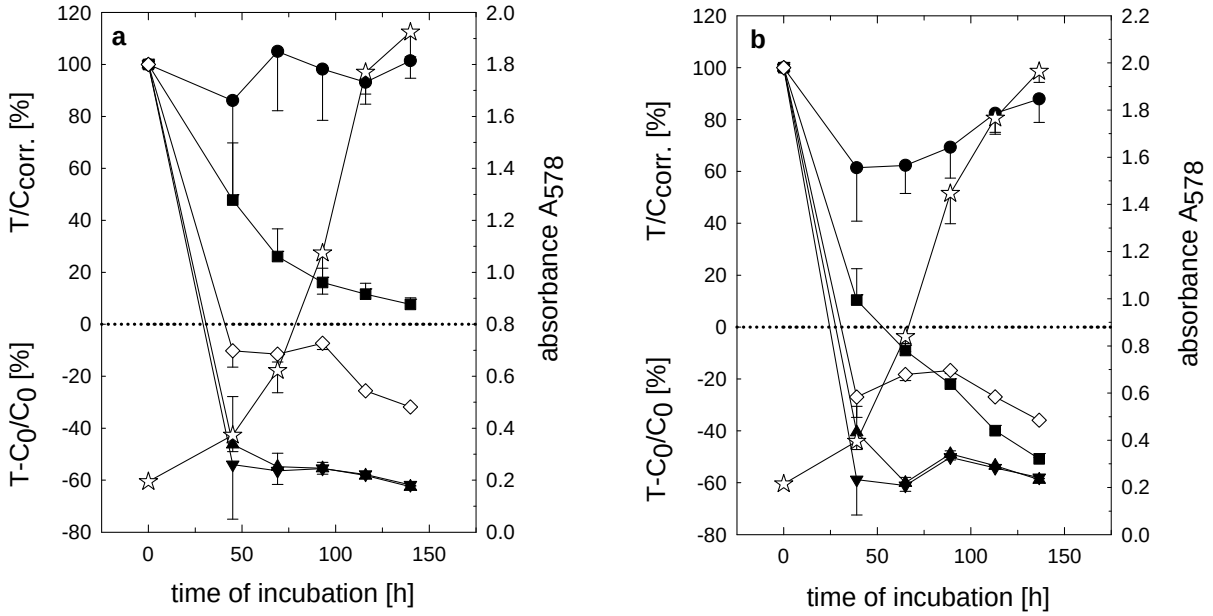

Figure 5.7: Effect of puromycin·2HCl on proliferating U-87 MG wildtype cells (a), 137th passage, and U-373 MG wildtype cells (b), 250th passage.

Cells were incubated with puromycin·2HCl at concentrations of: 0.05 µg/mL (filled circles), 0.25 µg/mL (filled squares), 0.75 µg/mL (filled triangles) and 1.5 µg/mL (filled inverted triangles). As a control, both cell lines were incubated with the vehicle water (open stars) and 10 nM of vinblastin (open diamonds).

Hygromicin at a concentration of 800 µg/mL caused comparable cytocidal effects on both, U-87 MG wildtype and U-373 MG wildtype cells (**Figure 5.8**).

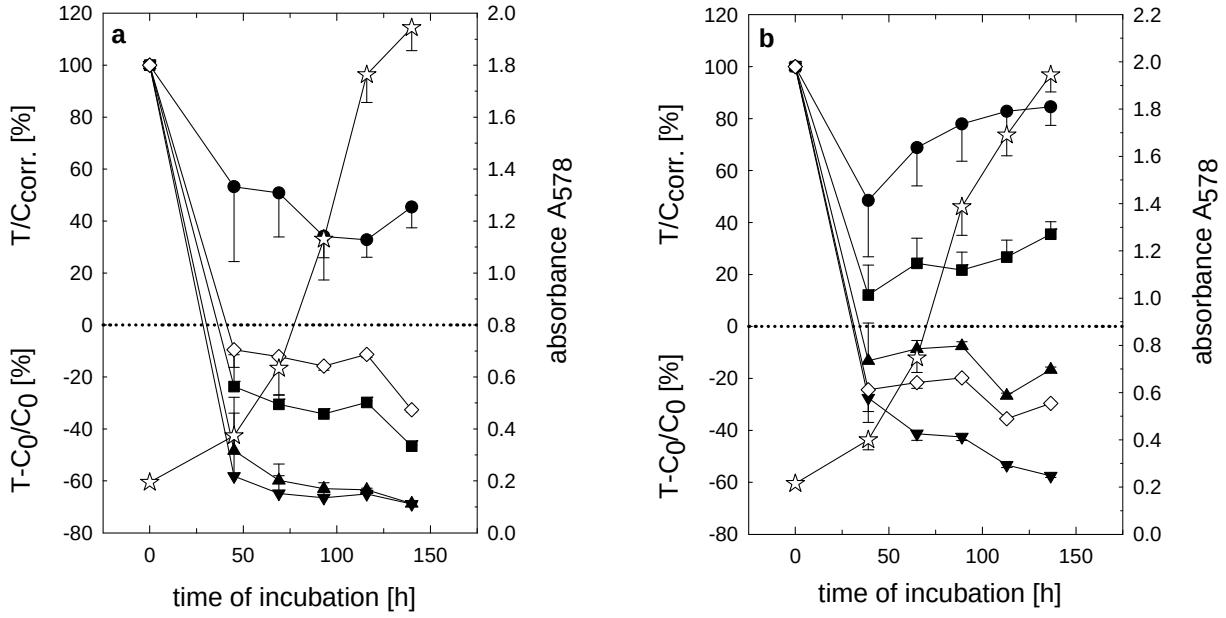

Figure 5.8: Effect of hygromycin on proliferating U-87 MG wildtype cells (a), 137th passage, and U-373 MG wildtype cells (b), 250th passage.

Cells were incubated with hygromycin at concentrations of: 10 µg/mL (filled circles), 100 µg/mL (filled squares), 400 µg/mL (filled triangles) and 800 µg/mL (filled inverted triangles). As controls, both cell lines were incubated with the vehicle water (open stars) and 10 nM of vinblastin (open diamonds).

Summing up, puromycin proved to be the most potent selectable marker of all investigated antibiotics. A quite low concentration of 750 ng/mL sufficed to mediate massive cytocidal effects on both human glioblastoma cell lines. To achieve similar effects by incubation of the cells with G418 and hygromycin, approximately 1000-fold higher concentrations (750 µg/mL and 800 µg/mL, respectively) were necessary on U-87 MG cells as well as on U-373 MG wildtype cells. Therefore, 750 µg/mL of G418 and 1.0 µg/mL of puromycin·2HCl were considered as sufficient concentrations for the selection of stable transfected U-87 and U-373 MG cells with the pGL4.20 (luc2/puro), pDsRed2-C1 and pTurboFP635-N vectors, respectively.

5.4.2 In vivo imaging using bioluminescent glioblastoma cell lines

5.4.2.1 Luciferase2 activity in cell lysates

To investigate the luciferase2 activity of the puromycin-resistant transfectants, different clones of U-87 and U-373 cells were seeded into 24-well plates and lysed after having reached appropriate confluency. Bioluminescence of the lysates, incubated with D-luciferin, was measured over a period of 10 s. U-87 MG and U-373 MG wildtype cells served as negative controls.

8 resistant U-87 clones were obtained by 2 different transfection procedures. On the one hand, a ratio of 3 parts FUGENE HD transfection reagent and 2 parts of plasmid DNA (3:2) was used, whereas the second preparation was performed with 9 parts of FUGENE HD and 2 parts of DNA (9:2). The 4 colonies which were obtained from the 3:2 preparations were termed Clone 1-4, whereas picked clones from the 9:2 transfection procedures were numbered from 5-8. The residual colonies were pooled and designated U-87 Luc2 (3:2) and U-87 Luc2 (9:2).

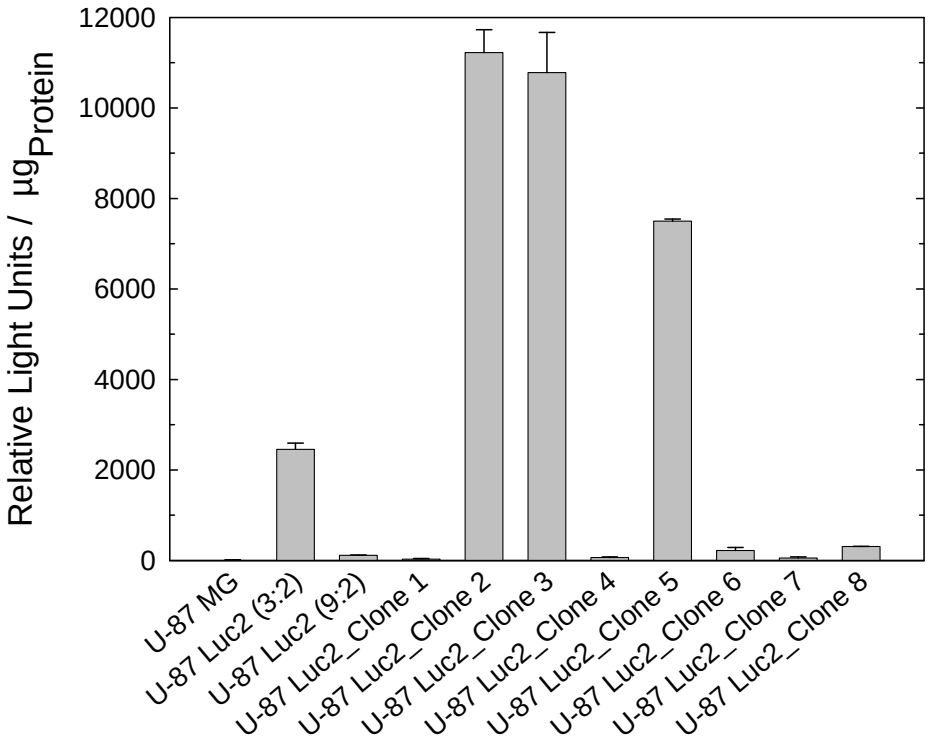

Figure 5.9: Specific luciferase2 activity determined in lysates of U-87 cells transfected with pGL4.20 (luc2/puro). U-87 MG wildtype cells served as negative control (mean values ± SEM, n=3).

As shown in **Figure 5.9,** clones 2, 3 and 5 of U-87 transfectants showed by far the highest enzyme activity. Clones 2 and 3 were generated from the 3:2 preparations whereas clone 5 was obtained by picking a resistant colony from the transfection sample which contained 9 parts of FUGENE HD and 2 parts of plasmid DNA. Comparing clones 2 and clone 3 with the U-87 MG wildtype cells, reveals approximately 800-fold higher RLU values (14 vs. 10,781 for clone 3 and 11,223 for clone 2). Hence, for further investigations U-87 Luc2_Clone 2, 3 and 5 cells were used.

In case of U-373 cells (**Figure 5.10**), 12 resistant colonies were obtained. By analogy with the U-87 transfectants, the clones were termed: Clones 1-4 (3:2, FUGENE HD:DNA ratio), clones 5-8 (6:2, FUGENE HD:DNA ratio) and clones 9-12 (9:2, FUGENE HD:DNA ratio). Residual colonies were also pooled.

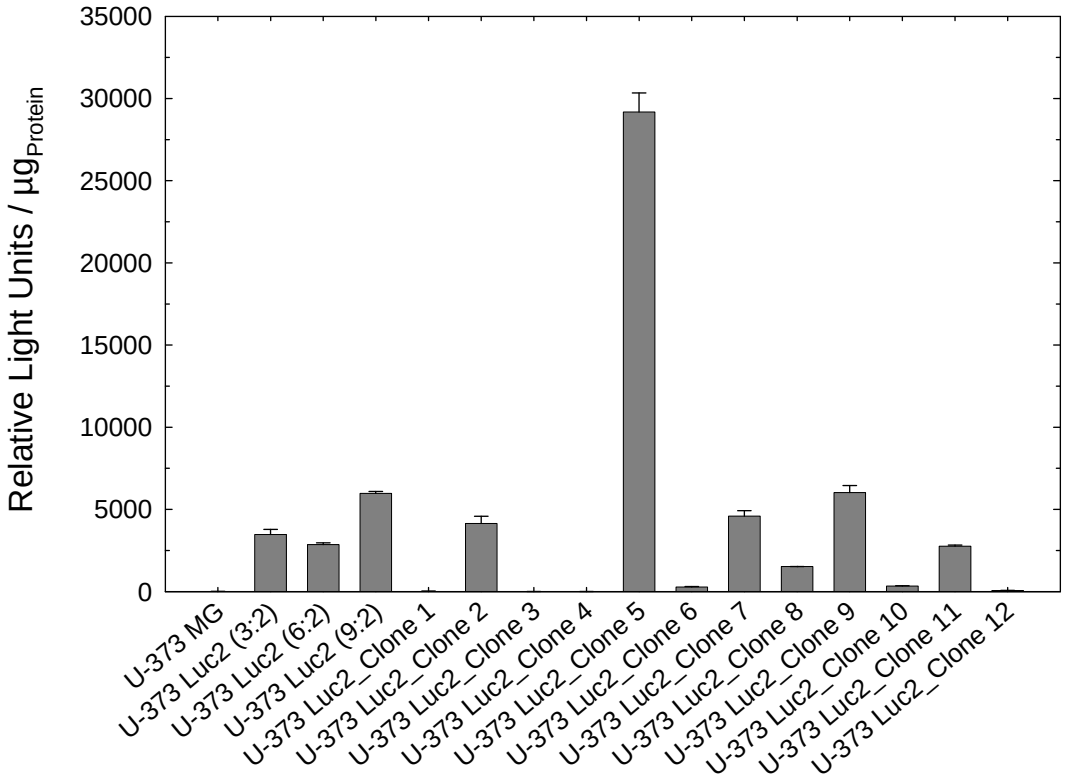

Figure 5.10: Specific luciferase2 activity in the lysates of U-373 cells transfected with the pGL4.20 (luc2/puro) plasmid. U-373 MG wildtype cells served as negative control (mean values ± SEM, n=3).

U-373 Luc2_Clone 5 showed paramount luciferase2 activity (**Figure 5.10**). However, clone 7 and clone 9 were also included into the subsequent studies.

5.4.2.2 Luciferase2 activity in living cells

To explore the sensitivity of the imaging device on live cells, serial dilutions of the transfectants were investigated in microtiter plates. Low-expressing subcultures or wildtype cells served as controls.

Figure 5.11 shows exemplary results obtained with U-87 Luc2_Clone 1, 3 and 5.

Clone 1, which was identified as a very weakly-expressing clone (cf. **Figure 5.9**), gave no signal up to 300,000 cells / well. By contrast, in case of U-87 Luc2_Clone 3 and 5 (cf. **Figure 5.9**) the limit of detection was 18,750 and 37,500 cells / well, respectively. In addition, the photon counts and cell numbers of U-87 Luc2_Clone 3 correlated directly over a range of 2 orders of magnitude with $r^2 = 0.983$. In view of the signal to noise ratio, 50,000 cells were considered appropriate for orthotopic implantations into the brain of nude mice.

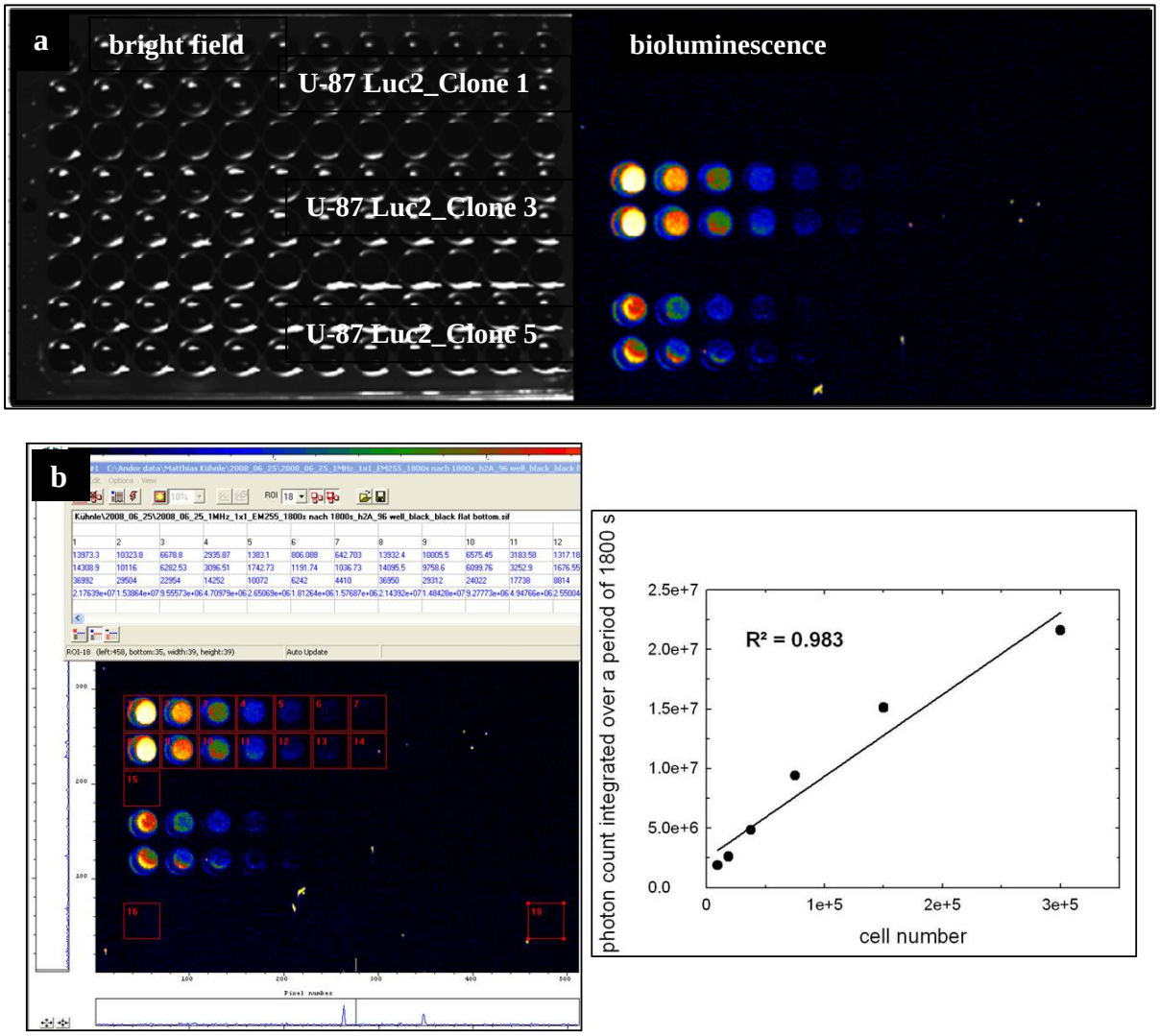

Figure 5.11: Specific luciferase2 activity of the clones U-87 Luc2_Clone 1, 3 and 5, 5th passage, detected in living cells by means of the in vivo imaging system. Bright field image and corresponding light signals (a) and correlation of photon count (determined in the "Regions of interest" (ROI, red marked squares)) vs. cell number of U-87 Luc2_Clone 3 cells (b). Cell suspensions were serially diluted 1:2 starting from 300,000 to 293 cells per well (decreasing cell numbers from left to right).

Instrument settings: stage height h2a, exposure time 1800 s, no binning, EM gain 255, readout rate 1 MHz. at 16 bit.

To investigate, if the luc2 expression is retained over a long period of time, the transfectants were imaged in different passages (**Figure 5.12** and **Figure 5.13**).

U-87 Luc2_Clone 2 cells (**Figure 5.12**) showed stable luciferase2 expression for at least 6 months. Similar results were obtained with the U-373 clones, namely Clone 5, 7 and 9 over 17 passages (**Figure 5.13**).

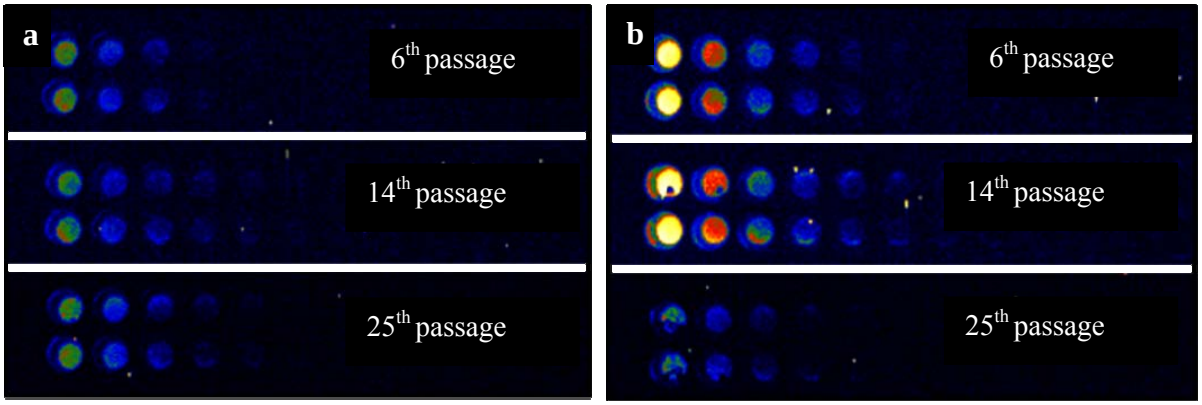

Figure 5.12: Long-term expression of luc2 activity in genetically engineered human glioblastoma cells (U-87 Luc2_Clone 2 (a) and clone 3 (b)) in vitro. The cells were investigated in passages 6, 14 and 25 at densities from 300,000 - 293 cells per well (1:2 dilution steps, decreasing cell numbers from left to right.)

Instrument settings: stage height h2a, exposure time 1800 s, no binning, EM gain 255, readout rate 1 MHz. at 16 bit.

However, in case of U-87 Luc2_Clone 3 cells, bioluminescence in passage 14 (detection limit ~ 18,750 cells / well) was slightly lower compared to passage 25 (detection limit ~ 37,500 cells / well) (**Figure 5.12b**).

With respect to the relative luciferase2 expression by the different glioblastoma transfectants, the results obtained in cell lysates and live cells are in good agreement (cf. **Figure 5.9, 5.10** and **Figure 5.12, 5.13**)

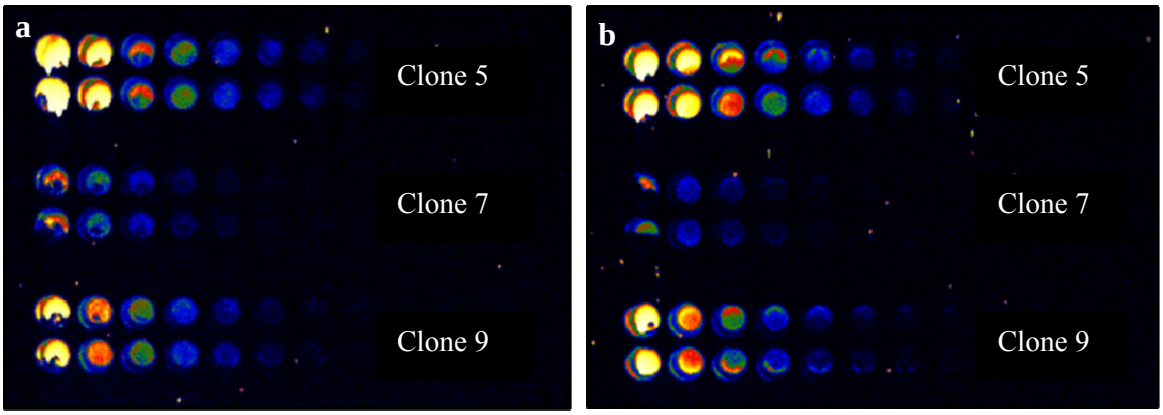

Figure 5.13: Long-term expression of luc2 activity in genetically engineered human glioblastoma cells (U-373 Luc2_Clone 5, 7 and 9) in vitro. The cells were investigated in passages 5 (a) and 17 (b) at densities from 300,000 – 293 cells per well (1:2 dilution steps, decreasing cell numbers from left to right), respectively.

Instrument settings: stage height h2a, exposure time 1800 s, no binning, EM gain 255, readout rate 1 MHz. at 16 bit.

5.4.2.3 Proliferation and chemosensitivity of U-87 and U-373 transfectants

As cancer cell lines are usually polyclonal and genetically extremely variable, which becomes obvious e.g. by karyotyping [Altenschöpfer, 1998], it must be kept in mind, that transfectants represent only a small subpopulation of the parent cells. Therefore, the transfectants were compared to the respective wildtype cells concerning growth kinetics and chemosensitivity.

5.4.2.3.1 Growth kinetics

U-87 Luc2_Clone 2 and U-87 Luc2_Clone 3 cells showed comparable in vitro growth kinetics (**Figure 5.14a**) compared to the U-87 MG wildtype cells.

There were also no significant differences between the genetically engineered U-373 Luc transfectants and the U-373 MG wildtype cells (**Figure 5.14b**). All investigated transfectants of U-373 cells proved to be comparable to the wild type cells according to their in vitro growth kinetics, indicating that obviously, the introduction of the gene encoding for the luciferase2 enzyme did not alter the cell proliferation.

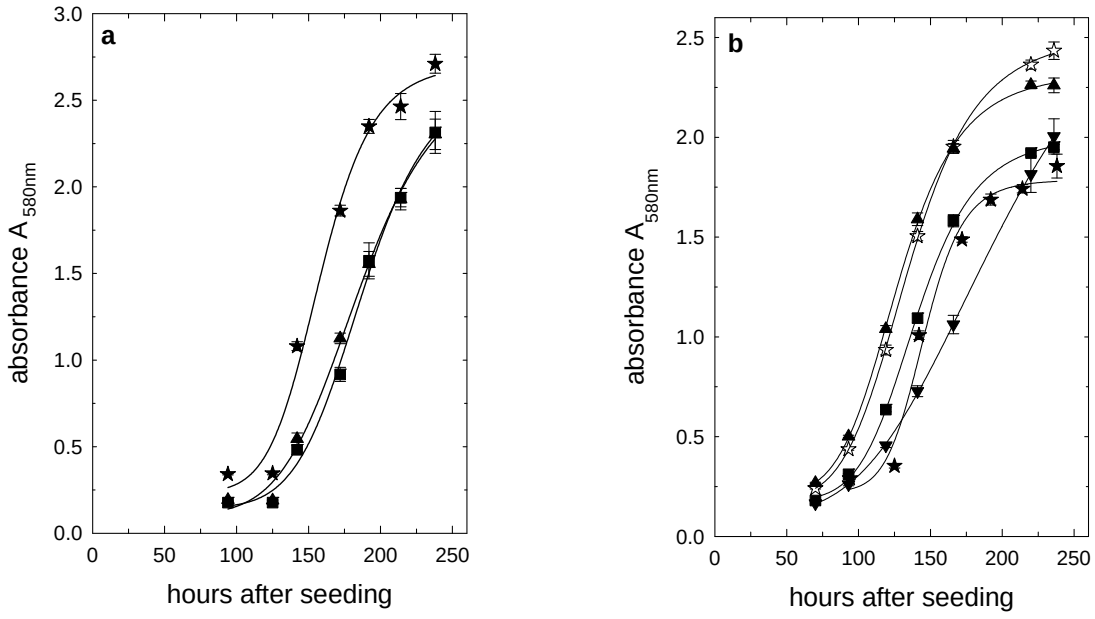

Figure 5.14: In vitro growth kinetics of different U-87 cell lines (a): U-87 MG (filled stars, 159th passage), U-87 Luc2_Clone 2 (filled squares, 13th passage) and U-87 Luc2_Clone 3 (filled triangles, 13th passage), and various U-373 cells (b): U-373 MG (filled stars, 213th passage and open stars, 217th passage), U-373 Luc2_Clone 5 (filled squares, 7th passage), U-373 Luc2_Clone 7 (filled triangles, 7th passage) and U-373 Luc2_Clone 9 (filled inverted triangles, 7th passage).

5.4.2.3.2 Chemosensitivity of transfectants against mitoxantrone and topotecan

In view of the co-administration of cytostatics, which are substrates of the ABCG2 transporter, with inhibitors of this efflux pump (see Chapter 4), the chemosensitivity of the transfectants against mitoxantrone and topotecan was investigated.

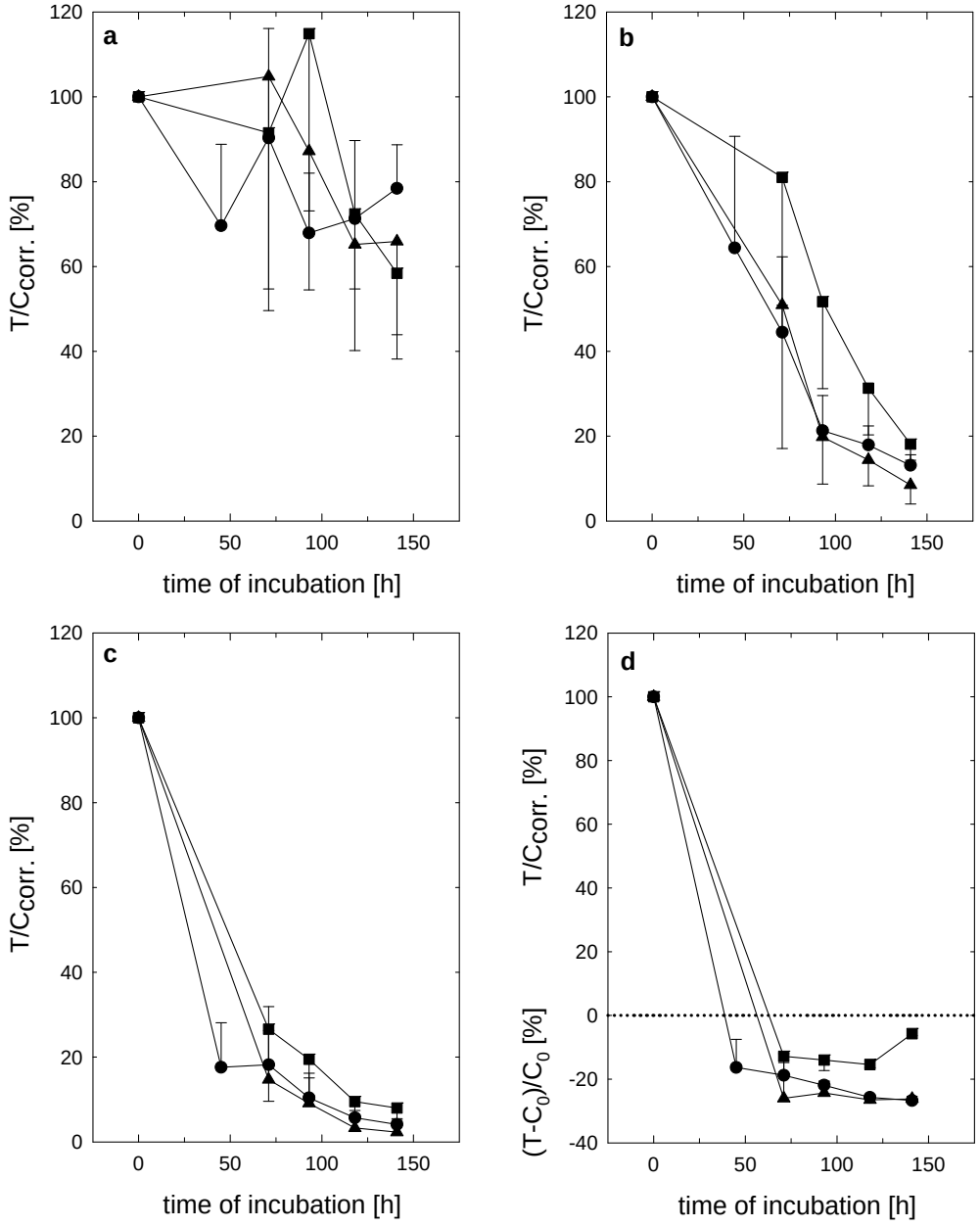

Figure 5.15: Effect of the cytostatic and ABCG2 substrate mitoxantrone on proliferating U-87 MG cells (filled circles; 161th passage), U-87 Luc2_Clone 2 cells (filled squares; 15th passage) and U-87 Luc2_Clone 3 cells (filled triangles; 15th passage)

Cells were incubated with mitoxantrone at concentrations of: 10 nM (a), 50 nM (b), 100 nM (c) and 500 nM (d).

Within the range of experimental errors, there were neither statistically significant differences in case of U-87 MG wildtype cells and transfectants (**Figure 5.15**, **Figure 5.17**) nor between the different U-373 glioblastoma variants (**Figure 5.16**, **Figure 5.18**).

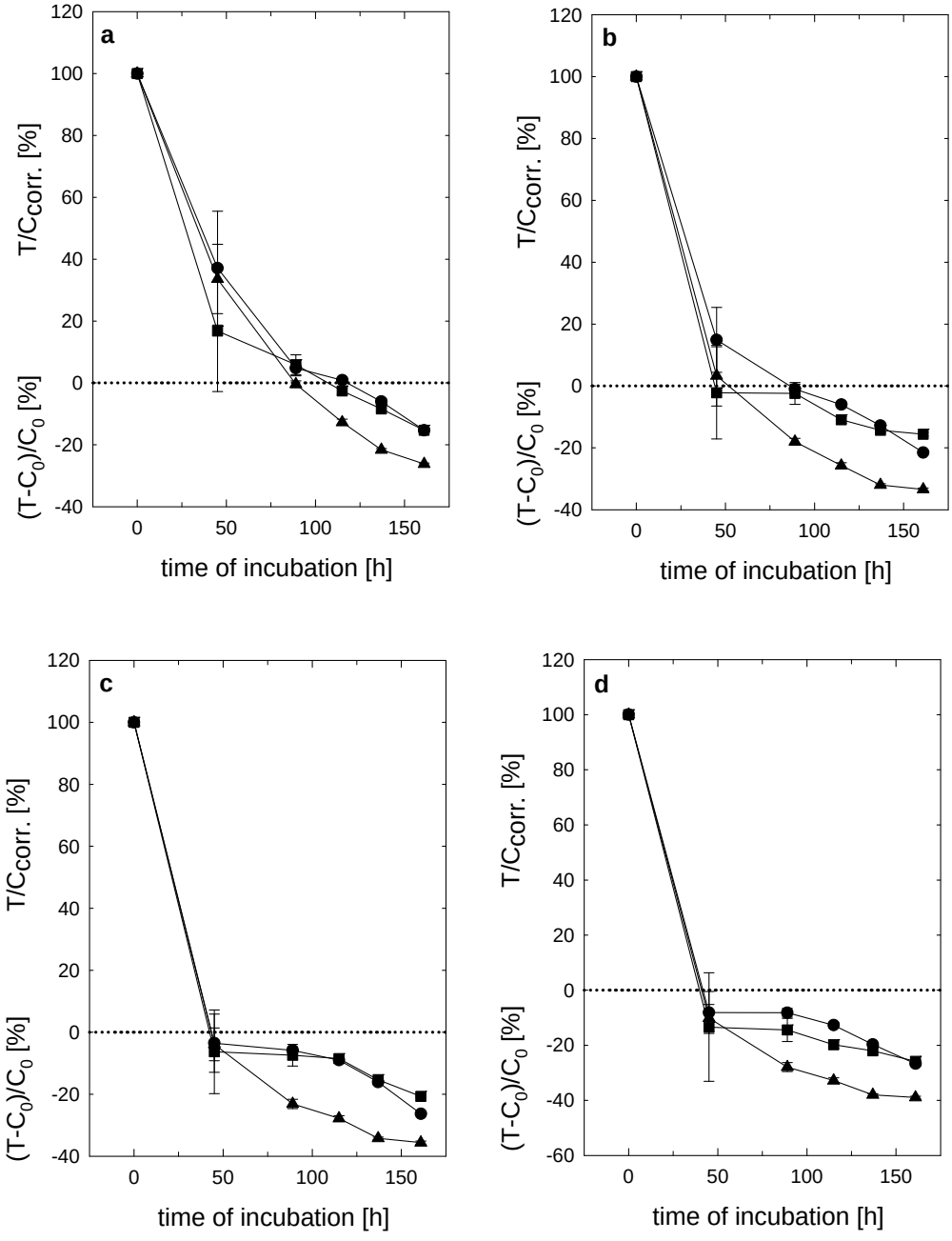

Figure 5.16: Effect of the cytostatic and ABCG2 substrate mitoxantrone on proliferating U-373 MG cells (filled circles; 216th passage), U-373 Luc2_Clone 5 cells (filled squares; 8th passage) and U-373 Luc2_Clone 9 cells (filled triangles; 8th passage).

Cells were incubated with mitoxantrone at concentrations of: 10 nM (a), 50 nM (b), 100 nM (c) and 500 nM (d).

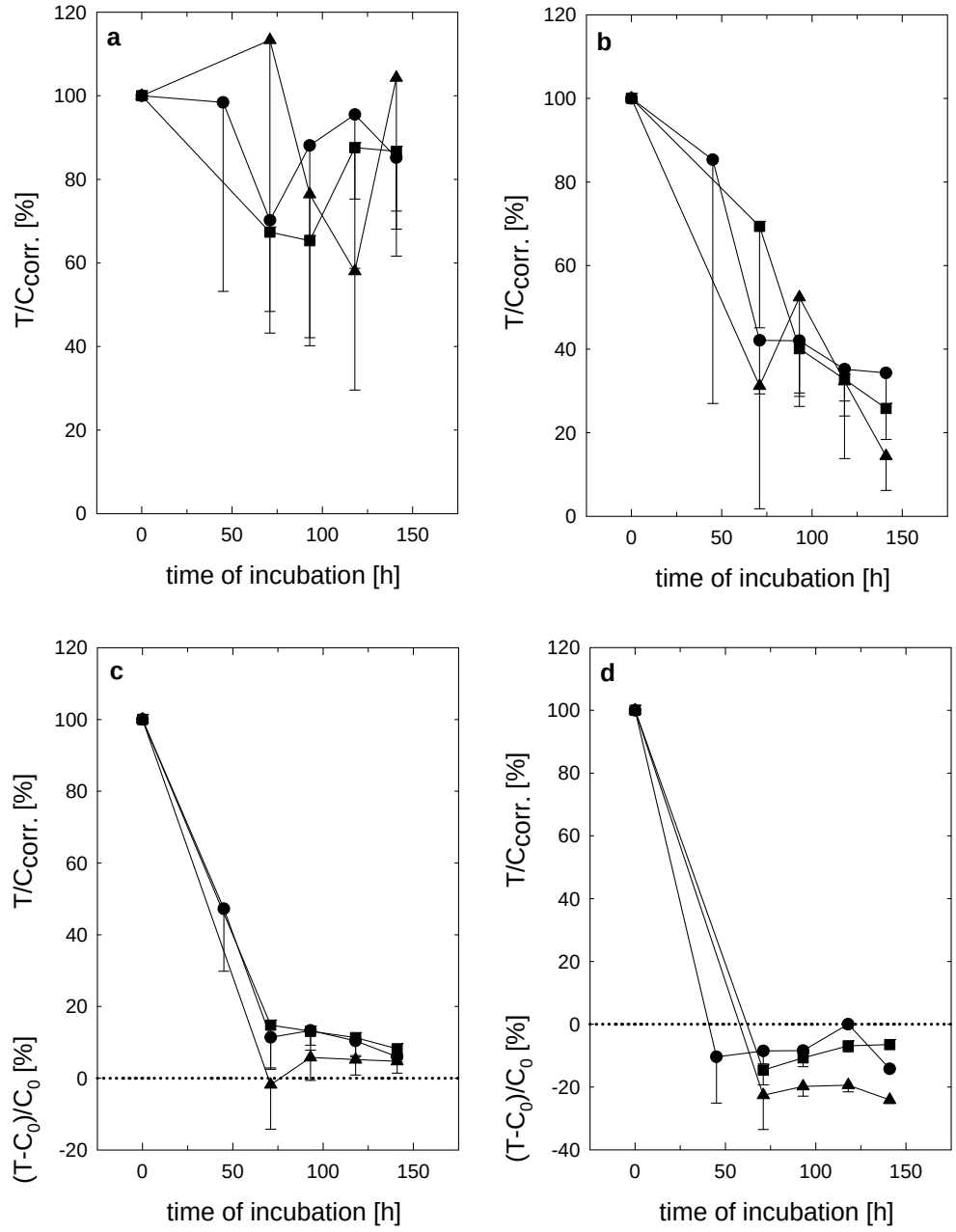

Figure 5.17: Effect of the cytostatic and ABCG2 substrate topotecan on proliferating U-87 MG cells (filled circles; 161th passage), U-87 Luc2_Clone 2 cells (filled squares; 15th passage) and U-87 Luc2_Clone 3 cells (filled triangles; 15th passage)

Cells were incubated with topotecan at concentrations of: 5 nM (a), 25 nM (b), 100 nM (c) and 500 nM (d).

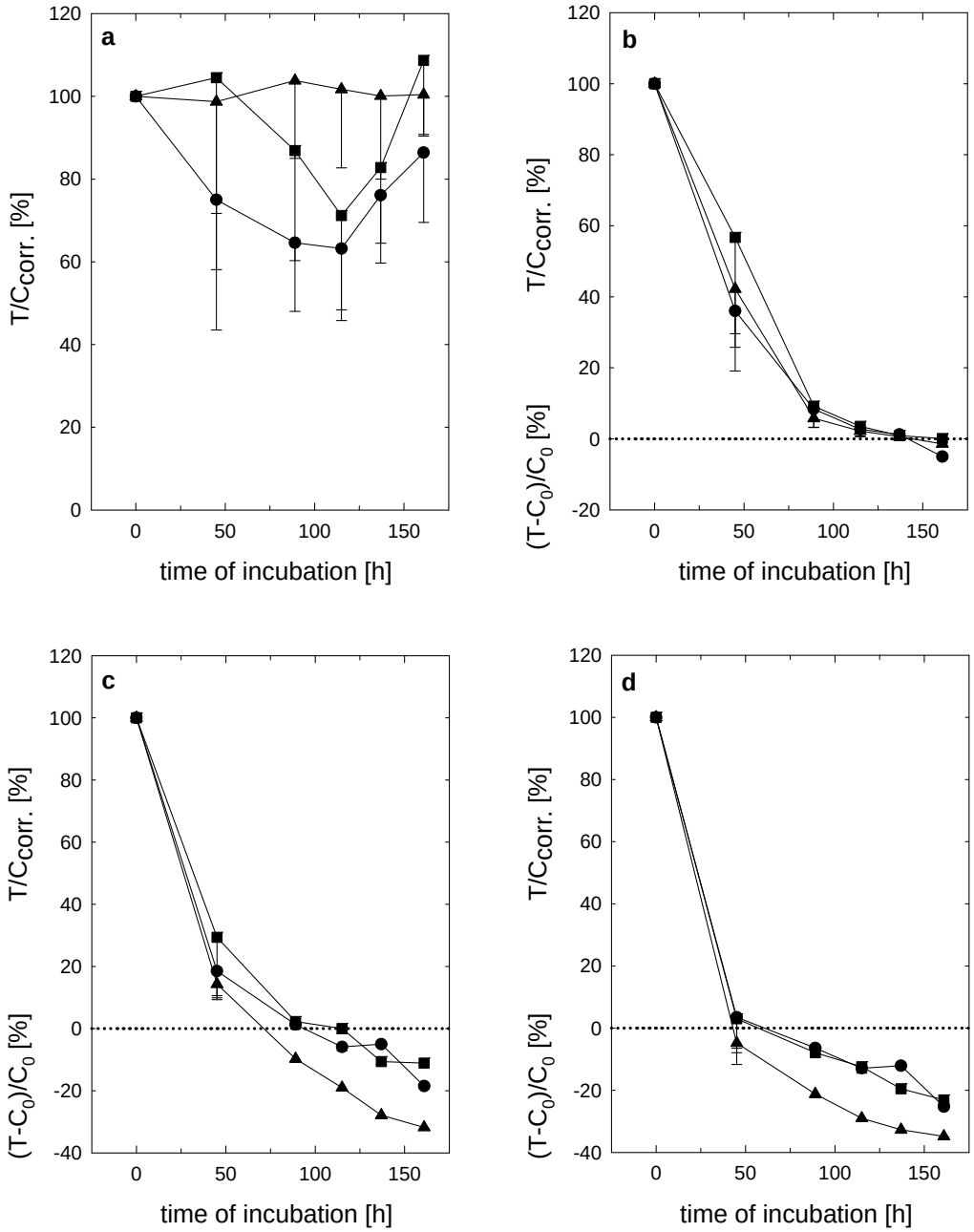

Figure 5.18: Effect of the cytostatic and ABCG2 substrate topotecan on proliferating U-373 MG cells (filled circles; 216th passage), U-373 Luc2_Clone 5 cells (filled squares; 8th passage) and U-373 Luc2_Clone 9 cells (filled triangles; 8th passage)

Cells were incubated with topotecan at concentrations of: 5 nM (a), 25 nM (b), 100 nM (c) and 500 nM (d).

5.4.2.4 Tumorigenicity and growth kinetics of transfectants in subcutaneous tumor models

Figure 5.19 shows the in vivo growth kinetics of U-87 Luc2_Clone 2 xenografts compared to the control U-87 MG. The maintenance of solid U-87 Luc2_Clone 2 tumors could only be sustained up to the 1st in vivo passage.

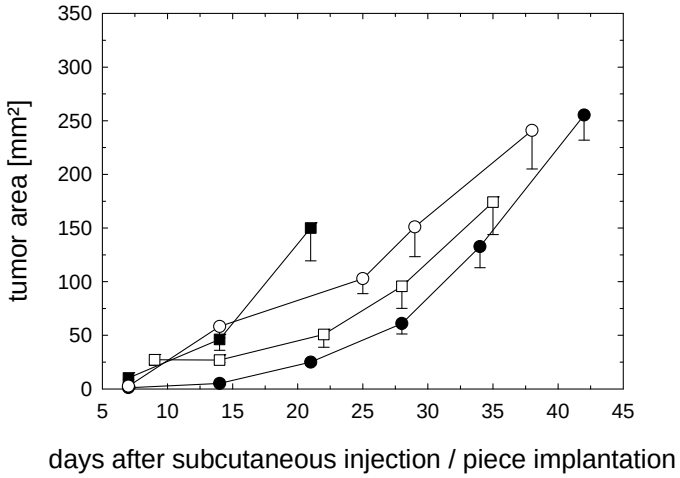

Figure 5.19: In vivo growth kinetics of subcutaneous U-87 MG (filled symbols) and *U-87 Luc2_Clone 2* tumors (open symbols) in nude mice: In vivo passage 0 (circles) and 1st in vivo passage (squares); (mean values ± SEM).

Table 5.1: Take rates of subcutaneous U-87 MG and *U-87 Luc2_Clone 2* tumors

Cell line	Passage	Take rate (%)
U-87 MG	0	80
	1	100
U-87 Luc2_Clone 2	0	100
	1	100

All investigated glioblastoma variants were highly tumorigenic (**Tables 5.1** and **5.2**) and showed reproducible growth, both, when injected as cell suspension or implanted as solid tumor pieces. Within the variability of xenograft progression, typically associated with errors up to 50 %, the growth kinetics were similar when comparing genetically engineered with wildtype cells (**Figures 5.19** and **5.20**).

This fact was further substantiated by long-term investigations on subcutaneous U-87 Luc2_Clone 3 tumors over a period of several months (10 serial passages) (**Figure 5.21**). The take rates of this human glioblastoma variant are summarized in **Table 5.3.**

Table 5.2: Take rates of subcutaneous U-87 MG and *U-87 Luc2_Clone 3* tumors shown for in vivo passages 0, 1 and 2.

Cell line	Passage	Take rate (%)
U-87 MG	0	80
	1	100
	2	100
U-87 Luc2_Clone 3	0	100
	1	100
	2	100

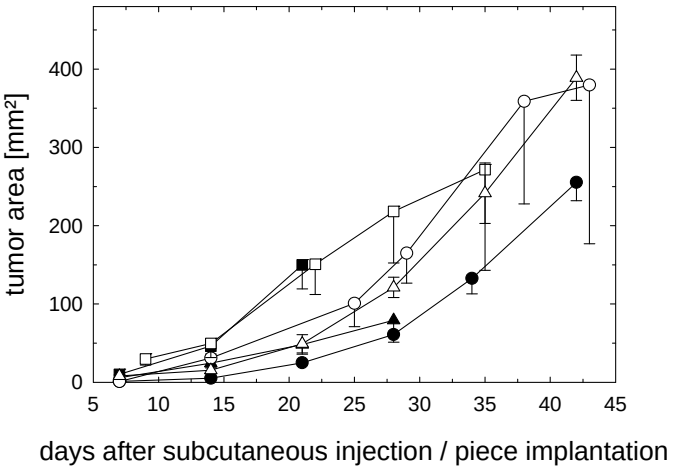

Figure 5.20: In vivo growth kinetics of subcutaneous U-87 MG (filled symbols) and *U-87 Luc2_Clone 3* tumors (open symbols) in nude mice: In vivo passage 0 (circles), 1st passage (squares) and 2nd passage (triangles); (mean values ± SEM).

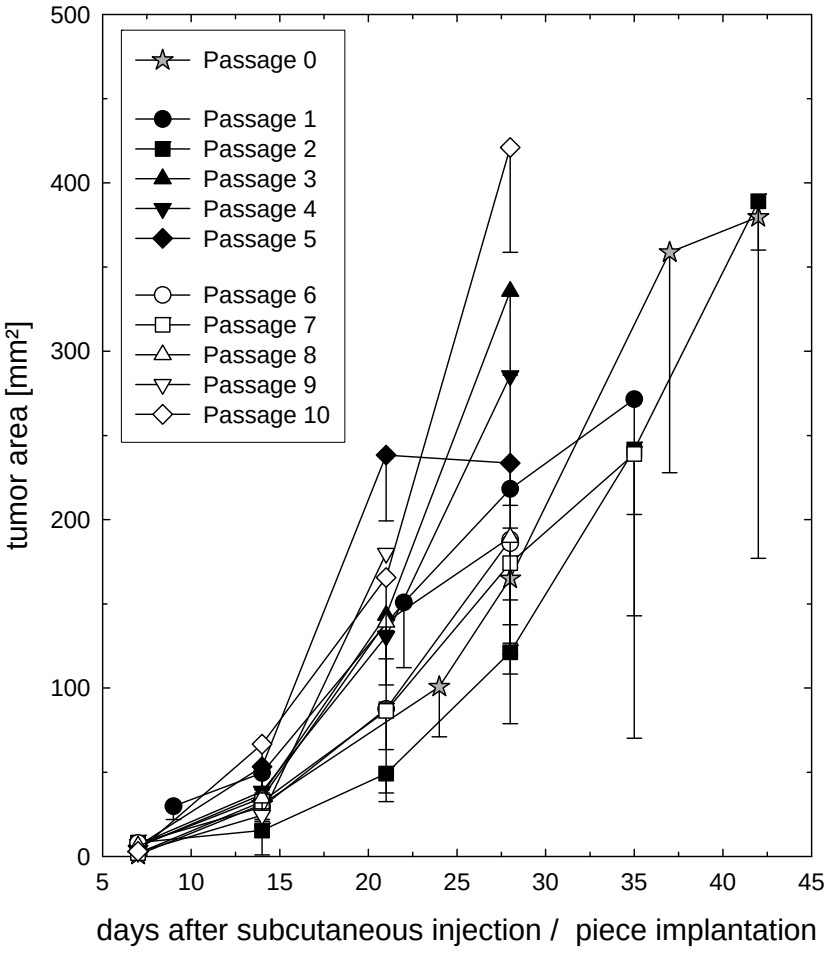

Figure 5.21: In vivo growth kinetics of subcutaneous *U-87 Luc2_Clone 3* tumors monitored over 10 in vivo passages (mean values ± SEM).

Table 5.3: Take rates of subcutaneous U-87 Luc2_Clone 3 tumors in nude mice. The studies revealed an average take rate of 88 ± 5 % (mean value ± SEM)

Passage	Take rate (%)
0	100
1	100
2	100
3	100
4	70
5	82
6	100
7	86
8	83
9	50
10	100

Unfortunately, efforts to establish an analogous in vivo model using U-373 cell lines, including MG wild type cells, U-373 Luc2_Clone 5 and clone 9 transfectants, failed. In contrast to U-87 glioblastomas, the tumorigenicity of the former variants was extremely low and tumor growth usually ceased at 1-2 mm³. **Figure 5.22** presents the growth and histology of 1 U-373 Luc2_Clone 5 reaching an area of 20 mm². However, the subsequent piece implants of this tumor did not form solid subcutaneous xenografts.

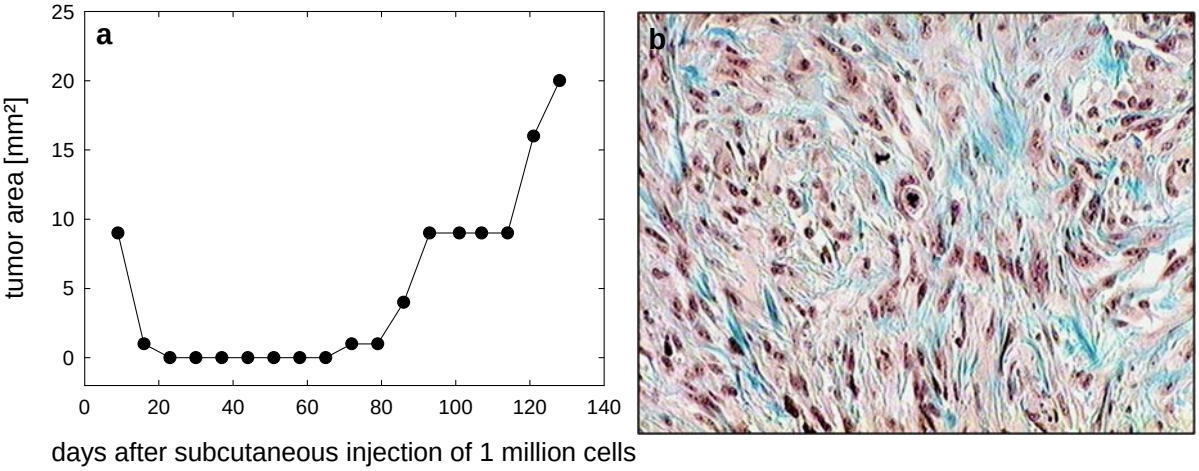

Figure 5.22: a) In vivo growth of a single subcutaneous U-373 Luc2_Clone 5 xenograft (passage 0) and b) corresponding histological proof of tumor tissue (Masson-Goldner staining).

The observed difficulties to maintain U-373 tumors growing in nude mice are in agreement with investigations performed by Dr. Peter Altenschöpfer [Altenschöpfer, 1998], who described an irregular growth behavior of U-373 MG cells in vivo, i.e. either tumorigenicity was extremely low or tumor progression was only stable over a few passages [Altenschöpfer, 1998].

5.4.2.5 Bioluminescence in vivo imaging (BLI) of subcutaneous, U-87 MG derived glioblastoma in nude mice

Due to selection pressure in vitro, mediated by the antibiotic puromycin, the subcutaneous U-87 Luc2 glioblastoma tumors had to be studied on their ability to stably express the luciferase2 enzyme under in vivo conditions. Therefore, the substrate D-luciferin was intraperitoneally injected into nude mice bearing subcutaneous U-87 Luc2_Clone 2 / U-87 Luc2_Clone 3 tumors, respectively, and the emitted light signals were recorded via the in vivo imaging system equipped with the Andor™ EMCCD camera as shown in **Figure 5.23**.

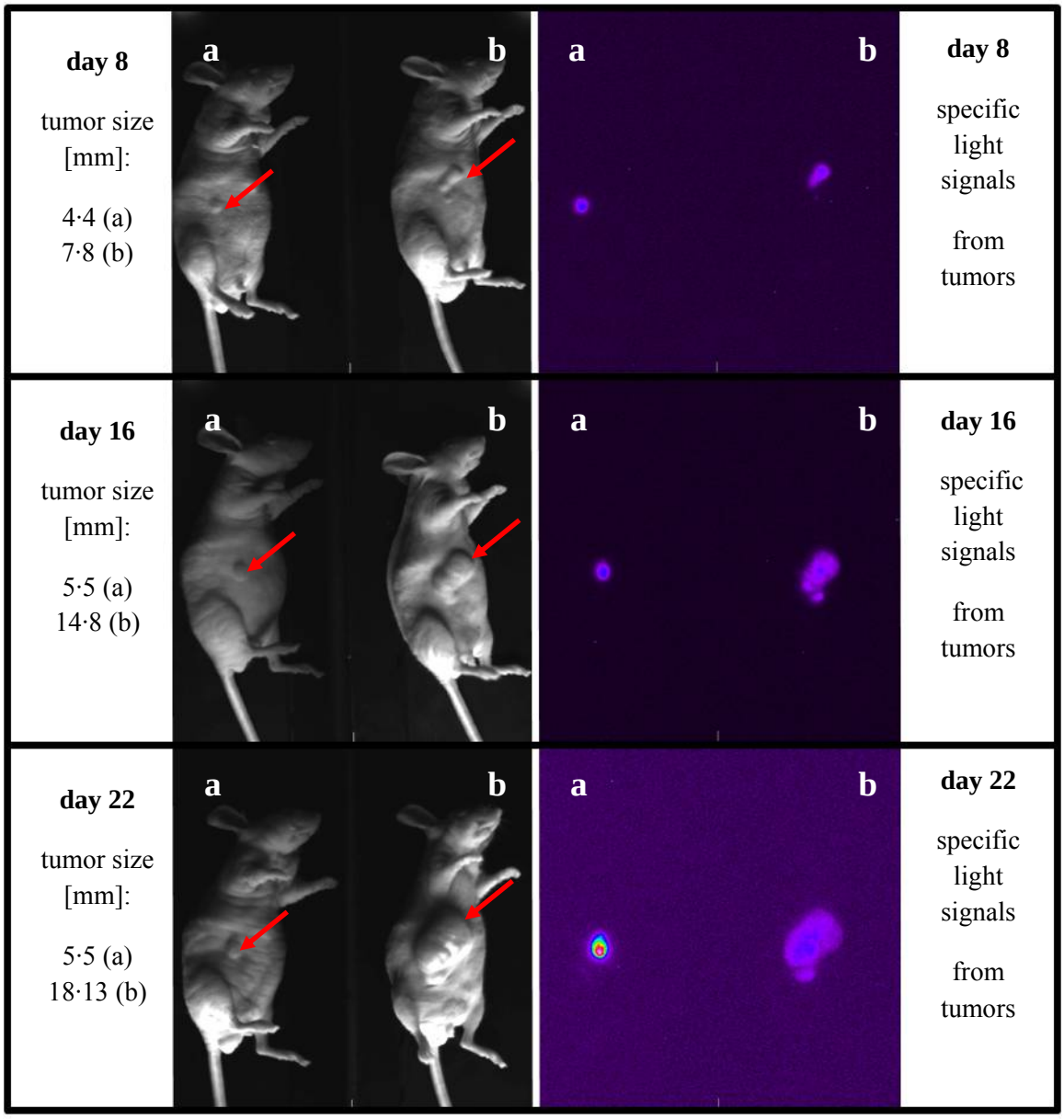

Figure 5.23: Bioluminescence in vivo imaging of subcutaneous U-87 Luc2_Clone 2 (a) and clone 3 (b) xenografts; 1st in vivo passage; 8, 16 and 22 days after tumor piece implantation. Specific light signals emitted from tumor tissues (red arrows in bright field images) were obtained 300 s after i.p. injection of 4 mg D-luciferin into each mouse.

Instrument settings: stage height h2a, exposure time 360 s, EM gain 1, no binning, readout rate 1 MHz. at 16 bit.

Figure 5.23 shows tumor progression in 2 randomly selected nude mice within a period of approximately 3 weeks.

Bioluminescence signals of subcutaneous U-87 Luc2_Clone 2 and Clone 3 xenografts were directly proportional to the tumor area, measured in parallel using an electronic caliper. Thus, the expression of luciferase2 in U-87 Luc2 cells turned out to be stable under in vivo conditions and resulted in sufficient enzyme activity for the detection of light signals by the optical imaging devices. It is noteworthy, that the required exposure times, at a relatively insensitive EM gain to resolve the resulting bioluminescence, were very short. This suggested that also small intracerebral tumors could be imaged in the orthotopic tumor model.

Figures 5.24 and **5.25** demonstrate, that for specific tumor-associated bioluminescence signals not only the tumor tissue has to be vital, but also that D-luciferin has to be provided to the tumor cells via an intact blood circulation.

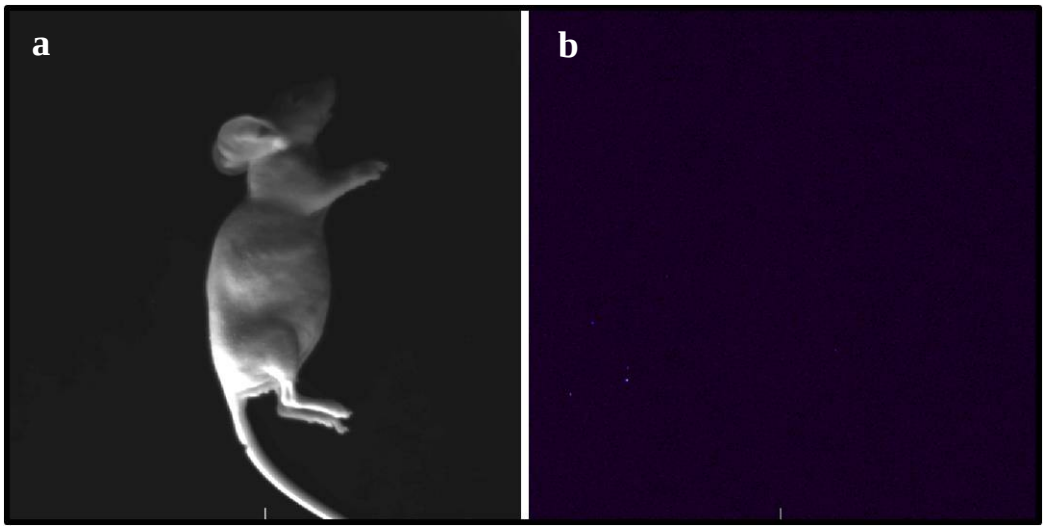

Figure 5.24: In vivo imaging of a control mouse without tumor: bright field image (a) and corresponding bioluminescence after the intraperitoneal injection of 4 mg D-luciferin (b).

Instrument settings: stage height h2a, exposure time 360 s (300 s after D-luciferin injection), EM gain 1, no binning, readout rate 1 MHz. at 16 bit.

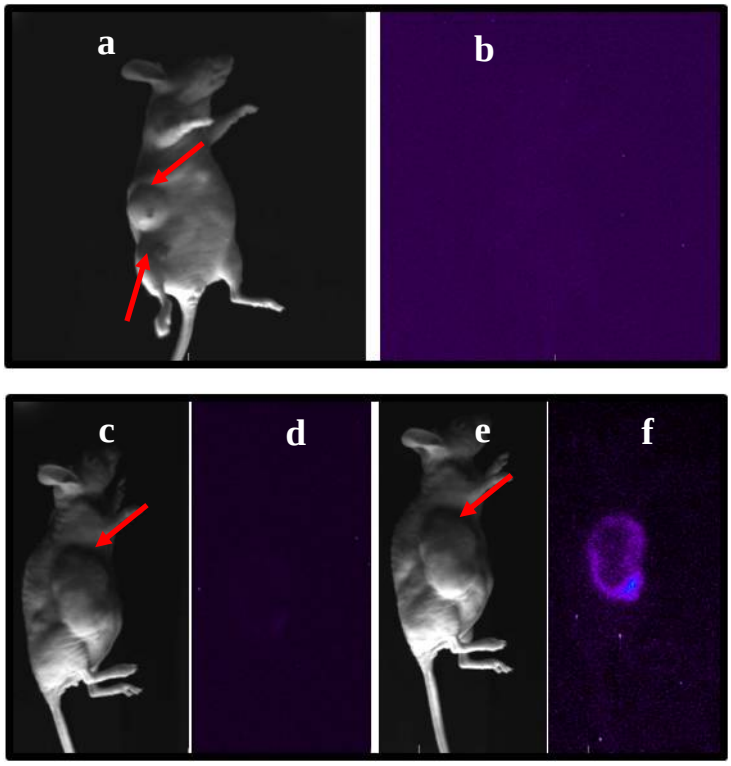

Figure 5.25: Effect of the blood supply and vitality of the tumor tissue on bioluminescence.

a, b): Optical imaging of a dead nude mouse bearing a subcutaneous U-87 Luc2 _Clone 3 tumor.

Instrument settings: stage height h2a, exposure time 360 s (300 s after D-luciferin injection), EM gain 1, no binning, read out rate 1 MHz. at 16 bit).

c-f): Although a massive tumor is visible in the bright field image (c), a high gain is required (f) to detect specific signals, since bioluminescence is only emitted by vital tumor tissue. Necrotic areas in the tumor appear dark using an EM gain of 1 (d).

e, f): EM gain 255 (maximum value) (stage height h2a, exposure time 360 s (900 s after injection of D-luciferin), no binning, readout rate 1 MHz. at 16 bit).

5.4.2.6 Long-term expression of luciferase2 in vivo

To investigate the in vivo stability of luc2 expression over a period of several months, the serially passaged subcutaneous tumors were controlled by bioluminescence in vivo imaging studies (**Figures 5.26** and **5.27**). These investigations were performed with subcutaneous U-87 Luc2_Clone 3 tumors.

As depicted in the corresponding figures, luc2 was expressed by the tumors at a constant level over a period of approximately 9 months. This is surprising, as no puromycin was administered to exert a selection pressure in vivo

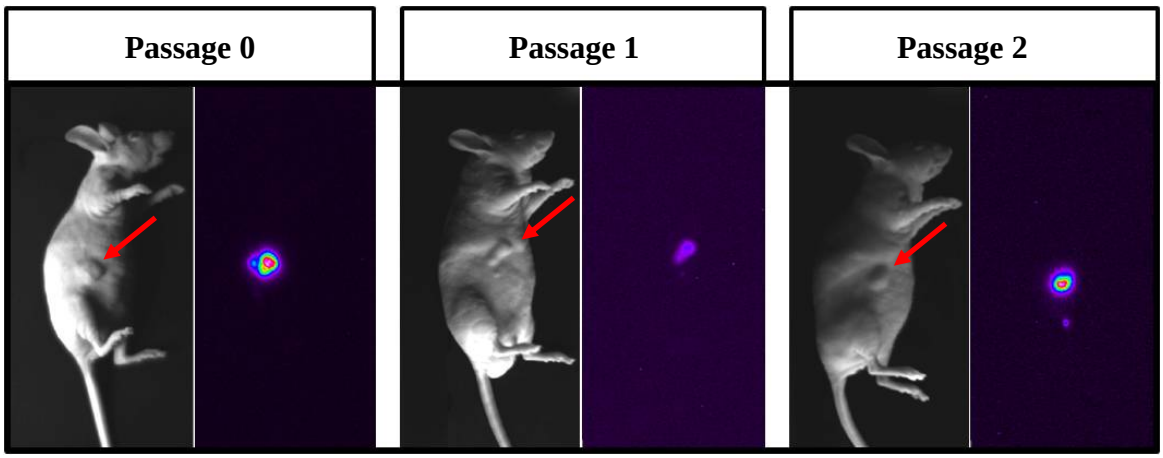

Figure 5.26: Long-term expression on luciferase2 by U-87 Luc2_Clone 3 xenografts (red arrows). Bright field (left) and corresponding bioluminescence (right) images of subcutaneous tumors, recorded for passages 0-2.

Instrument settings: stage height h2a, exposure time 360 s (300 s after injection of D-luciferin), EM gain 1, no binning, readout rate 1 MHz. at 16 bit.

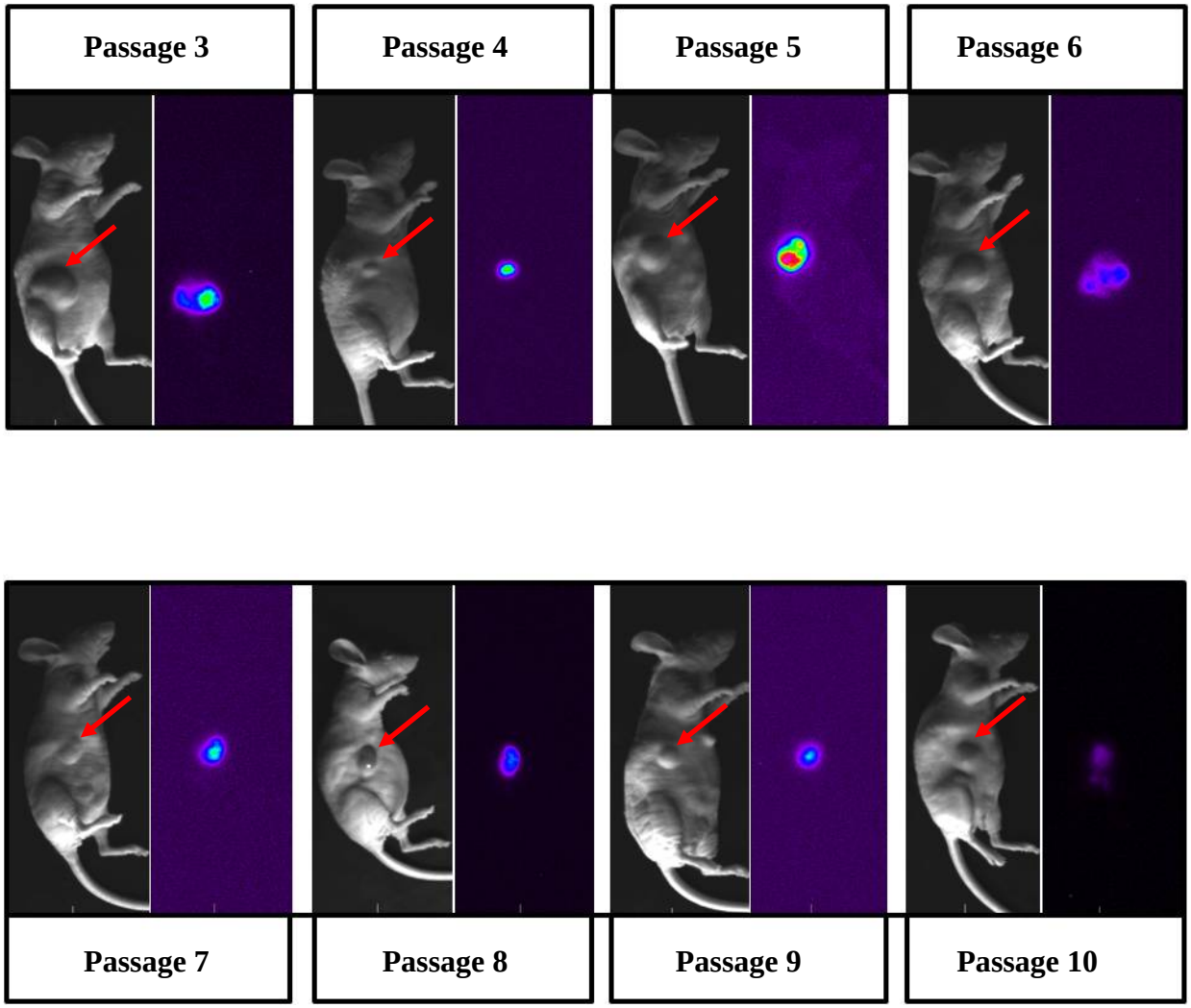

Figure 5.27: Long-term expression on luciferase2 by U-87 Luc2_Clone 3 xenografts (red arrows). Bright field (left) and corresponding bioluminescence (right) images of subcutaneous tumors, recorded for passages 3-10.

Instrument settings: stage height h2a, exposure time 360 s (300 s after injection of D-luciferin), EM gain 1, no binning, readout rate 1 MHz. at 16 bit.

5.4.2.7 Histopathology of subcutaneous luminescent glioblastoma xenografts

The histology shows the morphology of a high grade, cell rich and fast dividing glioma, comprising pleomorphic nuclei with prominent nucleoli. The U-373 MG tumors contained more stroma (data not shown) than the U-87 variants depicted in **Figure 5.28**.

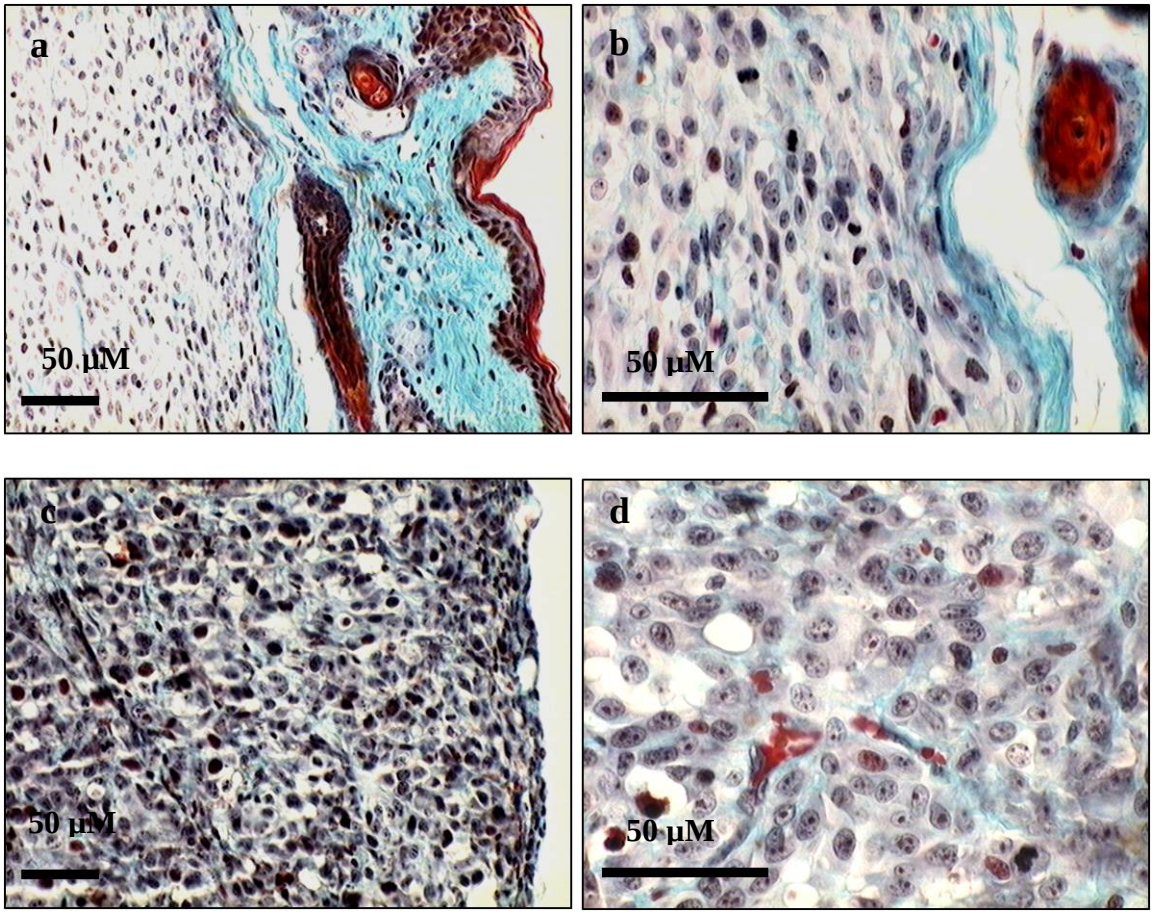

Figure 5.28: Masson-Goldner staining of subcutaneous U-87 Luc2_Clone 2 (a, b) and U-87 Luc2_Clone 3 (c, d) tumors. Objective 20 x (a, c), objective 40 x (b, d).

5.4.2.8 Bioluminescence in vivo imaging (BLI) of intracerebral, U-87 MG derived glioblastoma

Encouraged by the subcutaneous results, U-87 Luc2_Clone 2 and U-87 Luc2_Clone 3 cells were implanted into the brain of nude mice. Subsequently, the intracerebral tumor growth was monitored over a period of 4-5 weeks by means of noninvasive bioluminescence imaging. Prior to measurements, 8 mg of D-luciferin were intraperitoneally injected into each mouse, and the photon counts were integrated for 15 min at an EM gain of 255.

Due to these extremely sensitive instrument settings, control experiments prior to each BLI were required to investigate the effects on the detection of noise. For this reason, every mouse was imaged in the absence of D-luciferin using the identical instrument settings as applied for the subsequent investigations after substrate application. This procedure is exemplarily shown in **Figure 5.29**.

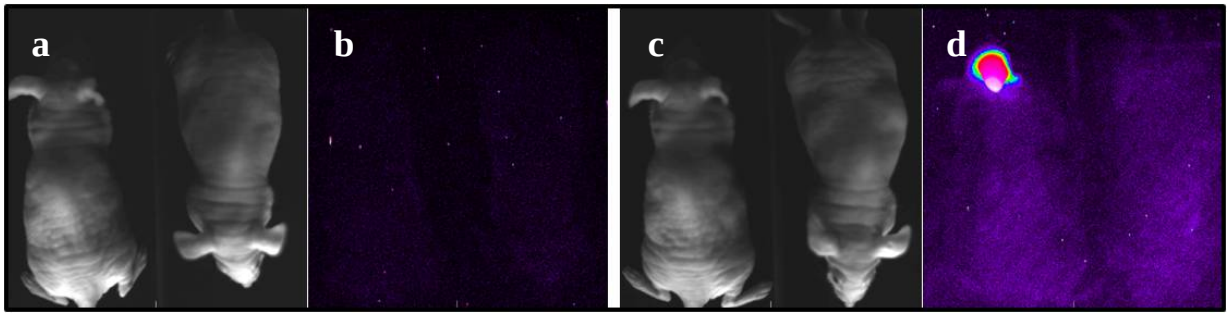

Figure 5.29: Detection of intracerebral glioblastoma xenografts by BLI.

Determination of background: bright field image (a), bioluminescence (b) image.

Optical imaging of the intracerebral tumor: bright field (c) and bioluminescence (d) image.

Instrument settings: stage height h2c, exposure time 900 s, EM gain 255, no binning, readout rate 1 MHz. at 16 bit.

Light signals (d) were obtained after i.p injection of 8 mg D-luciferin.

For validation of the model, U-87 Luc2_Clone 2 and clone 3 cells were implanted into the brain of nude mice (4 and 6 female nude mice, respectively). Subsequently, all animals were imaged over a maximal period of 33 days (**Figures 5.30** and **5.31**).

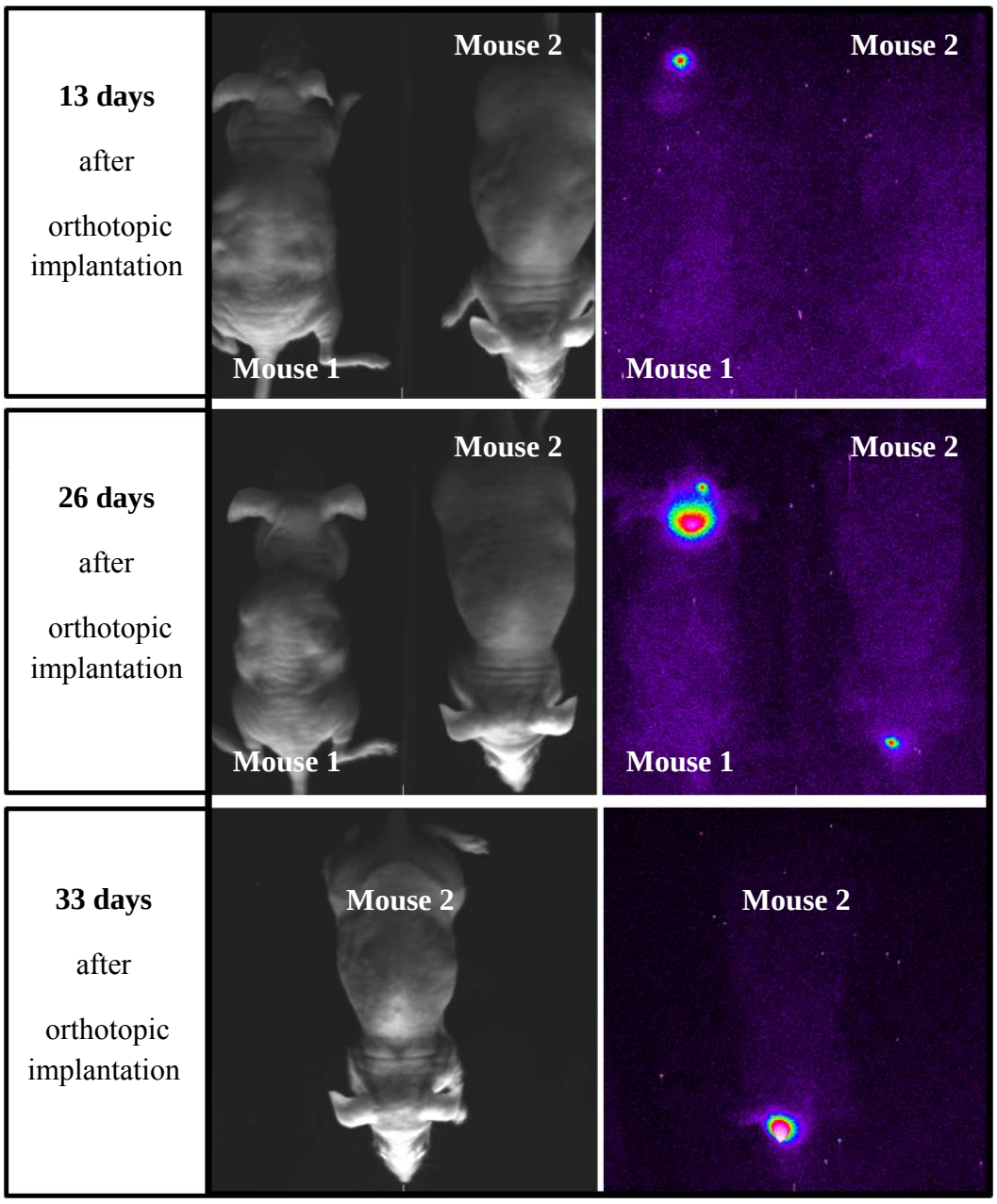

Figure 5.30: Optical in vivo imaging of orthotopic *U-87 Luc2_Clone 2* tumors in the brain of nude mice over a period of 26 and 33 days, respectively. Due to massive detraction by tumor growth, mouse 1 was killed after 26 days. Specific light signals were obtained after i.p. injection of 8 mg D-luciferin.

Instrument settings were as follows: stage height h2c, exposure time 900 s (300 s after substrate application), EM gain 255, no binning, readout rate 1 MHz. at 16 bit.

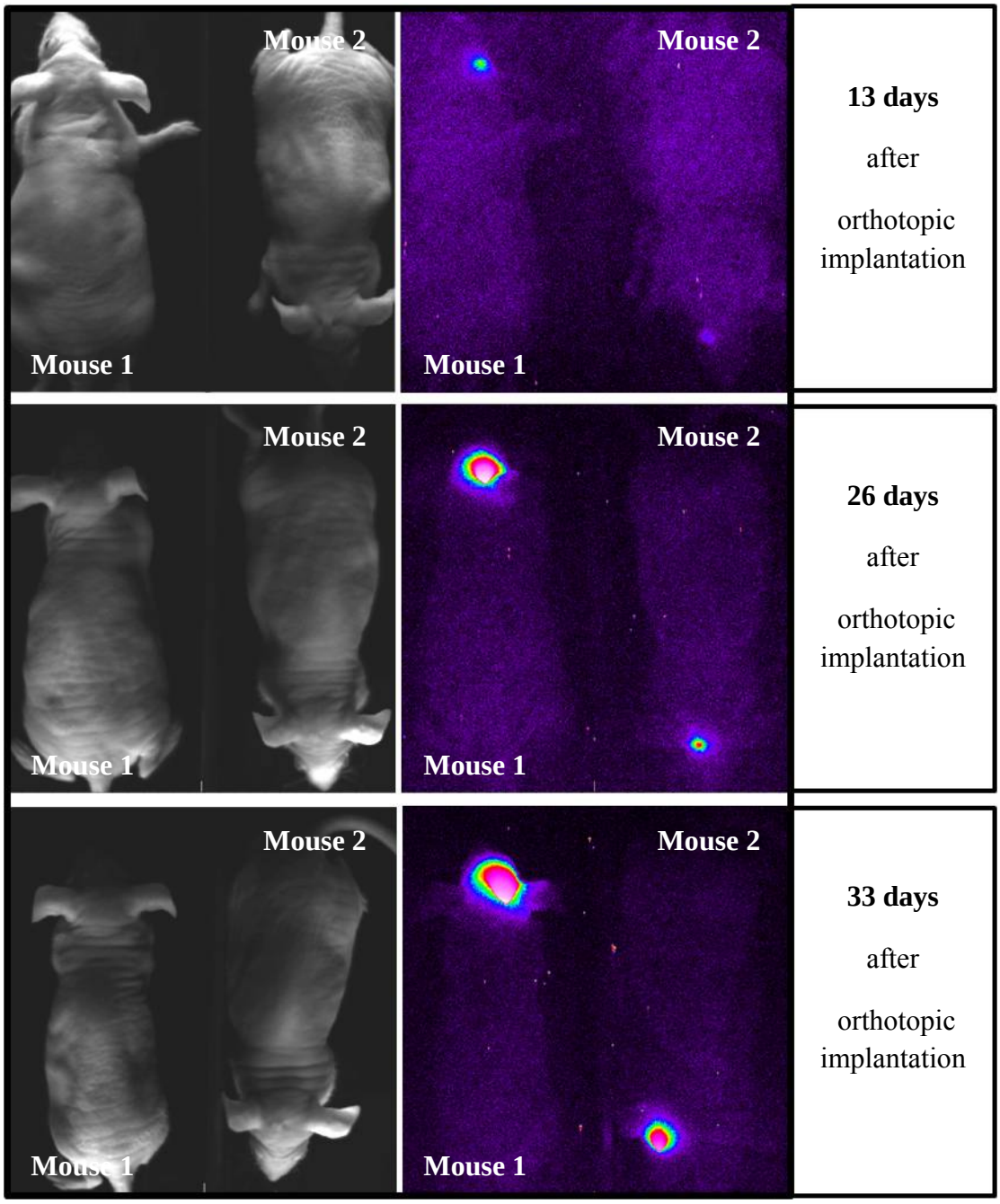

Figure 5.31: Optical in vivo imaging of orthotopic *U-87 Luc2_Clone 3* tumors in the brain of nude mice over a period of 33 days. Bioluminescence signals were obtained after i.p. injection of 8 mg D-luciferin.

Instrument settings were as follows: stage height h2c, exposure time 900 s (300 s after substrate application), EM gain 255, no binning, readout rate 1 MHz. at 16 bit.

Figure 5.30 shows the optical imaging of 2 selected mice bearing orthotopic U-87 Luc2_Clone 2 tumors. 13 days after tumor cell implantation a specific light signal was noticed in the head region of mouse 1, whereas no bioluminescence was determined in mouse 2. Within in the next 13 days, the intracerebral tumor growth proceeded in both animals, according to increasing signals in BLI. The measurements showed a pronounced light signal expanded over the whole head of mouse 1 indicating the existence of a massive intracerebral tumor, supported by the marked decrease in body weight. According to the guidelines of the animal's welfare, mouse 1 was killed by cervical dislocation and the brain tissue was dissected for histopathology. Since bioluminescence signals emitted from mouse 2 were less pronounced, and the body weight retained constant, the animal was imaged once again at day 33, showing an increased signal due to the progression of the intracerebral tumor.

The semi-quantitative evaluation of intracerebral U-87 Luc2_Clone 3 tumor progression is exemplarily demonstrated for 2 selected mice in **Figure 5.31**. Already 13 days after implantation, specific bioluminescence was recorded in both animals. Mouse 1 showed a significant stronger light signal than mouse 2, suggesting a faster tumor progression. These data were supported by the optical imaging 26 and 33 days after tumor cell implantation. The signals recorded from mouse 1 had a higher intensity suggesting a higher tumor load compared to that of mouse 2.

These investigations clearly demonstrate the semi-quantitative monitoring of the progression of orthotopic human brain tumors in nude mice by BLI. Only 6 days after tumor cell implantation, specific light signals were determined in 2 out of 10 mice. Another 5 animals had BLI detectable tumors at the end of the study.

5.4.2.9 Confirmation of orthotopic brain tumors by histopathology

To confirm the results of BLI investigations on orthotopic glioblastoma in nude mice, the animals were killed and dissected brain tissues were examined by histology. **Table 5.4** gives an overview of bioluminescence data and corresponding histology for each mouse of the experiment.

Table 5.4: Optical imaging results and histopathology data of intracerebral U-87 Luc2_Clone 2 / Clone 3 tumors

	Tumor detection by bioluminescence signal	Histological detection of orthotopic tumor growth
U-87 Luc2_Clone 2		
Mouse 1	+	+
Mouse 2	+	+
Mouse 3	+	-
Mouse 4	-	-
U-87 Luc2_Clone 3		
Mouse 1	+	+
Mouse 2	+	+
Mouse 3	+	+
Mouse 4	-	-
Mouse 5	+/-	-
Mouse 6	-/+	-

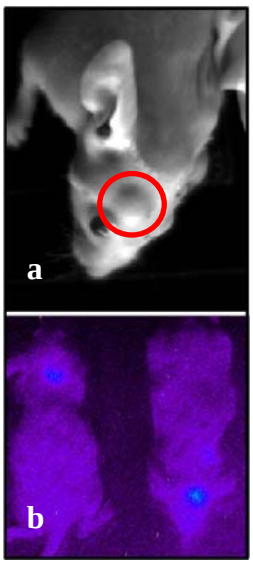

Figure 5.32: Mouse 3 of *U-87 Luc2_Clone 2* group with an extracranial tumor (a) and bioluminescence imaging (b) of mouse 5 (right) and mouse 6 (left) from the *U-87 Luc2_clone 3* group.

In 7 out of 10 cases, the histological examinations were in agreement with data obtained from optical imaging studies.

In the group of nude mice bearing *U-87 Luc2_Clone 2* tumors, mouse 3 showed high specific bioluminescence, indicating the existence of a massive tumor, but which could not detected by histological examination of brain sections. Presumably by the implantation procedure, an extracranial tumor was induced (**Figure 5.32a**).

Due to significant loss of body weight, mouse 5 and mouse 6 had to be killed already after 18 days. At day 18, only very weak bioluminescence signals were detected (**Figure 5.32b**). The discrepancy of bioluminescence and histopathology of such very small tumors might result from the procedure used to prepare the serial sections of the brain.

Figure 5.33 and **5.34** show exemplarily the histology of intracerebral U-87 Luc2_Clone 2 and clone 3 tumors as well as their corresponding BLI images. The histology images represent details, localized at the demarcation of the intracerebral tumor (marked by a red arrow) from the normal brain tissue (marked by a blue arrow).

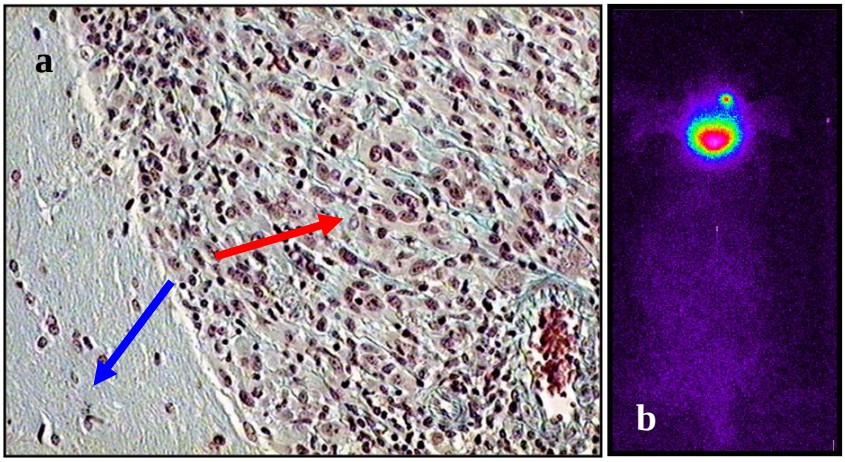

Figure 5.33: Histology of an intracerebral *U-87 Luc2_Clone 2* xenograft in mouse 1 (a) and corresponding BLI image (b), performed on day 26.

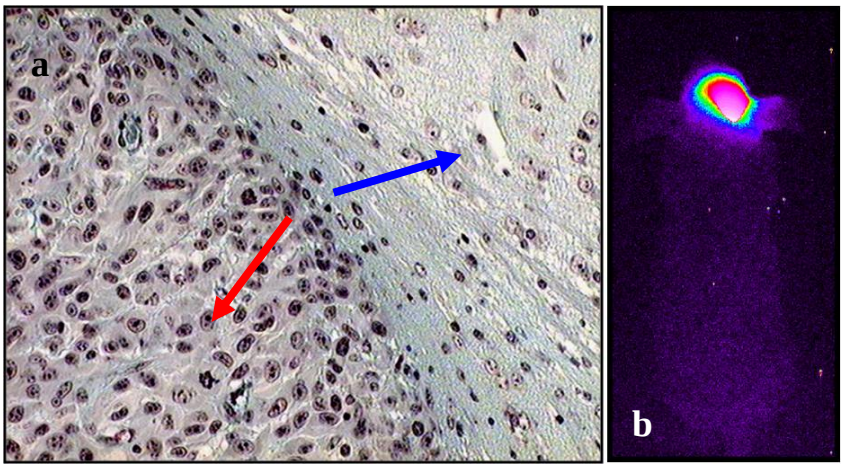

Figure 5.34: Histology of an intracerebral *U-87 Luc2_Clone 3* xenograft in mouse 1 (a) and corresponding BLI image (b), performed on day 33.

5.4.3 In vivo imaging using red fluorescent glioblastoma cells

By analogy with the generation of bioluminescent brain tumors, the human U-87 MG and U-373 MG glioblastoma cells were transfected with the gene encoding the far-red protein Katushka. These investigations were performed as an alternative approach to overcome the high technical complexity of bioluminescence in vivo imaging and to reduce limitations inherent in the method: the long exposure times and the need for application of the costly D-luciferin are disadvantages. Since the EM gain had to be elevated to its maximum for the determination of the extremely low signals emitted from orthotopic brain tumors, control experiments for every animal were indispensable to exclude any interference during the measurements. Furthermore, the injection of the substrate was not only associated with stress, but also with the necessity of an intact blood circulation.

The individual U-87 Katushka and U-373 Katushka clones were designated by analogy to those expressing luc2 (see **5.4.2.1**).

5.4.3.1 Fluorescence microscopy

To determine the transfection efficiency the Katushka fluorescence was checked via fluorescence microscopy. Those clones which showed the highest fluorescence were selected for further investigations.

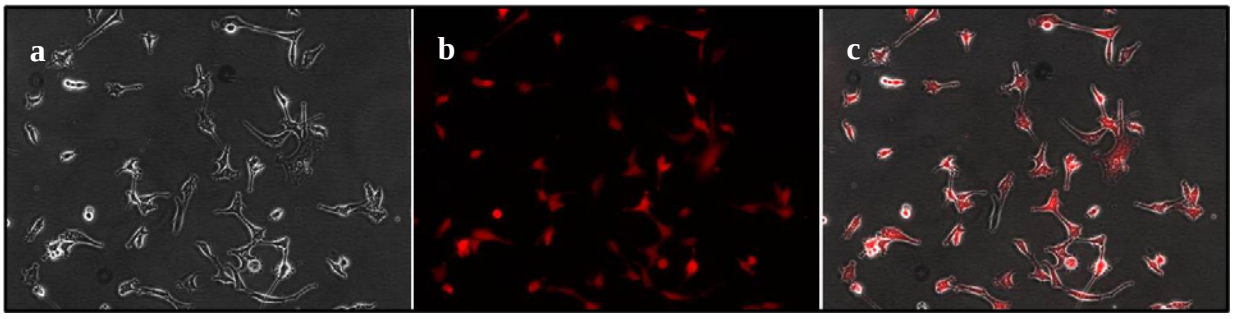

Figure 5.35: Microscopic phase contrast (a), epifluorescence (b) and merged (c) images of U-87 Katushka_Clone 3 cells.

Images were taken on the Carl Zeiss Cell Observer (Zeiss, Munich, Germany) using the Zeiss filter set *No. 43* (excitation wavelength 545/25 nm; FT 570; emission wavelength 605/70 nm)

5.4.3.2 Fluorescence detection by the means of a microtiter plate reader and the Maestro™ imaging system

5.4.3.2.1 Microtiter plate reader assays

Increasing numbers of Katushka expressing cells yielded an increase in fluorescence intensity. The fluorescence signals and cell numbers correlated in a linear manner (**Figure 5.36**). By contrast, the fluorescence intensity of wildtype cells stayed constant, independent of the cell number.

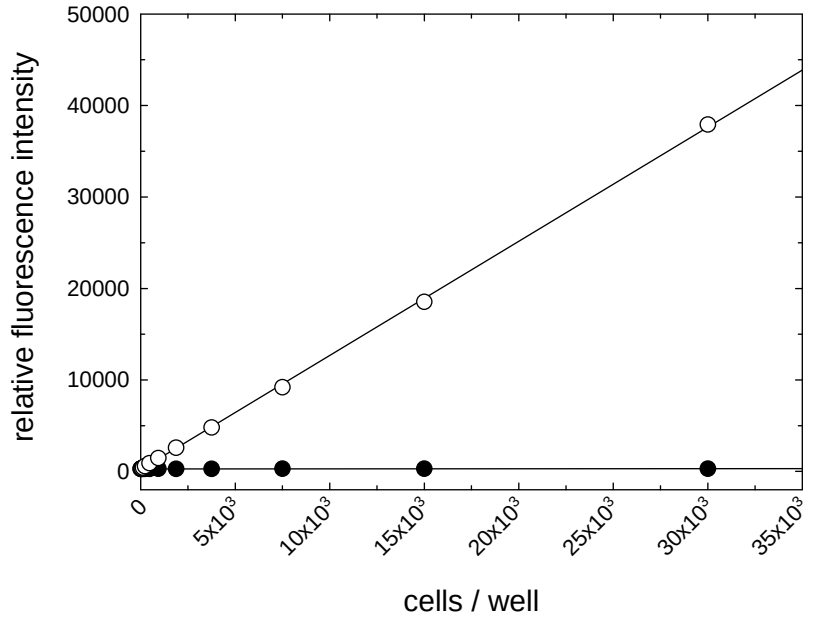

Figure 5.36: Comparison of relative fluorescence intensities determined for U-87 MG wildtype cells (filled circles; 165th passage) and U-87 Katushka_Clone 3 cells (open circles; 11th passage).

The excitation wavelength was 580 nm, whereas the emission was detected at 670 nm.

5.4.3.2.2 Katushka activity in living U-87 and U-373 cells

Excitation was performed using a bandpass filter with a range of 503-555 nm. For analysis, an image cube was generated by overlaying 23 single images in 10 nm steps, ranging from 580-800 nm. With respect to interfering spectra, a reference library containing the Katushka spectrum as well as autofluorescence spectra was recorded and applied in the unmixing procedure.

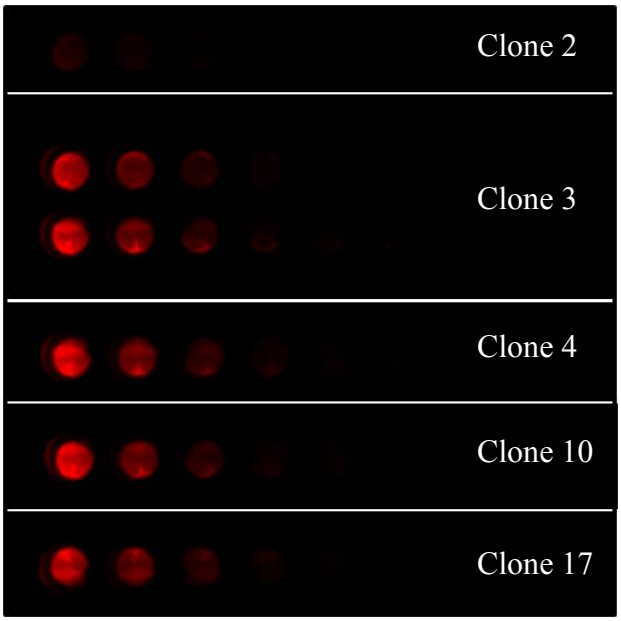

Figure 5.37: Specific Katushka fluorescence in several U-87 Katushka transfectants. The Katushka fluorescence is displayed as red pseudo-color. Cell suspensions were serially diluted 1:2 starting from 300,000 to 293 cells per well (decreasing cell numbers from left to right). The images show the unmixed overlay of 23 single pictures, exposed every 10 nm in the range from 580-800 nm.

Instrument settings: stage height h1c, exposure times 4,660 ms (Clone 3) and 5,000 ms (all other subcultures) for each single 10 nm step.

Taken together, most of the U-87 clones, transfected with pTurboFP635-N, showed higher expression levels of the red fluorescent protein than U-373 Katushka transfectants (data not shown). Whereas at least 37,500 cells of U-87 Katushka_Clone 3, 4, 10 and 17 were resolved by the Maestro™ system, clone 2 proved to be a low-expressing cell line, requiring at least 300,000 cells for detection. According to the signal to noise ratio, 50,000 cells were considered appropriate for orthotopic implantations into the brain of nude mice.

In case of different U-373 Katushka transfectants, only 2 subcultures, namely clone 10 and clone 18 proved to express Katushka at levels allowing the determination of at least 75,000-150,000 cells.

5.4.3.3 Proliferation and chemosensitivity of U-87 and U-373 transfectants against the ABCG2 substrates topotecan and mitoxantrone

5.4.3.3.1 Growth kinetics

Figure 5.38 shows comparative growth curves of U-87 MG wildtype and U-87 Katushka clones as well as U-373 MG wildtype cells and the transfectant U-373 Katushka_Clone 10.

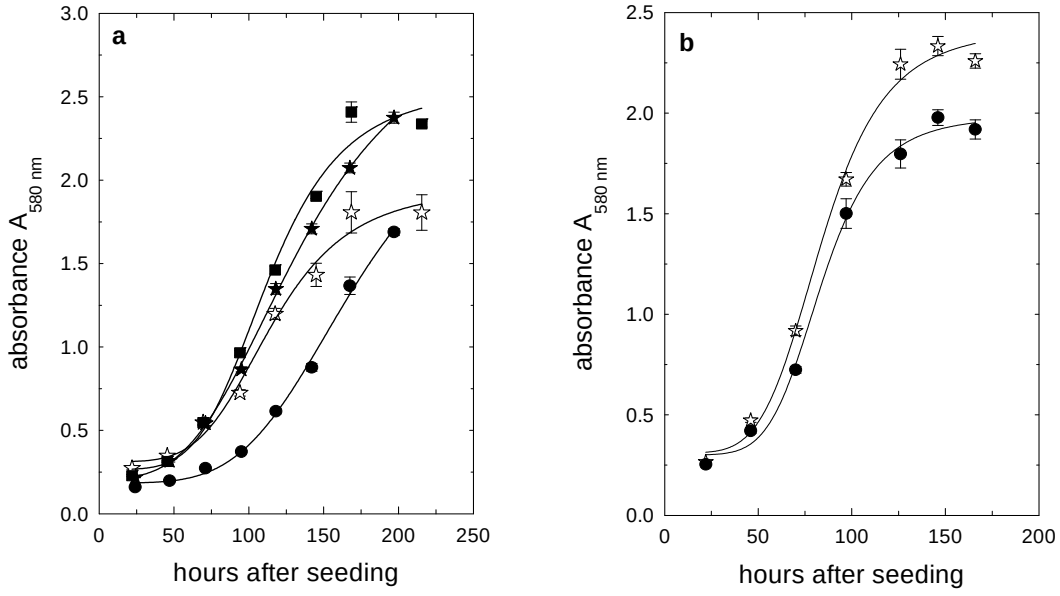

Figure 5.38: In vitro growth kinetics of different U-87 cell lines (a): U-87 MG wildtype cells (open stars 171st passage, filled stars 173rd passage), U-87 Katushka_Clone 3 cells (filled squares, 4th passage) and U-87 Katushka_Clone 10 cells (filled circles, 10th passage); and U-373 cell lines (b): U-373 MG wildtype cells (open stars, 192nd passage) and U-373 Katushka Clone 10 cells (filled circles, 3rd passage).

The transfectant U-87 Katushka_Clone 3 showed comparable in vitro growth kinetics as the U-87 MG wildtype cells, whereas clone 10 was characterized by a slightly retarded in vitro growth (**Figure 5.38a**). The reason for this slower proliferation is caused by a lower initial cell density.

Similar results were obtained in case of U-373 cell variants (**Figure 5.38b**).

5.4.3.3.2 Chemosensitivity of U-87 Katushka transfectants vs. U-87 MG wildtype cells against mitoxantrone and topotecan

Due to lower expression of Katushka and the lack of in vivo tumorigenicity, U-373 transfectants were not considered for the toxicity studies.

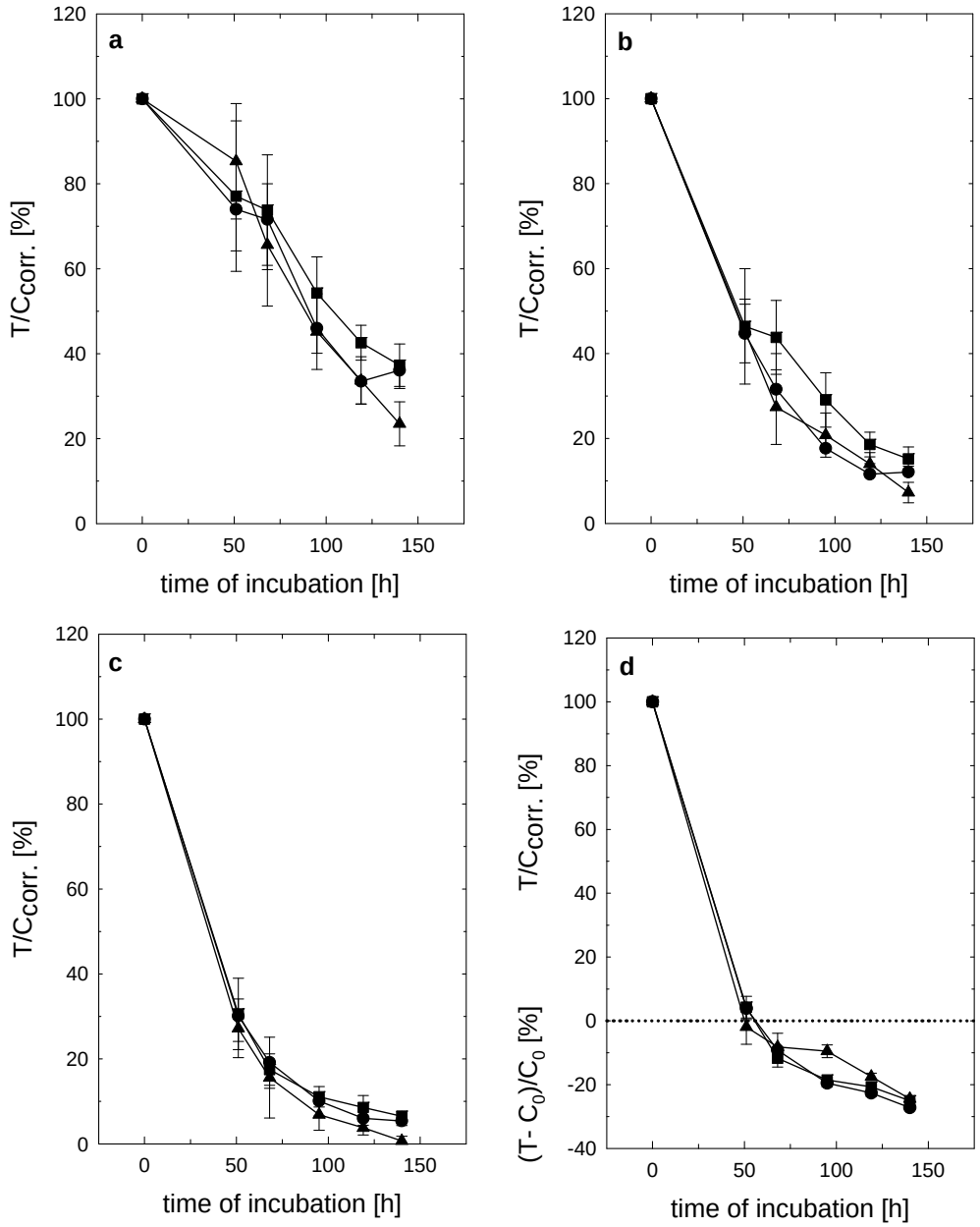

Figure 5.39: Effect of the cytostatic and ABCG2 substrate mitoxantrone on proliferating U-87 MG cells (filled circles; 160th passage), U-87 Katushka_Clone 3 cells (filled squares; 5th passage) and U-87 Katushka_Clone 10 cells (filled triangles; 4th passage)

Cells were incubated with mitoxantrone at concentrations of: 10 nM (a), 50 nM (b), 100 nM (c) and 500 nM (d).

When compared with the respective wildtypes, the sensitivities of all investigated U-87 transfectants against mitoxantrone and topotecan, respectively, were almost identical (**Figure 5.39**, **Figure 5.40**).

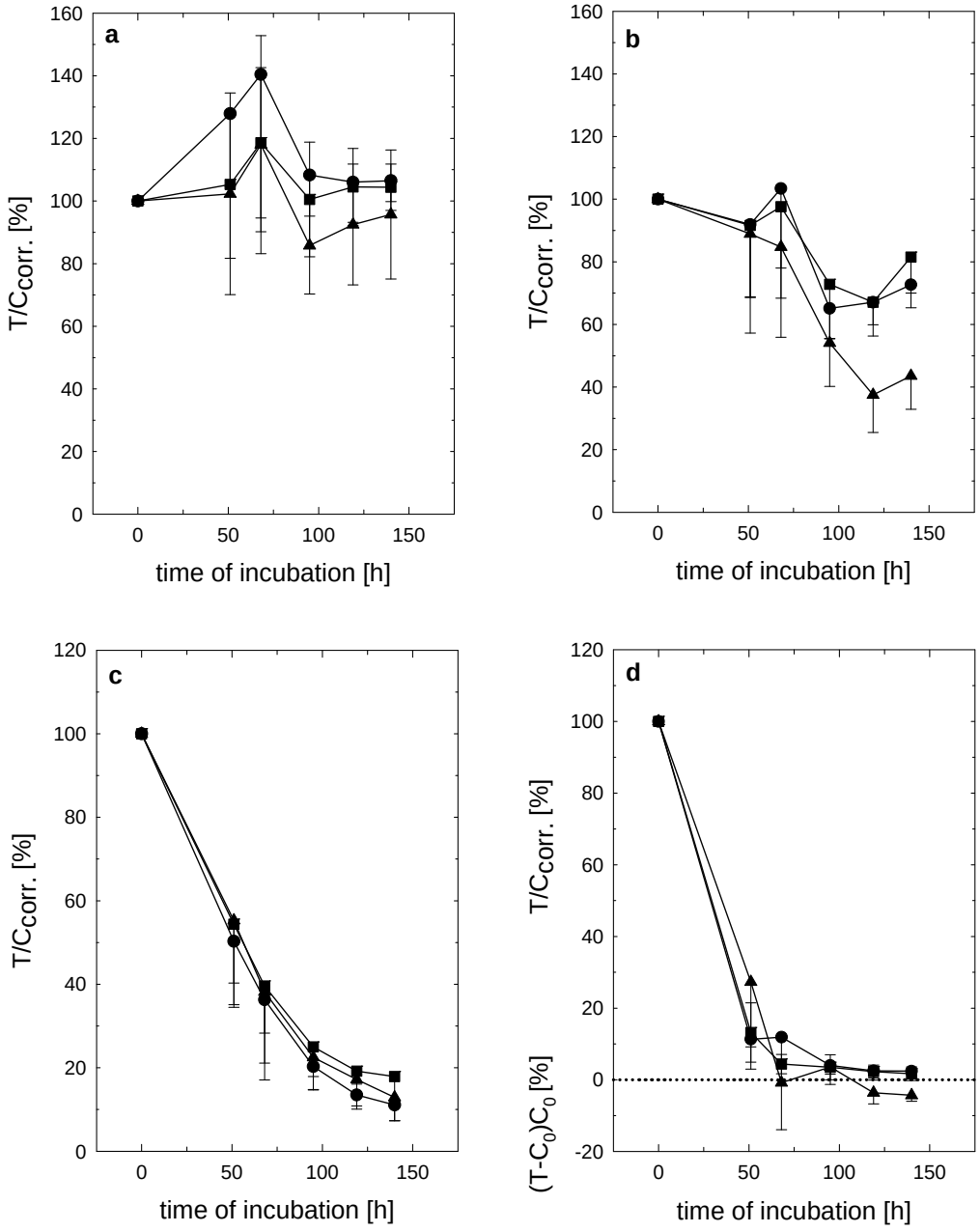

Figure 5.40: Effect of the cytostatic and ABCG2 substrate topotecan on proliferating U-87 MG cells (filled circles; 160th passage), U-87 Katushka_Clone 3 cells (filled squares; 5th passage) and U-87 Katushka_Clone 10 cells (filled triangles; 4th passage).

Cells were incubated with topotecan at concentrations of: 5 nM (a), 25 nM (b), 100 nM (c) and 500 nM (d).

5.4.3.4 Tumorigenicity and in vivo growth kinetics of subcutaneous Katushka-transfected glioblastoma

According to performed in vitro investigations on Katushka expression, growth kinetics and chemosensitivity, the transfectant U-87 Katushka_Clone 3 proved to be suitable for first in vivo studies in nude mice.

For this purpose, the cells were subcutaneously injected into several animals, and the tumorigenicity was recorded via the measurement of tumor diameters once a week. U-87 MG wildtype cells, which were subcutaneously implanted into mice, served as control for classification of the obtained data.

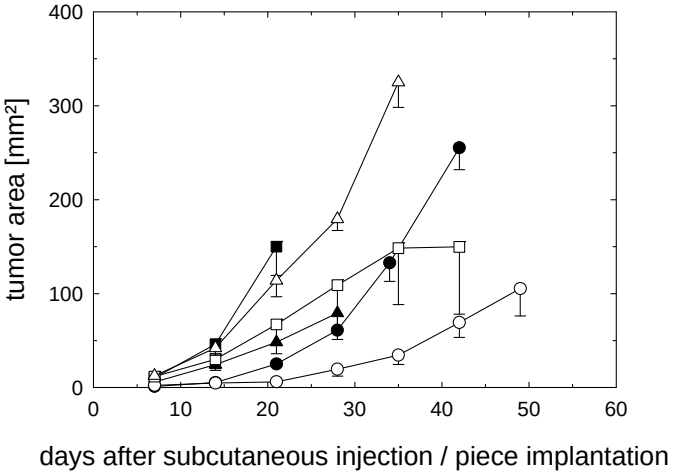

Figure 5.41: In vivo growth kinetics of subcutaneous U-87 MG (filled symbols) and *U-87 Katushka_Clone 3* tumors (open symbols) in nude mice: In vivo passage 0 (circles), 1st passage (squares) and 2nd passage (triangles); (mean values ± SEM).

Table 5.5: Take rates of subcutaneous U-87 MG and *U-87 Katushka_Clone 3* tumors shown for in vivo passages 0, 1 and 2.

Cell line	Passage	Take rate (%)
U-87 MG	0	80
	1	100
	2	100
U-87 Katushka _Clone 3	0	100
	1	100
	2	100

Whereas in passage 0 and 1 U-87 Katuhska_Clone 3 cells showed a delayed in vivo growth compared to the wildtype cells, this behavior was inverted in the second passage resulting in a faster growth rate of U-87 Katushka_Clone 3 tumors than observed for U-87 MG malignancies (**Figure 5.41**).

Nevertheless, the injection of transfected U-87 cells proved to cause persistent subcutaneous tumors with maximal take rates of 100 % in the first 3 in vivo passages.

These observations were confirmed by long-term investigations on the tumorigenicity of subcutaneous U-87 Katushka_Clone 3 tumors (**Figure 5.42**).

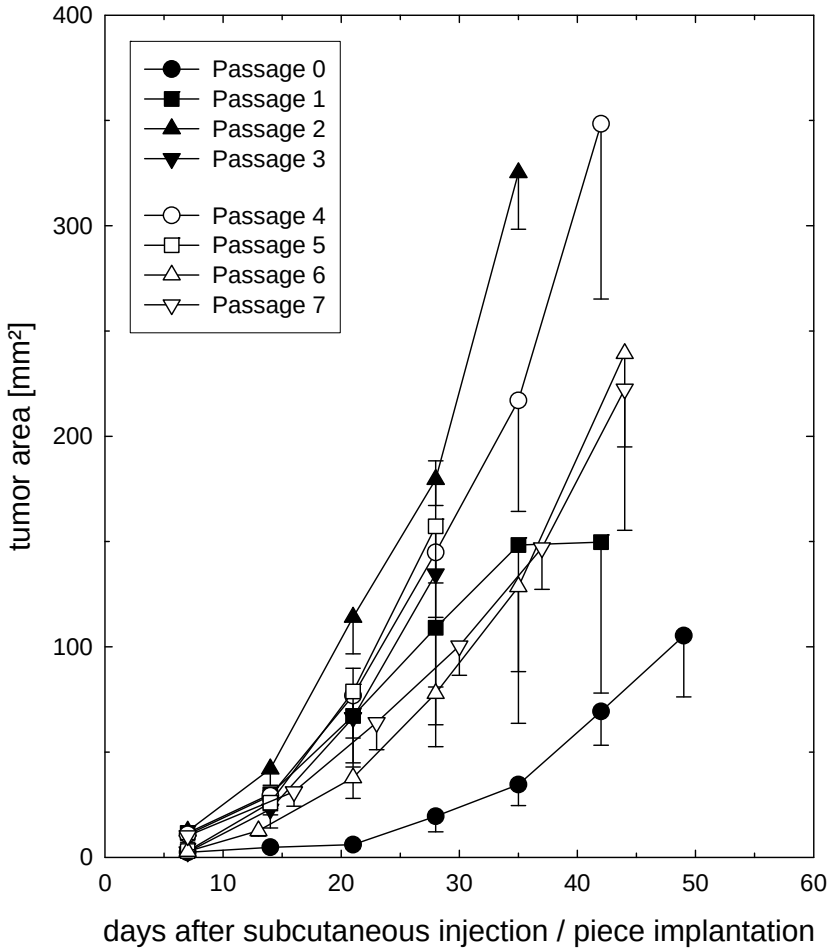

Figure 5.42: In vivo growth kinetics of subcutaneous U-87 Katushka_Clone 3 tumors monitored over 7 in vivo passages (mean values ± SEM).

Over a period of several months, the serially passaged tumor pieces caused a reproducible growth of subcutaneous U-87 Katushka_Clone 3 xenografts (**Figure 5.42**). The growth rates allowed an averaged observation period of approximately 40 days. Furthermore, the investigations proved highest possible take rates of 100 % for all 7 in vivo passages indicating the vitality and high malignancy of U-87 Katushka_Clone 3 tumors.

U-373 Katushka_Clone 10 cells, when subcutaneously implanted into nude mice, did not cause tumor formation for at least 3 months. As mentioned previously (**5.4.2.4**), attempts to establish subcutaneous U-373 MG wildtype tumors failed also. The same situation was observed for U-373 Katushka transfectants.

5.4.3.5 Fluorescence in vivo imaging (FLI) of subcutaneous U-87 Katushka_Clone 3 tumors

The luciferase2 expression of U-87 Luc2 tumors remained stable under in vivo conditions, even in the absence of puromycin, allowing semi-quantitative monitoring of tumor progression by noninvasive in vivo imaging (see **5.4.2.5** and **5.4.2.6**).

By analogy with these investigations, mice bearing solid U-87 Katushka_Clone 3 tumors were anesthetized and Katushka fluorescence was controlled on the Maestro™ fluorescence in vivo imaging system (**Figure 5.43**).

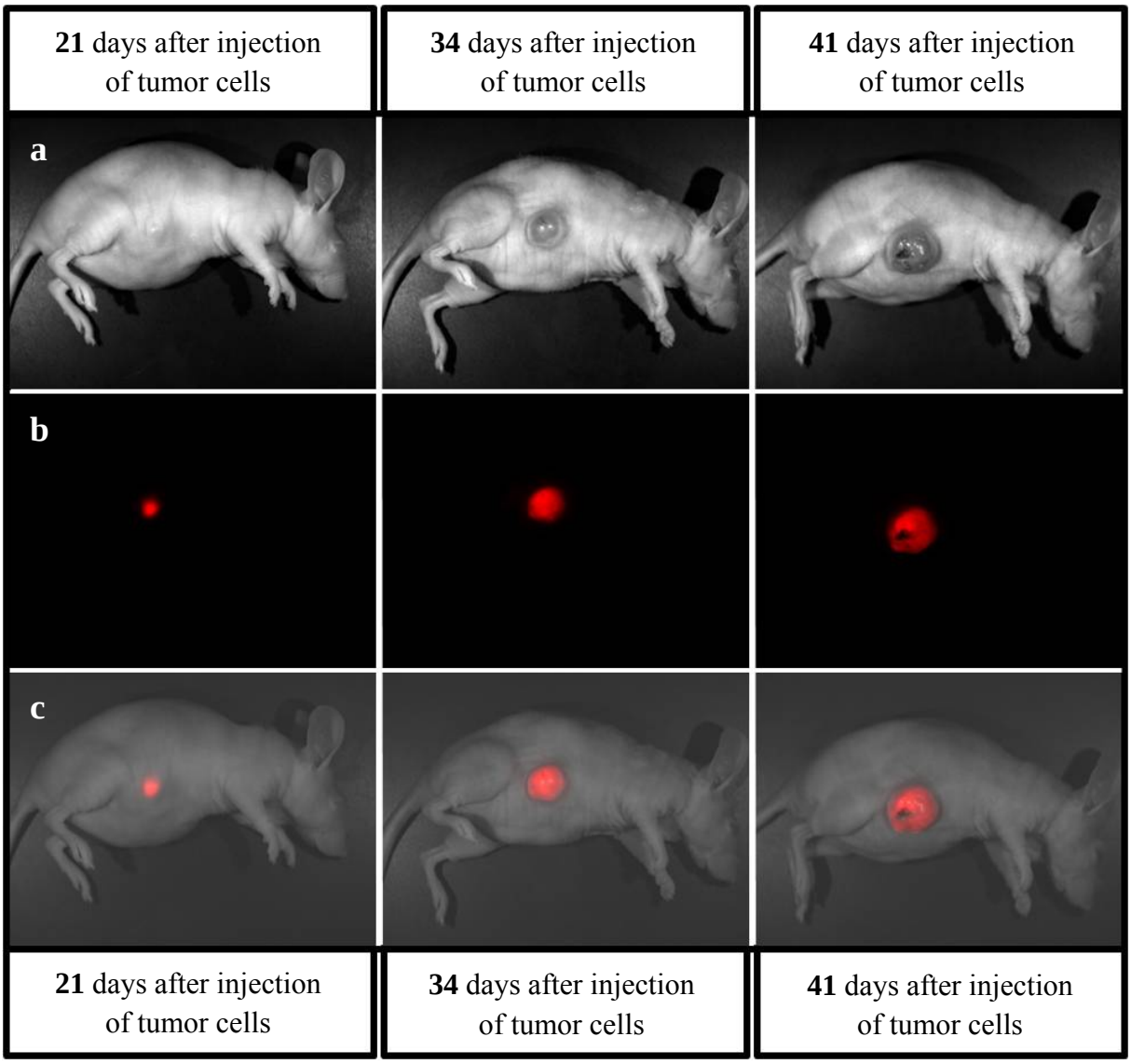

Figure 5.43: Fluorescence in vivo imaging of a subcutaneous U-87 Katushka_Clone 3 tumor. Monitoring over a period of 41 days: bright field images (a), Katushka fluorescence (b) (red pseudo-color; after unmixing procedure) and merge (c).

Instrument settings: excitation 503-555 nm, emission 580 nm cut off, stage height h1c. Images represent an overlay of 23 pictures in 10 nm steps ranging from 580-800 nm (Maestro™ image Cube). Exposure times for fluorescence detection were as follows: 450 ms (studies on day 21), 125 ms (studies on day 34) and 80 ms (studies on day 41).

The studies revealed high stable Katushka expression in subcutaneous U-87 Katushka_Clone 3 neoplasms for the determination of specific fluorescence signals emitted by the tumor tissue. Despite of the short exposure times, fluorescence signals were extremely extensive although there was no selection pressure due to lack of the antibiotic G418 under in vivo conditions.

Figure 5.44 shows an example of the "unmixing procedure" using the Maestro™ software. For analysis of specific fluorescence, the correct spectrum of the fluorophor in the corresponding environment (tissue) has to be determined. Autofluorescence and specific spectra of the transfectants, recorded in vitro, are the basis of a spectral library to be measured for the in vivo situation in various organs and tissues.

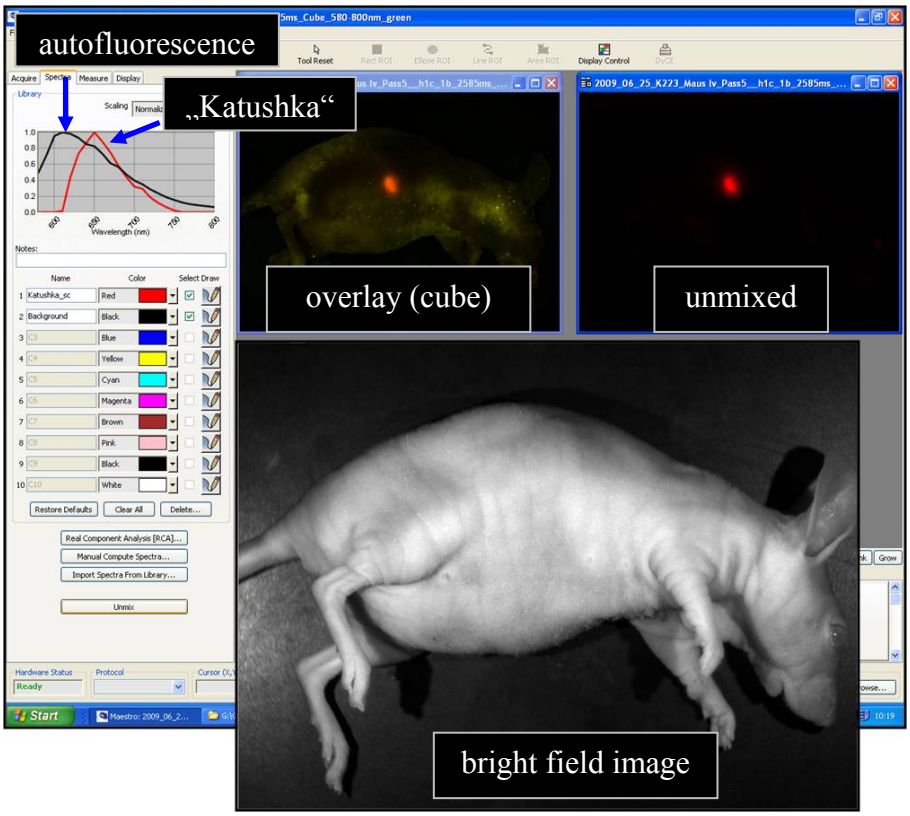

Figure 5.44: Unmixing procedure for fluorescence in vivo imaging demonstrated by means of a small subcutaneous U-87 Katushka_Clone 3 tumor. The autofluorescence in the unmixed overlay picture (black spectrum curve) can be eliminated from the specific Katushka signal (red spectrum curve) by computational analysis.

5.4.3.6 Long-term expression of Katushka in vivo

In order to investigate the growth as well as the Katushka expression of serially passaged subcutaneous tumors, randomly selected mice of each in vivo passage were imaged on the Maestro™ system.

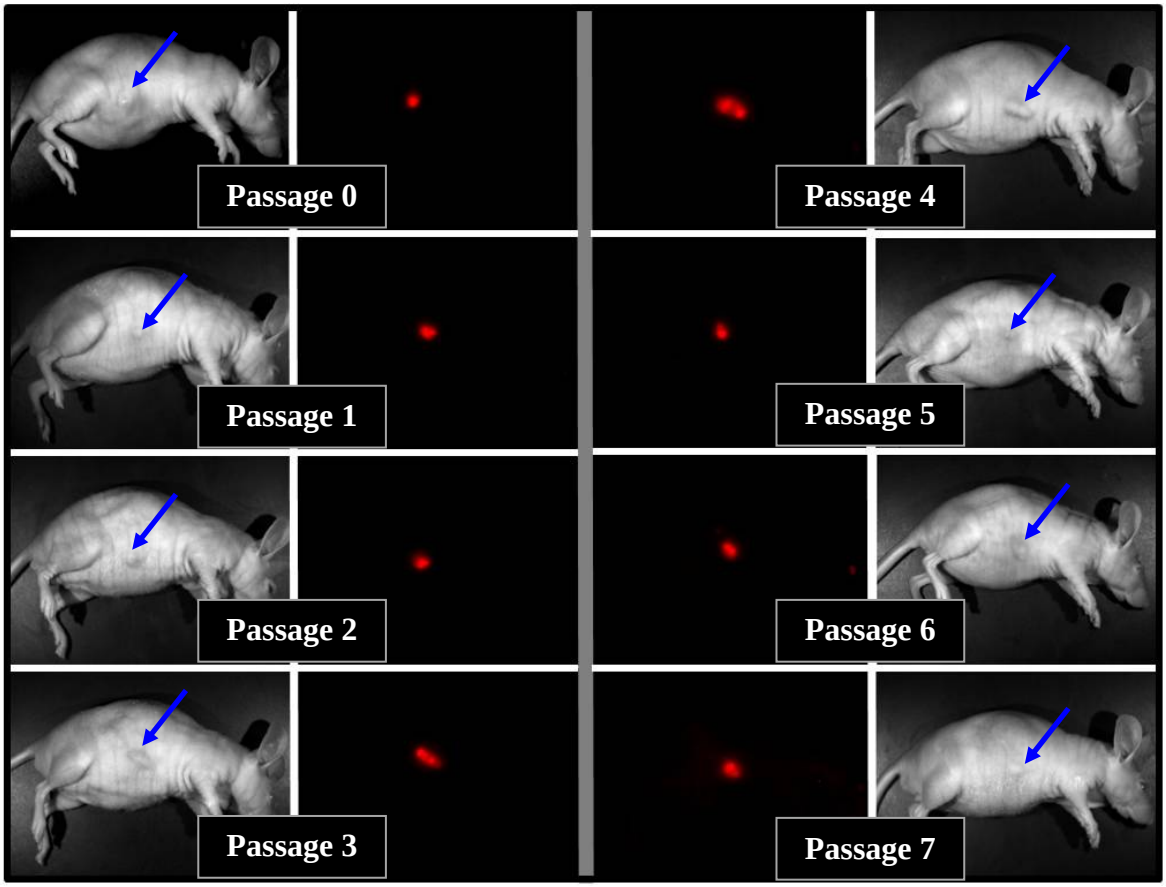

Figure 5.45: Fluorescence in vivo imaging of subcutaneous U-87 Katushka_Clone 3 tumors (marked by blue arrows in bright field images). The studies were performed over a period of 7 in vivo passages (representing several months).

Instrument settings: excitation 503-555 nm, emission 580 nm cut off, stage height h1c. Fluorescence images represent the unmixed overlay of 23 pictures in 10 nm steps ranging from 580-800 nm (Maestro™ image Cube). Exposure times for fluorescence detection were set to the calculated autoexposure values of the software.

The subcutaneous U-87 Katushka_Clone 3 tumors proved to be tissues with stable expression of the red fluorescent protein Katushka. Specific fluorescence signals of the tumors were detected in all investigated in vivo passages, demonstrating preservation of the Katushka encoding gene in these genetically modified tumor cells.

5.4.3.7 Histology of subcutaneous U-87 Katushka tumors

The subcutaneous U-87 Katushka tumors were subjected to histopathological examinations.

As observed for U-87 Luc2 tumors, high malignancy is reflected by numerous mitoses and the incidence of pleomorphic nuclei (**Figure 5.46**).

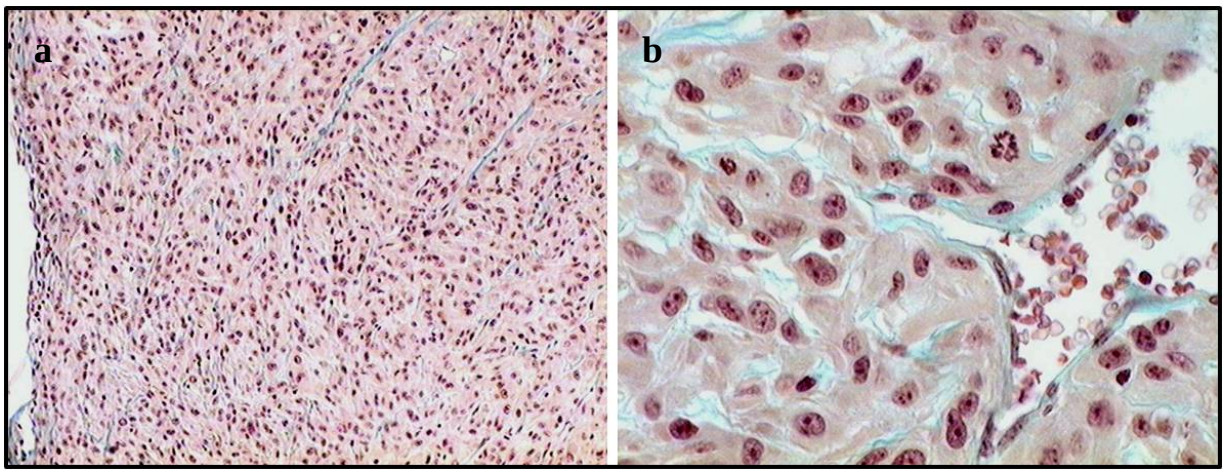

Figure 5.46: Masson-Goldner stains of a subcutaneous U-87 Katushka_Clone 3 tumor: low magnification (a) and high magnification (b).

5.4.3.8 Fluorescence in vivo imaging (FLI) of intracerebral U-87 Katushka_Clone 3 tumors in nude mice

The U-87 Katushka_Clone 3 transfectant was regarded as suitable for the intracerebral implantation into nude mice. 50,000 cells of U-87 Katuhska_Clone 3 were implanted into the brains of 13 female nude mice.

10 days after the implantation procedure, 2 of the 13 mice developed orthotopic human glioblastomas that could be detected by their fluorescence. After additional 10 days, orthotopic brain tumors were visualized by FLI in 7 out of 12 investigated animals. 1 mouse had to be killed earlier due to loss of body weight > 10 %. The final studies, performed on day 27, proved the existence of intracerebral brain tumors in 11 of 13 nude mice, demonstrating a high take rate of 85 %.

Figure 5.47 shows representative fluorescence images of 2 selected mice bearing intracerebral U-87 Katushka_Clone 3 tumors. The animals were investigated by FLI for a total of 27 days. Whereas the whole body of mouse 1 was imaged, the FLI pictures of mouse 2 represent details of the animal's head region. These examples demonstrate the suitability of FLI as a semi-quantitative method to monitor intracerebral tumor progression.

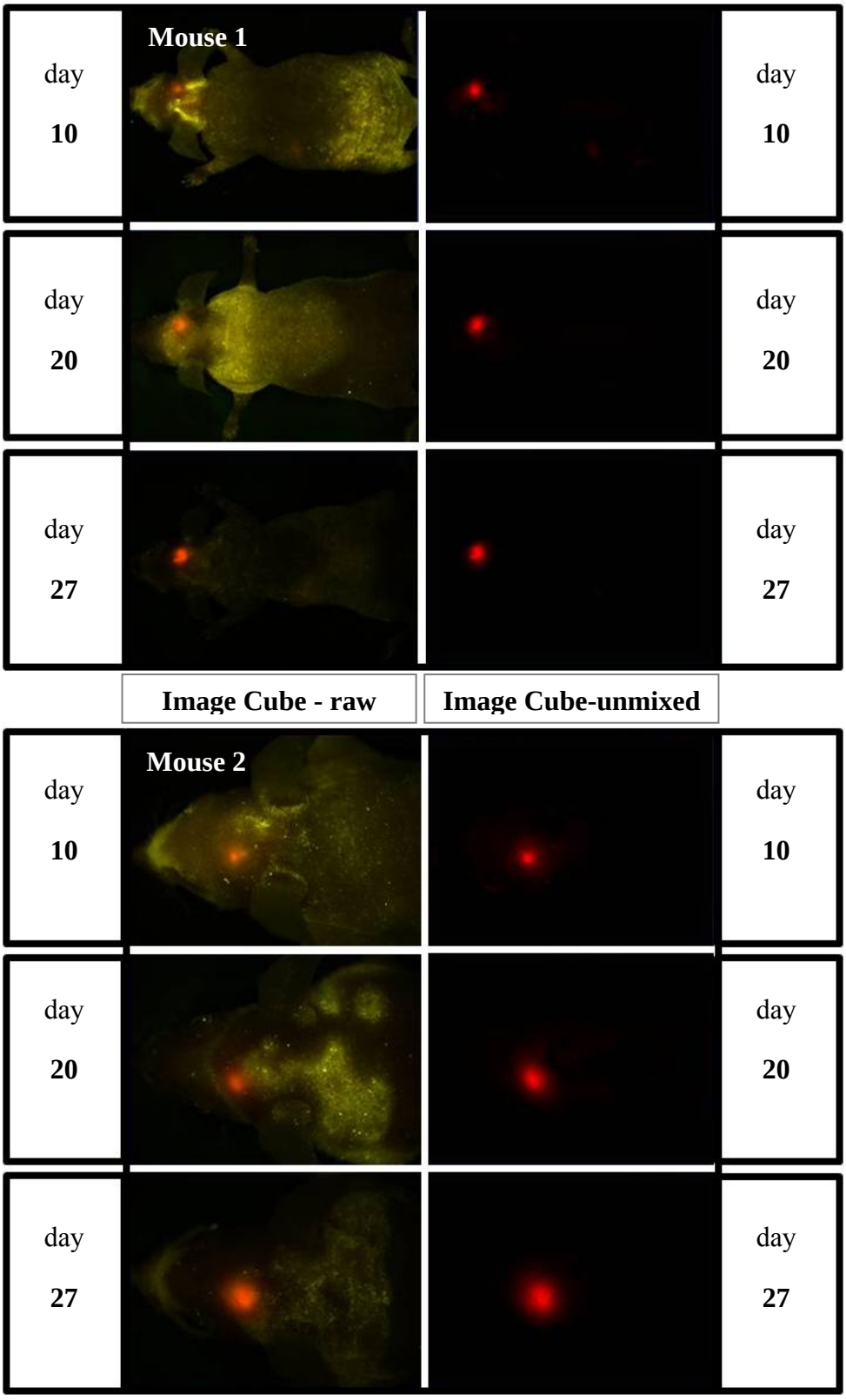

Figure 5.47: Fluorescence in vivo imaging of nude mice bearing intracerebral U-87 Katushka_Clone 3 xenografts. The studies were performed 10, 20 and 27 days after tumor cell implantation. Left images show the "raw" image cubes (580-800 nm, 10 nm steps) containing unspecific signals such as autofluorescence, whereas right images represent corresponding unmixed pictures.

Instrument settings: excitation filter 503-555 nm, emission filter 580 nm cut off, stage height h2 (mouse 1) and h3 (mouse 2). Exposure times were set to the calculated autoexposure values of the software.

5.4.3.9 Comparison of FLI data and histopathology of orthotopic U-87 Katushka_Clone 3 tumors

Table 5.6 summarizes both, the FLI data and the histology, displayed for each individual mouse.

Table 5.6: Overview of results obtained from FLI studies and histopathological examinations on orthotopic human glioblastoma (*U-87 Katushka_Clone 3*) in nude mice.

	Tumor detection by Fluorescence signal	**Histological detection of orthotopic tumor growth**
Mouse 1	+	+
Mouse 2	+	+
Mouse 3	+	+
Mouse 4	+	+
Mouse 5	+	+
Mouse 6	+	+
Mouse 7	+	+
Mouse 8	+	+
Mouse 9	+	+
Mouse 10	+	+
Mouse 11	+/-	-
Mouse 12	+	+
Mouse 13	-	+

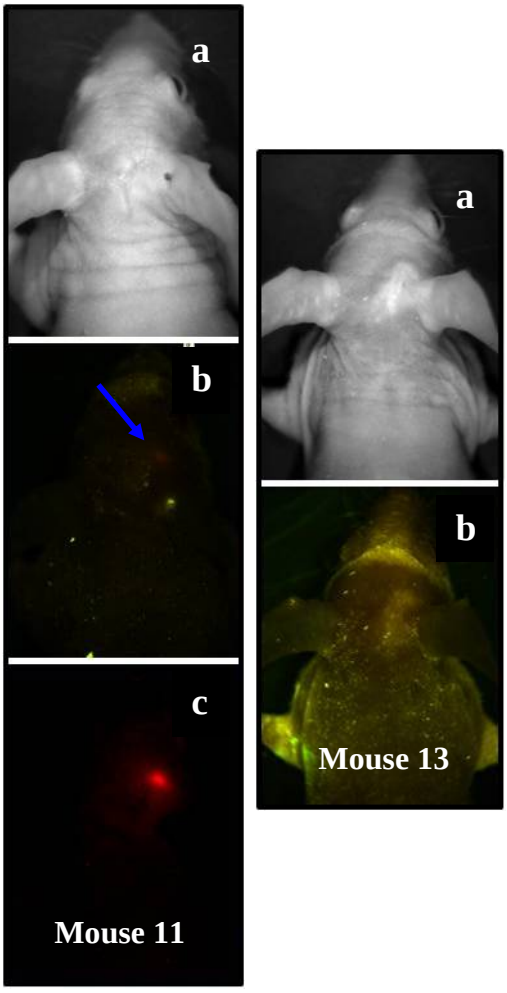

Figures 5.48: FLI of mouse 11 and mouse 13: bright field (a), overlay (b) and unmixed cube (c). Unmixing procedure for mouse 13 was not performed due to missing specific Katushka fluorescence. The blue arrow in the overlay of mouse 11 marks a weak fluorescence signal which could be confirmed by the unmixing procedure.

The histopathological investigations confirmed 11 intracerebral U-87 Katushka_Clone 3 tumors. Hence, in 11 of totally 13 cases, the FLI data were in agreement with histopathology. Even signals as low as of mouse 11 could be detected via FLI (left part of **Figure 5.48**).

A possible reason for a false-negative result of the histopathological examination has been discussed under **5.4.2.9**. Inversely, a false-negative result of FLI (see mouse 13; right part of **Figure 5.48**) can be explained either by a very deep localization of a small tumor, or factors affecting fluorescence e.g. pH, oxygen partial pressure as well as physical properties of the environment such as lipophilicity. It is well known that the microenvironment of tumor cells in different areas of the neoplasm is very heterogeneous.

The reproducibility of the established orthotopic glioblastoma model was checked in a second independent experiment using 5 male nude mice. The implantation procedure was performed as described for the first study, and mice were investigated by FLI after 10, 16, 22 and 29 days. At the end, intracerebral U-87 Katushka_Clone 3 tumors were detected in all animals by FLI and confirmed by histopathological investigation (for an example, cf. **Figure 5.49**) in 4 out of 5 brains.

Taken together, the FLI of orthotopic U-87 Katushka_Clone 3 tumors and the successive histological examinations of dissected brain tissues were in very good agreement. In 83 % of all investigated mice, orthotopic human glioblastoma were detected by both, noninvasive fluorescence in vivo imaging and histopathology.

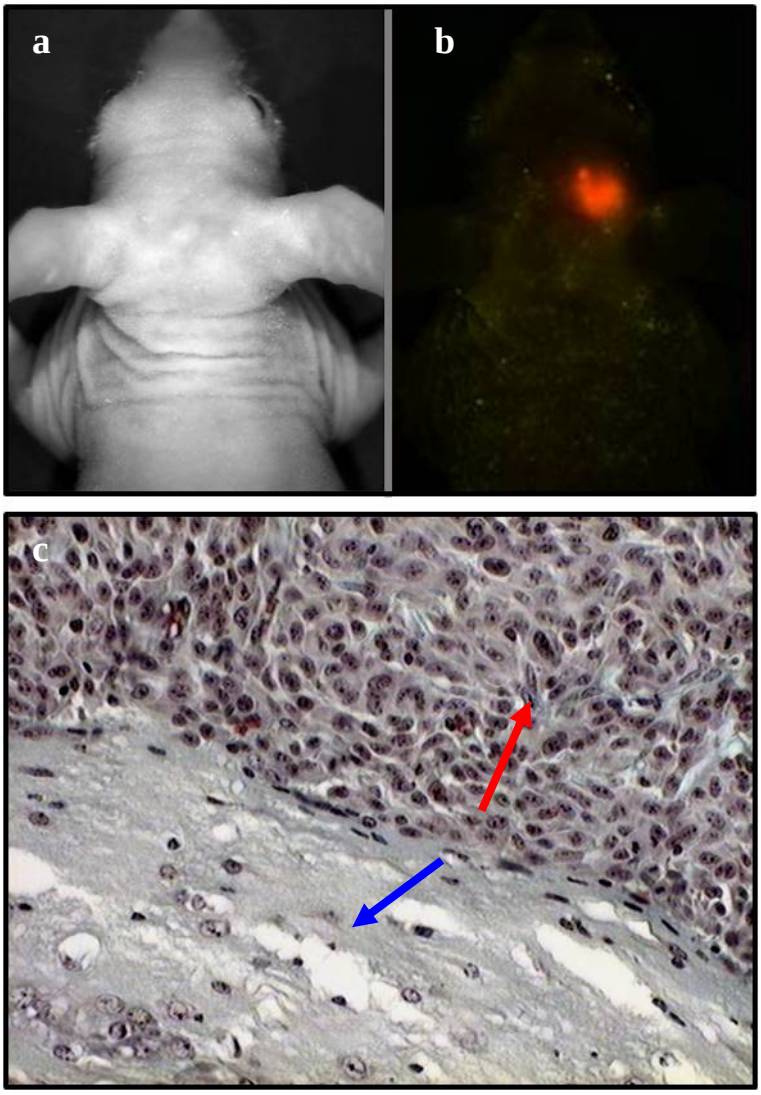

Figure 5.49: Bright field image of mouse 1 (a), and corresponding fluorescence image with a high intensity specific fluorescence signal localized in the brain of mouse 1 (b).

Histopathology of a human glioblastoma, orthotopically grown in nude mouse 1 (c): Masson-Goldner staining; the normal, non-malignant brain tissue (blue arrow) and the intracerebral high grade glioblastoma (red arrow).

The morphology of intracerebral U-87 Katushka_Clone 3 tumors appeared similar to that of orthotopic U-87 Luc2 tumors.

5.4.4 In vivo imaging using co-transfected human glioblastoma cells bearing bioluminescent and fluorescent reporter genes

In order to directly compare the advantages and limitations of BLI and FLI in one and the same specimen, U-87 and U-373 cells were co-transfected with the genes encoding the luc2 enzyme and the red fluorescent proteins Katushka or DsRed2, respectively. For this purpose, U-87 MG and U-373 MG cells were simultaneously transfected with the pGL4.20 vector and the pDsRed2-C1 vector, whereas stably expressing U-87 Luc2 and U-373 Luc2 cells were used for co-transfection studies with the pTurboFP635-N vector. As described for the mono-transfectants, the co-transfectants were characterized in vitro with respect to protein expression, growth kinetics and chemosensitivity. Furthermore, the tumorigenicities of the cell lines and the applicability of reporter gene expression for BLI and FLI were studied in subcutaneous tumor models. Finally, suitable co-transfectants were implanted into the brain of nude mice, and the tumor progression was noninvasively monitored by means of both optical imaging devices.

Approximately 4 weeks after transfection, several resistant colonies were picked for cultivation (designated according to the nomenclature of the mono-transfectants). Residual cells were pooled and termed U-87 and U-373 Luc2/DsRed2 3:2, 6:2 and 9:2 (according to the nomenclature of the mono-transfectants).

5.4.4.1 Luciferase2 and DsRed2 expression in co-transfected U-87 and U-373 cell lines

The determination of luc2 activity in cell lysates as well as epifluorescence microscopy revealed that all U-87 Luc2/DsRed2 co-transfectants lost at least 1 of the 2 reporter genes immediately after transfection. Hence, further investigations on U-87 Luc2/DsRed2 cells could not be performed. However, the in vitro investigations of U-373 co-transfectants were successful.

1 promising clone, namely U-373 Luc2/DsRed2_Clone 2, was identified by both, luciferase2 expression (luc2 activity in cell lysates) and DsRed2 fluorescence (**Figure 5.50**).

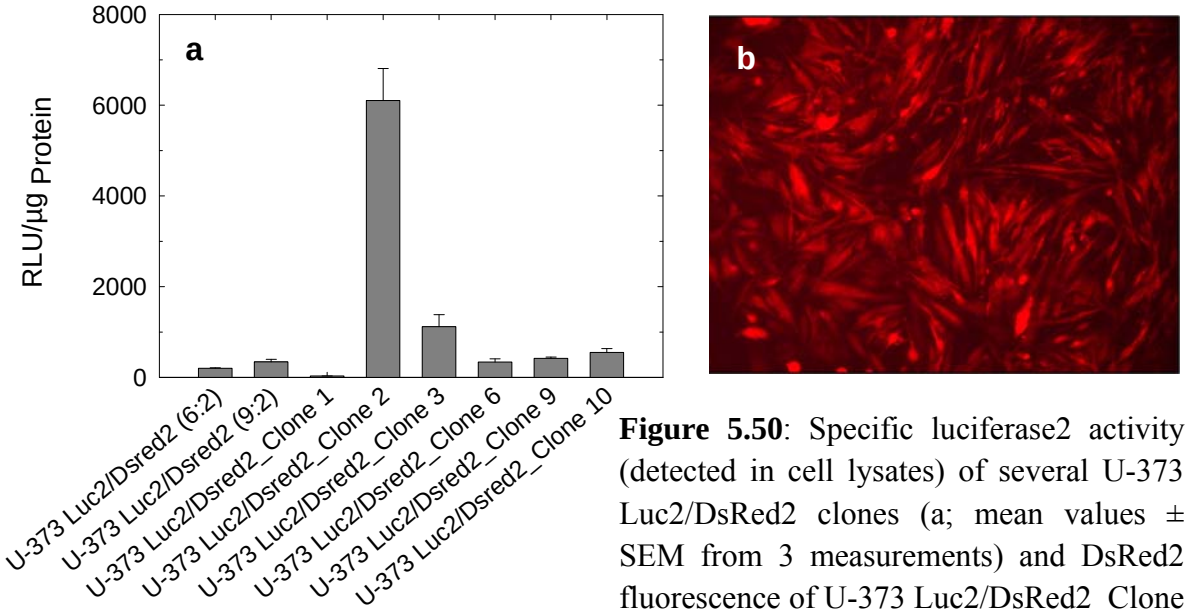

Figure 5.50: Specific luciferase2 activity (detected in cell lysates) of several U-373 Luc2/DsRed2 clones (a; mean values ± SEM from 3 measurements) and DsRed2 fluorescence of U-373 Luc2/DsRed2_Clone 2 cells (b; Leica DM-IRB microscope (Texas Red filter cube), exc. 560/40 nm, em. 645/75 nm).

5.4.4.2 Effect of cell number on luc2 expression and Katushka fluorescence

A dilution series of U-373 Luc2/DsRed2_Clone 2 cells was prepared in EMEM without phenol red. Subsequently, the cells were seeded into 2 separate 96-well plates at various densities. For the determination of luc2 activity on living cells, the transfectants were incubated with D-luciferin, and the emitted photons were integrated over a period of 30 min. In parallel, the DsRed2 fluorescence of U-373 Luc2/DsRed2_Clone 2 cells was measured using the Maestro™ in vivo imaging system. The minimal cell number per well which could be detected by both methods was about 75,000 (**Figure 5.51**). The limit of detection was low enough with respect to the intended cell number for the implantation into the brain of nude mice.

Figure 5.51: BLI and FLI of U-373 Luc2/DsRed2_Clone 2 cells, seeded into 96-well plates (300,000 – 293 cells / well; 1:2 dilution steps; decreasing cell numbers from left to right).

Instrument setting for BLI: stage height h2a, EM gain 255, exposure time 1800 s (300 s after D-luciferin application, no binning, readout rate 1 MHz. at 16 bit; instrument settings for FLI: stage height h1, exc. 503-555 nm, em. 580 nm cut of, exposure time 5000 ms for each 10 nm step (range: 580-800 nm (cube)).

5.4.4.3 Proliferation and chemosensitivity of U-373 Luc2/DsRed2_Clone 2 cells against the ABCG2 substrates topotecan and mitoxantrone

The investigation on U-373 Luc2/DsRed2_Clone 2 cells revealed comparable growth kinetics of the co-transfectants and the corresponding U-373 MG wildtype cells (**Figure 5.52**), and there was no difference in the chemosensitivity against mitoxantrone (**Figure 5.53**) and topotecan (**Figure 5.54**) respectively, between the co-transfectants and the wildtype cells.

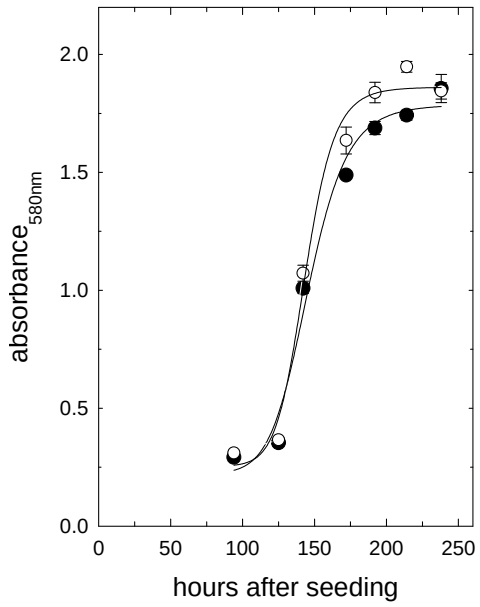

Figure 5.52: In vitro growth kinetics of U-373 MG wildtype cells (filled circles; 213th passage) and U-373 Luc2/DsRed2_Clone 2 cells (open circles; 12th passage).

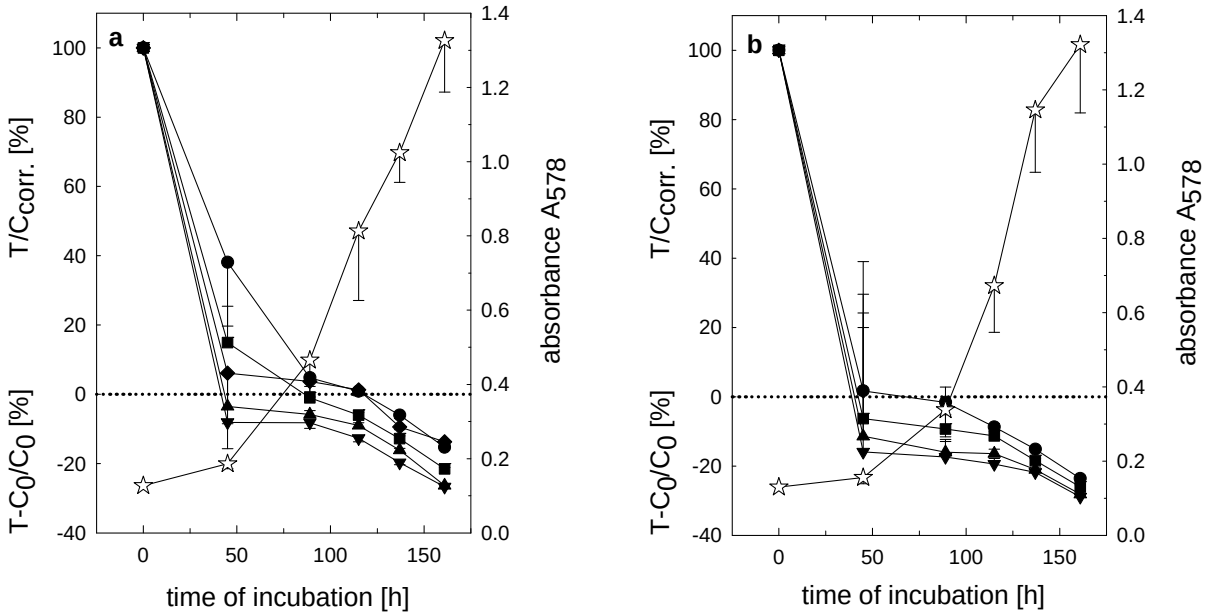

Figure 5.53: Effect of the cytostatic and ABCG2 substrate mitoxantrone on proliferating U-373 MG wildtype cells (a; 216th passage) and U-373 Luc2/DsRed2_Clone 2 cells (b; 14th passage)

Cells were incubated with ethanol 70 % (open stars; vehicle control) and increasing concentrations of mitoxantrone: 10 nM (filled circles), 50 nM (filled squares), 100 nM (filled triangles) and 500 nM (filled inverted triangles).

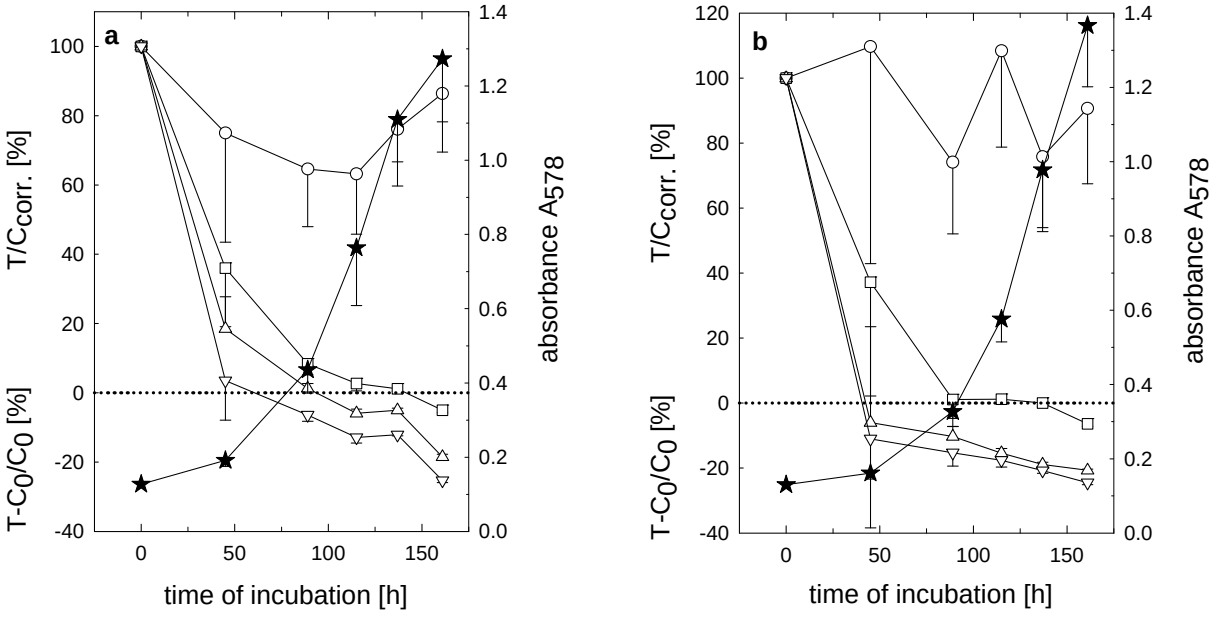

Figure 5.54: Effect of the cytostatic and ABCG2 substrate topotecan on proliferating U-373 MG wildtype cells (a; 216th passage) and U-373 Luc2/DsRed2_Clone 2 cells (b; 14th passage).

Cells were incubated with ethanol 70 % (filled stars; vehicle control) and increasing concentrations of topotecan: 5 nM (open circles), 50 nM (open squares), 100 nM (open triangles) and 500 nM (open inverted triangles).

5.4.4.4 Tumorigenicity of U-373 Luc2/DsRed2_Clone 2 cells after subcutaneous injection into nude mice

After subcutaneous injection of U-373 Luc2/DsRed2_Clone 2 cells into thymus aplastic mice, 1 animal developed a solid tumor after a period of approximately 2 months. The respective mouse was killed and the tumor was dissected for tumor propagation in vivo. Furthermore, to confirm malignancy of the tissue, several tumor pieces were fixed with Bouin's fixative for histopathology. **Figure 5.55** shows the growth kinetics and the histology of the subcutaneous U-373 Luc2/DsRed2_Clone 2 xenograft.

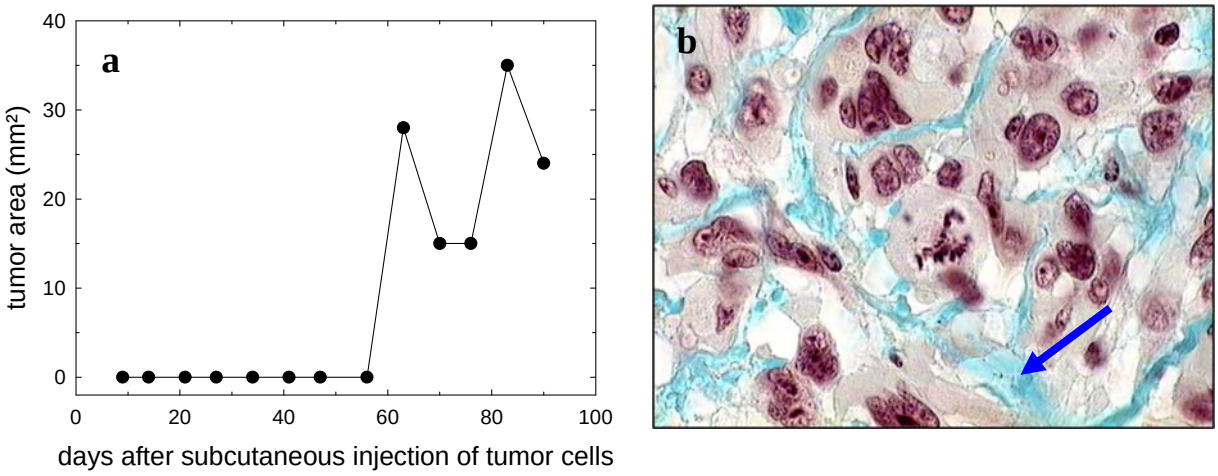

Figure 5.55: In vivo growth kinetics of the single U-373 Luc2/DsRed2_Clone 2 tumor (a) and its corresponding microscopy image of the histopathology (b).

The histology confirmed high-grade malignancy of the generated subcutaneous tumor. Numerous mitoses were detected. As described for U-373 MG wildtype tumors by Dr. Peter Altenschöpfer [Altenschöpfer, 1998], the subcutaneous U-373 Luc2/DsRed2_Clone 2 tumor was characterized by extreme pleomorphology and higher extents of connective tissue (**Figure 5.55b**, marked by an blue arrow) than observed for U-87 tumors.

The subcutaneous passaging of small tumor pieces (1st in vivo passage) resulted in faster tumor formation and higher take rates than observed for the injection of suspended cells (data not shown). However, this effect was already inverted in the 2nd in vivo passage yielding again only a few solid tumors (data not shown). These observations underline the described problems associated with U-373 xenografts.

5.4.4.5 Optical imaging of subcutaneous U-373 Luc2/DsRed_Clone 2 tumors using bioluminescence in vivo imaging (BLI) and fluorescence in vivo imaging (FLI)

To detect the expression levels of luc2 and DsRed2 in vivo, 2 mice bearing subcutaneous U-373 Luc2/DsRed2_Clone 2 tumors were studied by BLI and FLI (**Figure 5.56**). The animals were anesthetized and light signals were recorded after application of D-luciferin. Subsequently, the DsRed2 fluorescence intensity of these tumors was investigated by means of FLI.

However, although the subcutaneous tumors were visible, both BLI and FLI failed to detect the malignancies, indicating absence or dysfunction of luc2 and DsRed2. Obviously, the tumor tissue which was used for serial passaging (from passage 0 to passage 1) had already lost the transfected genes. Hence, the studies on luc2 and DsRed2 co-transfected glioblastoma cells were discontinued.

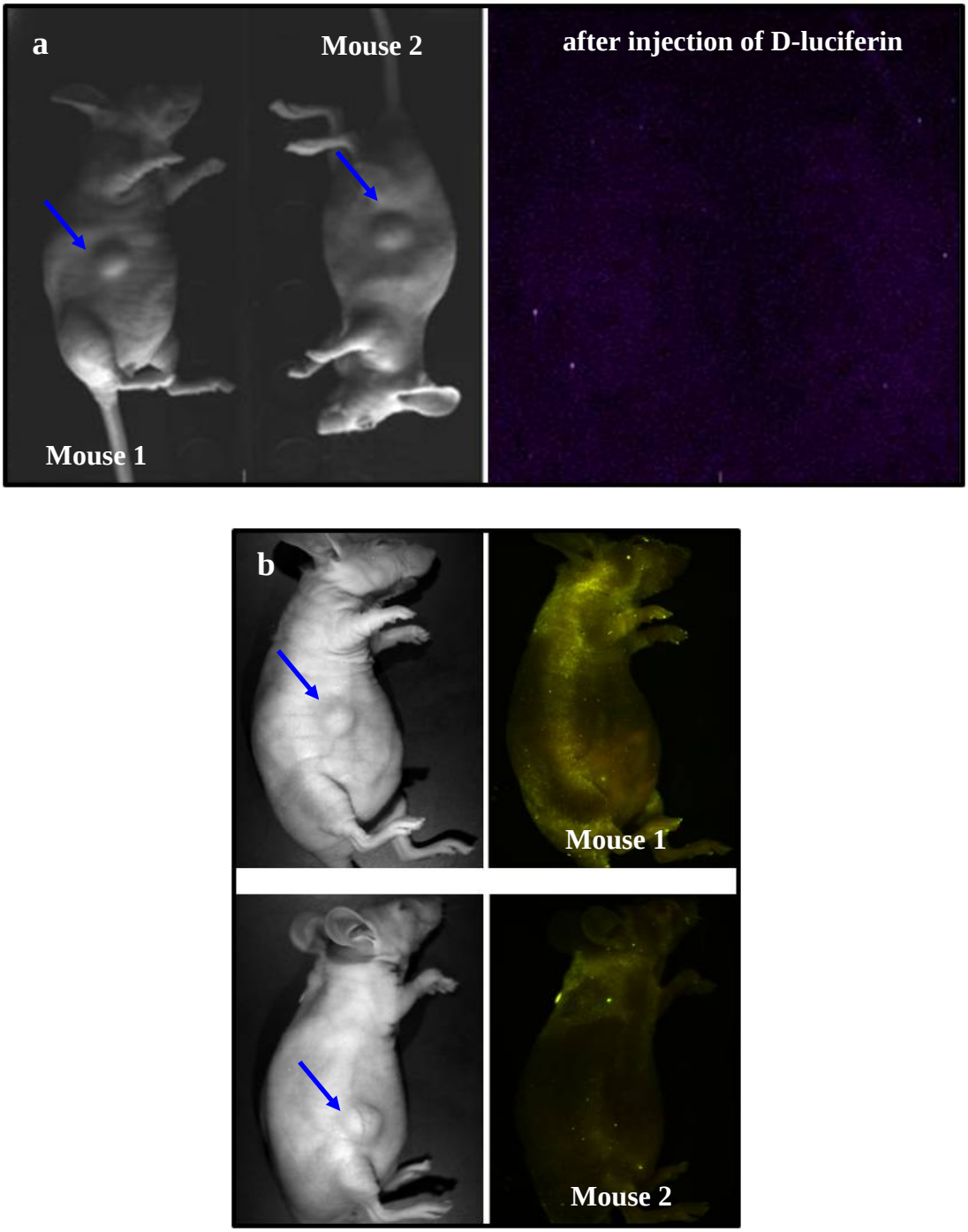

Figure 5.56: BLI (a) of subcutaneous U-373 Luc2/DsRed2_Clone 2 tumors (marked by blue arrows in bright field images) and corresponding FLI (b) experiments. Specific tumor signals could not be detected, neither by bioluminescence nor by fluorescence.

Instrument settings of BLI: stage height h2a, EM gain 255, exposure time 600 s (600 s after D-luciferin application), no binning, readout rate 1 MHz. at 16 bit.

Instrument settings of FLI: stage height h2, exposure times were set to the calculated autoexposure values of the software, excitation filter 503-555 nm, and emission filter 580 nm cut off; fluorescence images represent a cube of 23 single exposures in the range from 580-800 nm.

5.4.4.6 Luciferase2 activity and Katushka fluorescence in live U-87 and U-373 co-transfectants

Several subcultures of U-87 Luc2 and U-373 Luc2 cells, which had been additionally transfected with the gene encoding the Katushka protein, showed fluorescence (conventional fluorescence microscopy; data not shown). For this reason, the sensitivity of both, FLI and BLI, was detected for these promising co-transfected clones.

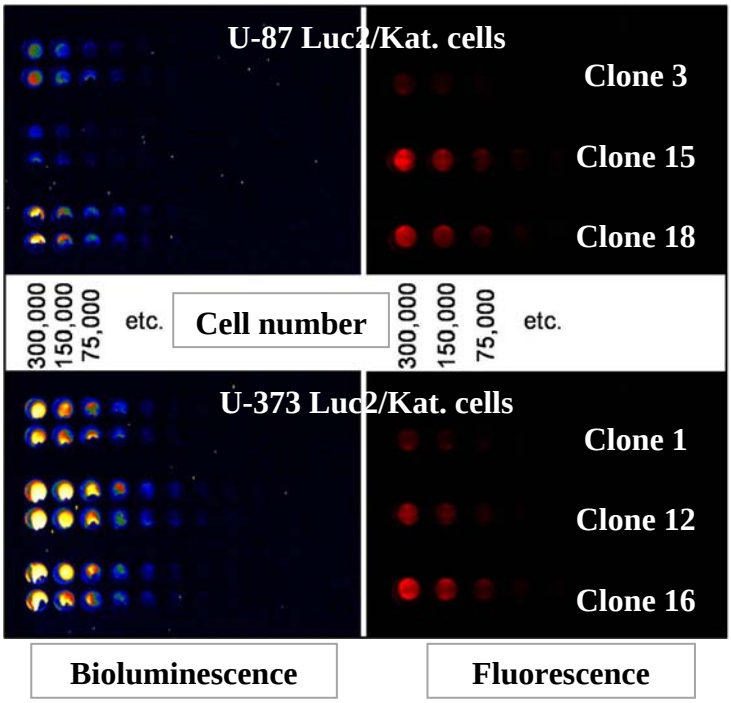

Figure 5.57: BLI and FLI of different U-87 Luc2/Katushka and U-373 Luc2/Katushka clones.

Instrument settings of BLI: stage height h2a, EM gain 255, exposure time 1800 s (300 s after incubation with D-luciferin), no binning, readout rate 1 MHz. at 16 bit.

Instrument settings of FLI: stage height h1c, exposure time 5000 ms for each single image of the cube (overlay of 23 pictures ranged from 580-800 nm), exc. 503-555 nm, emission 580 nm cut off.

The investigations on U-87 Luc2 / Katushka co-transfectants revealed stable expression of luciferase2 and Katushka in several clones. Depending on the clone and the used imaging method (BLI or FLI), the measurements allowed the detection of at least 38,500 – 75,000 cells (**Figure 5.57**). The U-373 co-transfectants showed high activity of luciferase2 in all investigated clones allowing determination of at least 9,375 cells by bioluminescence, whereas the Katushka associated fluorescence proved to be sufficient to detect a minimum of 37,500 cells (**Figure 5.57**).

Thus, the lowest detectable cell numbers of co-transfected human glioblastoma cells were at least in the same range as the amount of cells (50,000 cells in a total volume of 10 µL) used for the implantation into the brain of nude mice.

5.4.4.7 Proliferation and chemosensitivity of U-87 and U-373 co-transfectants against the ABCG2 substrates topotecan and mitoxantrone

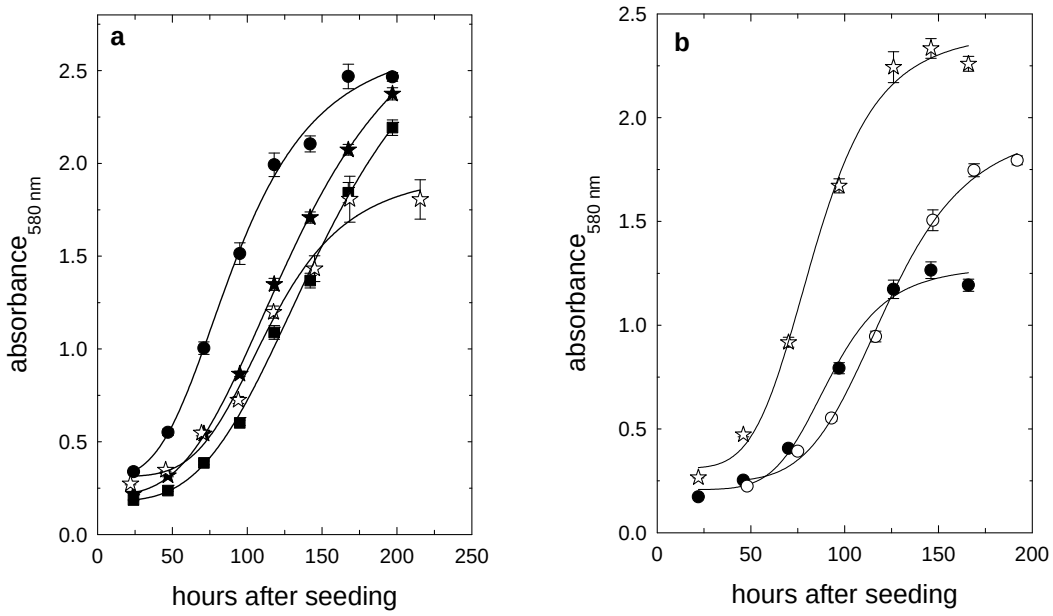

Figure 5.58: In vitro growth kinetics of U-87 cells (a): U-87 MG (171st passage open stars, 173rd passage filled stars), U-87 Luc2/Katushka_Clone 15 (filled circles, 5th passage) and U-87 Luc2/Katushka_Clone 18 (filled squares, 5th passage); and U-373 cells (b): U-373 MG (open stars, 192nd passage) and U-373 Luc2/Katushka_Clone 16 cells (3rd passage filled circles, 5th passage open circles); mean values ± SEM.

Whereas U-87 Luc2/Katushka_Clone 15 and clone 18 cells showed comparable growth kinetics as the wildtype cells (**Figure 5.58a**), clone 16 of U-373 co-transfectants was growing more slowly and less dense than U-373 MG cells (**Figure 5.58b**). However, this effect is most probably due to the seeding at a lower density.

With respect to the chemosensitivity there was no difference against mitoxantron (**Figure 5.60**) and topotecan (**Figure 5.59**) respectively, between the co-transfectants and the wildtype cells.

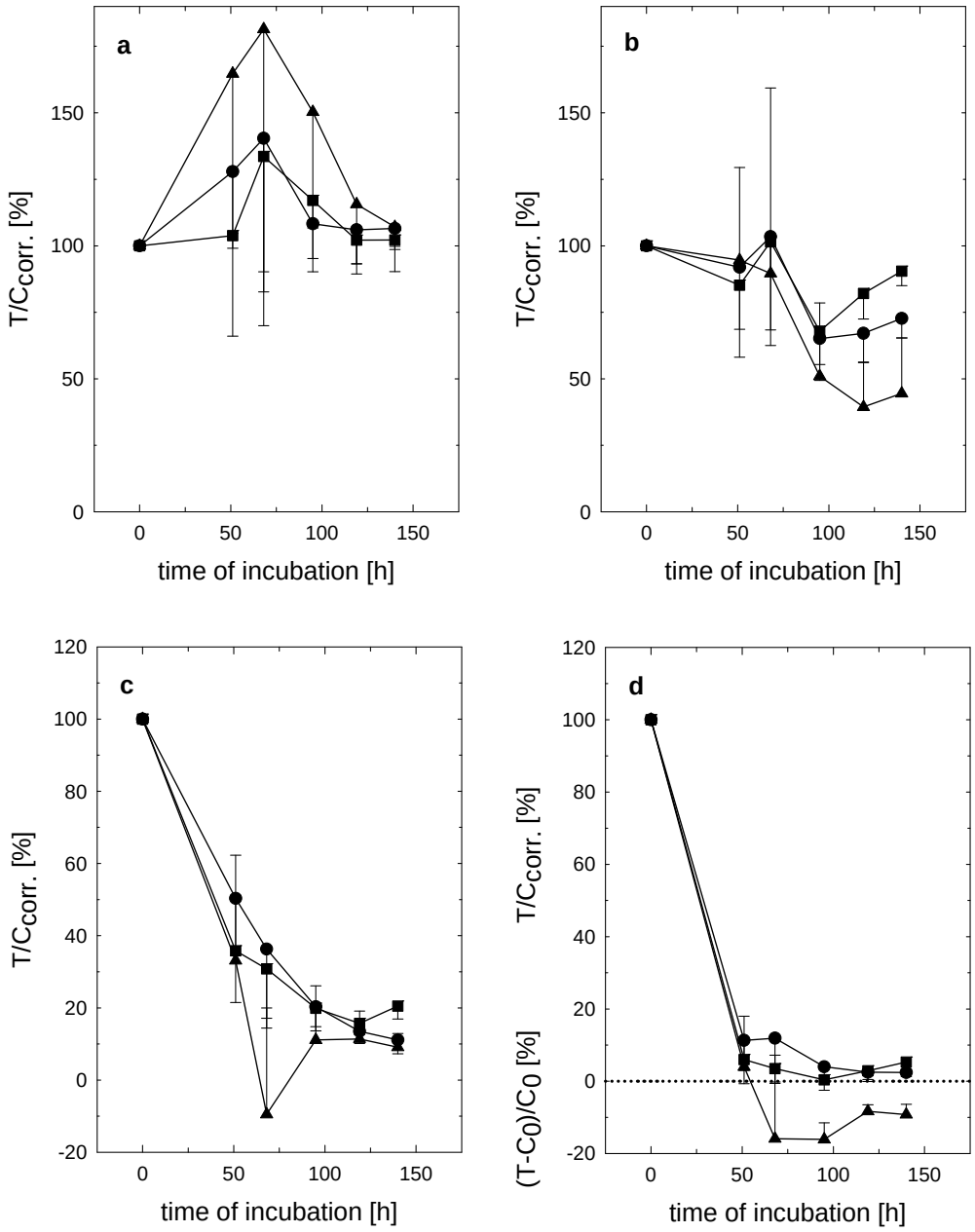

Figure 5.59: Effect of the cytostatic and ABCG2 substrate topotecan on proliferating U-87 MG cells (filled circles; 160th passage), U-87 Luc2/Katushka_Clone 15 cells (filled squares; 4th passage) and U-87 Luc2/Katushka_Clone 18 cells (filled triangles; 4th passage).

Cells were incubated with topotecan at concentrations of: 5 nM (a), 25 nM (b), 100 nM (c) and 500 nM (d).

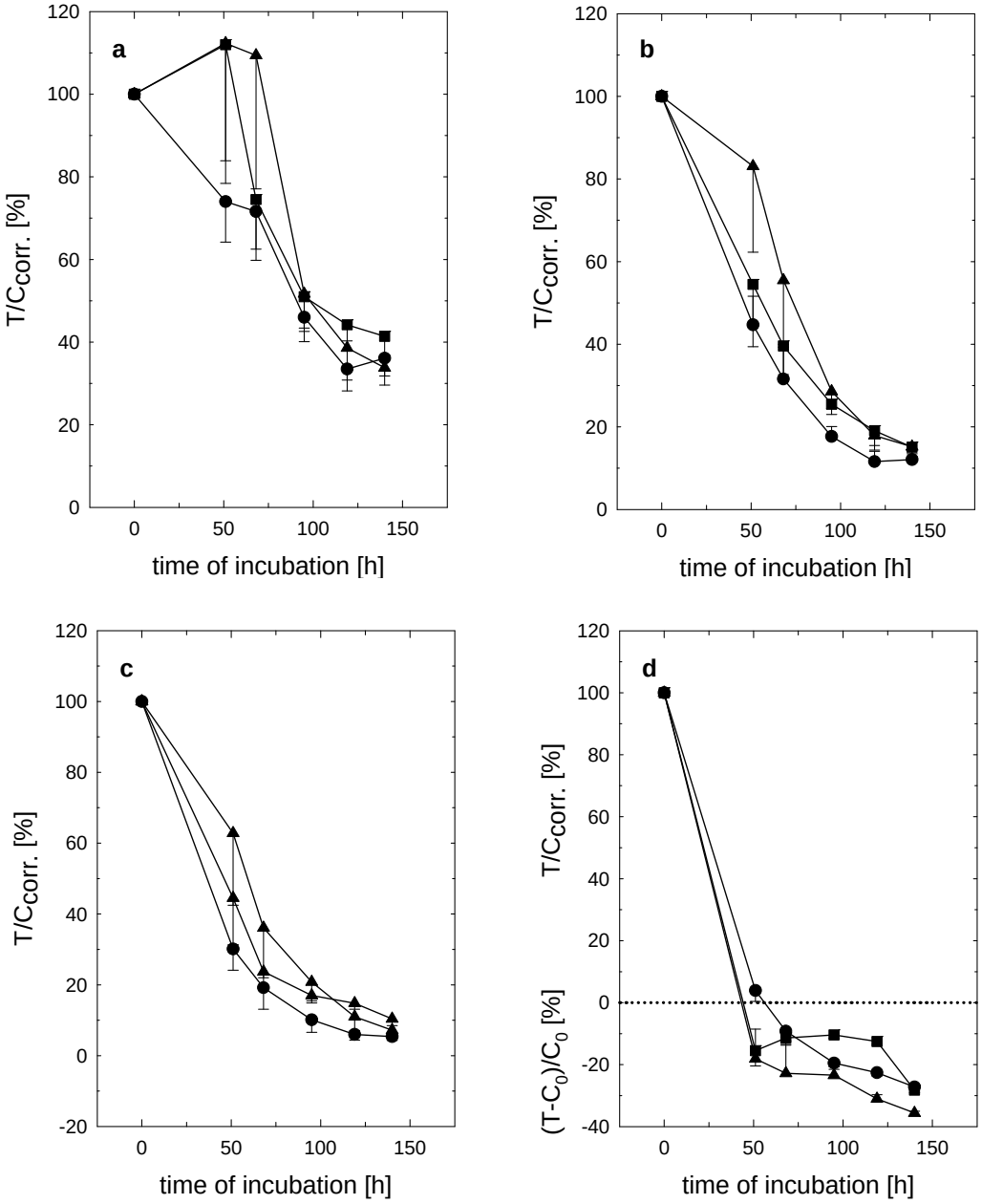

Figure 5.60: Effect of the cytostatic and ABCG2 substrate mitoxantrone on proliferating U-87 MG cells (filled circles; 160th passage), U-87 Luc2/Katushka_Clone 15 cells (filled squares; 4th passage) and U-87 Luc2/Katushka_Clone 18 cells (filled triangles; 4th passage).

Cells were incubated with mitoxantrone at concentrations of: 10 nM (a), 50 nM (b), 100 nM (c) and 500 nM (d).

5.4.4.8 Tumorigenicity of subcutaneously injected co-transfectants in nude mice

U-87 Luc2 / Katushka_Clone 15 and clone 18 co-transfectants were subcutaneously injected into nude mice.

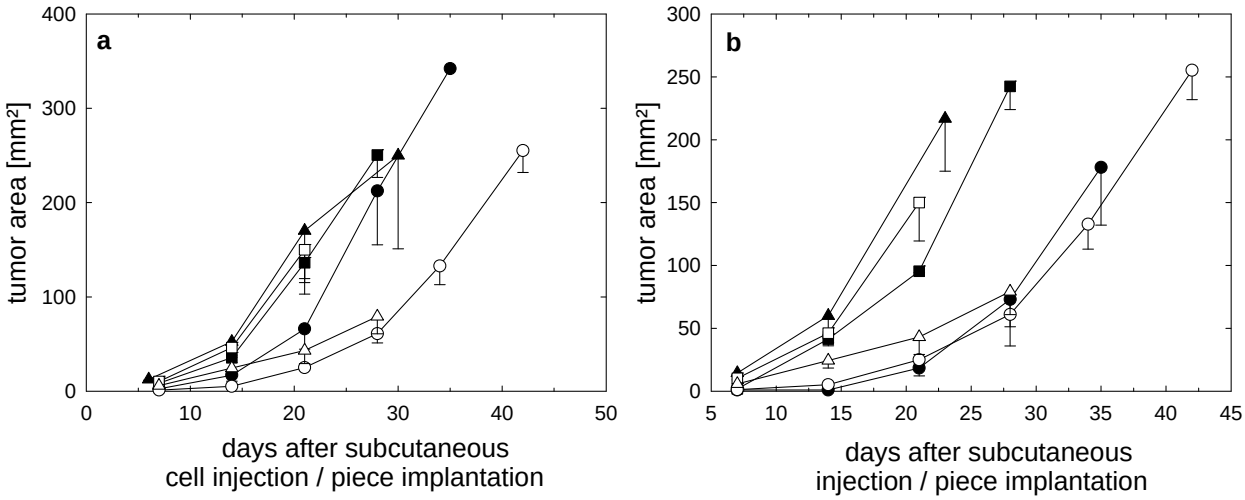

Figure 5.61: In vivo growth kinetics of subcutaneous U-87 MG tumors (open symbols) compared to U-87 Luc2/Katushka_Clone 15 (a) and U-87 Luc2/Katushka_Clone 18 (b) tumors (filled symbols) recorded for the 0^{th} (circles), 1^{st} (squares) and 2^{nd} (triangles) in vivo passage.

Tumors originating from these co-transfectants showed similar growth rates as the U-87 MG controls (**Figure 5.61**). Indeed, in several in vivo passages discrepancies between the growth rates of transfectants and wildtype tumors were observed, but there was no clear tendency towards a reduced velocity in tumor formation depending on the number of in vivo passages.

In total, the transfectants proved to be comparably tumorigenic as the U-87 MG wildtype cells. This observation was further substantiated by the high take rates of U-87 Luc2/Katushka tumors (**Table 5.7**).

Table 5.7: Overview of take rates for subcutaneous U-87 MG, *U-87 Luc2/Kat_Clone 15* and *U-87 Luc2/Kat_Clone 18* tumors presented for the first 3 in vivo passages.

Cell line	**Passage**	**Take rate (%)**
U-87 MG	0	80
	1	100
	2	100
U-87 Luc2/Kat. _Clone 15	0	80
	1	100
	2	100
U-87 Luc2/Kat. _Clone 18	0	75
	1	100
	2	100

5.4.4.9 Optical imaging of subcutaneous U-87 Luc2/Katushka co-transfectant xenografts using BLI and FLI

The subcutaneous tumors were investigated by both, BLI and FLI, in order to investigate luc2 activity and Katushka fluorescence. For this purpose, mice were imaged first by means of 1 of the 2 in vivo imaging methods, followed by the second investigation on the next day.

BLI and FLI experiments demonstrated the ability to specifically determine bioluminescence and fluorescence signals arising from the genetically modified tumors. As observed in vitro, the luciferase2 activity of U-87 Luc2/Katushka_Clone 15 cells turned out to be lower than that of clone 18 cells (**Figure 5.62**). However, by increasing the electron multiplying gain of the EMCCD camera to the maximum value, the bioluminescence of the U-87 Luc2/Katushka_Clone 15 tumors was easily detectable. By contrast, the Katushka fluorescence was significantly lower in subcutaneous tumors formed after injection of clone 18 cells than in U-87 Luc2/Katushka_Clone 15 neoplasms (**Figure 5.62**).

Obviously, the expression of 1 reporter gene was suppressed when the second protein was efficiently expressed simultaneously.

This assumption was supported by long-term investigations (data not shown) which showed a total loss of Katushka fluorescence in U-87 Luc2/Katushka_Clone 18 tumors during the first 3 in vivo passages, whereas the luciferase2 enzyme retained active in the aforementioned tumors.

Comparing the luc2 and Katushka expression in U-87 Luc2/Katushka_Clone 15 xenografts over several passages, the imaging studies demonstrated that the red fluorescent protein was stably expressed. Furthermore, the activity of luc2 remained sufficient to detect specific tumor-associated signals although the EM gain of the EMCCD camera had to be set to its maximum.

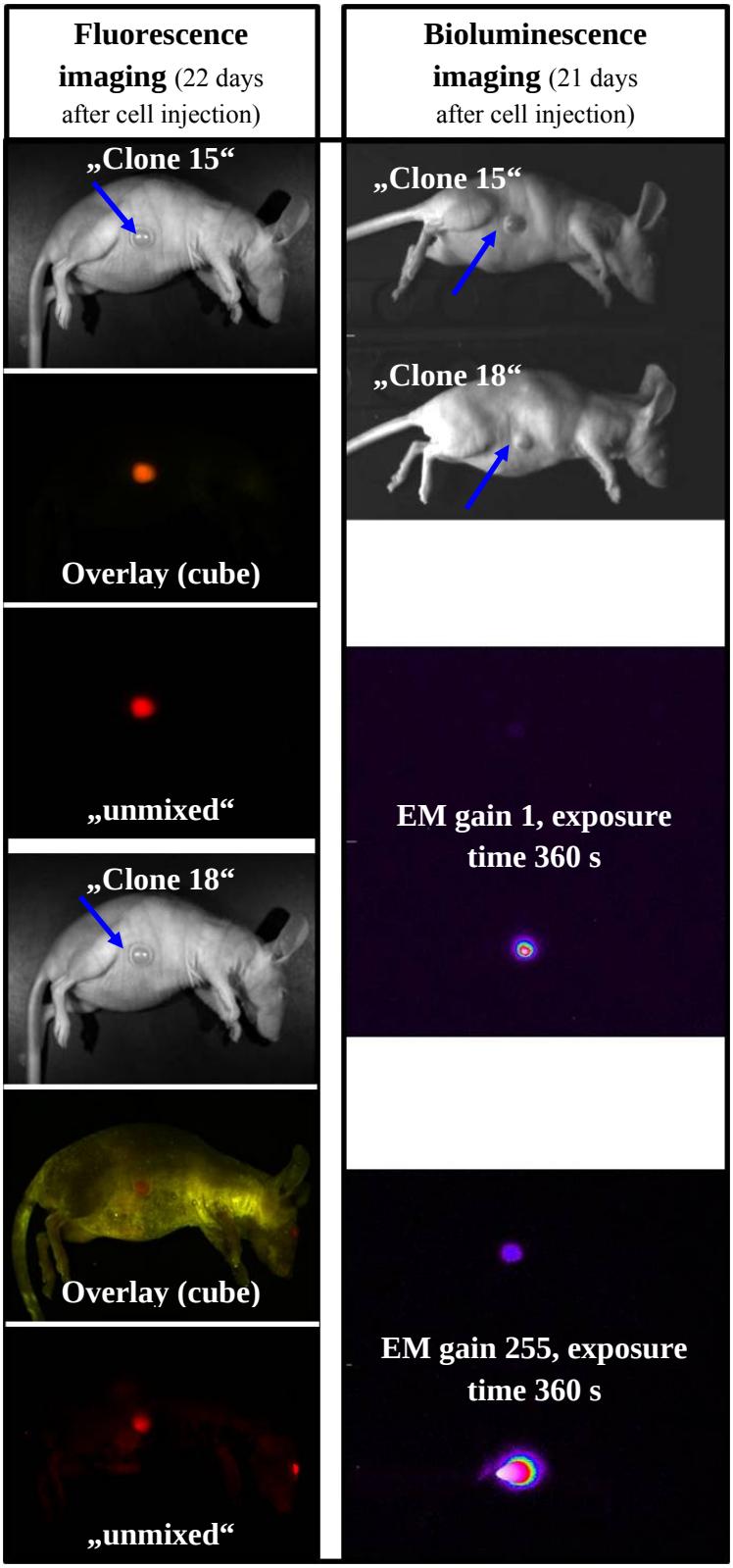

Figure 5.62: BLI and FLI of subcutaneous U-87 Luc2/Katushka_Clone 15 and clone 18 tumors (0^{th} passage). Whereas the subcutaneous U-87 Luc2/Katushka_Clone 15 tumor shows high fluorescence due to Katushka expression, the determination of light signals after D-luciferin application was possible as recently as the multiplier gain was set to its maximum. Contrarily, the U-87 Luc2/Katushka_Clone 18 tumor showed high expression of luciferase2 allowing the determination of specific light signals even without increased EM gains, but instead proved to express the red fluorescent protein Katushka only in low amounts. Furthermore, due to the weak fluorescence signals, the unmixing procedure turned out to be useful only in particular for the analysis of specific Katushka fluorescence.

Instrument settings of FLI: exc. 503-555 nm, em. 580 nm cut off, cube range 580-800 nm (10 nm steps), autoexposure time.

5.4.4.10 Histology of subcutaneous U-87 Luc2/Katushka_Clone 15 / 18 tumors

The morphology of subcutaneous U-87 Luc2/Katushka_Clone 15 and clone 18 tumors (**Figure 5.63**) turned out to be comparable to the morphology of subcutaneous U-87 Luc2 and U-87 Katushka tumors.

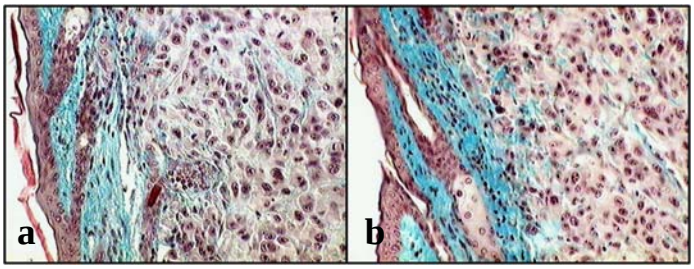

Figure 5.63: Masson-Goldner stain sections of subcutaneous U-87 Luc2/Katushka_Clone 15 (a) and U-87 Luc2/Katushka_Clone 18 (b) tumors (0^{th} in vivo passage).

5.4.4.11 Optical imaging of orthotopic human glioblastoma in nude mice by means of BLI and FLI

Since luc2 expression retained stable over multiple in vivo passages, and the Katushka fluorescence proved to suffice the specific monitoring of tumor signals, U-87 Luc2/Katushka_Clone 15 cells were orthotopically implanted into the brain of nude mice. For the subsequent imaging studies, mice were investigated by both, BLI and FLI, within a period of 24 h.

BLI experiments, which were performed 9 days after cell implantation procedure, showed no intracerebral growth of glioblastoma in all 8 investigated animals. This observation was in good agreement with FLI studies 24 h later, which failed also to detect brain tumors. On day 21 and 22 intracerebral tumors were detected in 5 mice by means of BLI but only in 2 mice by fluorescence imaging caused by the different sensitivities of the 2 different techniques (**Figures 5.64** and **5.65)**. Finally, fluorescence imaging studies on day 28 confirmed 4 of the 5 brain tumors detected by BLI. Unfortunately, the 5^{th} tumor could not be confirmed by FLI due to premature dead of the respective animal. The strong increase in volume of intracerebral brain tumors in 3 animals inevitably caused massive detractions of the mice, so that the experiments had to be discontinued prior to the final BLI studies. All remaining mice of the test group were examined once more by BLI, confirming the absence of glioblastoma in 3 animals, but detecting a brain tumor in mouse 8. The semi-quantitative monitoring of tumor progression in the brain of mouse 8 is demonstrated in **Figure 5.66**.

Taken together, the orthotopic implantation of U-87 Luc2/Katushka_Clone 15 cells enabled semi-quantitative monitoring of tumor progression by both, BLI and FLI.

As expected, the bioluminescence was more sensitive than fluorescence imaging; intracerebral tumors could be detected in an earlier phase of the experiment by means of BLI.

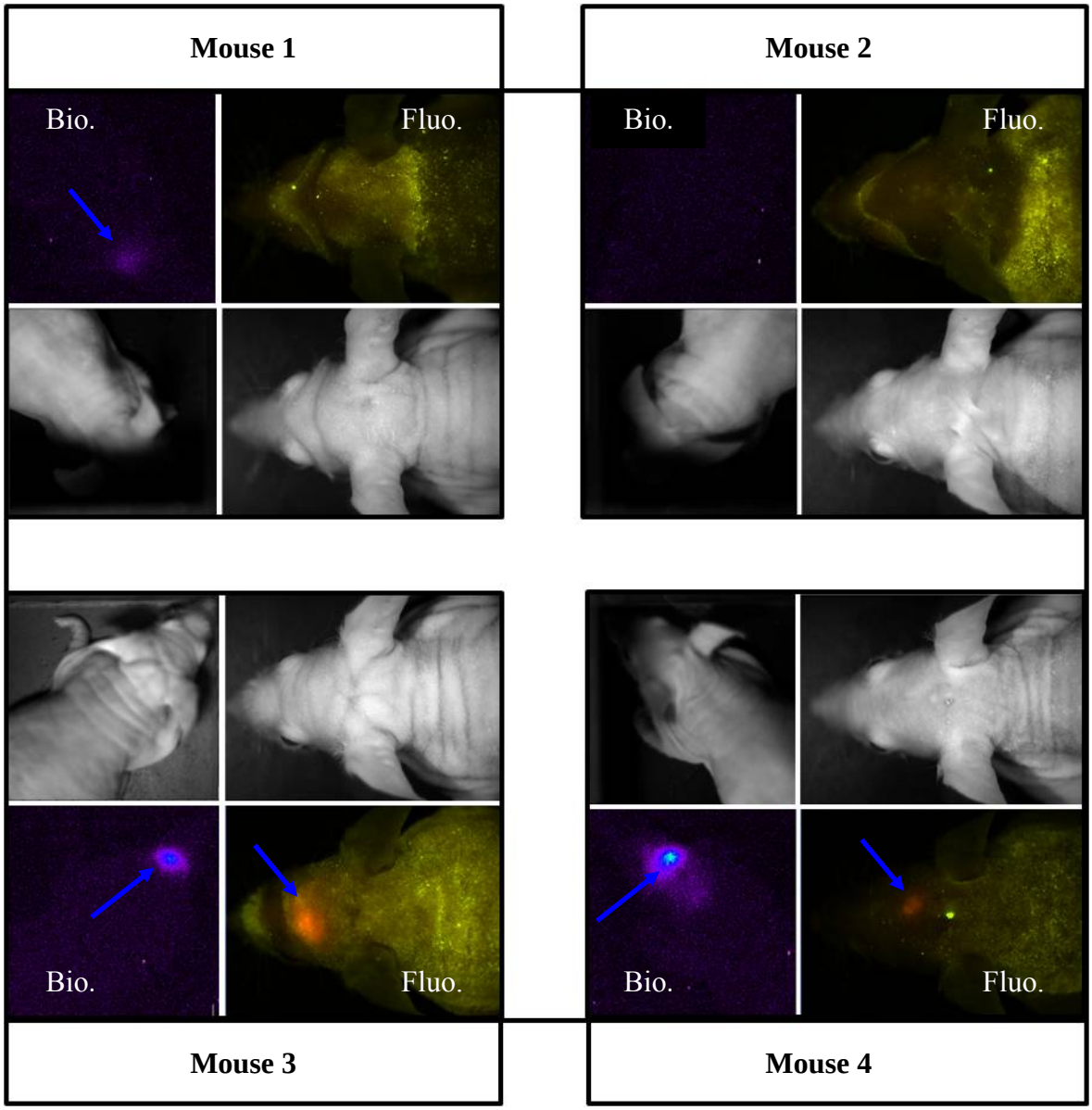

Figure 5.64: Optical imaging of orthotopic U-87 Luc2/Katushka_Clone 15 glioblastoma in nude mice (mouse 1 – mouse 4) via bioluminescence and fluorescence in vivo imaging. Experiments were performed 21 (bioluminescence) and 22 (fluorescence) days after tumor cell implantation into the brain. Blue arrows mark the signals derived from orthotopic glioblastoma.

Instrument setting of BLI: stage height h2c, EM gain 255, exposure time 900 s (300 s after intraperitoneal injection of 8 mg D-luciferin), no binning, readout rate 1 MHz. at 16 bit.

Instrument setting of FLI: stage height h3, exc. filter 503-555 nm, em. filter 580 nm cut off, autoexposure time; fluorescence images represent an overlay of 23 pictures (image cube with 10 nm steps from 580-800 nm).

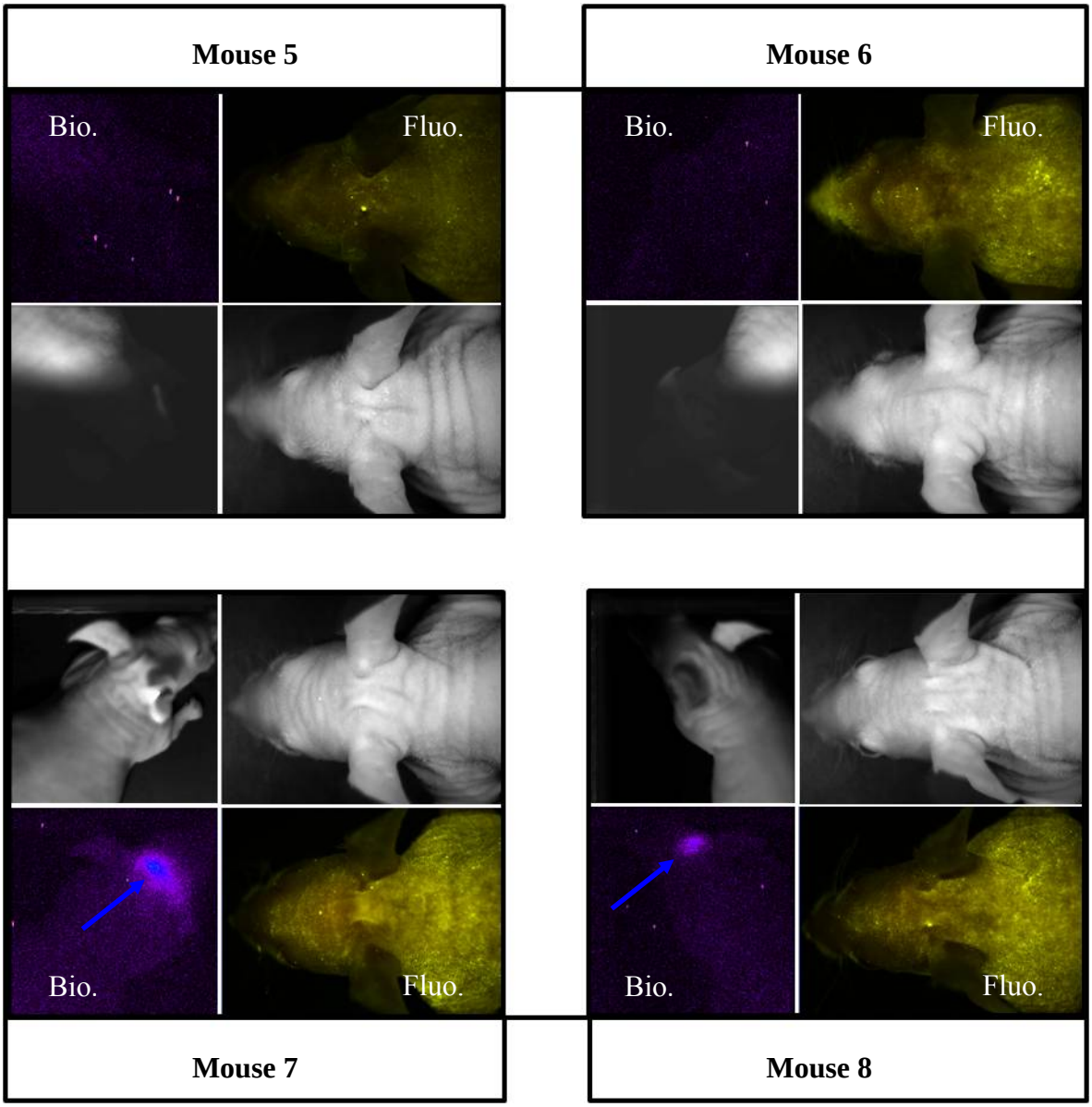

Figure 5.65: Optical imaging of orthotopic U-87 Luc2/Katushka_Clone 15 glioblastoma in nude mice (mouse 5 – mouse 8) via bioluminescence and fluorescence in vivo imaging. Experiments were performed 21 (bioluminescence) and 22 (fluorescence) days after tumor cell implantation into the brain. Blue arrows mark the signals derived from orthotopic glioblastoma.

Instrument setting of BLI: stage height h2c, EM gain 255, exposure time 900 s (300 s after intraperitoneal injection of 8 mg D-luciferin), no binning, readout rate 1 MHz. at 16 bit.

Instrument setting of FLI: stage height h3, exc. filter 503-555 nm, em. filter 580 nm cut off, autoexposure time; fluorescence images represent an overlay of 23 pictures (image cube with 10 nm steps from 580-800 nm).

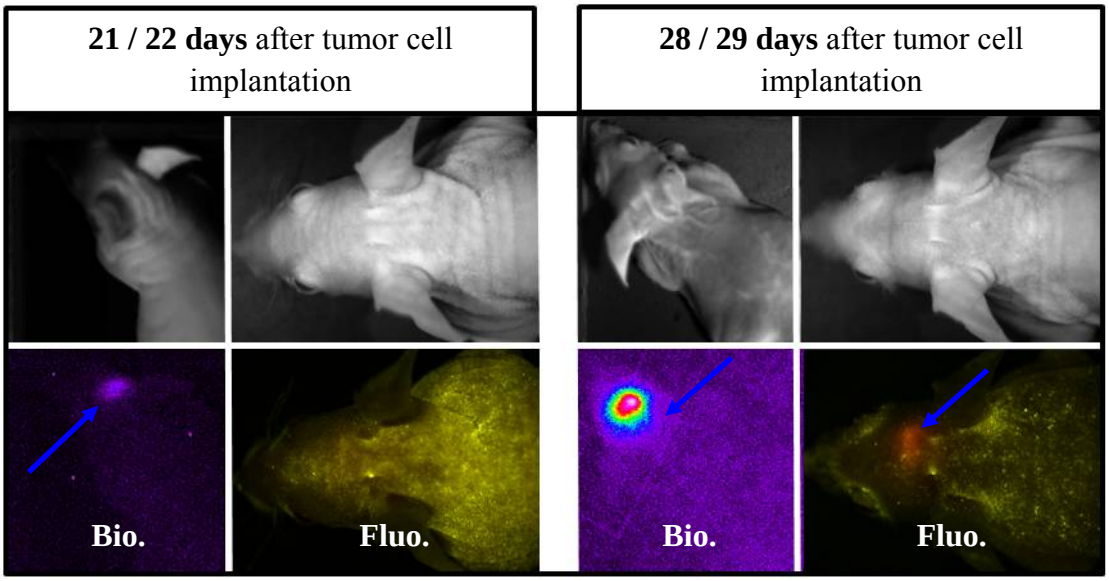

Figure 5.66: Optical imaging of an orthotopic U-87 Luc2/Katushka_Clone 15 glioblastoma in *mouse 8* via bioluminescence and fluorescence measurements. Blue arrows mark the signals derived from orthotopic glioblastoma.

Instrument setting of bioluminescence imaging studies: stage height h2c, EM gain 255, exposure time 900 s (300 s after intraperitoneal injection of 8 mg D-luciferin), no binning, readout rate 1 MHz. at 16 bit.

Instrument setting of fluorescence measurements: stage height h3, exc. filter 503-555 nm, em. filter 580 nm cut off, autoexposure time; fluorescence images represent an overlay of 23 pictures (image cube with 10 nm steps from 580-800 nm).

5.4.4.12 Correlation of histology with optical imaging of orthotopic co-transfectants

Table 5.8 summarizes BLI and FLI data from individual animals as well as the corresponding results of histopathological studies.

The overall agreement of imaging results and histopathology was 63 %. Intracerebral U-87 glioblastomas were detected in 3 mice (mouse 1, mouse 7 and mouse 8) by BLI, FLI and histopathology. Histopathological investigation of the brain of mouse 2 proved the existence of an orthotopic glioblastoma, however, this malignancy could not be detected by optical imaging, neither by BLI nor by FLI. Probably, this tumor was too small and presumably located to deeply to be detected by the noninvasive imaging techniques. Reasons for false-negative and false-positive results have been discussed above.

The morphology of orthotopic U-87 Luc2/Katushka_Clone 15 tumors proved to be comparable to subcutaneous malignancies (data not shown).

Table 5.8: Overview of results obtained from BLI, FLI and histopathological examinations on orthotopic human glioblastoma (*U-87 Luc2/Katushka_Clone 15*) in nude mice.

	Tumor detection by Bioluminescence signal	**Tumor detection by Fluorescence signal**	**Histological detection of orthotopic tumor growth**
Mouse 1	+	+	+
Mouse 2	-	-	+
Mouse 3	+	+	-
Mouse 4	+	+	no histology
Mouse 5	-	-	-
Mouse 6	-	-	-
Mouse 7	+	+	+
Mouse 8	+	+	+

5.5 Summary and discussion

For the refinement of an existing orthotopic brain tumor model in nude mice, the human U-87 MG and U-373 MG glioblastoma cells were transfected with the genes encoding an enhanced version of the firefly luciferase (luc2) and the recently discovered far-red emitting protein Katushka. These genetic modifications were performed with the aim of establishing noninvasive methods for optical imaging of intracerebral tumor progression, predominantly during the performance of neuro-oncologic studies.

Over the last decades, an increasing amount for applications of bioluminescence and fluorescence in vivo imaging has been reported in the field of preclinical neuro-oncology. For example Murray et al. [Murray et al., 2003] developed an in vivo breast cancer bone metastasis model, which enabled the control of tumor growth by bioluminescence imaging. Moreover, the therapeutic efficacy of the receptor tyrosine kinase inhibitor SU11248 against tumor growth and tumor-induced osteolysis was evaluated in this model [Murray et al., 2003]. By analogy, the progression and treatment efficacy of radioimmunotherapy against intraperitoneal tumors [Buchhorn et al., 2007] as well as orthotopic human bladder carcinoma [Pfost et al., 2009] in mice was reported to be efficiently visualized by BLI. In parallel, the development of far-red light emitting fluorescent proteins during the last years offered an interesting starting point for the noninvasive monitoring of cancer processes in vivo by means of FLI. For example, the red fluorescent protein DsRed2 was demonstrated to be a powerful tool for optical tumor imaging in an orthotopic model of human pancreatic cancer [Katz et al., 2004] and in an orthotopic human colon carcinoma model [Jarzyna, 2007]. Furthermore, the investigations by Katz et al. [Katz et al., 2004] proved the potential of fluorescence in vivo imaging to evaluate the efficacy of new antitumor agents. In addition, fluorescence in vivo imaging (FLI) of orthotopic pancreatic cancers genetically engineered to express DsRed2, revealed high resolution of FLI and turned out to highly correlate with tumor volume and size, simultaneously imaged by MRI [Bouvet et al., 2005]. However, so far, there are only few applications using the exceedingly interesting far-red protein Katushka for fluorescence in vivo imaging in the field of preclinical oncology.

Encouraged by the successful applications of BLI and FLI reported in the literature, the idea of this project was, that the stable expression of luc2 in transfected human glioblastoma cells should provide the opportunity to specifically detect light signals from intracerebral tumors after application of the substrate D-luciferin.

On the other hand, the stable transfection of the glioblastoma cells with the gene encoding the Katushka protein was regarded as an alternative method for the noninvasive confirmation of intracerebral brain tumors by using fluorescence in vivo imaging devices. Therefore, the red emitted light of Katushka expressing tumors should be exploited for the monitoring of orthotopic tumor progression. Furthermore, to directly compare advantages and limitations of both techniques within the same model, the human brain tumor cells were co-transfected with reporter genes, namely luciferase2 and 1 of the 2 red fluorescent proteins, either DsRed2 or Katushka, enabling both optical imaging methods.

Preliminary in vitro studies on luc2 activity and Katushka fluorescence confirmed high protein expression in several genetically engineered glioblastoma cells. Moreover, the transfectants showed growth kinetics and chemosensitivity against cytostatics (the ABCG2 substrates mitoxantrone and topotecan) comparable with the corresponding wildtype cells. Since the detection limits of transfectants on the in vivo imaging devices turned out to be in the same range as the amount of cells which are used for intracerebral implantation, several clones were selected for preliminary in vivo studies. For this purpose, the cells were subcutaneously injected into nude mice in order to assess tumorigenicity and the suitability of luc2 and Kathushka expression for the monitoring of tumor progression in vivo. These investigations revealed high take rates in the case of transfected U-87 cells, whereas the attempts to establish a subcutaneous U-373 glioblastoma model failed due to lack of tumorigenicity. Furthermore, solid U-87 Luc2 and U-87 Katushka tumors proved to express luciferase2 and Katushka at high levels, allowing the imaging of tumor progression by noninvasive optical methods. Additionally, it was shown, that even in the absence of antibiotics (lack of selection pressure) in vivo, both proteins, namely luciferase2 and Katushka, were stably expressed over a period of several months.

Since studies on subcutaneous U-87 Luc2 and U-87 Katushka tumors demonstrated tumorigenicity comparable with that of the wildtype cells, as well as expression of luciferase2 and Katushka remained high in vivo, the aforementioned tumor cells were intracerebrally implanted into nude mice. Aiming at monitoring the intracerebral tumor growth, the animals were investigated by means of the in vivo imaging devices over several weeks. Thereby, the expression of luciferase2 and Katushka in the genetically modified U-87 cells enabled semi-quantitative determination of the intracerebral tumor growth.

Hence, in case of BLI, it could be proven, that the substrate D-luciferin sufficiently crosses the blood-brain barrier to visualize intracerebral human glioblastoma progression in nude mice. These results are of great value since only few reports in the literature describe the monitoring of orthotopic malignant brain tumors, especially xenografts, by means of BLI. However, two studies by Szentirmai et al. [Szentirmai et al., 2006] and Dinca et al. [Dinca et al., 2007] demonstrated similar efficiency of BLI to monitor the intracranial progression of U-87 MG xenografts in nude mice. In case of FLI, it was shown, that the noninvasive imaging of orthotopic brain tumors by means of the far-red light emitting protein Katushka is a powerful tool to monitor intracerebral tumor progression. Moreover, both optical imaging studies, namely BLI and FLI, were in good agreement with subsequent histopathological examinations.

The co-transfection of glioblastoma cells with the genes encoding luciferase2 and Katushka, revealed several clones with high functionality of both proteins. In agreement with the mono-transfectants, only the genetically modified U-87 cell clones showed reproducible in vivo tumorigenicity as well as stable expression of luciferase2 and Katushka. The implantation of such stably expressing U-87 Luc2/Katushka co-transfectants into the brain of nude mice allowed the monitoring of tumor progression by both, BLI and FLI. Thereby, intracerebral tumor growth was detectable earlier, when BLI was used instead of FLI. Thus, as expected, bioluminescence in vivo imaging offers higher sensitivity compared to the FLI method.

A disadvantage of bioluminescence compared to FLI is the considerably higher complexity of such experiments (D-luciferin application, background measurements, exclusion of any external light etc.). Moreover, BLI requires an intact blood supply as the substrate, D-luciferin, has to be transported to the tumor across the blood-brain barrier. Contrarily, the detection of fluorescence signals by the tumor is even possible after the death of the animals, as long as the protein remains functionally active, provided that the light (excitation and emission) is able to penetrate surrounding tissues. In spite of the aforementioned limitations of BLI and FLI, both techniques represent an explicit refinement of the available methodology in the preclinical investigation of the therapy of glioblastomas. Predominantly, the ability to guarantee the existence of intracerebral tumors at the beginning of neuro-oncologic studies, and the option to evaluate differences in tumor sizes, represent major improvements with respect to future in vivo studies.

In conclusion, the semi-quantitative monitoring of tumor progression by such noninvasive optical imaging methods in live animals should be a powerful tool to study new approaches in the chemo-/radiotherapy of malignant brain tumors including strategies to overcome the blood-brain barrier.

References

Altenschöpfer, P. (1998). Tumorpharmakologische und analytische Untersuchungen zur Optimierung neuer Zytostatika-beladener bioabbaubarer Implantate für die interstitielle Chemotherapie maligner Hirntumoren; Doctoral thesis.

Amoh, Y., Katsuoka, K. and Hoffman, R. M. (2008). Color-coded fluorescent protein imaging of angiogenesis: the AngioMouse models. Curr. Pharm. Des. **14**(36): 3810-9.

Bernhardt, G., Reile, H., Birnböck, H., Spruss, T. and Schönenberger, H. (1992). Standardized kinetic microassay to quantify differential chemosensitivity on the basis of proliferative activity. J. Cancer Res. Clin. Oncol. **118**(1): 35-41.

Bouvet, M., Spernyak, J., Katz, M. H., Mazurchuk, R. V., Takimoto, S., Bernacki, R., Rustum, Y. M., Moossa, A. R. and Hoffman, R. M. (2005). High correlation of whole-body red fluorescent protein imaging and magnetic resonance imaging on an orthotopic model of pancreatic cancer. Cancer Res. **65**(21): 9829-33.

Bradford, M. M. (1976). A rapid and sensitive method for the quantitation of microgram quantities of protein utilizing the principle of protein-dye binding. Anal. Biochem. **72**: 248-54.

Buchhorn, H. M., Seidl , C., Beck, R., Saur, D., Apostolidis, C., Morgenstern, A., Schwaiger, M. and Senekowitsch-Schmidtke, R. (2007). Non-invasive visualisation of the development of peritoneal carcinomatosis and tumor regression after 213Bi-radioimmunotherapy using bioluminescence imaging. Eur. J. Nucl. Med. Mol. Imag. **34**(6): 841-849.

Campbell, R. E., Tour, O., Palmer, A. E., Steinbach, P. A., Baird, G. S., Zacharias, D. A. and Tsien, R. Y. (2002). A monomeric red fluorescent protein. Proc. Natl. Acad. Sci. U. S. A. **99**(12): 7877-7882.

Carlson, A. and Copeland, J. (1985). Flash communication in fireflies. Q. Rev. Biol. **60**: 415-436.

Chishima, T., Miyagi, Y., Wang, X., Yamaoka, H., Shimada, H., Moossa, A. R. and Hoffman, R. M. (1997). Cancer invasion and micrometastasis visualized in live tissue by green fluorescent protein expression. Cancer Res. **57**(10): 2042-7.

Cock, R. and Matthysen, E. (1999). Aposematism and Bioluminescence: Experimental evidence from Glow-worm Larvae(Coleoptera: Lampyridae). Evol. Ecol. **13**(7): 619-639.

Cormack, B. P., Valdivia, R. H. and Falkow, S. (1996). FACS-optimized mutants of the green fluorescent protein (GFP). Gene **173**(1): 33-38.

Crameri, A., Whitehorn, E. A., Tate, E. and Stemmer, W. P. C. (1996). Improved Green Fluorescent Protein by Molecular Evolution Using DNA Shuffling. Nat. Biotechnol. **14**(3): 315-319.

Day, J. C., Tisi, L. C. and Bailey, M. J. (2004). Evolution of beetle bioluminescence: the origin of beetle luciferin. Luminescence **19**(1): 8-20.

De Cock, R. and Matthysen, E. (2003). Glow-worm larvae bioluminescence (Coleoptera: Lampyridae) operates as an aposematic signal upon toads (Bufo bufo). Behav. Ecol. **14**(1): 103-108.

Dinca, E. B., Sarkaria, J. N., Schroeder, M. A., Carlson, B. L., Voicu, R., Gupta, N., Berger, M. S. and James, C. D. (2007). Bioluminescence monitoring of intracranial glioblastoma xenograft: response to primary and salvage temozolomide therapy. J. Neurosurg. **107**(3): 610-616.

Evrogen pTurboFP635-N vector description. http://www.evrogen.com/vector-descriptions/pTurboFP635-N/pTurboFP635-N.pdf

Fradkov, A. F., Chen, Y., Ding, L., Barsova, E. V., Matz, M. V. and Lukyanov, S. A. (2000). Novel fluorescent protein from Discosoma coral and its mutants possesses a unique far-red fluorescence. FEBS Lett. **479**(3): 127-130.

Gross, L. A., Baird, G. S., Hoffman, R. C., Baldridge, K. K. and Tsien, R. Y. (2000). The structure of the chromophore within DsRed, a red fluorescent protein from coral. Proc. Natl. Acad. Sci. U. S. A. **97**(22): 11990-11995.

Hastings, J. W. (1983). Chemistry and Control of Luminescence in Marine Organisms. Bull. Mar. Sci. **33**: 818-828.

Hastings, J. W. (1996). Chemistries and colors of bioluminescent reactions: a review. Gene **173**(1): 5-11.

Hoffman, R. (2009). Imaging cancer dynamics in vivo at the tumor and cellular level with fluorescent proteins. Clin. Exp. Metastasis **26**(4): 345-355.

Hoffman, R. M. and Yang, M. (2006). Color-coded fluorescence imaging of tumor-host interactions. Nat. Protocols **1**(2): 928-935.

Jarzyna, P. (2007). Preclinical investigations on the effect of the human hyaluronidase Hyal-1 on growth and metastasis of human colon carcinoma; Doctoral thesis.

Katz, M. H., Bouvet, M., Takimoto, S., Spivack, D., Moossa, A. R. and Hoffman, R. M. (2004). Survival efficacy of adjuvant cytosine-analogue CS-682 in a fluorescent orthotopic model of human pancreatic cancer. Cancer Res. **64**(5): 1828-33.

Matz, M. V., Fradkov, A. F., Labas, Y. A., Savitsky, A. P., Zaraisky, A. G., Markelov, M. L. and Lukyanov, S. A. (1999). Fluorescent proteins from nonbioluminescent Anthozoa species. Nat. Biotechnol. **17**(10): 969-973.

Merzlyak, E. M., Goedhart, J., Shcherbo, D., Bulina, M. E., Shcheglov, A. S., Fradkov, A. F., Gaintzeva, A., Lukyanov, K. A., Lukyanov, S., Gadella, T. W. J. and Chudakov, D. M. (2007). Bright monomeric red fluorescent protein with an extended fluorescence lifetime. Nat. Methods **4**(7): 555-557.

Moriyama, E. H., Bisland, S. K., Lilge, L. and Wilson, B. C. (2004). Bioluminescence Imaging of the Response of Rat Gliosarcoma to ALA-PpIX-mediated Photodynamic Therapy. Photochem. Photobiol. **80**(2): 242-249.

Murray, L., Abrams, T., Long, K., Ngai, T., Olson, L., Hong, W., Keast, P., Brassard, J., O'Farrell, A., Cherrington, J. and Pryer, N. (2003). SU11248 inhibits tumor growth and CSF-1R-dependent osteolysis in an experimental breast cancer bone metastasis model. Clin. Exp. Metastasis **20**(8): 757-766.

Pfost, B., Seidl, C., Autenrieth, M., Saur, D., Bruchertseifer, F., Morgenstern, A., Schwaiger, M. and Senekowitsch-Schmidtke, R. (2009). Intravesical {alpha}-Radioimmunotherapy with 213Bi-Anti-EGFR-mAb Defeats Human Bladder Carcinoma in Xenografted Nude Mice. J. Nucl. Med. **50**(10): 1700-1708.

Prasher, D. C., Eckenrode, V. K., Ward, W. W., Prendergast, F. G. and Cormier, M. J. (1992). Primary structure of the Aequorea victoria green-fluorescent protein. Gene **111**(2): 229-233.

Promega (2004-2007). pGL4 Luciferase Reporter Vectors. Technical Manual.

Romeis, B. (1989). Mikroskopische Technik, Urban und Schwarzenberg.

Shaner, N. C., Campbell, R. E., Steinbach, P. A., Giepmans, B. N. G., Palmer, A. E. and Tsien, R. Y. (2004). Improved monomeric red, orange and yellow fluorescent proteins derived from Discosoma sp. red fluorescent protein. Nat. Biotechnol. **22**(12): 1567-1572.

Shcherbo, D., Merzlyak, E. M., Chepurnykh, T. V., Fradkov, A. F., Ermakova, G. V., Solovieva, E. A., Lukyanov, K. A., Bogdanova, E. A., Zaraisky, A. G., Lukyanov, S. and Chudakov, D. M. (2007). Bright far-red fluorescent protein for whole-body imaging. Nat. Methods **4**(9): 741-746.

Sivinski, J. (1998). Phototropism, bioluminescence and the Diptera. Fla. Entomol **81**: 577-593.

Szentirmai, O., Baker, C. H., Lin, N., Szucs, S., Takahashi, M., Kiryu, S., Kung, A. L., Mulligan, R. C. and Carter, B. S. (2006). Noninvasive Bioluminescence Imaging of Luciferase Expressing Intracranial U87 Xenografts: Correlation with Magnetic Resonance Imaging Determined Tumor Volume and Longitudinal Use in Assessing Tumor Growth and Antiangiogenic Treatment Effect. Neurosurgery **58**(2): 365-372

Tagami, A., Ishibashi, N., Kato, D.-i., Taguchi, N., Mochizuki, Y., Watanabe, H., Ito, M. and Tanaka, S. (2009). Ab initio quantum-chemical study on emission spectra of bioluminescent luciferases by fragment molecular orbital method. Chem. Phys. Lett. **472**(1-3): 118-123.

Underwood, T., Tallamy, D. and Pesek, J. (1997). Bioluminescence in firefly larvae: A test of the aposematic display hypothesis (Coleoptera: Lampyridae). J. Insect Behav. **10**(3): 365-370.

Vooijs, M., Jonkers, J., Lyons, S. and Berns, A. (2002). Noninvasive imaging of spontaneous retinoblastoma pathway-dependent tumors in mice. Cancer Res. **62**(6): 1862-7.

Walter, I., Fleischmann, M., Klein, D., Müller, M., Salmons, B., Günzburg, W., Renner, M. and Gelbmann, W. (2000). Rapid and Sensitive Detection of Enhanced Green Fluorescent Protein Expression in Paraffin Sections by Confocal Laser Scanning Microscopy. Histochem. J. **32**(2): 99-103.

Wegrzyn, G., Czyz, A. and Olszewska, K. (2004). Biological functions and early evolution of bacterial luminescence. Current Trends in Microbiology **1**: 43-49.

Wood, K. V. (1995). THE CHEMICAL MECHANISM and EVOLUTIONARY DEVELOPMENT OF BEETLE BIOLUMINESCENCE. Photochem. Photobiol. **62**(4): 662-673.

Yang, M., Baranov, E., Jiang, P., Sun, F.-X., Li, X.-M., Li, L., Hasegawa, S., Bouvet, M., Al-Tuwaijri, M., Chishima, T., Shimada, H., Moossa, A. R., Penman, S. and Hoffman, R. M. (2000). Whole-body optical imaging of green fluorescent protein-expressing tumors and metastases. Proc. Natl. Acad. Sci. U. S. A. **97**(3): 1206-1211.

Yang, M., Reynoso, J., Bouvet, M. and Hoffman, R. M. (2009). A transgenic red fluorescent protein-expressing nude mouse for color-coded imaging of the tumor microenvironment. J. Cell. Biochem. **106**(2): 279-284.

Zolotukhin, S., Potter, M., Hauswirth, W., Guy, J. and Muzyczka, N. (1996). A "humanized" green fluorescent protein cDNA adapted for high-level expression in mammalian cells. J. Virol. **70**(7): 4646-4654.

Chapter 6

Summary

The treatment of malignant brain tumors, especially of high-grade gliomas, poses one of the major challenges in cancer therapy. Despite seminal advancements in imaging techniques for the early diagnosis of CNS neoplasms as well as amendments in surgery and radiooncology, the prognosis of patients with glioma is very poor. The administration of temozolomide adjuvant to irradiation after resection of the tumor - the current “gold standard” in the treatment of glioblastoma - has only marginally improved median survival by ca. 3 months. Hence, there is an urgent need for novel approaches to the treatment of malignant brain tumors. To investigate the efficiency of such regimens in vivo, predictive preclinical animal models are indispensible.

In this thesis, three subject areas were dealt with:
- evaluation of doxorubicin-loaded poly(butylcyanoacrylate) (PBCA) nanoparticle (NP) formulations as drug-carriers,
- modulation of the ATP-binding cassette transporter ABCG2, which is expressed in brain capillaries, by newly synthesized inhibitors, as a strategy to overcome the blood-brain barrier (BBB) with chemotherapeutics, which are substrates of this efflux pump, and
- refinement of orthotopic glioblastoma models in nude mice to allow noninvasive optical imaging of intracerebral tumors.

Human glioblastoma cells U-87 MG, U-118 MG and U-373 MG were incubated with free doxorubicin and doxorubicin loaded onto PBCA NPs. As the glioblastoma cells do neither express ABCB1 nor ABCG2, Kb-V1 and MCF-7/Topo cells were included, to study effects on both efflux pumps. In the crystal-violet chemosensitivity assay, cytotoxicities of the doxorubicin-loaded NPs and of the dissolved cytostatic were similar against all glioblastoma cells. By contrast, a higher efficacy of the NP formulations was observed on ABCB1-overexpressing Kb-V1, but not on ABCG2-expressing MCF-7/Topo cells, indicating an interaction of the NPs with the ABCB1 efflux pump. Therefore, increased drug concentrations in the brain after administration of such drug-loaded NPs to animals, as reported in literature, might be due interactions of the NPs with ABCB1 at the BBB.

The modulation of ABC transporters at the BBB represents an attractive strategy to increase intracerebral levels of drugs, which are known to be substrates of such efflux pumps.

For this reason, the identification of potent efflux pump inhibitors is a promising approach to improve the chemotherapy of brain tumors. A series of analogs, derived from the original ABCB1 inhibitor tariquidar, was investigated for potency against ABCG2 and selectivity vs. ABCB1. To expand methodology and to by-pass problems associated with the flow cytometric (FACS) mitoxantrone-efflux assay, two 96-well plate assays, using the fluorescent ABCG2 substrates Hoechst 33342 and pheophorbide a, were developed. Interestingly, slight structural modifications of tariquidar analogs yielded potent and selective inhibitors of ABCG2. The most potent modulator showed an IC_{50} value of 60 nM in the FACS assay and 65 and 126 nM in the microtiter plate assays. In view of future in vivo studies, the most potent inhibitors were investigated for stability in plasma by the means of HPLC-MS analysis. Unfortunately, these compounds are prone to rapid enzymatic cleavage at the central benzamide moiety. Therefore, compounds with improved drug-like properties are required. Since a regulation of ABCG2 by estrogens is discussed in literature, MCF-7/Topo cells were treated with estradiol and subjected to treatment with topotecan. No differences in the antiproliferative effect between estradiol-treated and non-treated controls were observed, indicating, at best, a therapeutically irrelevant regulation of the ABCG2-level by estradiol.

To investigate the therapeutic value of new concepts, e.g. the combined administration of selective inhibitors of ABC-transporters with appropriate cytostatics, the main focus of this work was the refinement of in vivo xenograft models. Indeed, orthotopic brain tumor models, allowing the monitoring of tumor progression by noninvasive optical imaging, were established in nude mice. For this purpose, human U-87 MG glioblastoma cells were transfected with the genes encoding luciferase2 (Luc2) and the recently discovered far-red fluorescent protein Katushka (Kat), respectively. Numerous clones were characterized in vitro with respect to bioluminescence / fluorescence, growth kinetics and chemosensitivity. As the transfectants were tumorigenic subcutaneously (s.c.), and Luc2 as well as Kat expression persisted in the s.c. model, the human glioblastoma variants were injected into the brains of nude mice, where reproducibly growing tumors developed. Most important is the fact that these intracerebral xenografts were accessible to both, bioluminescence and fluorescence imaging. Moreover, there was a direct correlation between the optical signals and the tumor load, confirmed by histology.

Appendix

Development of an automated freezing-procedure for the cryopreservation of solid tumors

A Introduction

The cryopreservation of microorganisms and mammalian cells (e.g. spermatozoa, hybridoma, and tumor cells) is common practice for long-term storage of these biological materials in cell banks [Royere et al., 1996; Oktay, 2001]. By contrast, the cryopreservation of solid tissues, in particular human tumors, is of great importance with respect to oncological research on tumor biology and experimental pharmacology. Viable small pieces should offer advantages over cell suspensions from in vitro culture, especially in case of slowly proliferating cells. In addition, cryopreservation of solid tissues will reduce the number of animals required to establish and maintain in vivo tumor models. Furthermore, specimen banks gain importance with respect to the identification, characterization and expression analysis of human genes as well as in proteomics [Loken and Demetrick, 2005].

Since tumor tissue is very inhomogeneous containing different cell types, i.e. tumor cells and many stromal constituents such as fibroblasts and endothelial cells, cryopreservation is associated with various problems [Ehrhart et al., 2009]. Therefore, only very few freezing protocols, claiming the successful cryopreservation of human tumor tissues, are available [Ehrhart et al., 2009]. A multitude of parameters such as osmotic tolerance of the cells, nucleation and growth of ice crystals, recrystallization and vitrification are known to influence the effective freezing of individual cell material [Meryman, 2007]. For example, the presence of blood vessels and large proteins of the extracellular matrix, such as collagen, can disturb the freezing process or interfere with cryoprotectants [Ehrhart et al., 2009]. Due to the fact that intracellular ice nuclei are usually not formed in living cells [Meryman, 2007], ice almost always develops extracellularly, and the growth of ice detracts water from the extracellular solution [Meryman, 2007]. This mechanism leads to concentration of the medium, resulting in an increase in osmotic pressure and a concomitant dehydratation of cellular components [Meryman, 2007]. Since ice formations inside the cells can damage intracellular structures mechanically, intracellular vitrification, instead of freezing, seems a prerequisite for successful cryopreservation [Meryman, 2007]. Therefore, in a number of freezing procedures the addition of cryoprotectants, such as glycerol or DMSO, is recommended, as these compounds enter the cells and thereby counteract the loss of water yielding an effective vitrification [Meryman, 2007].

B Objective

With respect to long-term cryopreservation, various tissue preparations of subcutaneous, human cancer xenografts were used to establish a standardized freezing method in collaboration with Peter Höcherl. The work focused on the validation of the automated freezing procedure by studying the tumorigenicity of frozen and re-thawed tumor tissues in nude mice.

C Materials and methods

Chemicals and culture media

DMSO was purchased from Merck, Darmstadt, Germany in analytical quality. Eagle's Minimum Essential Medium (Sigma, Deisenhofen, Germany) was supplemented with 2.2 g/L $NaHCO_3$ (Merck, Darmstadt, Germany) and 110 mg/L sodium pyruvate (Serva, Heidelberg, Germany). DMEM (Dulbecco's Modified Eagle's Medium) was obtained from Sigma, Deisenhofen, Germany and supplemented with 3.7 g/L $NaHCO_3$ and 110 mg/L sodium pyruvate.

Computer controlled rate freezer IceCube 14S

To devise an automated freezing procedure, a computer controlled rate freezer IceCube 14S (SYLAB Geräte GmbH, Neupurkersdorf, Austria) was used. By means of a pressurized liquid cylinder, nitrogen is injected into the freezing chamber towards a turbine wheel [SYLAB Geräte GmbH, 2004]. Scripting of the freezing programs is carried out on an external personal computer, which is connected to the internal process controller within the freezing chamber. These internal controlling elements guarantee that, even in case of malfunction of the external computer, the IceCube freezer continues working until the end of the program [SYLAB Geräte GmbH, 2004]. The operating program of IceCube allows the set-up of freezing protocols with a number of variations, such as diverse start temperatures, freezing rates and additional features, e.g. the controlled start of crystallization by "autoseeding". Furthermore, the software displays the operating parameters such as the liquid nitrogen uptake as well as chamber and probe temperatures, which are registered by numerous Pt-thermometers [SYLAB Geräte GmbH, 2004].

Figure 1 shows an overview of the freezing device, containing the liquid nitrogen container, the IceCube freezing chamber and the external personal computer for controlling.

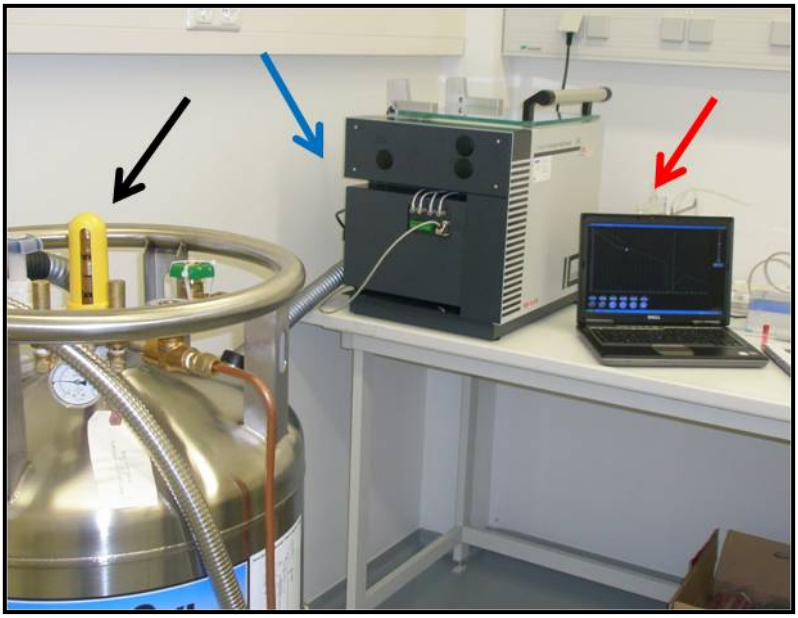

Figure 1: Technical assembly of the liquid nitrogen reservoir container (black arrow) and the corresponding computer-controlled (red arrow) rate freezer IceCube 14S (blue arrow).

Freezing procedure

For cryopreservation of tumor tissues, culture medium was modified as follows: Eagle's Minimum Essential Medium or DMEM (Sigma, Munich, Germany) were supplemented with DMSO (Merck, Darmstadt, Germany) to reach a final concentration of the cryoprotectant of 10 %. Subsequently, the mixture was sterile filtered and transferred into 2-mL CRYO.S™ reservoirs from Greiner Bio-One (Frickenhausen, Germany) under laminar air flow.

Differently seized tumors (mean area: 70-200 mm^2) were selected, and the animals were killed by cervical dislocation. The tumors were resected and carefully washed with sterile PBS (for preparation see Chapters 3, 4 and 5). For cryopreservation, the neoplasms were cut into small pieces of approximately 2 · 2 mm and immediately transferred into the cryo-tubes.

These tubes, containing a total of 6-10 tumor pieces, were stored on ice until the time of computer controlled rate freezing by means of the IceCube 14S freezer according to the following standard protocol:

Samples were taken from ice and allowed to stand at room temperature for approximately 10 min. Storage times on ice up to 2 h were well tolerated by the tissues. Subsequently, the samples were transferred into the freezing chamber of IceCube 14S, and the fully automated cryopreservation procedure was started according to the programmed parameters. The samples were linearly cooled down from the starting temperature at 20 °C to 0 °C within a period of 10 min, and the temperature was held at 0 °C for another 5 min, allowing the specimen to equilibrate. Thereafter, the freezing chamber was cooled down to approximately -15 °C, a temperature close to the experimentally determined crystallization point of the samples, within 15 min. In order to counteract tissue damage, mediated by the release of heat of crystallization, the chamber temperature was rapidly (within 56 seconds) decreased to -70 °C by massive influx of nitrogen (held for 30 s, supported by “autoseeding”). Having overcome this critical phase, the samples were linearly cooled down to -27 °C (within 2.15 min) and finally to -22 °C within another 2.50 min. The freezing protocol ended with cooling of the samples from -22 °C to -40 °C over a period of 18 min and from - 40 °C to -140 °C within another 50 min.

When the fully automated freezing process was finished, the cryo-tubes were immediately transferred into special plastic boxes and stored in Dewar containers over liquid nitrogen in the gas phase.

Figure 2 shows a detail of the temperature profile during automated freezing, measured by sensors in the sample and the freezing chamber. The starting point of crystallization is indicated by the black arrow in the graph. Abrupt, extensive cooling rapidly compensates the released heat, becoming manifest in a short overshoot of temperature.

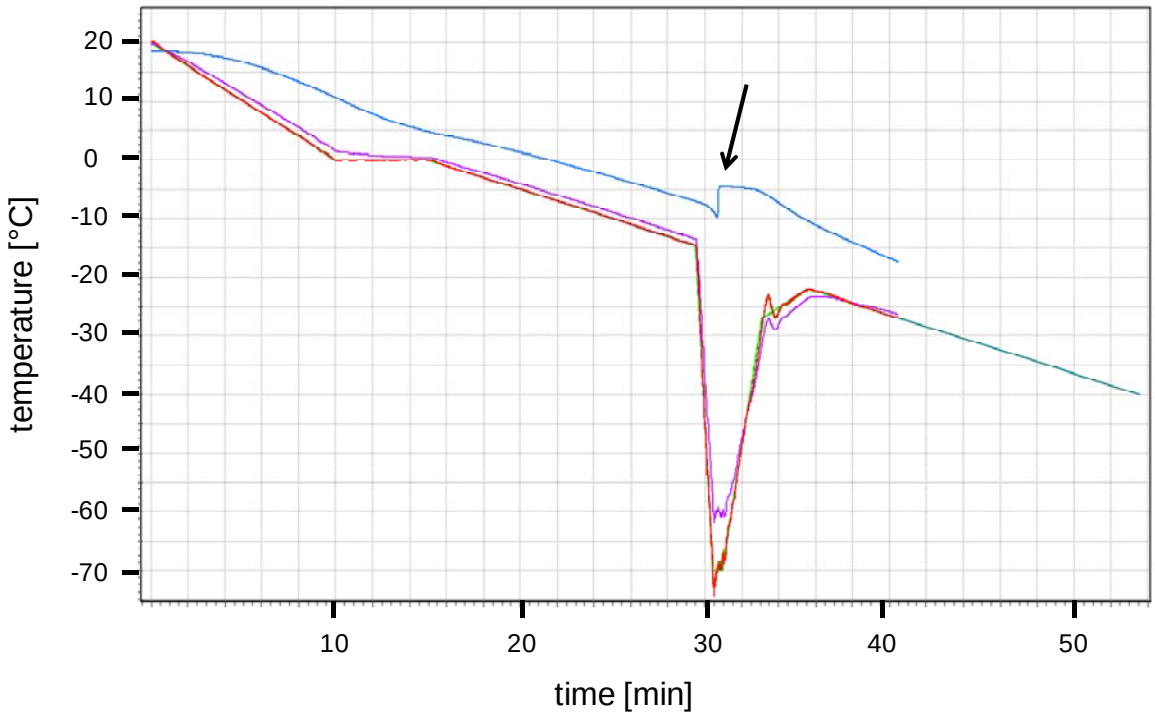

Figure 2: Details of the temperature registration (optimized freezing protocol) at different positions of the technical assembly. The blue curve represents the actual temperature within the sample, which shows a rise in temperature at the time of starting crystallization (black arrow). Temperature of the chamber at two different positions is shown in red and in violet, whereas the turquoise curve shows the programmed temperature profile and the green curve the actual course of the temperature during progressive cryopreservation.

Thawing procedure for subcutaneous xenograft implantation into nude mice

The cryo-tubes, containing the frozen tumor tissues, were transported on liquid nitrogen to the specific pathogen free (SPF) area of the animal laboratory. For subcutaneous implantation, the tumors where thawed by swiveling the cryo-tubes in warm water (37 °C) as long as the ice had been completely melted. Subsequently, the tissue pieces were carefully washed with sterile PBS in order to get rid of culture medium and DMSO. Finally, the tumor pieces were subcutaneously implanted under the thoracic dermis of nude mice by means of a trocar. Once a week, tumorigenicity and the body weight were monitored.

In vivo imaging procedures

To inspect the effect of freezing and thawing on the activity of luciferase and the functionality of Dsred2, tumor-bearing nude mice were imaged by BLI and FLI as described in detail in Chapter 5.

D Results

Effect of freezing and thawing on the tumorigenicity of selected tumor cells

To validate the elaborated freezing method, several subcutaneous tumors were selected for investigations on their tumorigenicity. Non-frozen tumor pieces, implanted into nude mice, served as a control.

Figure 3 shows the in vivo growth of genetically modified, human colon carcinoma HT-29 DsRed2 tumors. Whereas frozen and re-thawed tumor pieces showed retarded subcutaneous growth, compared to the controls, the take-rates of both groups turned out to be identical. In all mice xenograft implantation yielded solid tumors.

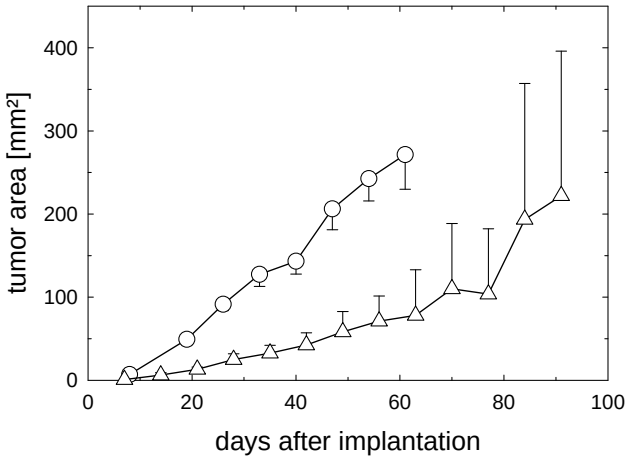

Figure 3: In vivo growth curves of genetically modified HT-29 tumors. The cells were transfected in vitro with the gene encoding the red fluorescent protein DsRed2 (HT-29 Dsred2 cells). Circles represent the growth kinetics of tumors, serially transplanted into control mice (12^{th} in vivo passage, mean values (±SEM), take-rate 100 %), whereas the triangles represent neoplasms that were obtained by implantation of frozen and re-thawed tumor pieces (12^{th} in vivo passage, mean values (±SEM), take-rate 100 %)

The growth kinetics of subcutaneous HT-29 Luc tumors at different in vivo passages is shown in **Figure 4**. In passage 5 (**Figure 4a**), both investigated groups showed high take-rates (control 83 %, test group 100 %), and the tumors formed in both groups demonstrated comparable growth characteristics. Similarly, these properties of HT-29 Luc tumors were also observed at higher in vivo passages (**Figure 4b** and **4c**).

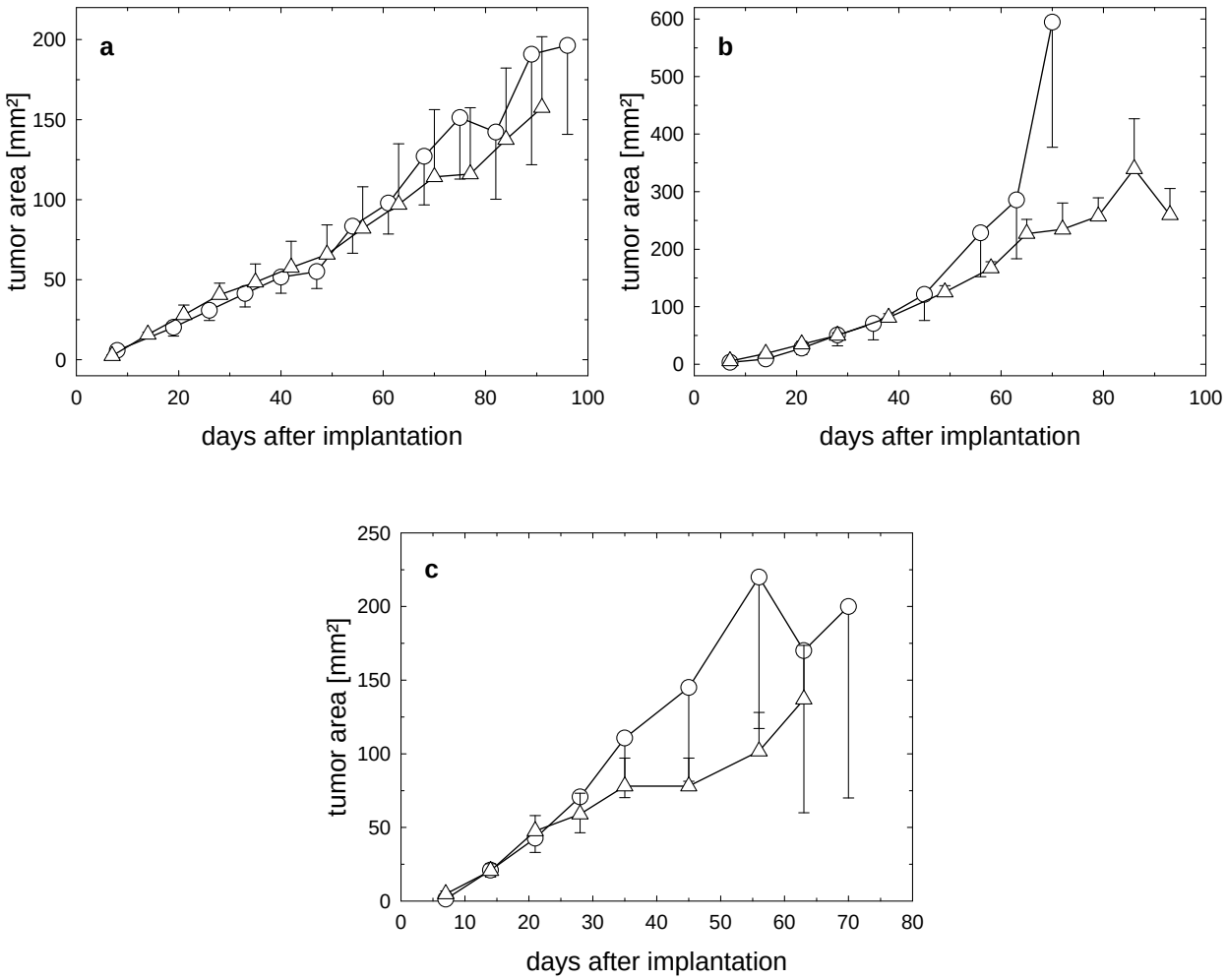

Figure 4: In vivo growth curves of subcutaneous, genetically modified human colon carcinoma HT-29 Luc, in different in vivo passages. Circles represent the growth kinetics of human xenografts in serially transplanted control mice, whereas the triangles show malignancies that were obtained by implantation of frozen and re-thawed tumor pieces. In vivo passage 5 (a) (mean values ± SEM, take-rate control mice 83 %, take-rate investigational group 100 %); in vivo passage 7 (b) (mean values ± SEM, take-rate control mice 100 %, take-rate investigational group 100 %); in vivo passage 8 (c) (mean values ± SEM, take-rate control mice 100 %, take-rate investigational group 100 %).

Frozen and re-thawed tumor pieces of HT-29 V_{alt} Hyal1 DsRed2 tumors (**Figure 5**) exhibited comparable retardation of subcutaneous tumor progression as previously described for HT-29 DsRed2 tumors. Nevertheless, freezing and thawing did not affect the take-rates of these xenografts (100 % for both colon carcinoma variants).

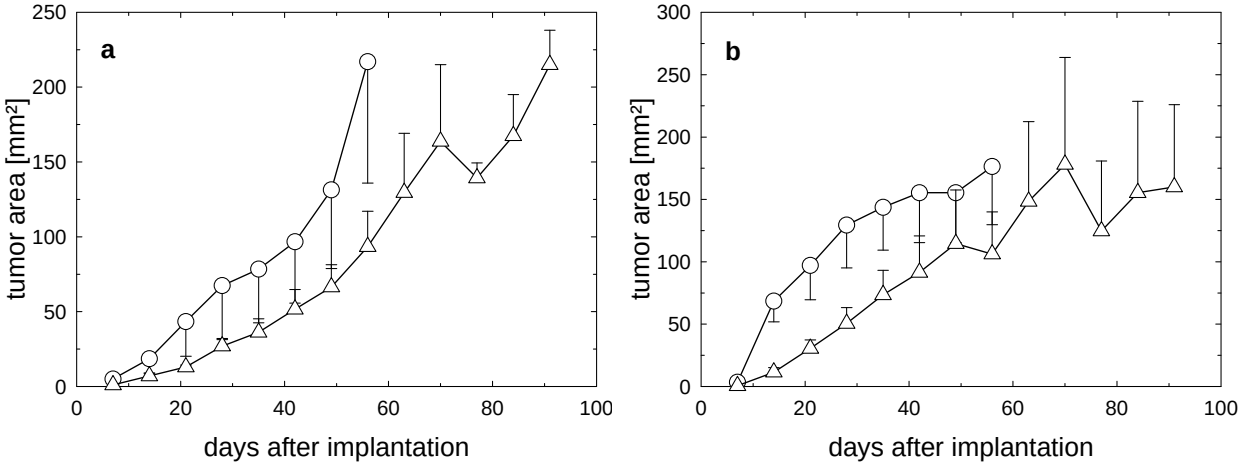

Figure 5: In vivo growth curves of subcutaneous HT-29 V_{alt} Hyal1 Dsred2 tumors (a). Circles represent the growth kinetics of tumors in control mice (6^{th} in vivo passage, mean values (±SEM), take-rate 100 %), whereas the triangles represent neoplasms, which were obtained by implantation of frozen and re-thawed tumor tissue (6^{th} in vivo passage, mean values (±SEM), take-rate 100 %).

Growth kinetics of subcutaneous HT-29 S_{neu} Hyal1 Dsred2 tumors (b). Circles represent the growth kinetics of tumors in control mice (12^{th} in vivo passage, mean values (±SEM), take-rate 100 %), whereas the triangles show malignancies that were obtained by implantation of frozen and re-thawed tissue pieces (12^{th} in vivo passage, mean values (±SEM), take-rate 100 %).

Figure 6 shows the in vivo growth kinetics of the human triple-negative breast cancers HCC 1806 and HCC 1937. The graphs show the 0^{th} in vivo passage, representing tumor formation after tumor cell injection, and the 1^{st} in vivo passage of subcutaneous tumors, which was obtained by the implantation of frozen and re-thawed solid tumor pieces. The freezing procedure did not affect the tumorigenicity of the cells, and the take-rates retained at maximum (100 % for both mammary carcinoma variants after implantation of tumor pieces).

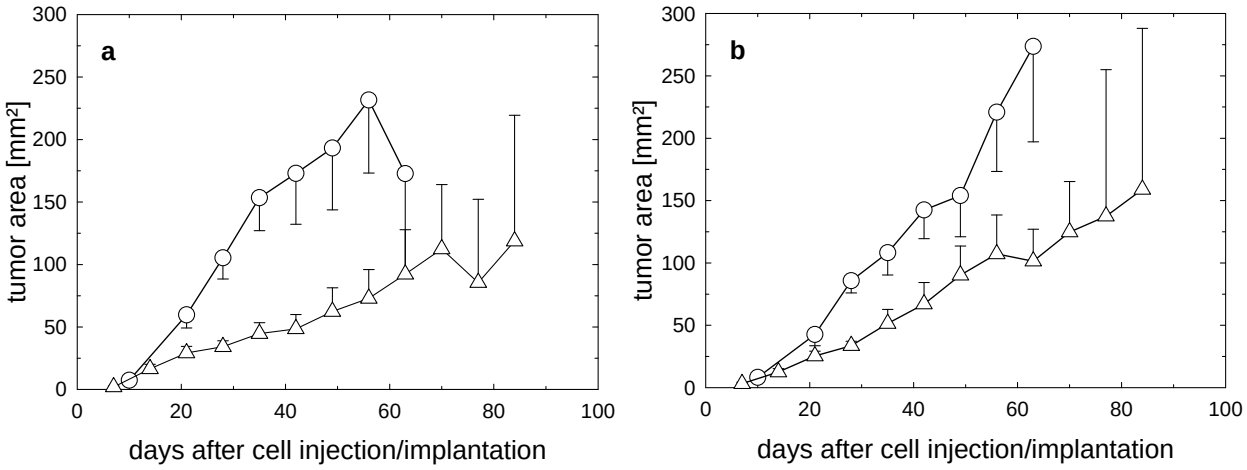

Figure 6: In vivo growth curves of subcutaneous, human breast cancer xenografts in nude mice. HCC 1806 tumors (a); circles represent the growth behavior of subcutaneously injected cells (0^{th} in vivo passage, mean values (±SEM), take-rate 100 %), whereas triangles show the growth kinetics of tumors that were obtained by implantation of frozen and re-thawed tissue pieces (1^{st} in vivo passage, mean values (±SEM), take-rate 100 %). HCC 1937 tumors (b); circles represent the growth behavior of subcutaneously injected cells (0^{th} in vivo passage, mean values (±SEM), take-rate 100 %), whereas triangles show the growth kinetics of tumors, obtained after implantation of frozen and re-thawed tissue pieces (1^{st} in vivo passage, mean values (±SEM), take-rate 100 %).

Effect of freezing and thawing on the activity of luciferase and DsRed2 fluorescence

Since cryopreservation of solid, genetically modified tumors might be interesting for animal experiments, the functionality of introduced proteins had to be proven after freezing and thawing. For this purpose, the luciferase activity and the DsRed2 fluorescence were investigated by BLI and FLI (see Chapter 5).

Freezing and thawing did not affect the activity of luciferase. The intraperitoneal injection of 4 mg D-luciferin into nude mice, bearing subcutaneous HT-29 Luc colon carcinoma, resulted in strong specific bioluminescence signals, not only when the tumor tissues were implanted freshly, but also when frozen and re-thawed tissue samples were used for implantation (**Figure 7**).

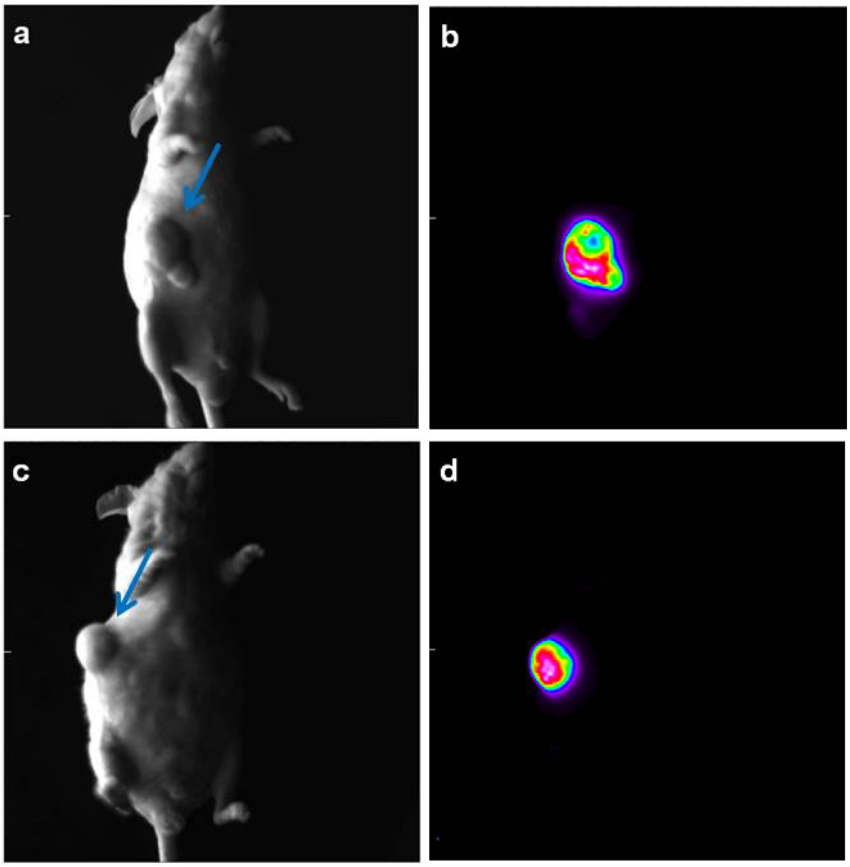

Figure 7: Optical imaging of subcutaneous HT-29 Luc tumors (5th in vivo passage) using BLI.

Bright field image and corresponding bioluminescence signal originating from a "control-tumor" which had formed after implantation of a fresh small tumor piece into the animal (a, b).

Bright field image and the specific bioluminescence from a tumor, which had grown after implantation of a frozen and re-thawed tissue piece (c, d).

Instrument settings of BLI: stage height h2b, exposure time 90 s, normal gain 0, readout rate 1 MHz. at 16 bit. Tumors are marked by blue arrows in the bright field images.

Effects of freezing and thawing on the functionality of the red fluorescent protein Dsred2 were investigated by means of FLI (**Figure 8**). As observed for the activity of luciferase, the freezing did not affect the functionality of DsRed2. Tumors, which had developed after implantation of frozen and re-thawed tumor pieces, could be easily visualized by their fluorescence.

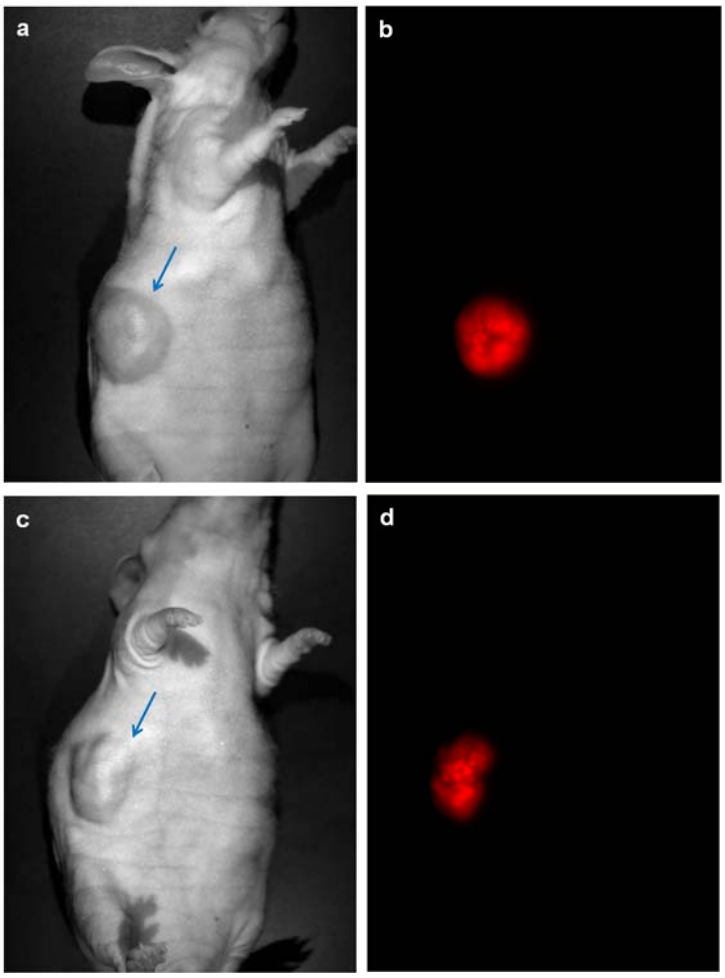

Figure 8: Optical imaging of subcutaneous HT-29 Dsred2 xenografts (a, b), 6^{th} in vivo passage, and HT-29 S_{neu} Hyal1 Dsred2 double-mutants (c, d), 12^{th} in vivo passage. Tumors were generated after implantation of frozen and re-thawed tissue pieces. Blue arrows point to the tumors in bright field images.

Fluorescence images show the overlay of 23 fluorescence images in the range of 580-800 nm in 10 nm steps, analyzed by the unmixing procedure.

Instrument settings were as follows: stage height h2, excitation filter 503-555 nm, emission 580 nm cut off, exposure time 70 ms (HT-29 Dsred2 tumor) and 60 ms (HT-29 Sneu Hyal1 Dsred2 tumor).

E Summary

With respect to long-term storage of solid tumor samples, a standard procedure for computer controlled rate freezing was developed. Several parameters were optimized in order to reduce putative tissue damaging by released heat of crystallization. For validation of the method, several human tumor types were investigated with respect to tumorigenicity after controlled freezing and thawing. Furthermore, effects of freezing and thawing on the functionality of luciferase or the fluorescent protein DsRed2 were inspected by BLI and FLI.

Tumorigenicity studies showed that in several cases the implantation of cryopreserved tissue samples yielded in a slightly retarded growth compared to the implanted freshly dissected tumor pieces. Nevertheless, all investigated types of xenografts showed a take-rate of 100 % after implantation subsequent to freezing and re-thawing. In addition, the functionalities of luciferase as well as the red fluorescent protein DsRed2 were retained during cryopreservation. Thus, future tumorpharmacological studies using human xenografts in immunodeficient mice will be facilitated a lot by the established automated freezing procedure.

References

Ehrhart, F., Schulz, J. C., Katsen-Globa, A., Shirley, S. G., Reuter, D., Bach, F., Zimmermann, U. and Zimmermann, H. (2009). A comparative study of freezing single cells and spheroids: Towards a new model system for optimizing freezing protocols for cryobanking of human tumours. Cryobiology **58**(2): 119-127.

Loken, S. D. and Demetrick, D. J. (2005). A novel method for freezing and storing research tissue bank specimens. Hum. Pathol. **36**(9): 977-980.

Meryman, H. T. (2007). Cryopreservation of living cells: principles and practice. Transfusion (Paris). **47**(5): 935-945.

Oktay, K. (2001). Ovarian tissue cryopreservation and transplantation: preliminary findings and implications for cancer patients. Hum. Reprod. Update **7**(6): 526-534.

Royere, D., Barthelemy, C., Hamamah, S. and Lansac, J. (1996). Cryopreservation of spermatozoa: a 1996 review. Hum. Reprod. Update **2**(6): 553-559.

SYLAB Geräte GmbH (2004). Operator Manual 14S.